THE UNIVERSITY OF CHICAGO

NEXT GENERATION MEASUREMENTS OF THE COSMIC MICROWAVE BACKGROUND WITH NEW OPTICAL DESIGN AND ANALYSIS

A DISSERTATION SUBMITTED TO
THE FACULTY OF THE DIVISION OF THE PHYSICAL SCIENCES
IN CANDIDACY FOR THE DEGREE OF
DOCTOR OF PHILOSOPHY

DEPARTMENT OF PHYSICS

BY
GRACE EDITH CHESMORE

CHICAGO, ILLINOIS
JUNE 2023

Table of Contents

LIST OF FIGURES vii

LIST OF TABLES xv

ACKNOWLEDGMENTS xvii

ABSTRACT xxi

1 INTRODUCTION 1
1.1 Overview of Λ-CDM Cosmology 2
1.2 Questions to be Answered 5
1.3 Signals in the Comsic Microwave Background 5
1.4 Why Care About Beams? 9
1.5 Status of the Field 10
1.6 Outline of Thesis 11

2 INSTRUMENT OVERVIEW 14
2.1 Atacama Cosmology Telescope 15
2.2 The Simons Observatory 18
2.2.1 Large Aperture Telescope 19
2.2.2 Small Aperture Telescope 21
2.3 Optics Tubes 23
2.3.1 The Status of the Simons Observatory 24

3 METAMATERIAL MICROWAVE ABSORBER (MMA) AND ITS CRYOGENIC APPLICATIONS 25
3.1 Introduction 25
3.2 Optical Design 26
3.3 Optical Testing 28
3.3.1 Optical Hardware 29
3.3.2 Receiver Electronics 30
3.3.3 Measurement 31
3.4 Reflection Measurement 33
3.5 Scattering Measurement 34
3.6 Future Applications 36

3.7 Discussion . . . 38

4 SILICON PROPERTIES AT MILLIMETER WAVELENGTHS . . . 40
4.1 Introduction . . . 40
4.2 Procedure . . . 42
4.2.1 Optical Hardware . . . 42
4.2.2 Receiver Electronics . . . 42
4.2.3 Samples: Neutron-irradiated and Intrinsic Silicon . . . 43
4.3 Reflectometry and Transmissivity . . . 43
4.3.1 Modeling . . . 43
4.3.2 Fitting . . . 45
4.4 Results . . . 46
4.5 Discussion . . . 47

5 CHARACTERIZING THE LARGE APERTURE TELESCOPE RECEIVER WITH RADIO HOLOGRAPHY . . . 48
5.1 Introduction . . . 48
5.2 SO Large Aperture Telescope Optics Tubes Design . . . 50
5.3 Measurement Approach . . . 52
5.3.1 Cryogenic System . . . 52
5.3.2 Holography System . . . 54
5.4 Results and Interpretation . . . 56
5.4.1 Near-Field Beam Maps . . . 56
5.4.2 Propagation of Fields . . . 57
5.5 Filter Removal . . . 60
5.6 Cross-Polarization . . . 62
5.6.1 Modeling . . . 62
5.6.2 Results . . . 63
5.7 Public Code . . . 64
5.7.1 Optics Simulation . . . 64
5.7.2 Open Source Holography . . . 66
5.8 Discussion . . . 66

6 PRELIMINARY CHARACTERIZATION OF THE SMALL APERTURE TELESCOPE WITH RADIO HOLOGRAPHY . . . 68
6.1 Introduction . . . 68
6.2 Measurement Approach . . . 70
6.2.1 Cryogenic System . . . 70
6.2.2 Holography System . . . 71
6.3 Results and Interpretation . . . 72
6.3.1 Near-Field Beam Maps . . . 72
6.3.2 Propagation of Fields . . . 75
6.4 Discussion . . . 75

7 HOLOSIM-ML: MACHINE LEARNING APPLIED TO THE EFFICIENT ANALYSIS OF RADIO HOLOGRAPHY MEASUREMENTS OF COMPLEX OPTICAL SYSTEMS . . . 81
7.1 Introduction . . . 81
7.2 Motivation . . . 83
7.3 Beam Simulation . . . 85
7.4 Panel Fitting with Machine Learning . . . 88
7.5 Measurement Practicalities and Robustness of Method . . . 92
7.6 Public Code . . . 94
7.7 Discussion . . . 95

8 THE ATACAMA COSMOLOGY TELESCOPE: BEAM ESTIMATION FOR DR6 WITH POINT-SOURCE STACKING . . . 97
8.1 Introduction . . . 97
8.2 Observations . . . 99
8.3 Methods . . . 100
8.3.1 Point-source Selection . . . 100
8.3.2 Stacking . . . 103
8.3.3 Bias From Stacking . . . 106
8.3.4 Radial Profiles . . . 106
8.3.5 Beam Window Functions . . . 107
8.4 Simulation Pipeline . . . 108
8.4.1 point-source Map Simulation . . . 109
8.4.2 CMB Simulation . . . 110
8.4.3 Noise Simulation . . . 110
8.5 Results . . . 112
8.5.1 Main Beam . . . 112
8.5.2 Temperature to Polarization Leakage Beam . . . 113
8.6 Discussion . . . 117

9 CONCLUSION . . . 118
9.1 Summary of Research . . . 119
9.2 Forecasting the Future of Cosmology . . . 121

A OPEN SOURCE HOLOGRAPHY . . . 123
A.1 Open-Source Holography . . . 123
A.2 Forward Modelling . . . 125
A.3 Measurement Requirements . . . 127

B HOLOGRAPHY RECEIVER POLARIZATION THROUGH THE LARGE APERTURE TELESCOPE OPTICS TUBE . . . 129
B.1 General Notation . . . 130
B.1.1 Stokes Parameters . . . 130
B.1.2 Jones into Mueller Matrix . . . 130
B.1.3 Rotation . . . 131

B.2 Mueller Matrices 131
B.2.1 Polarized Source 131
B.2.2 Polarizing Grid 132
B.2.3 Optics Tube (Generic Instrument) 133
B.2.4 Detector 134
B.3 Putting It All Together 135

C HARMONIC TRANSFORM OF THE ON-SKY BEAM 136

BIBLIOGRAPHY 139

List of Figures

1.1 Left: Spectrum of the CMB from the COBE satellite. The deviation from an ideal blackbody is magnified $\times 400$ in the bottom panel. Right: First-year maps from the COBE Differential Microwave Radiometer in 1992. Source: COBE Collaboration [1, 2]. 2

1.2 The history of the universe as we understand it today. After the Big Bang, the CMB is emitted during the Recombination era at around 380,000. The photons emitted then traversed large-scale structure to get to our detectors, and therefore we can study late universe large-scale structure through measurements of the CMB. Source: ESA/Planck Team [3], re-touched by Chesmore. 3

1.3 The CMB temperature power spectra measured by WMAP (yellow), the South Pole Telescope (blue) and the Atacama Cosmology Telescope (purple). The temperature anisotropies of the CMB will be measured with the Simons Observatory and CMB-S4, two upcoming cosmology experiments, with further precision. Source: The Atacama Cosmology Telescope Collaboration [4]. 6

1.4 The polarization modes of the CMB. The E modes have no curl, while the B modes have no divergence. 7

1.5 Temperature and polarization spectra measured by the Atacama Cosmology Telescope in 2018 [5], compared to spectra measured by WMAP and Planck, as well as ACT's residuals after fitting to cosmological model spectra. Source: ACT 2018 Cosmological Results [5]. 8

1.6 The simulated CMB power spectrum at varying spectral index of inflation n_{s}, and varying neutrino species N_{eff}. Simulations are made with CAMB [6] and show the TT spectrum's deviation from nominal values, with $n_s \pm \sigma_{n_s}$, and $N_{\mathrm{eff}} \pm \sigma_{N_{\mathrm{eff}}}$. In red is the sensitivity achieved by Planck, and in blue is the sensitivity goal of Simons Observatory. The right-most panel simulates a mischaracterized instrument beam and how it can mimic deviations in the TT spectrum of the CMB. 10

2.1 The Atacama Cosmology Telescope, surrounded by its outer ground screen. The inner co-moving screen further shields the instrument from any stray-light. The primary mirror is behind the co-moving screen. Source: Debra Kellner. 15

2.2 The Simons Observatory (SO) and Atacama Cosmology (ACT) site in the Atacama Desert, Chile. The ACT telescope sits within a ground-shield which can be sen in the bottom center. The outer ground screen protects the telescope from stray light. The inner co-moving ground-screen further protects the telescope from stray light during observations. Source: Debra Kellner 16

2.3 Ray-trace diagram of the Atacama Cosmology Telescope [7]. The telescope is an off-axis Gregorian with two reflectors: the primary is 6 m in diameter and the secondary 2 m. The rays trace into the Millimeter Bolometer Array Camera (MBAC) cryostat which houses the telescope's detectors. Source: The Atacama Cosmology Telescope Collaboration [7]. 17
2.4 Ray-trace diagram of the Simons Observatory Large Aperture Telescope [8]. The telescope is a cross-Dragone with two reflectors, both 6 m in diameter. The rays trace into the Large Aperture Telescope Receiver (LATR) cryostat which houses 13 optics tubes. The optics tubes guide the photons onto the detectors in the focal plane, which are cooled to 100 mK. Source: The Simons Observatory Collaboration. 18
2.5 Left: Three Small Aperture Telescope cryostats, with the front cross-section showing the inner optics tube. Right: Ray-trace diagram of the Simons Observatory Small Aperture Telescope [9]. Source: The Simons Observatory Collaboration. 20
2.6 Large Aperture Telescope Receiver (LATR) optics tube in the Simons Observatory. A detailed rendering of the optics tube design is shown in the upper part, and a simplified schematic cross-section is shown in the bottom part. Incoming light enters the optics tube from the right and focuses on the detector arrays on the left via three lenses. The yellow-shaded region in the bottom part shows the geometric light ray profile. Operational temperatures for different parts of the optics tube are also annotated. More details of the optics tubes are described in [10]. The MMA tiles are installed in the regions between lens 1 and lens 2 at 4 K. Fig. 3.2 shows a cross-section of the MMA tile assembly (box with red dashed lines) in the optics tube and the detailed design of one tile. A flat version of the MMA tile (Section 3.6) was also used to cover the front and back of the Lyot stop at 1 K. 22

3.1 Manufactured MMA tiles. The manufactured tiles are presented from different perspectives. The top left photo shows one tile from the absorbing surface. A microscope photo of the pyramids is shown in the insert. The pitch between pyramids is kept as 0.6 mm as designed. The bottom left two photos show the back of the tile from two other perspectives. The light weighting pockets are visible along with the brass injected M3 nut for fastening. The photo on the right shows the assembly of 240 tiles installed on the wall of the optics tube section (see Fig. 2.6). A ruler (~ 30 cm) is placed in the center for scale. Note that the absorbing surface appears to be black and featureless in the assembly photo. The condition stays the same regardless of lighting in the room, which supports the effectiveness of the AR-coating design even in optical. 27

3.2 MMA tile design. A snapshot of a single tile design is shown. The tilted upper surface has the pyramidal structures as described in Section 3.2. A zoom-in plot shows details of the pyramidal structures, acting as a metamaterial anti-reflection coating. Another insert on the right zooms in further and shows one single unit of the metamaterial structure, with a pitch, $p = 0.6\,\text{mm}$ and a height, $h = 1.5\,\text{mm}$. The tile bottom is curved to fit the cylindrical inside surface of the metallic optics tube, which is used for structural support, heat sinking, and reflective optical termination for the absorptive tiles. A lip and a dent are for seamless tessellating. A cross-section of the segmented tilted surface is shown in the lower left part. In a time-reverse fashion, light rays coming from the left would hit the tilted surface with a $< 64^\circ$ angles of incidence, where the absorbing surface achieves the desired optical performance. 29
3.3 Specular reflectance measurements. The two panels show the specular reflectance measurements of the MMA tiles and the TK tiles at different angles of incidence, including 15°, 30°, 45°, 60°, and 65°. The samples are measured in W-band (90 GHz to 110 GHZ) and D-band (130 GHz to 170 GHz). The left panel shows the W-band (90 GHz to 110 GHZ) and D-band (130 GHz to 170 GHz) reflectance of the MMA tiles. The measurement gap in the left panel is due to the different frequency bands of the two sources used in the setup. The right panel measures the W-band (90 GHz to 110 GHZ) reflectance of the TK tiles. The two panels share the same y scale for comparison. The measurement of a flat black polyethylene sample without a AR-coating is included in both panels, which is conducted with a 30° angle of incidence. Comparing the sample without an AR-coating (purple triangles) and the MMA tiles (blue crosses), $\sim -20\,\text{dB}$ specular reflectance reduction is achieved with the metamaterial AR-coating. 30
3.4 Optical measurement setup sketch. The orange lines represent the beam as it travels from the source feed-horn, collimated off of the first mirror and to the sample. After being reflected/scattered by the second mirror, the beam is focused into the receiver to be measured. Incident (θ_i) and receiver (θ_r) angles are controlled by a motor for measuring different angles of incidence and scattered power. 31
3.5 The correlation receiver setup diagram. A splitter sends one signal from a millimeter-wave source to a Pacific Millimeter harmonic mixer, while sending the same signal to be modulated by the device under test. The reference and modulated signal are mixed with an LO with an offset frequency f_{offset} from the millimeter wave source. The two Pacific Millimeter harmonic mixers extract interference information caused by f_{offset} and sends this to the ROACH-2 field programmable gate array (FPGA) board where the two signals are correlated. . 32
3.6 MMA measurement sample. MMA tiles are individually bolted into a 3D-printed plate such that each absorbing surface sits flat to form a $30.5 \times 30.5\,\text{cm}$ testing surface. 33

3.7 Scattering measurement. The four panels show front scattered power off the sample with the source located at four angles of incidence θ_i: (a) 15°, (b) 30°, (c) 45°, and (d) 65°. The source was set at 110 GHz. Each of the measured data points was averaged over 17 different sample rotation angles, from which the associated error bars were also estimated. The error bars are too small to be visible at these y scales. The vertical black lines indicate the position of the specular reflection directions. The blue data points show the results from the MMA tiles, while the red data points show the results from the TK tiles. The TK tiles are measured to have an overall higher scattering than the MMA tiles, which leads to a higher integrated scattering power, as shown in Table 3.1. . . . 35
3.8 Manufactured square tiles. The 2.5 cm × 2.5 cm flat tiles are also manufactured via injection molding with the same pyramidal structure on the absorbing surface. The main photo on the bottom shows two square tiles from the front and the back. Major features on the tiles were denoted as well. A microscope photo of the pyramids is shown on the top left. The photo shows sharp features of the pyramids, which are only 0.6-mm wide and 1.5-mm tall. The pyramids show sharper features compared to the ones in the tilted tiles (Fig. 3.1). That is because the square tiles are smaller with a simpler shape, which facilitates the manufacturing process. 37

4.1 Reflectivity of intrinsic (top) and neutron-irradiated (bottom) Silicon against frequency [GHz]. 44

5.1 The Simons Observatory (SO) Large Aperture Telescope (LAT), featuring a segmented primary and secondary mirror. The mirror's focus is hidden inside the conical baffle near the front of the receiver. The receiver can hold up to thirteen optics tubes. Source: The Simons Observatory Collaboration. 49
5.2 The Simons Observatory LATR optics tube. Light enters the optics tube from the right through an ultra-high-molecular-weight polyethylene (UHMWPE) window, and travels through a series of Infrared-Blocking filters (IR), including one alumina IR filter, and passes through the 4 K Low-Pass Edge mesh filter (LPE). The light is focused on the detector arrays on the left by the three lenses, with two additional LPE filters near the 1 K and 100 mK stages. The components within the optics tube are further described in [10]. 51
5.3 Schematic of holography setup. Two local oscillators (LOs) supply frequencies (LO1 and LO2 = LO1 + f_{off}), one of which is multiplied by the active multiplier factor M , while the other serves to down convert the reference and modulated signals into the intermediate frequency. 53
5.4 Holography beam map measurements in the mid-frequency band. Top: Power at each measured frequency (peak-normalized in each map). The hexagonal sidelobes in the power beam maps are higher in power than the signal-to-noise of the system (45 dB). Bottom: Wrapped phase at each measured frequency. 55
5.5 Near-field band-averaged MF1 and MF2 beams, simulated and measured with radio holography. Left panel: Radially binned. Right panel: 2D simulated and measured near-field beams. 56

5.6 All beam maps propagated at the secondary illumination of the Large Aperture Telescope. The spilled power to 300 K is calculated by integrating power outside the boundary of the secondary (red line) with respect to total integrated power of the map. 57
5.7 Top row: Using FD, the LATRt measurements are propagated through the LAT from the near-focal plane, to the far-field. Bottom row: Radial profile of the measured(simulated) far-field beams in the F90 and F150 bands, plotted in red(black). The lack of diffraction rings in the radial average is explained by the convolution of the measurement(simulation) due to the rectangular source aperture physically in the setup (artificially in the model, see Appendix A.2). . . 59
5.8 A) Time-reversed ray-trace of the SO LAT Optics Tube (OT) with one filter (orange), near the second lens. With 0% on-axis reflectivity of the filter, rays(blue) emerge from the focal plane and exit the OT window. With an on-axis reflectivity of 5.64 % (average LPE filter reflectivity in the full band), rays reflected off of the filter(red) go back to the reflective focal plane (copper and reflective), and then propagate out the front of the window. This is verified in the simulation, as the main beam in front of the OT shows the shape of the focal plane at -25 dB. B) In orange is the measured reflectivity (1-transmission) of the 6.8 cm^{-1} LPE filter, which is placed at the 1-K stage in the optics tube. The red(blue) line shows the measured integrated fractional power outside the main beam at each frequency with(without) the filter in the optics tube. C) Band-averaged near-field beam maps with and without the filter in the optics tube. With the filter, beam maps show extra scattering in the top parts of the map, through the upper portion of the LATRt hexagonal window (hexagonal power around the main beam at roughly -20 dB due to reflection). 61
5.9 Left: Polarization measurement setup on the LATRt. The dielectric polarizing grid sits over the holography receiver's beam path and rotates about the vertical axis, polarizing the source as it enters the cryostat. A hexagonal aluminum plate covers the rest of the window and is secured in place with aluminum tape. Right: Polarized beam power (band-averaged from 85-120 GHz) as a function of grid rotation, measured with the holography setup described in Section 5.3. Co-polarization (blue) holds the source waveguide aligned with the receiver orientation. Cross-polarization (green) uses a 90° waveguide to make the source aligned perpendicular to the receiver orientation. The polarization model (Eq. B.1) is fit using an MCMC and with no instrument polarization. 63
5.10 Constrained parameters from polarization model (Eq. B.1), detector angle ϕ_{det}, grid efficiency η_{grid}, and cross polarization ϵ. The dashed lines show the 16^{th}, 50^{th}, and 84^{th} quantiles of the fit. We find a cross polarization of less than 1%, a detector tilt of roughly -31 deg, and a grid efficiency of roughly 97%. 65

6.1 Left: Cross-section of the Small Aperture Telescope (SAT) optics tube. Light enters through the high-density polyethylene window (UHMWPE) and through the cryogenic half-wave plate (CHWP). The lenses re-image the beam onto the focal plane, where the holography detector measures power and phase at a given source position. Right: SAT cryostat used in holography testing. Source: The Simons Observatory Collaboration, Remington Gerras. 69
6.2 SAT Focal Plane. The two holography receivers are outlined in red, separated by 120°. Two receivers are installed for redundancy, but also served as a useful tool when characterizing systematics (such as "ghosting", or spurious signal in the beam maps, and polarization effects). 70
6.3 Lab photos of the holography setup on the SAT. Left: The holography source, covered in a sheet of eccosorb to control scattering, is centered above the SAT window and points directly into the SAT, sitting below. Right: The holography electronics sit on a cart next to the SAT readout. The SAT window in the top left is made of UHMWPE. 72
6.4 Left: Preliminary near-field beam shape of the SAT in MF-1. Beams are averaged over all frequencies measured, and the averaged beam is then radially averaged to get the near-field beam profile. Right: Preliminary beam sizes of the SO SAT in MF-1. Far-field beams measured with holography (blue) are radially binned and the FWHM is obtained from the resulting 1D beam profile. Simulations are obtained using a diffractive optics simulation, and plotted are where the measured beam sizes with 2σ errorbars. 73
6.5 Preliminary far-fields of the SAT optics tube in the MF-1. The near-field measured beam is propagated to the far-field for each frequency. The aliasing of the measured phase in the near-field (discussed in Section 6.3) caused an artificial directional shift in the on-sky beam, which we center before plotting. 74
6.6 Co-polar normalized power of the Simons Observatory Small Aperture Telescope near-field beam. 77
6.7 Co-polar phase of the Simons Observatory Small Aperture Telescope near-field beam. 78
6.8 Cross-polar normalized power of the Simons Observatory Small Aperture Telescope near-field beam. 79
6.9 Cross-polar phase of the Simons Observatory Small Aperture Telescope near-field beam. 80

7.1 Top: Far-field beam simulation of a 150 GHz source, with surface error RMS of $0\,\mu$m, $20\,\mu$m, $35\,\mu$m, and $50\,\mu$m. The side-lobes around the central beam increase as RMS of panel errors increases. Center: Window function W_ℓ of far-field beams at 150 GHz with combined surface RMS of $50\,\mu$m, $35\,\mu$m, $20\,\mu$m, and $0\,\mu$m. Bottom: Difference of window functions W_ℓ in top plot, w.r.t. window function of far-field beam with surface error RMS of $0\,\mu$m, $W_{\ell,0\mu}$. 84

7.2 Holography geometry. A source on a 5 m tower sits at a distance R_{source} above the aperture plane of the LAT. Two receivers, one "reference" receiver pointed straight at the source, and the receiver in the focal plane, measure the amplitude and phase of the source. The focal plane receiver is offset δf from the nominal focus. 85
7.3 Simulated HWFE at the aperture plane with surface errors of 35 μm RMS on a) only M1, b) only M2, and c) both M2 and M1. 87
7.4 Results from simulation. The top left panel shows the input simulation, which had 35 micrometer RMS HWFE. The top right panel shows the predicted aperture phase given the ML determined estimates for the panel errors, and the bottom shows the residuals. 89
7.5 The left and middle columns show the surface errors on the Primary and Secondary mirrors after holography has been used to correct the mirror surfaces. The right column shows the HWFE as a function of focal plane position. The top row shows results for holography taken at a single position (see red dot). The middle row shows results for binocular holography (combining measurements from two positions, see red dots). The bottom row shows results for trinocular holography (combining measurements from three positions, see red dots). 91

8.1 Distribution of the total number of point-sources that were in the catalog (greys) and ultimately became part of the final beam analysis (colored) for all arrays combined, shown by observing seasons from 2017–21. point-sources used in the stacking are separated into Special(red dots) and ML(gradient hexagonal bins) sources (the two types of sources are described in §8.3.1). 101
8.2 Spatial distribution of all point-sources in the catalog(grey) and the selected point-sources used in stacking(colored). The color bar shows the flux of the Special(ML) sources, which are plotted as triangles(circles). The regions of the map with no used point-sources indicate regions which are masked out prior to stacking. The mask ensures that the stacked point-sources are in the same regions of the sky used in cosmology science. 103
8.3 Inpainting-subtracted method as described in §8.3.2 for F090 PA5. Top row: Stacked beam without inpainting subtraction (left) and stacked beam including inpainting-subtracted method (right). Bottom: Inpainting signal which is subtracted during the stacking procedure for F090 PA5 (note the linear scale colorbar). This shows the large angular-scale signal which is removed from the stacked beam with the inpainting method. 105
8.4 Example of a simulated map used to characterize the stacking bias. This example is for PA5 in the F090, zoomed in to an area of 2 deg $\times$2 deg. Top left: Point-source map using the input catalog RA and DEC coordinates. Top right: Simulated CMB. Bottom left: Simulated noise [11]. Bottom right: Final simulated map after combining the previous three components. This process is done for each PA and F-band, and repeated 100 times to estimate radial profile errors. 109

8.5 Mean simulated radial profile at each F-band and PA, averaged over 100 simulations. Mean simulated profiles are shown for Special(red) and ML(blue) sources, with error bars calculated from the covariance matrix of the 100 profiles. Each profile is then compared to the corresponding planet-derived beam(black) in the bottom panel of each plot. This shows the bias from the stacking procedure is minimal and can be neglected in the subsequent analysis. 111
8.6 Stacked radial profile at each F-band and PA. Profiles are shown for Special(red) and ML(blue) sources, with error bars calculated from the covariance matrix of 100 simulated stacked beams. Each profile is then compared to the corresponding planet-derived beam(black) in the bottom panel of each plot. 112
8.7 The panels show the ratio of the window function derived from the stack to those of the preliminary Uranus-derived window functions, separated by high and low RA and DEC. The top two rows are Special sources, and the bottom two rows are the ML sources. Each ratio is set to 1 at $\ell = 1050$ for F090 and $\ell = 1525$ for F150 and F220. The stack made up of the combined set of point-sources is depicted by the red curve. 114
8.8 Polarization leakage from stacked F090 PA5 beam, for the ML sources. Top row: $T \to Q$ leakage. Bottom row: $T \to U$ leakage. Left column: stacked map, Middle column: modeled polarization leakage, Right column: difference between stacked and modeled beams. The low signal in the right column suggests that the one-dimensional leakage model is able to capture the polarization leakage of the stacked profiles. 115
8.9 Polarization leakage, $B_\ell^{T\to P}$, from stacked and planet-derived profiles. Leakage beams are separated by Special(dashed-dotted) and ML(dashed) sources, with leakage from the planet profile(solid) plotted for comparison. 116

9.1 A snapshot of every chapter in this thesis, with the temperature power spectrum of the CMB overlaid. 118

A.1 The Simons Observatory Large Aperture Telescope optics tube focal plane readout, which is cooled to 4 K during measurements. The holography receivers (two receivers for redundancy) are approximately 7.4 cm from the center of the focal plane. 124
A.2 Forward modelling method with the F150 band-averaged holography data. Column 1: Near-field holography data(top) and convolved simulation with a scattering term(bottom). Square is 12×12 cm. Column 2: Far-field holography data(top) and convolved simulation with a scattering term(bottom). Diffraction spikes consistent with a convolution from a square aperture are present in both the measured far-fields and the simulated far-fields, due to the source horn having a rectangular aperture face. Square is 20×20 arcmin. Column 3: Far-field holography data with diffraction model removal(top) and convolved simulation with a scattering term with diffraction model removal(bottom). Square is 20×20 arcmin. 126
A.3 Simulated scattering term (power) in the near-field(left), at the secondary illumination(middle) and propagated to the far-field(right). Each subplot is the band-averaged simulation over all F150 frequencies. 127

List of Tables

1.1 The most recent cosmological parameters as from the 2018 Planck release [12] and the 2020 ACT release [5]. Baryonic and cold dark matter densities Ω_b, Ω_c, dark energy density Ω_Λ spectral index of inflation n_s, acoustic horizon at decoupling θ_*, reionization depth τ, and the age of the Universe in Gyr, t_0. 11

2.1 ACT Key Characteristics for the three frequency bands: : Low-Frequency (LF), Mid-Frequency (MF) and High-Frequency (HF) [13]. 18

2.2 SO Key Characteristics [14]. Detectors are split evenly between the three frequency bands: Low-Frequency (LF), Mid-Frequency (MF) and Ultra-High-Frequency (UHF). Note: the LF beam size is estimated by scaling down the MF and UHF beam sizes. 19

3.1 Integrated scattering power (in percentage) with different source angle of incidence θ_I at 110 GHz for MMA and TK tiles. Integration is from $\theta_\mathrm{R} = 0°$ to 45° away from the specular reflection direction. The cited error is calculated from the standard error of the mean over the 17 repeated measurements for each angle of incidence. 36

4.1 Optical properties of Silicon. Properties extracted from the data when fit with the theoretical model. Properties n is the index of refraction, D is the thickness of the sample in millimeters, and $\tan(\delta)$ is the loss tangent. 46

7.1 Allowed variation in signal-to-noise and positional knowledge needed to keep error contributions from these effects below 2.5 μm HWFE. 92

A.1 Near-field simulated measurement signal-to-noise and resulting simulated sidelobe power (at the secondary illumination and into the far-field). Signal-to-noise is calculated as the standard deviation of the signal outside an 8.5 cm radius of the peak-normalized beam (same resolution as Table A.2). 128

A.2 Near-field scan size and resolution, and resulting scan size and resolution at the secondary illumination and in the far-field. 128

This thesis represents the motivations, results, and conclusions from the following works:

[15] *The Atacama Cosmology Telescope: Beam Estimation for DR6 with Point Source Stacking.* G. E. Chesmore, et al. in progress.

[16] *The Simons Observatory: Characterizing the Large Aperture Telescope Receiver with Radio Holography.* G. E. Chesmore, et al. Applied Optics, 2022.

[17] *The Simons Observatory: HoloSim-ML: machine learning applied to the efficient analysis of radio holography measurements of complex optical systems.* G. E. Chesmore, et al. Applied Optics, 2021.

[18] *The Simons Observatory: Metamaterial Microwave Absorber (MMA) and its Cryogenic Applications.* Z. Xu, G. E. Chesmore, et al. Applied Optics, 2021.

[19] *Reflectometry Measurements of the Loss Tangent in Silicon at Millimeter Wavelengths.* G. E. Chesmore, et al. Proceedings from the 8th ESA Workshop on Millimetre-Wave Technology and Applications, 2018.

Acknowledgments

I cannot thank my advisors and post-doc advisors enough. First and foremost, thank you to **Jeff McMahon** for your mentorship and support throughout the years. Thank you, **Sara Simon**, who started out as my post-doc and ended as my co-advisor at FNAL. You are an amazing researcher, and I've learned so much from you over the years. Thank you to **Katie Harrington** for advising me and making the radio holography measurement possible. I cannot imagine graduate school without you. Grazie a **Martina Gerbino** per tutte le chiamate su Skype (mentre tutti usavano Zoom). Specialmente durante la pandemia, le nostre telefonate sono state il momento clou della mia giornata e il tuo tutoraggio mi ha aiutato a superare momenti molto solitari. Thank you to **Patricio Gallardo** for being my "optics post-doc". I'm extremely grateful for you as a post-doc and friend. Thank you to **Adri Duivenvoorden** for advising the final project of my thesis. And thank you to **Zhilei Xu** for helping me grow as a writer as we co-authored our paper. **Ed Wollack**: every article I have published, you have edited and picked apart. This deepened my understanding of the topic and drastically improved my writing, so thank you. Thank you also to **Jon Gudmundsson** for giving me the opportunity of visiting Stockholm University. I've looked up to you as a researcher for the entirety of grad school, so visiting Stockholm University was the biggest honor, and I made two wonderful friends.

A highlight of grad school was working with the junior members of the Simons Observatory, many of which have become my good friends. I am extremely grateful for my LATRt lab mates, **Carlos Sierra**, **Shreya Sutariya** and **Tommy Alford**. You all supported

me and helped me grow as a researcher. The SAT holography measurements would not be possible without **Remington Gerras**, **Joseph Seibert**, **Michael Randall**, **JB (John) Lloyd**, and **Max Silva-Feaver**, **Tran Tsan**. Thank you for working so hard during those two weeks and being so wonderful to work with. Thank you to my fellow beam-fanatics, **Alexandre Adler** and **Nadia Dachlythra**, for hosting me at the Stockholm University and for being so incredibly supportive through the years. You are brilliant scientists and wonderful friends.

I, of course, want to thank my early educators, who encouraged me to pursue physics as a career. Thank you to high school physics teachers: **Mr. Brown** and **Mr. Appel**. Had it not been for your encouragement, I'm not sure that I would've gone for physics. Thank you, **Dr. Kesten**, for supporting my career through the years and helping me with every single grad school application. A huge thank you to **Dr. Barber** for hiring me as a researcher after only one semester of college physics. I recall that first summer working full-time in the lab and feeling so fulfilled. Lastly, thank you to **Gary Sloan** for teaching me to be a machinist. You made me confident in my machining skills and made the machine shop the coolest hangout spot on campus.

I'm extremely grateful for my Santa Clara University family. **Hayley Raquer**, you really were my big sister in college and I continue to look up to you. Thank you to my dear friend **Sara Youlton** for being my homework buddy in physics. Having you around was such a saving grace and made me feel far less alone in classes. Lastly, thank you to **Mitch Bugaj** and **Kyle Bandaccari** for being the coolest lab-mates. During my first research experience, you two treated me as an equal in the group right off the bat. You constantly valued my input and believed in me as a researcher. I couldn't ask for a better first research experience. So, thank you.

Thank you to **Arijana Ramic** and **Patty Hamilton**, my two good friends from high school, who are constantly cheering me on. Even after years of not seeing each other, we jump back into friendship like it's only been a week. To the girls in my Ann Arbor Beakes

Street house: **Nora Bailey**, **Liz Hanley**, **Jessica Robbins**, and **Jazmine Ehrhardt**, thank you for being the coolest house-mates during my first year of grad school 🏠 I love you all dearly. And to **Hanna Ruth**, thank you for your friendship throughout grad school. You are, in fact, the coolest person I know. And to **Andrew Gardner**, my Little, my comedic relief, thank you for keeping me young by sending me TikToks every single day. Lastly, thank you to my friend (lab-mate, work-wife, etc.), **Shreya Sutariya**, for making me laugh non-stop and being the most solid friend throughout the years.

When I transferred to the University of Chicago, I found a whole community of friends, and I am so grateful for how they welcomed me. **Kavi Chintam**, thank you for cracking me up constantly and for being a friend throughout the years. Thank you to my office mates **John Hood**, **Rebecca Diesing**, **Andrea Bryandt**, and **Emily Simon**. The office is a place I love to be, and it's because of all of you. Thank you, **Abby Lee**, **Karia Gilbert**, and **Shreya Sutariya** for being such solid friends. My fondest memories of grad school have been travelling, going out, or just hanging around the ERC with you all. I love my friends so much!

Thank you to my cousins, **Ariana Meyrich-Blomquist** and **Caitlin Meyrich-Blomquist**, for being the cool Seattle girls I've always looked up to. To my nieces and nephews, **Bentley**, **Ashtyn**, **Lily** and **Lincoln**, "auntie Grace" has and will always be my favorite title. Grazie ai miei genitori italiani, **Patrizia** e **Tarcisio**, e al resto della mia famiglia italiana, per avermi accolto nella vostra famiglia. Vi adoro.

To my **Mom** and **Dad**, thank you for loving me unconditionally and encouraging me to pursue a higher education. You have both been a source of comfort and inspiration when I feel overcome with imposter syndrome. I knew I could lean on you both when my anxiety got bad, and you always pulled me out of it. **Auntie Ann** and **Uncle Peter**, you have been like a second set of parents to me. I cherish the hours spent at your home in fleece jackets and slippers. Caffeine! ☕ And **Auntie Ann**, our phone calls and kitchen table conversations have helped me grow into who I am and how I navigate the world. Thank you

for your friendship.

Graduate school has changed my life for the better in many ways, but perhaps the greatest was meeting you, **Matteo**. You've brought so much joy into my life, even while we waited for borders to open. Thank you for truly the most constant support and love. I look forward to spending my life with you. Ti amo da matti 🌽

Abstract

The Cosmic Microwave Background (CMB) carries the imprints of the conditions in the early universe and the large-scale structure it has traversed as it travels to our telescopes. Thus, the CMB serves as a window into the physics of our universe allowing measurements of primordial gravitational waves, large scale structure formation, the sum of neutrino masses, dark energy, dark matter, and fundamental physics. Achieving these ambitious science goals requires equally ambitious instrumentation.

The Simons Observatory, a ground-based CMB experiment, is designed to observe the CMB temperature and polarization signals to an unprecedented sensitivity. A combination of one Large Aperture Telescope (LAT) and three Small Aperture Telescopes (SATs) will measure the temperature and polarization anisotropy of the CMB with ≈60,000 background noise-limited detectors operating at ≈100 mK, covering frequencies from ≈20 to ≈300 GHz.

To measure the tiniest signals of the CMB, we must control optical systematics and advance detector sensitivity to unprecedented levels. I present techniques to control optical systematics, design highly sensitive detectors and feedhorn arrays, and characterize their performance. I present the design and performance of the optical properties of novel microwave absorbers, and beam map a complete cryogenic optical system. I present software to model these systems, including hardware imperfections, demonstrating how systematics propagate into measurements; the software uses machine learning to correct such systematic errors by correcting alignment of mirrors. Lastly, I present a measurement of the Atacama Cosmology Telescope (ACT) beam that is central to the ACT Data Release 6 (DR6). This

beam measurement is made possible with a novel approach for characterizing the on-sky beam by stacking point sources. Understanding the beam of the instrument is critical for characterizing the angular response of the instrument, and therefore critical for achieving the ambitious measurement goals for inflationary signals and light relativistic species in ACT and other future experiments.

Chapter 1

Introduction

In 1965 at Bell Labs, Arno Penzias and Robert Wilson serendipitously detected "noise" with their microwave antenna. This noise was isotropic (same in all directions) and homogenous (same in all locations), and was ultimately determined to be the first measurement of the Cosmic Microwave Background; radiation from the early universe. The temperature spectrum of the Cosmic Microwave Background (CMB) was measured to be a near-perfect black-body, with a mean temperature of [20]:

$$T_{\text{CMB}} = 2.725\,K \tag{1.1}$$

The spectrum lies in the infra-red range of the electromagnetic spectrum, and peaks at a wavelength $\lambda = 1.5\,\text{mm}$ (Figure 1.1).

This near-perfect black-body is understood to originate during the early universe by the rapid collision of photons with free electrons (Thompson scattering) that keep radiation in thermal equilibrium with hot dense matter. As the universe expanded and cooled, however, this spectrum kept its same form [21]. Because it formed during the early universe, the CMB is a backlight into not only early universe properties, but also late universe physics such as large-scale structure and dark matter. The CMB, therefore, carries a wealth of information about the fundamental physics of our universe.

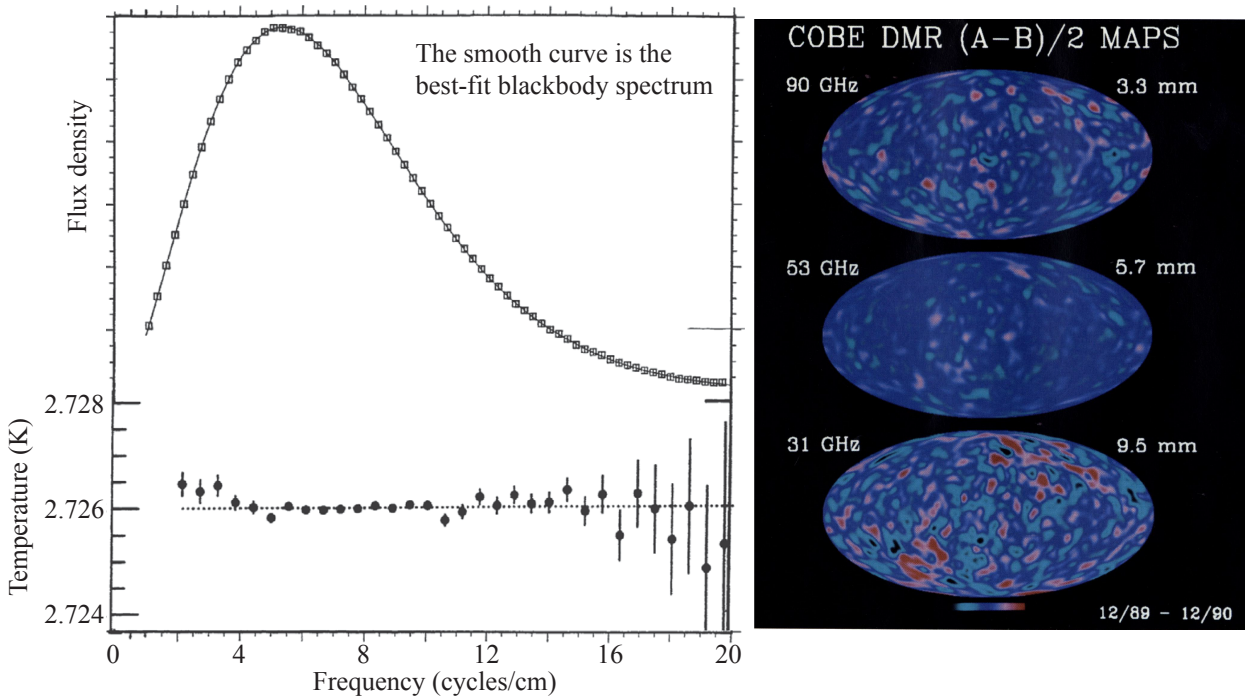

Figure 1.1: Left: Spectrum of the CMB from the COBE satellite. The deviation from an ideal blackbody is magnified $\times 400$ in the bottom panel. Right: First-year maps from the COBE Differential Microwave Radiometer in 1992. Source: COBE Collaboration [1, 2].

1.1 Overview of Λ-CDM Cosmology

Figure 1.2 shows the history of our universe as we understand it today. The universe is described by the ΛCDM model, which assumes a flat universe ($\Omega_{\text{tot}} = 1$) which is expanding at an accelerating rate, and is dominated by cold dark energy and cold dark matter. Further, the ΛCDM model assumes dark energy taking the form of a cosmological constant Λ, which is expressed as a constant energy density:

$$\rho_\Lambda = \frac{c^2}{8\pi G}\Lambda \tag{1.2}$$

The ΛCDM model neatly models the universe in six parameters: the baryonic density $\Omega_b\, h^2$, the cold dark matter density $\Omega_c\, h^2$, $\ln\left(10^{10} A_s\right)$, the spectral index of inflation n_s, the size of the acoustic horizon at decoupling $100\,\theta_*$, and the reionization optical depth τ. Further, the standard model assumes a constant number of neutrino N_{eff} and sum of neutrino masses

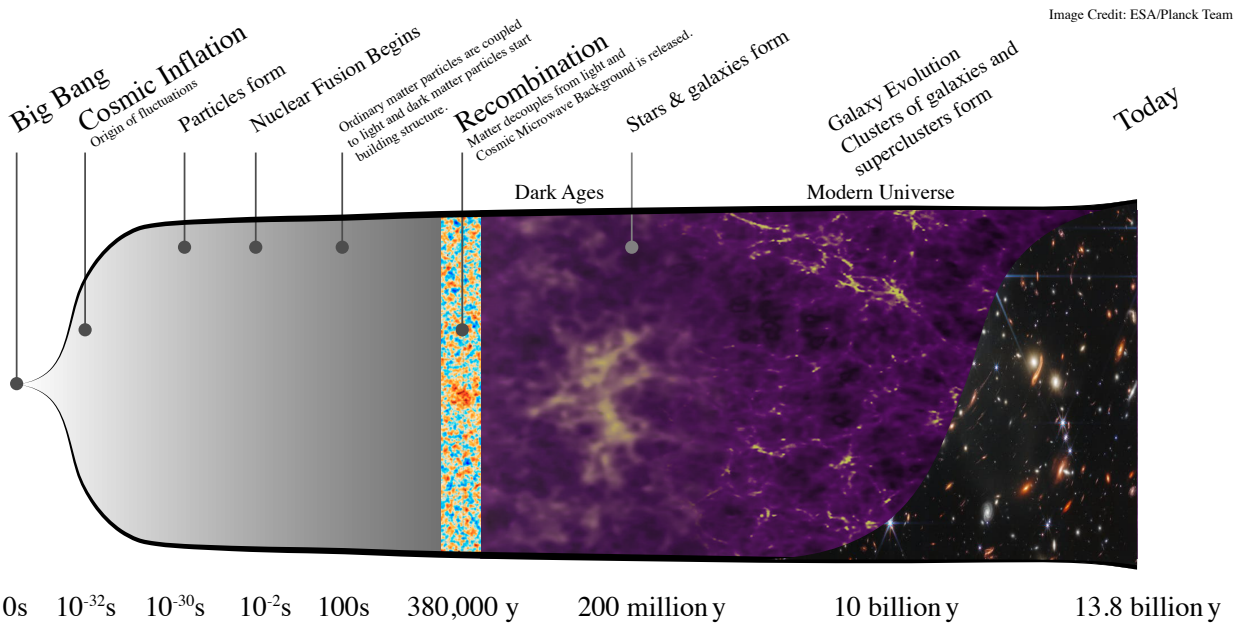

Figure 1.2: The history of the universe as we understand it today. After the Big Bang, the CMB is emitted during the Recombination era at around 380,000. The photons emitted then traversed large-scale structure to get to our detectors, and therefore we can study late universe large-scale structure through measurements of the CMB. Source: ESA/Planck Team [3], re-touched by Chesmore.

Σm_ν. The most up-to-date values are listed in Table 1.1. All of these parameters impact the shape of the CMB spectra which we measure today. Three pillars provide evidence for the Big Bang Theory, whereupon our universe came into existence.

The Expanding Universe: As we've previously discussed in this chapter, the universe is predicted to be currently expanding. This has been studied and proven by observations of late-universe objects like galaxies [22]. By measuring the velocity and distance of an object, scientists determined (using the Hubble Law) objects in the past were closer together, and today are farther apart.

The Cosmic Microwave Background: Radiation from a source of known temperature is described by a black-body spectrum. We've introduced the CMB as radiation from the early universe. We've also introduced the CMB as a blackbody spectrum. It can be shown that, in an expanding universe, the blackbody will maintain its shape, its temperature will decrease as the wavelength shifts lower. Therefore, the CMB serves as evidence of a dense

hot radiation source before the universe expanded, with a consistent black-body shape.

Abundance of Light Elements: Such an abundance of light elements in today's universe suggests a hot, dense beginning to the universe. As the universe cooled and expanded, light particles formed by a fusion process called Big Bang Nucleosynthesis (BBN). The amount of light particles measured today are in agreement with predictions made by BBN.

These three pillars indicate a valid understanding of cosmology, but this cosmology remains incomplete. Problems which remain are listed below. The theory of inflation has the potential to explain the mentioned puzzles.

Flatness problem: Measurements of the observable universe present a nearly flat spatial geometry ($\Omega_{\text{total}} = 1$). This would imply a flat geometry at the initial moments of our universe as well. But for what reason would the universe begin with a flat geometry? Inflation answers this by suggesting our universe might have curvature, but this rapid expansion blows up any curvature such that the tiny amount we can observe appears flat.

Horizon problem: The sky appears remarkably (and statistically) uniform in all directions. The CMB confirms this, as we measure this radiation to be uniform to one part in $100,000$. The particle horizon distance is only 2°, so how could the entire sky be so nearly uniform? Inflation solves this because such an accelerated expansion creates a paradigm where all the observed sky has a chance to come into causal contact.

Magnetic monopole problem: Magnetic monopoles are analogous to electrons, which would emit a magnetic charge. However, we have never measured a single monopole in our universe, nor do we know that they exist. Meanwhile, the Grand Unified Theory (GUT) predicts an extremely low density of magnetic monopoles; GUT predicts one monopole per Hubble radius. Inflation solves this by diluting the expected number of monopoles thus explaining why we have not measured a single one.

1.2 Questions to be Answered

Many questions remain in cosmology, which are being investigated using measurements of the CMB. The Hubble Constant, for example, quantifies the expansion of our universe:

$$H_0 \equiv \left(\frac{\dot{a}}{a}\right)_{t=t_0} \tag{1.3}$$

In recent decades, astronomers and cosmologists have worked to determine the exact value of H_0 using both early- and late-universe physics. As the two methods return differing values of the Hubble Constant, this field continues to evolve with new statistical methods and precision instrumentation.

During inflation, tensor fluctuations manifested as gravitational waves, which are then imprinted in the CMB polarization. The tensor-to-scalar ratio, r, is measured from the CMB polarized signal, and therefore directly quantifies the signatures of primordial gravitational waves. To date, we have upper limits from various previous CMB experiments, but constraining to higher precision remains to be done.

Many cosmological parameters remain to be constrained by improved measurements of the CMB. The spectral index of inflation, n_s, illuminates the geometry of our universe, and is constrained by the "damping tail" of the CMB temperature spectrum, or at small angular scales. Additionally, the effective number of neutrino species, N_{eff}, will push forward the field of particle physics.

1.3 Signals in the Comsic Microwave Background

The Cosmic Microwave Background carries rich science in its temperature and polarization spectra. The CMB temperature spectrum can be decomposed into spherical harmonics, which result in power spectra as a function of multipole moment ℓ, where $\ell \approx 180/\theta$ and θ is angular scale on the sky. The temperature fluctuations of the CMB are decomposed into

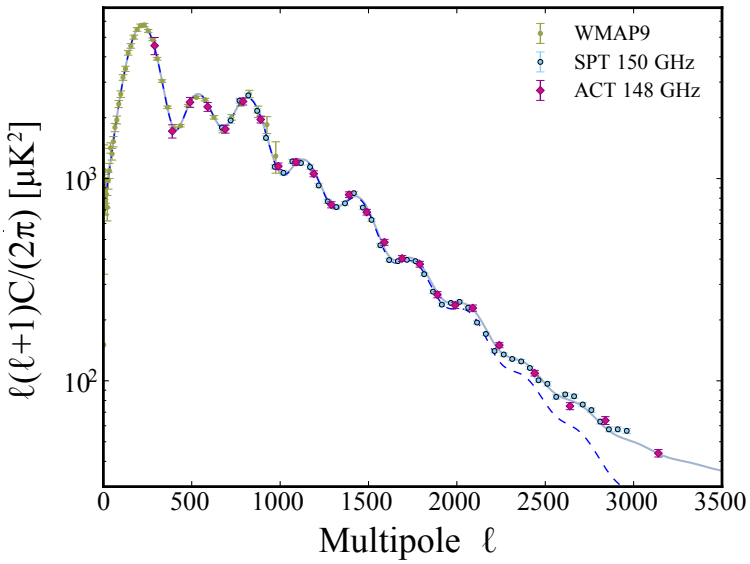

Figure 1.3: The CMB temperature power spectra measured by WMAP (yellow), the South Pole Telescope (blue) and the Atacama Cosmology Telescope (purple). The temperature anisotropies of the CMB will be measured with the Simons Observatory and CMB-S4, two upcoming cosmology experiments, with further precision. Source: The Atacama Cosmology Telescope Collaboration [4].

spherical harmonics:

$$\frac{\delta T}{T}(\theta,\phi) = \sum_{\ell=2}^{\infty} \sum_{m=-\ell}^{\ell} a_{\ell m} Y_{\ell m}(\theta,\phi) \ , \tag{1.4}$$

where ℓ and m are multipoles of the spherical harmonic $Y_{\ell m}$, $a_{\ell m}$ are expansion coefficients, and θ and ϕ represent the angular position on the sky. You'll notice the first summation of Equation 1.4 begins at $\ell = 2$ rather than $\ell = 0$; the $\ell = 1$ coefficient corresponds to the earth's motion with respect to the CMB, and the $\ell = 0$ coefficient is the mean temperature of the CMB, so we neglect those terms. The coefficients $a_{\ell m}$ are independent variables, and relate to the CMB's angular power spectra via:

$$C_\ell^{TT} = \frac{1}{2\ell+1} \sum_{m=-\ell}^{m=\ell} |a_{\ell m}|^2 \ . \tag{1.5}$$

This is the temperature power spectrum of the CMB. Figure 1.3 shows the measured CMB temperature power spectrum from the Atacama Cosmology Telescope, the South Pole

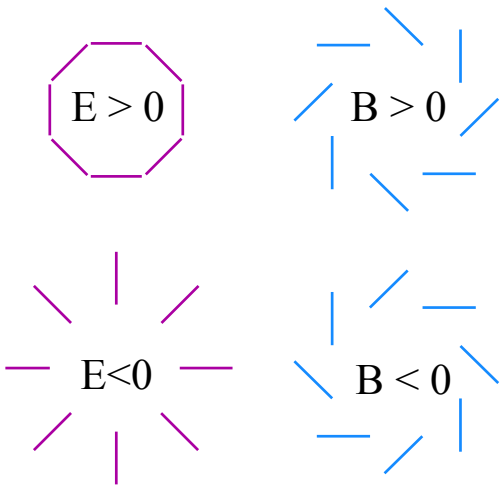

Figure 1.4: The polarization modes of the CMB. The E modes have no curl, while the B modes have no divergence.

Telescope, and WMAP [4].

The shape of the CMB power spectra unlocks properties of the early universe. For example, the first peak in the power spectrum at around $\ell \approx 220$ corresponds to the angle at which we observe the sound horizon, or the distance that sound can travel between the big bang and recombination. The measurement of this power spectrum's morphology can also determine physical matter and baryon densities. The dark energy properties of our universe can be constrained by the power spectrum peak, as the dark energy and matter densities jointly alter the distance to last scattering [23]. The matter density of the universe alters the expansion of the universe, which determines when the universe reaches the temperature of last scattering, or when photons begin to stream freely. The smaller angular scale distortions are in part due to an inhomogeneous universe at the time of last scattering ($z \approx 1100$).

The CMB is predicted to be polarized, due to Thompson scattering by free electrons during the era of recombination [21, 24]. Measuring this polarization would indicate the beginning of reionization and further have the potential to uncover primordial gravitational waves. Just as the CMB's temperature spectrum is decomposed in spherical harmonics, we also decompose the polarized components. We refer to the CMB's polarization signals as "E-modes" and "B-modes" after their likeness to curl-free (electric) and divergence-free

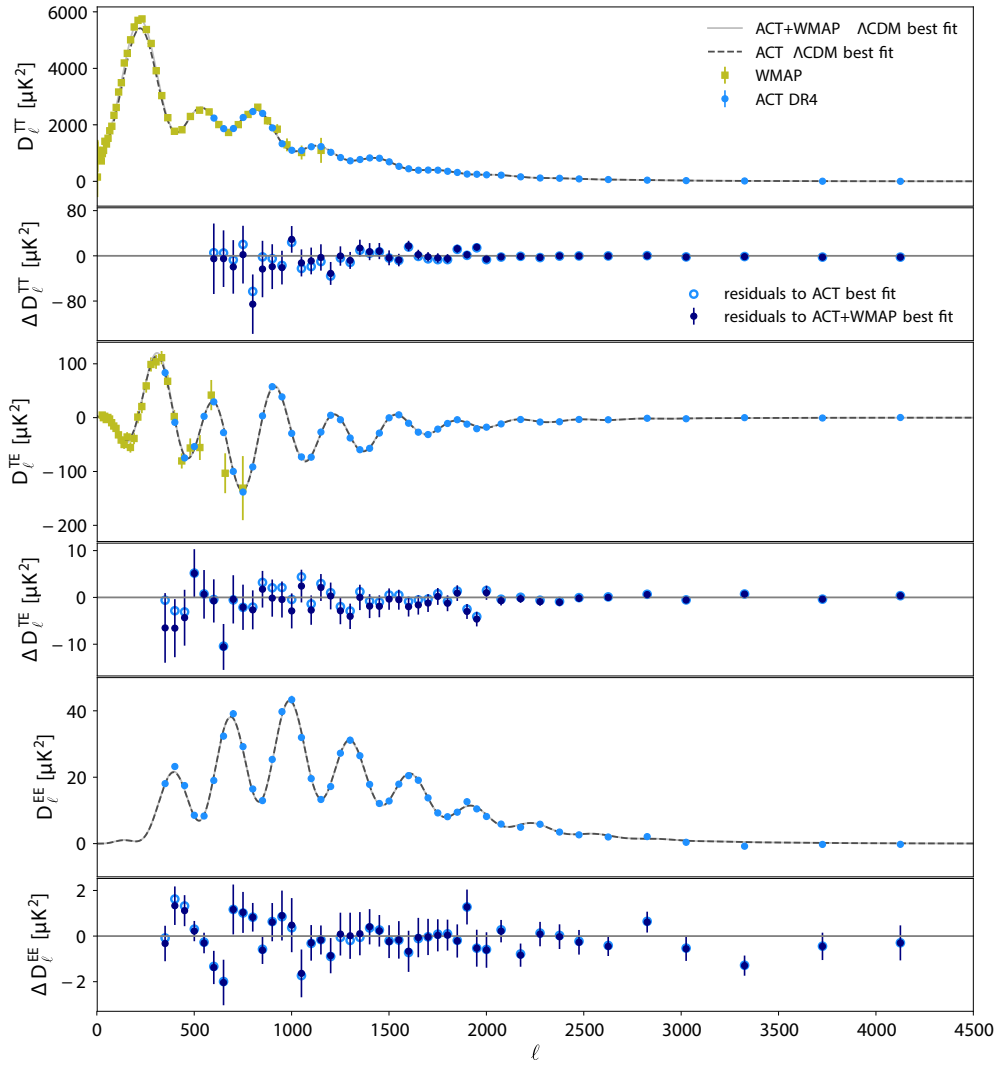

Figure 1.5: Temperature and polarization spectra measured by the Atacama Cosmology Telescope in 2018 [5], compared to spectra measured by WMAP and Planck, as well as ACT's residuals after fitting to cosmological model spectra. Source: ACT 2018 Cosmological Results [5].

(magnetic) fields (Figure 1.4). The E- and B-modes of the CMB are then defined as

$$\begin{aligned} E(\theta,\phi) &= \sum_{\ell m} a^E_{\ell m} Y_{\ell m}(\theta,\phi) \\ B(\theta,\phi) &= \sum_{\ell m} a^B_{\ell m} Y_{\ell m}(\theta,\phi) \ , \end{aligned} \tag{1.6}$$

and the CMB's polarized spectra are defined as

$$C_\ell^{XY} = \frac{1}{2\ell+1}\sum_m \langle a_{\ell m}^X a_{\ell m}^{Y*}\rangle \ . \tag{1.7}$$

Here, X and Y can either be E-mode, B-mode, or temperature T spectra of the CMB, indicating cross-correlated spectra.

The E-modes are produced by the density perturbations via Thompson scattering from a local quadrupole. For this reason, the EE spectra peaks when scattering is highest, and when velocity is highest, between the two temperature spectrum peaks. Primordial gravitational waves produce B-modes through Thompson scattering. Further, the large-scale structure gravitationally lenses CMB photons traveling through, adding to the B-mode polarization spectra. The scalar-to-tensor ratio, r, is directly determined through measurements of the B-mode polarization, as scalar perturbations generate E-mode polarization.

1.4 Why Care About Beams?

Every camera has a "beam" (or optical response) which determines the optical performance (how your picture will turn out). The smaller your beam, the higher the resolution of your picture. The Field-of-View (FOV) determines how wide your picture can be. The noise of your camera's detector determines how grainy the picture comes out. All of these optical properties are defined by the camera's beam. To take a picture of the CMB, the telescope is our camera; the beam of the instrument determines the optical performance at a given angular scale.

This not only affects the immediate quality of our CMB maps, but also impacts the ability to study cosmological science. Let's consider two cosmological parameters: the spectral index of inflation n_s, and the number of neutrino species $N_{\rm eff}$. The spectral index of inflation n_s describes how fluctuations vary with angular scale. Figure 1.6 shows the CMB power spectra at three different values of n_s and at two different values of $N_{\rm eff}$.

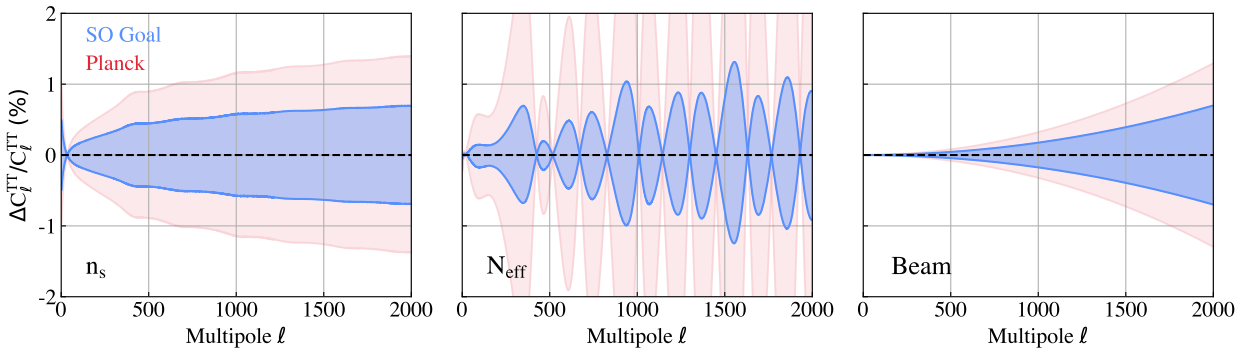

Figure 1.6: The simulated CMB power spectrum at varying spectral index of inflation $n_{\rm s}$, and varying neutrino species $N_{\rm eff}$. Simulations are made with CAMB [6] and show the TT spectrum's deviation from nominal values, with $n_s \pm \sigma_{n_s}$, and $N_{\rm eff} \pm \sigma_{N_{\rm eff}}$. In red is the sensitivity achieved by Planck, and in blue is the sensitivity goal of Simons Observatory. The right-most panel simulates a mischaracterized instrument beam and how it can mimic deviations in the TT spectrum of the CMB.

The red curve plots the achieved sensitivity of Planck for determining the spectral index $n_{\rm s}$ and $N_{\rm eff}$, showing $n_s \pm \sigma_{n_s}$, and $N_{\rm eff} \pm \sigma_{N_{\rm eff}}$. The science goals of SO are plotted in blue to show the increase in sensitivity compared to Planck. The right-most plot then shows that a mischaracterization of the instrument's beam can mimic the aforementioned uncertainties. At small angular scales (large ℓ values), slight variations of n_s change the slope of the power spectrum (Figure 1.6). For this reason, the beam must be well understood and characterized to achieve such ambitious science goals.

Entire classes of inflationary models can be ruled out by constraining n_s. Achieving this goal, however, requires precise beam calibration on these small angular scales. Further, characterizing the polarization leakage from the telescope's beam is critical to map the tiniest signals of the CMB's polarization. For this reason, this work focuses on beam calibration, both for the Simons Observatory and the Atacama Cosmology Telescope.

1.5 Status of the Field

Since the detection by Penzias and Wilson in 1965, the cosmology community has made leaps to constrain the black-body of the CMB. The Cosmic Background Explorer (COBE) was the

first to measure the CMB power spectrum from space. Since COBE, the measurement of fluctuations in the CMB has increased in precision, with experiments like WMAP, Planck, for example. The South Pole Telescope and the Atacama Cosmology Telescope, two ground-based telescopes, have pushed the measurement further with increased resolution mapping of the sky.

In the coming years, cosmologists aim to detect the tiniest signals of the polarized CMB. An ongoing challenge in cosmology instrumentation has been characterizing the polarization spectra of the CMB. Specifically, the B-mode polarization of the CMB offers a unique window into early-universe physics [21]. Because scalar perturbations generate E-mode polarization, a measurement of the B-mode polarization directly quantifies the scalar-to-tensor ratio, r. The BB-power spectra has been reported by the Polarbear, South Pole Telescope and ACTPol collaborations [25–27].

1.6 Outline of Thesis

First, I overview two ground-based cosmology experiments in Chapter 2: the Atacama Cosmology Telescope (ACT) and the Simons Observatory (SO). This work focuses on the development and characterization of optical components for the SO. In the final chapter of this

Parameter	Planck 2018 Release	ACT 2020 Release
$100\,\Omega_b h^2$	2.241±0.015	2.153±0.030
$100\,\Omega_c h^2$	11.97±0.14	11.78± 0.38
$\ln(10^{10} A_s)$	3.040±0.016	3.050±0.030
Ω_Λ	0.687±0.008	0.696±0.022
n_s	0.967±0.004	1.008±0.005
$100\,\theta_*$	1.0410±0.00046	1.0425±0.0007
τ	0.052±0.008	0.065±0.014
t_0	13.791±0.025	13.832±0.047

Table 1.1: The most recent cosmological parameters as from the 2018 Planck release [12] and the 2020 ACT release [5]. Baryonic and cold dark matter densities Ω_b, Ω_c, dark energy density Ω_Λ spectral index of inflation n_s, acoustic horizon at decoupling θ_*, reionization depth τ, and the age of the Universe in Gyr, t_0.

work, I characterize the optical performance of ACT.

In Chapter 3, I present an overview of the meta-material absorbers used in the SO Large Aperture Telescope optics tubes to control stray light. I also present the characterization of their optical properties using a radio holography receiver. These tiles are comprised of an outer metamaterial layer, which approximates a lossy gradient index anti-reflection coating. They are fabricated via injection molding commercially-available carbon-loaded polyurethane (25% by mass). The injection molding technology enables mass production at low cost. Room temperature optical measurements verify their control of reflectance to less than 1% up to 65° angles of incidence, and control of wide angle scattering below 0.01%.

The characterization of optical components is continued in Chapter 4, where I characterize the reflectivity and loss tangent measured in the W-band (80-125 GHz) and D-band (125-180 GHz) in two samples of float zone silicon with intrinsic stoichiometry - one irradiated by neutrons, which increases the resistivity by introducing crystalline defects, and the other unperturbed. I find the loss tangent $\tan\delta$ of 2.8×10^{-4} and 1.5×10^{-5} for neutron-irradiated silicon and intrinsic silicon, respectively, both with an index of refraction of 3.41. The results demonstrate the applicability of silicon as a warm optical component in millimeter-wave receivers. The depth of the reflection nulls provides a sensitive measurement of dielectric losses.

In Chapter 5, I present near-field radio holography measurements of the SO LATR optics. These measurements demonstrate that radio holography of complex millimeter-wave optical systems comprising cryogenic lenses, filters, and feed horns can provide detailed characterization of wave propagation before deployment. I used the measured amplitude and phase, at 4 K, of the receiver near-field beam pattern to predict two key performance parameters: 1) the amount of scattered light that will spill past the telescope to 300 K and 2) the beam pattern expected from the receiver when fielded on the telescope. These cryogenic measurements informed the removal of a filter, which led to improved optical efficiency and reduced side-lobes at the exit of the receiver. This is the first time such parameters have

been confirmed in the lab prior to deployment of a new receiver.

Chapter 6 presents additional near-field radio holography measurements, this time on the Small Aperture Telescope (SAT) optics tube. Using the identical holography setup as described in Chapter 5, I present preliminary characterization of the SAT's optical performance; more specifically, I predict two key performance parameters: 1) the beam profile in the near-field and 2) the far-field beam pattern of the telescope expected from the receiver.

Chapter 7 presents Holosim-ML: a Python code for beam simulation and analysis of radio holography data from complex optical systems. This code uses machine learning to efficiently determine the position of hundreds of mirror adjusters on multiple mirrors with few micrometer accuracy. I apply this approach to the example of the SO 6 m telescope. The ML framework makes the analysis of these measurements from many receiver positions straightforward to analyze. I present an example of the SO dual reflector optical system and demonstrated that this approach can yield $< 5\,\mu m$ alignment errors, the requirement for SO science goals.

In Chapter 8, I analyze maps from the Atacama Cosmology Telescope Data Release 6. From the maps, I select point sources and stack them in order to determine the temperature and temperature-to-polarization beams of the instrument. This method is compared to the planet-derived beams of ACT. We find the temperature-to-polarization leakage beams are consistent between the two methods, indicating that the planet-derived beams are sufficient for subsequent cosmology analysis. We also find a spatial dependence of the point sources in the window functions, which we investigate and present several explanations for what might be causing this effect.

Lastly, in Chapter 9, I summarize the results from this work and discuss their implications for the future of precision cosmology.

Chapter 2

Instrument Overview

We are in the age of precision cosmology, and measurements of the CMB spectra continue to improve in sensitivity. Now, to measure the CMB polarization anisotropies, scientists are pushing forward the sensitivity of the instruments by increasing detector numbers, improving detector sensitivity, and controlling optical systematics, to name a few. For example, the Atacama Cosmology Telescope (ACT), a ground-based cosmology experiment, used roughly 3000 bolometric detectors. The Simons Observatory is scaling its detector count up to more than 50,000 bolometric detectors in order to improve mapping speed and sensitivity. Looking ahead, the CMB-S4 collaboration, a next-generation cosmology project, plans to scale up even further: to roughly 500,000 detectors. This, along with the many other improvements in instrumentation, aim to detect the faintest signals of the CMB polarization spectra.

In this chapter, I describe two ground-based cosmology experiments covered in this work: the Atacama Cosmology Telescope (ACT), an operational cosmology experiment [7], and the Simons Observatory (SO), this generation's cutting-edge cosmology experiment [28]. I describe the Simons Observatory Large Aperture Telescope instrument further in Chapters 3, 5, and 7, and the Small Aperture Telescope in Chapter 6.

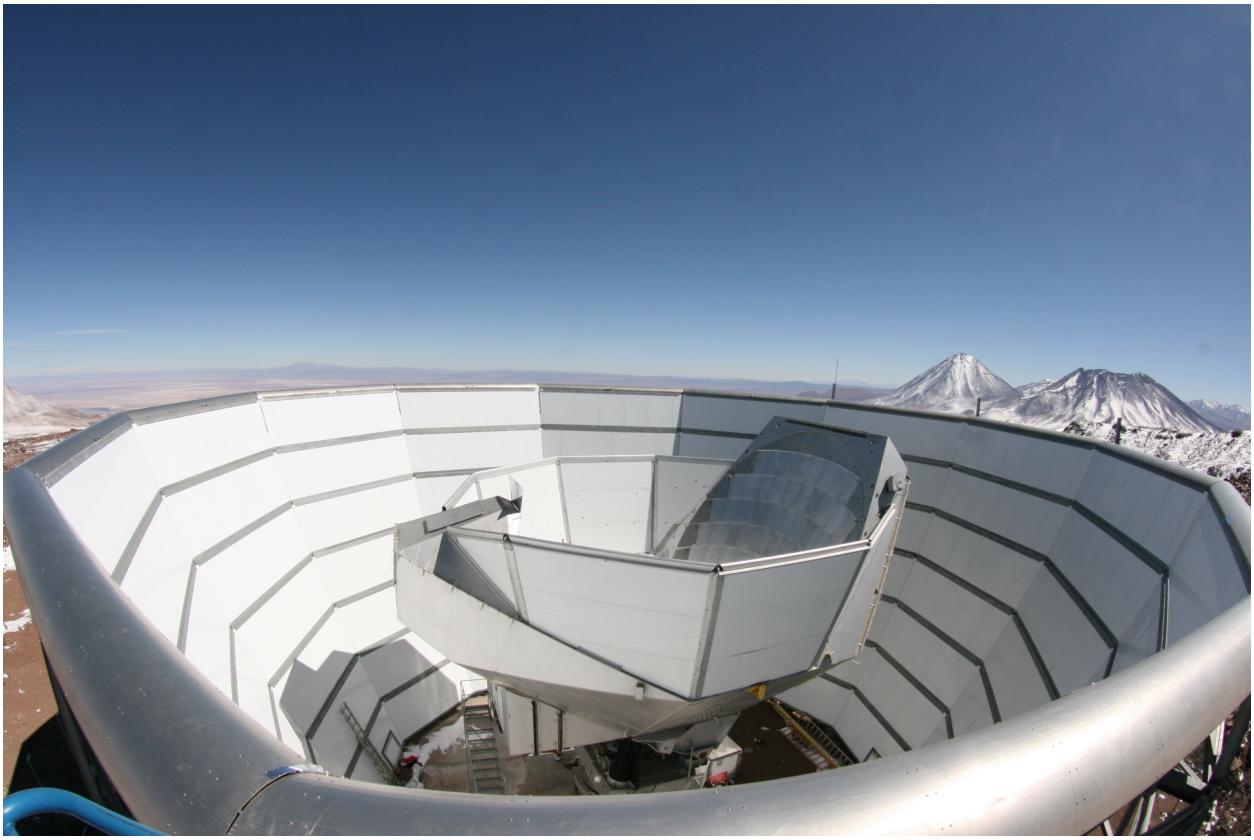

Figure 2.1: The Atacama Cosmology Telescope, surrounded by its outer ground screen. The inner co-moving screen further shields the instrument from any stray-light. The primary mirror is behind the co-moving screen. Source: Debra Kellner.

2.1 Atacama Cosmology Telescope

The Atacama Cosmology Telescope (ACT) is a millimeter-wave telescope located on Cerro Toco in the Atacama Desert of Chile at an altitude of 5190 m. The full ACT is shown in Figure 2.1 and the ACT site in Figure 2.2. Since its first observations in 2007, the telescope has seen two major instrumentation upgrades: 1) ACTPol and 2) Advanced ACT. In Chapter 8, I present the characterization of the ACT mid-frequency beam and polarization leakage using point-source stacking.

The Advanced ACT, or "AdvACT", is an upgrade to ACT's three detector arrays and their optics. Filters and lenses were replaced to operate with the four new multichroic arrays. This upgrade mapped the CMB in bands from 28 GHz to 280 GHz, and mapped approximately half of the sky. Along with improved angular resolution ($1.4'$ at 150 GHz

Figure 2.2: The Simons Observatory (SO) and Atacama Cosmology (ACT) site in the Atacama Desert, Chile. The ACT telescope sits within a ground-shield which can be sen in the bottom center. The outer ground screen protects the telescope from stray light. The inner co-moving ground-screen further protects the telescope from stray light during observations. Source: Debra Kellner

and $7.1'$ at 28 GHz), the detectors improved polarization and temperature sensitivity due to twice the original number of detectors.

Figure 2.3 shows the ray-trace of ACT's off-axis Gregorian geometry with two reflectors which guide photons into the receiver cabin; the 6 m primary is made of 71 adjustable aluminum panels and the 2 m secondary is made of 11 adjustable aluminum panels [7]. The off-axis optical design minimizes scattered power and therefore drastically improves detector sensitivity [29]. Within the receiver cabin, three cryogenic optics tubes re-image the sky onto the detector arrays [30]. Light first enters through a 6.4 mm-thick ultra-high molecular

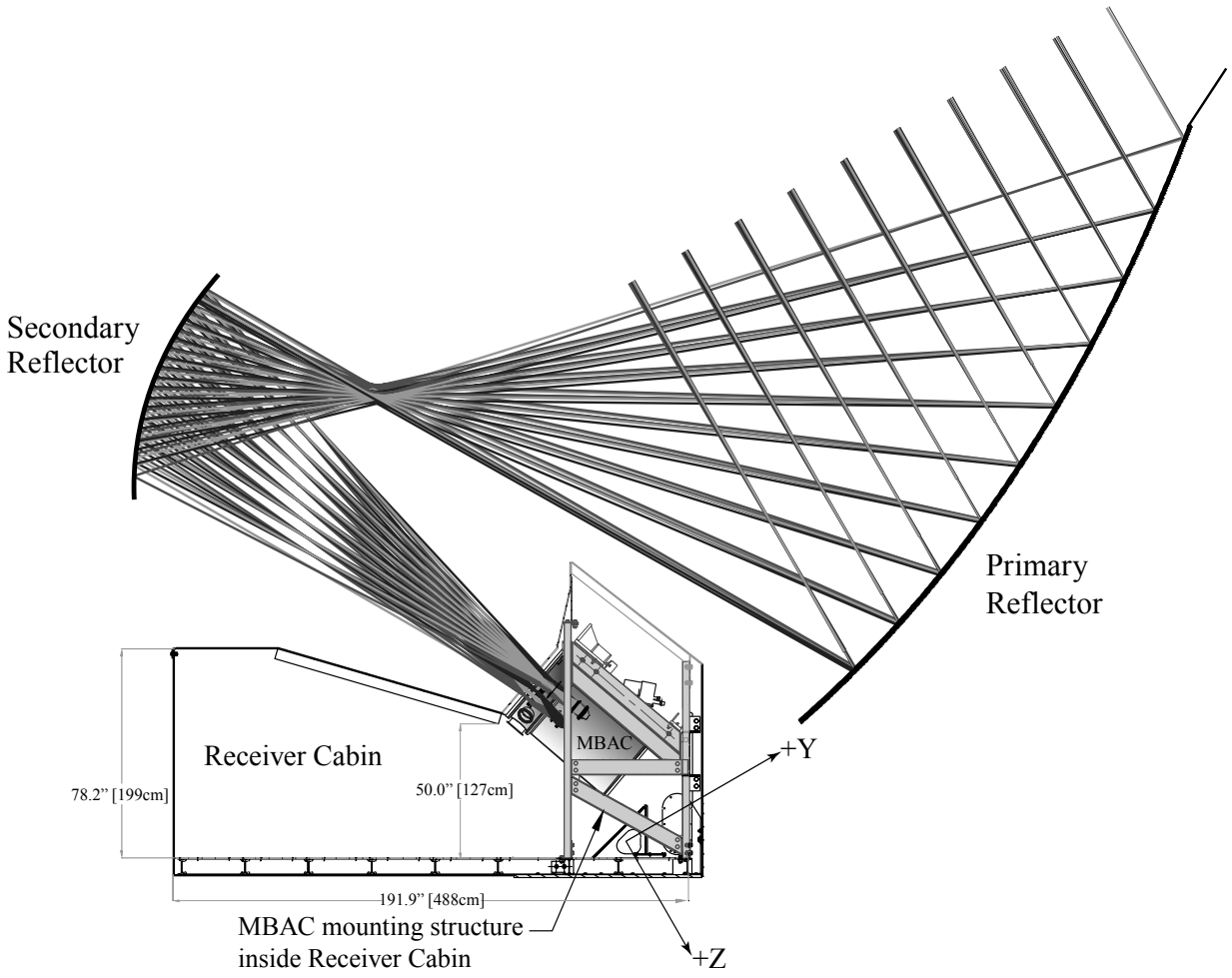

Figure 2.3: Ray-trace diagram of the Atacama Cosmology Telescope [7]. The telescope is an off-axis Gregorian with two reflectors: the primary is 6 m in diameter and the secondary 2 m. The rays trace into the Millimeter Bolometer Array Camera (MBAC) cryostat which houses the telescope's detectors. Source: The Atacama Cosmology Telescope Collaboration [7].

weight polyethylene window, followed by a series of Infra-red (IR) blocking filters at 300 K, 40 K, and 4 K, which reflect out-of-band signal in order to reduce loading on the detectors. The focal plane of the optics tube is cooled to 100 mK. Table 2.1 summarizes the optical properties of the ACTPol instrument.

Since its inception in 2016, AdvACT has achieved many of its ambitious science goals [13]. With improved sensitivity, ACTPol has measured the intrinsic temperature and polarization anisotropy at high-multipoles, which determines the spectral index of inflation, the primordial helium abundance, and neutrino properties [31]. Galaxy clusters have also been studied

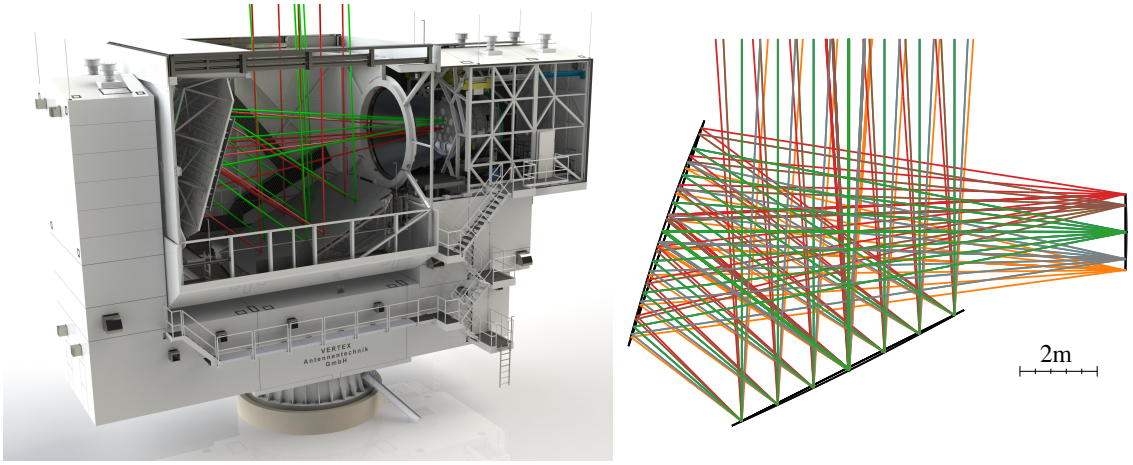

Figure 2.4: Ray-trace diagram of the Simons Observatory Large Aperture Telescope [8]. The telescope is a cross-Dragone with two reflectors, both 6 m in diameter. The rays trace into the Large Aperture Telescope Receiver (LATR) cryostat which houses 13 optics tubes. The optics tubes guide the photons onto the detectors in the focal plane, which are cooled to 100 mK. Source: The Simons Observatory Collaboration.

from their Sunyaev-Zel'dovich effect, where CMB photons are scattered by high-energy electrons in the galaxy cluster along the line of sight [21]. It has determined the Hubble Constant as 67.6 ± 1.1 km/s/Mpc, the age of the universe to be 13.832 ± 0.047 billion years, and the spectral index of inflation n_s to be 0.9729 ± 0.0061 (to name a few) [13]. Soon to release its sixth data release (DR6), ACT has turned off observations and scientists will continue to use its groundbreaking data.

2.2 The Simons Observatory

The Simons Observatory (SO) is a series of millimeter-wave telescopes designed to observe the Cosmic Microwave Background (CMB) temperature and polarization signals to an un-

Parameter	**LF**	**MF/HF**	**HF**
Number of Bolometers	176	4430	1006
Angular Resolution (arcmin)	$7.1'/4.8'$	$2.2'/1.4'$	$0.9'$
Center Frequency (GHz)	28/41	90/150	230

Table 2.1: ACT Key Characteristics for the three frequency bands: : Low-Frequency (LF), Mid-Frequency (MF) and High-Frequency (HF) [13].

precedented sensitivity [28, 32]. With the combination of one Large Aperture Telescope (LAT) [10, 33–35] and three Small Aperture Telescopes (SAT) [36], the experiment will measure the temperature and polarization anisotropy of the cosmic microwave background with $\sim$70,000 background noise limited detectors operating at $\sim$100 mK, covering six frequency bands centered on 27-280 GHz (Table 2.2).

SO will provide new constraints on inflationary signals, neutrino mass, and particles beyond the standard model while further improving our understanding of dark energy and galaxy evolution and the era of cosmic reionization [28]. The resolution of SO will result in a catalog of extragalactic sources, including active galactic nuclei (AGN), dusty star-forming galaxies, and transient sources including Gamma Ray Burst (GRB) afterglows [37]. SO expects to catalog 10,000-15,000 AGN sources at flux-densities above 7 mJy [38]. The low frequency coverage of SO will complement comparison work with other catalogs (e.g. VLA/VLASS, ASKAP/EMU, MeerKAT/MIGHTEE) [37]. Dusty star-forming galaxies seen by SO will include local galaxies ($z < 0.1$) and high redshift galaxies (approximately $2 < z < 4$), and strong lensed galaxies beyond this range [39].

2.2.1 Large Aperture Telescope

The LAT is a crossed-Dragone telescope [40–42] developed in collaboration with the Fred Young Sub-millimeter Telescope (FYST) [43, 44] Collaboration. The LAT Receiver (LATR) can hold up to 13 optics tubes, which can accommodate more than 60,000 detectors dis-

Parameter	**LF**	**MF**	**UHF**
Number of Bolometers	>20,000	>20,000	>20,000
Angular Resolution (arcmin)	$3.3'/3.0'$	$2.10'/1.30'$	$0.95'/0.84'$
Center Frequency (GHz)	27/39	90/150	220/270

Table 2.2: SO Key Characteristics [14]. Detectors are split evenly between the three frequency bands: Low-Frequency (LF), Mid-Frequency (MF) and Ultra-High-Frequency (UHF). Note: the LF beam size is estimated by scaling down the MF and UHF beam sizes.

tributed across 39 detector wafers for CMB studies [8, 45, 46]. Each optics tube holds a set of lenses, filters, and baffles which couple light from the telescope onto a set of three polarization sensitive detector arrays.

The Large Aperture Telescope (LAT) will map roughly 40% of the sky at arcminute resolution [10]. Figure 2.4 shows a cross-section and ray-trace of the LAT. The primary mirror is 6 m in diameter and constructed out of 77 individual adjustable panels, while the secondary mirror is 6 m in diameter and constructed out of 69 adjustable panels [32].

Light from the sky is then reflected into the LAT Receiver (LATR), which houses up to thirteen optics tubes [18]. The LATR optics tubes re-image the optics onto the detector arrays (three detector arrays per optics tube). Chapter 5 presents radio holography measurements of the LAT optics tube, where I characterize the optical performance of the LAT Receiver optics tube.

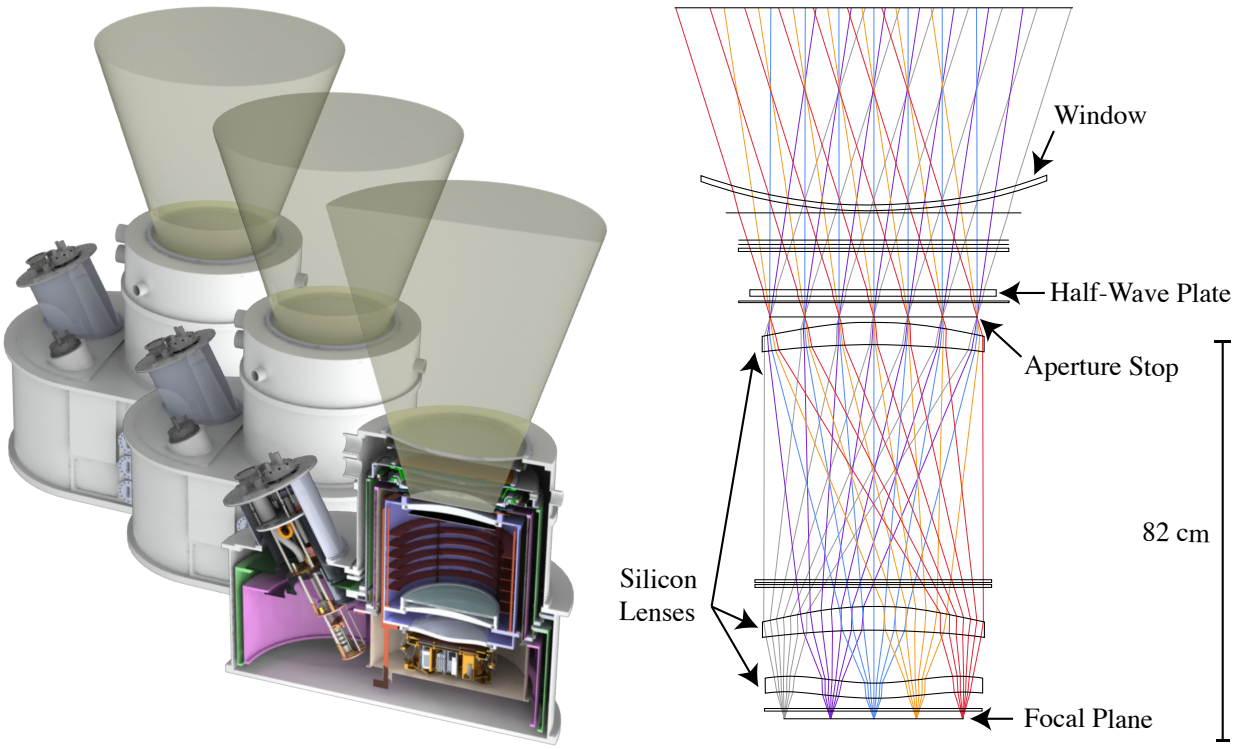

Figure 2.5: Left: Three Small Aperture Telescope cryostats, with the front cross-section showing the inner optics tube. Right: Ray-trace diagram of the Simons Observatory Small Aperture Telescope [9]. Source: The Simons Observatory Collaboration.

2.2.2 Small Aperture Telescope

The Simons Observatory (SO) will employ three Small Aperture Telescopes (SATs) to measure the largest angular scales visible from the Atacama Desert in Chile. One SAT has an aperture diameter of 0.42 m and will measure roughly 10% of the sky with more than 300,000 bolometer detectors across the three SATs [9]. Among the three SAT's are three frequency bands – each with 10,000 detectors: Low-Frequency (LF) bands are centered at 27 and 39 GHz, Mid-Frequency (MF) bands are centered at 93 and 145 GHz, and Ultra-High-Frequency (UHF) bands are centered at 225 and 280 GHz

Mapping the three frequency bands will allow for the separation of the CMB from galactic foregrounds (sourced from synchrotron and dust radiation). The primary goal of the SATs is to measure the primordial tensor-to-scalar ratio, r, to within $\sigma(r) = 0.003$, which is one of SO's many ambitious science goals [36]. Another ambitious science goal is to characterize the tiny polarization signal of the CMB. Primordial B-mode spectra peaks at $\ell \approx 90$ (or roughly 2°), and therefore precision measurements at large angular scales are critical. In Chapter 6, I present radio holography measurements of the SAT optics tube.

Here we provide a brief overview of the SAT optics, starting at the window of the telescope and ending at the detectors. The full SAT design is described in [9, 36] and shown in Figure 6.1. The SAT optics is purely refractive; three anti-reflection coated silicon lenses [47, 48] control the beam size and shape onto seven hexagonal detector arrays. The SAT lenses are the largest Si lenses used for a CMB telescope to date [36]. Figure 2.5 shows the ray-trace from the focal plane out the SAT window. Light enters through a 3 mm thick ultra-high molecular weight polyethylene hexagonal window with an anti-reflection coating [33]. A Cryogenic Half-Wave Plate (CHWP) polarization modulator then reconstructs the polarization of the CMB at 40 K. A 1 K Lyot stop is the first cold optical element, and is followed by the SAT refractor. Three anti-reflection coated silicon lenses [47, 48] re-image the light onto seven hexagonal detector arrays. Photons are then coupled onto the detectors by individual feedhorns. The focal plane of each optics tube houses seven hexagonal detector arrays and

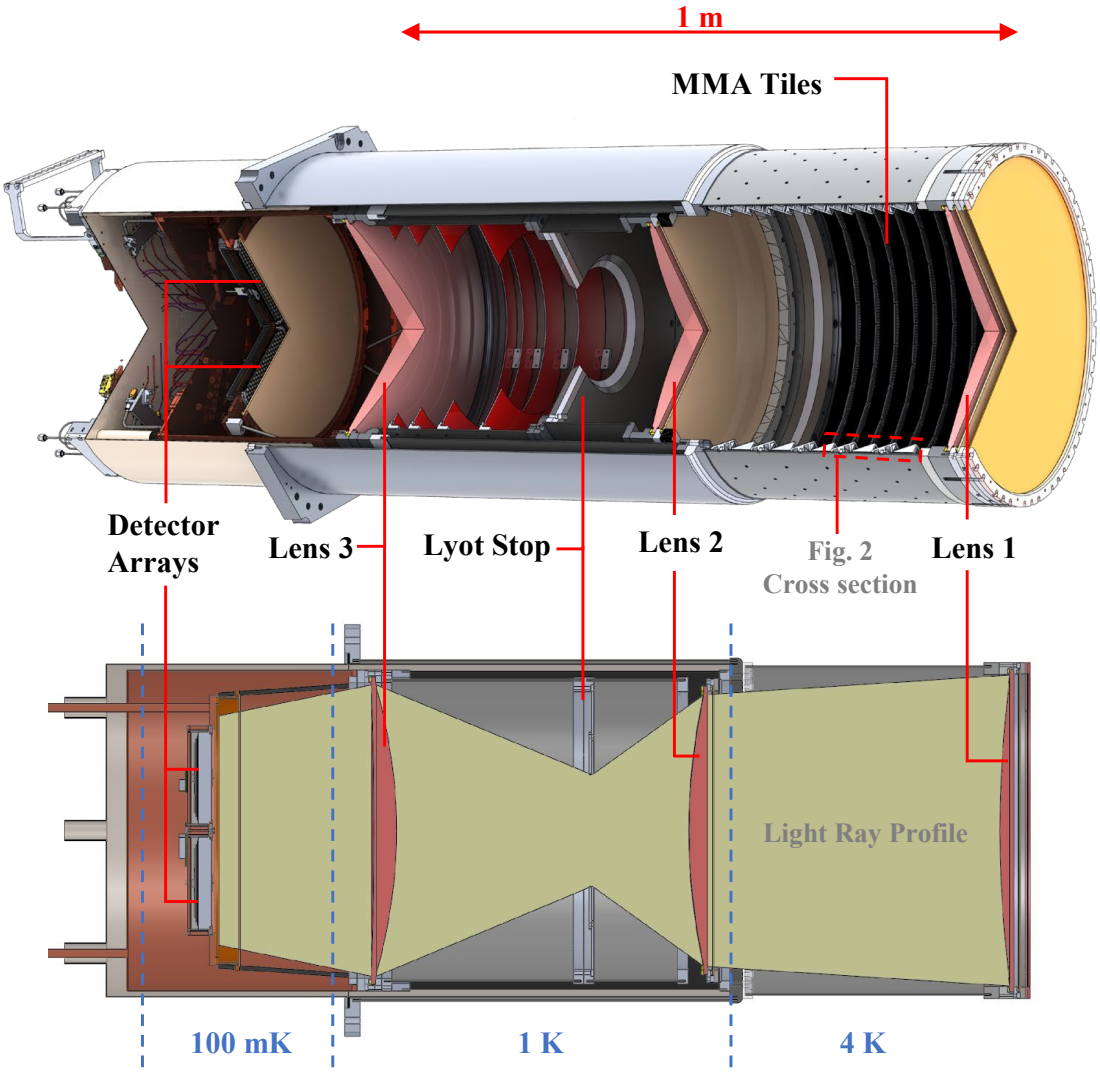

Figure 2.6: Large Aperture Telescope Receiver (LATR) optics tube in the Simons Observatory. A detailed rendering of the optics tube design is shown in the upper part, and a simplified schematic cross-section is shown in the bottom part. Incoming light enters the optics tube from the right and focuses on the detector arrays on the left via three lenses. The yellow-shaded region in the bottom part shows the geometric light ray profile. Operational temperatures for different parts of the optics tube are also annotated. More details of the optics tubes are described in [10]. The MMA tiles are installed in the regions between lens 1 and lens 2 at 4 K. Fig. 3.2 shows a cross-section of the MMA tile assembly (box with red dashed lines) in the optics tube and the detailed design of one tile. A flat version of the MMA tile (Section 3.6) was also used to cover the front and back of the Lyot stop at 1 K.

are cooled to 100 mK.

2.3 Optics Tubes

Modern ground-based millimeter-wave telescope receivers have advanced to the point where detector noise is dominated by photon noise, meaning the thermal or electronic noise intrinsic to the detectors (and the associated readout system) is less than the photon noise from the incident light. The in-band optical power incident on the detectors—closely related to the photon noise—arises from the sky signal, the atmosphere, and stray light outside the desired optical path. The out-of-band instrument spectral and angle response is largely set by filter stack and baffle implementation.

The cross-section of the SAT optics tube is shown in Figure 2.5 and the LAT optics tube is shown in Figure 2.6. Components of the optics tubes are common; Silicon is used in all lenses due to its optical properties, enabling fast-imaging of the beam onto the detectors at millimeter wavelengths. Windows of the optics tubes are often made of high-density polyethylene, as it is transparent to millimeter-wavelengths and can sustain vacuum as the optics tubes are cooled. Feedhorn arrays in the focal plane guide the photons onto the cryogenic detectors, and can be a source of cross-polarization in the optics, making it critical to characterize prior to deployment.

The sky signal and the atmosphere power loading observed by the detectors cannot be reduced by improving the instrument, whereas the stray light loading can be reduced by a more effective design. Instead of following the main optical path, stray light is reflected or scattered by the side walls of cryogenic receivers before being absorbed by the detectors. Characterizing and constraining such scattering, and other optical systematics, is critical for achieving the precision cosmology.

2.3.1 The Status of the Simons Observatory

The Simons Observatory is currently being deployed in the Parque Astronomico located in the Atacama Desert in Chile (Figure 2.2). The telescope site is situated at an elevation of 5,200 meters near the peak of Cerro Toco at 22° 57' S, 67°47' W. The arid conditions and elevation at the site minimize contamination to millimeter wave signals from water vapor.

Integration and testing occurs in parallel with deployment, as the rollout of the Simons Observatory continues. In the year to come, SO will begin observations and characterize the CMB with unprecedented sensitivity, with many discoveries of the nature of our universe to come.

Chapter 3

Metamaterial Microwave Absorber (MMA) and its Cryogenic Applications

3.1 Introduction

Stray light in optics tubes can not only compromise image fidelity through ghosting or glint, but also degrades the detector sensitivity. This chapter concentrates on suppressing stray light by minimizing reflection and scattering within cryogenic receivers [30, 49, 50]. Terminating stray light at the lowest possible temperature is typically achieved by cryogenic baffling design, which minimizes reflection and scattering. Ideally, the baffling surfaces are constructed of millimeter-wave absorbing material, with high absorptivity and low reflection/scattering over a wide range of incident angles and frequencies. Beyond the required optical properties, the absorbers should be efficiently cooled to cryogenic temperatures with robust thermal contacts and be able to withstand the mechanical stress associated with thermal cycling. Since cryogenic space is scarce, the absorbing material is often required to be as compact as possible. Ideally, the absorber should be light in mass, especially for future

space missions.

Available options include conductively-loaded-epoxy [51], and commercially-available absorptive sheets[1]/tiles[2]. The conductively-loaded-epoxy relies on the conductive materials to absorb the radiation; however, the high index of refraction of the epoxy gives high reflectance and scattering, depending on the roughness of the surface. In addition, the epoxy normally has a $> 2\,\mathrm{g{\cdot}cm^3}$ density, adding a significant mass to the cryogenic system. The commercially-available absorptive sheets and tiles provide high absorption, while mechanically and cryogenically attaching them to low-temperature surfaces poses great challenges. Recent development on 3D printing also enables more absorber designs [52], while mass production at low cost is still a challenge. To overcome these obstacles, the SO team developed injection-molded tiles with a metamaterial gradient index anti-reflection coating. Metamaterials are artificially engineered materials, in terms of content and geometry, to achieve physical properties that are not available in nature [53–55]. Our solution provides high absorption with customized thermal and mechanical interface for cryogenic applications.

Here I describe the design (Section 3.2) and characterization (Section 3.3) of the tiles, along with its application within the Simons Observatory (SO) Large Aperture Telescope Receiver (LATR) [33, 34] and Small Aperture Telescopes (SAT) [36][3]. I also discuss potential future applications in Section 3.6[4].

3.2 Optical Design

The ideal baffling material minimizes reflection and scattering of light over the relevant range of angles of incidence, while mechanically (and even cryogenically) fitting within optical

1. For example, HR-10 sheets from Emerson & Cummings.

2. For example, Tessellating Terahertz Radar Absorbing Materials (RAM), Thomas Keating Ltd.

3. The MMA tiles are also used in CCAT-Prime cam [56].

4. The following was published in Applied Optics in 2021 [18]. The paper was selected as Editor's Pick and given a press release here [57].

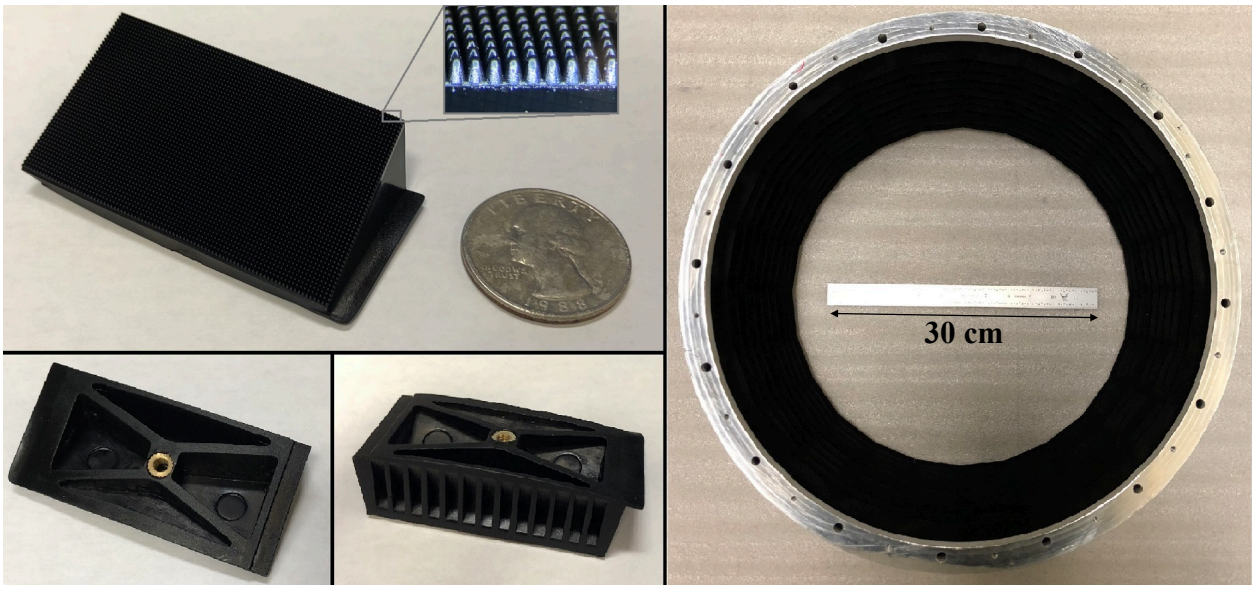

Figure 3.1: Manufactured MMA tiles. The manufactured tiles are presented from different perspectives. The top left photo shows one tile from the absorbing surface. A microscope photo of the pyramids is shown in the insert. The pitch between pyramids is kept as 0.6 mm as designed. The bottom left two photos show the back of the tile from two other perspectives. The light weighting pockets are visible along with the brass injected M3 nut for fastening. The photo on the right shows the assembly of 240 tiles installed on the wall of the optics tube section (see Fig. 2.6). A ruler (~ 30 cm) is placed in the center for scale. Note that the absorbing surface appears to be black and featureless in the assembly photo. The condition stays the same regardless of lighting in the room, which supports the effectiveness of the AR-coating design even in optical.

systems. In the case of the SO LATR [10, 33–35], the desire to close-pack the optics tubes limits the radial extent of the absorbing material to about 1 cm to avoid clipping the beam near the front of the optics tubes (between Lens 1 and Lens 2 in Fig. 2.6).

A detailed study of the SO LATR optics tubes revealed that improving light absorption near the front of the optics tubes would most significantly reduce optical power loading [14]. This study also showed that stray light on that section of the optics tubes ranges from 55° to 90° relative to the surface normal, taking up $\sim 2\,\%$ of the solid angle. Controlling the stray light in that section improves the telescope's mapping speed by $40-80\%$,[5] significantly increasing the sensitivity of the instrument. The Fresnel Equations show that the reflectance

5. Mapping speed is defined as $1/\mathrm{NET}^2$, where NET is the noise-equivalent-temperature (NET). More details about mapping speed are available in [58].

for dielectric materials approaches unity near grazing angles. To improve performance at these high angles, the absorbers were fabricated with the absorbing surface tilted at 26° relative to the normal of the optics tube surface (Fig. 3.2). The tilting reduces the angle of incidence by 26° to $< 64°$ (incoming light cannot exceed 90° angle of incidence) where the absorbing surface provides desired optical performance. Note that the angle of incidence is viewed in a time-reverse fashion here.

The goal of mass production led to the selection of injection molding carbon-loaded plastics. The carbon content increases the optical loss of the plastic materials so that the radiation is sufficiently attenuated within a small depth of bulk materials. However, the carbon-loaded plastics have relatively high dielectric functions, leading to high reflectance on a flat surface. Therefore, an effective anti-reflection coating is designed. The full design and thermal testing is described in [18].

3.3 Optical Testing

Optical properties of the MMA tiles were measured for diffuse reflection, or scattering, at 110 GHz and specular reflection in the frequency range from 90 GHz to 170 GHz. The measurements also covered different angles of incidence. The results verified that the tiles achieved the designed high absorptivity and low reflection and scattering.

The optical measurements were conducted at room temperature. A consideration in using the technology at low temperatures is the following—the detailed composition and realization of the material (e.g., amorphous lamp black, activated carbon, pyrolytic carbon, graphite, etc.) influences the temperature dependence of the bulk resistivity and thus the dielectric function of the plastic [59, 60]. From the measurement of the bulk resistivity at 3 K relative to ambient, this is a modest effect for the carbon loaded TPU formulation explored here. The design of the MMA tiles is insensitive to the dielectric function of the bulk dielectric mixture. Therefore, dramatic changes of the tile's optical properties are not

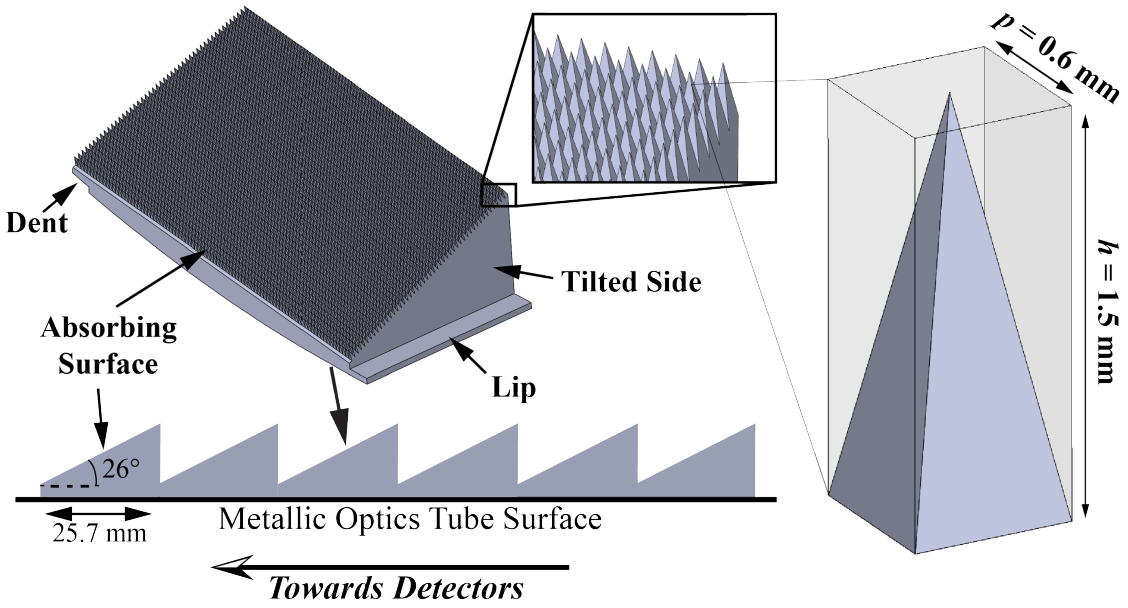

Figure 3.2: MMA tile design. A snapshot of a single tile design is shown. The tilted upper surface has the pyramidal structures as described in Section 3.2. A zoom-in plot shows details of the pyramidal structures, acting as a metamaterial anti-reflection coating. Another insert on the right zooms in further and shows one single unit of the metamaterial structure, with a pitch, $p = 0.6\,\text{mm}$ and a height, $h = 1.5\,\text{mm}$. The tile bottom is curved to fit the cylindrical inside surface of the metallic optics tube, which is used for structural support, heat sinking, and reflective optical termination for the absorptive tiles. A lip and a dent are for seamless tessellating. A cross-section of the segmented tilted surface is shown in the lower left part. In a time-reverse fashion, light rays coming from the left would hit the tilted surface with a $< 64^\circ$ angles of incidence, where the absorbing surface achieves the desired optical performance.

expected in cryogenic temperatures down to 3 K or lower.

3.3.1 Optical Hardware

In the measurement setup, a source emits a millimeter-wave through a feed-horn toward a parabolic mirror, which then reflects a plane wave toward the sample, at an angle of incidence controlled by a rotary stage. The signal reflected off the sample propagates to a second mirror, followed by the receiver feed-horn [19]. The sketch of the setup is shown in Fig. 3.4. Eccosorb HR-10 sheets are placed on surrounding surfaces to reject multipath propagation. The alignment of the receiver is controlled with a three-axis stage. The tilt of

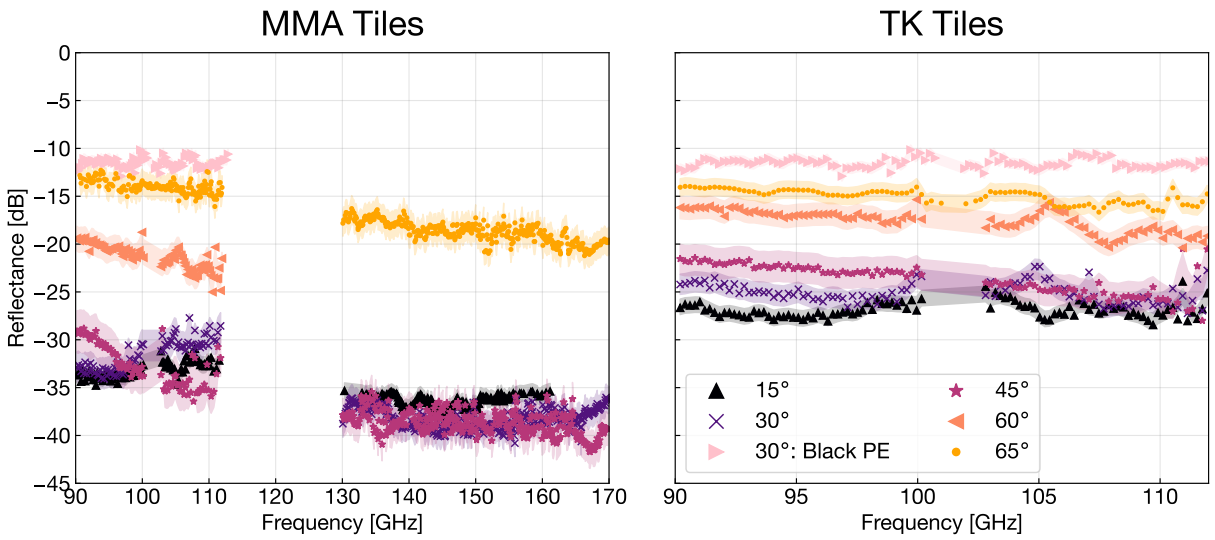

Figure 3.3: Specular reflectance measurements. The two panels show the specular reflectance measurements of the MMA tiles and the TK tiles at different angles of incidence, including 15°, 30°, 45°, 60°, and 65°. The samples are measured in W-band (90 GHz to 110 GHZ) and D-band (130 GHz to 170 GHz). The left panel shows the W-band (90 GHz to 110 GHZ) and D-band (130 GHz to 170 GHz) reflectance of the MMA tiles. The measurement gap in the left panel is due to the different frequency bands of the two sources used in the setup. The right panel measures the W-band (90 GHz to 110 GHZ) reflectance of the TK tiles. The two panels share the same y scale for comparison. The measurement of a flat black polyethylene sample without a AR-coating is included in both panels, which is conducted with a 30° angle of incidence. Comparing the sample without an AR-coating (purple triangles) and the MMA tiles (blue crosses), ~ -20 dB specular reflectance reduction is achieved with the metamaterial AR-coating.

the sample is controlled with a three-point micrometer mount.

3.3.2 Receiver Electronics

A correlation receiver is used for these measurements. The receiver compares a reference tone to a signal which has passed through the optical path, creating an interference pattern between the two [19]. The correlation receiver is summarized in Fig. 3.5. The Re-configurable Open Architecture Computing Hardware (ROACH-2) board correlates the reference and modulated signals [61].

The millimeter-wave source sends a signal, ranging from 10.5 GHz to 13 GHz, to a mul-

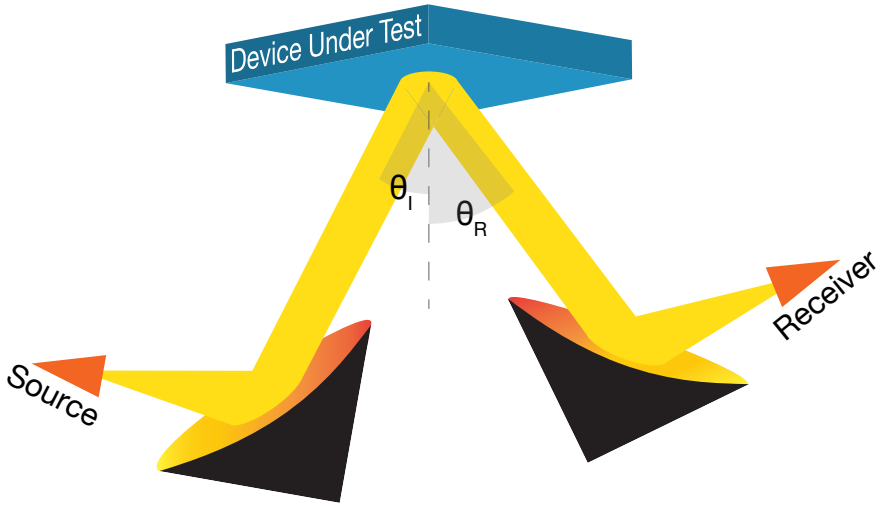

Figure 3.4: Optical measurement setup sketch. The orange lines represent the beam as it travels from the source feed-horn, collimated off of the first mirror and to the sample. After being reflected/scattered by the second mirror, the beam is focused into the receiver to be measured. Incident (θ_i) and receiver (θ_r) angles are controlled by a motor for measuring different angles of incidence and scattered power.

tiplier which passes through a passive multiplying chain. The W-band (90 – 110 GHz) and D-band (130 – 180 GHz) millimeter-wave sources use multiplication factors of 9 and 12, respectively. The signal is then modulated by the sample. The modulated and the reference signals are separately sent to two harmonic mixers. The mixers extract interference information caused by the offset frequency and send it to the correlation device. This receiver outputs the amplitude and phase of the signal in narrow (50 MHz) spectral bands. Only the amplitude is used in this analysis, though I note that the phase information could be used to improve these measurements in the future.

3.3.3 Measurement

In order to measure their optical properties, an array of tiles are screwed down to a 3D-printed plate. The 3D-printed plate compensates the wedge shape of individual tiles so that absorbing surfaces of all tiles are aligned and oriented upward, forming a 30.5×30.5 cm flat surface (Fig. 3.6).

For comparison, we acquired the Tessellating Terahertz RAM from TK Instruments. The

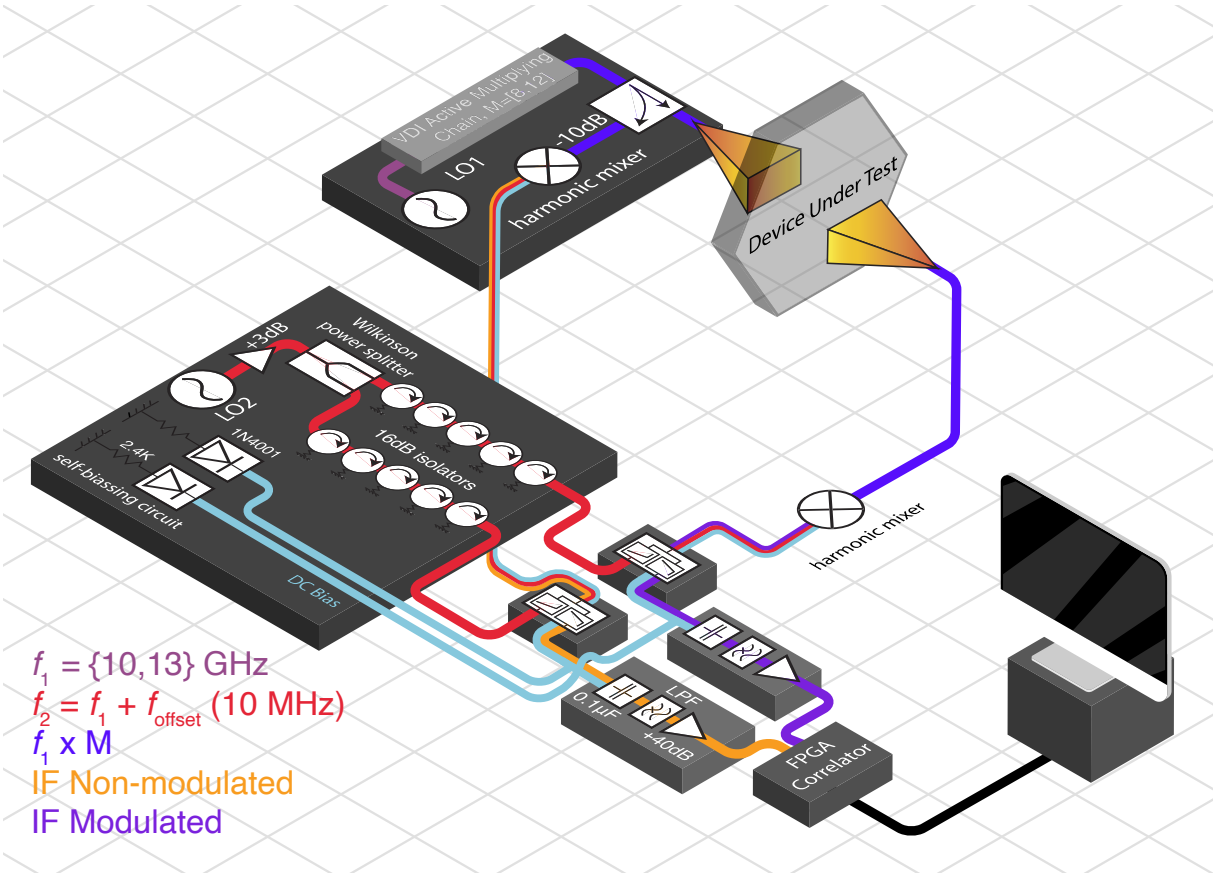

Figure 3.5: The correlation receiver setup diagram. A splitter sends one signal from a millimeter-wave source to a Pacific Millimeter harmonic mixer, while sending the same signal to be modulated by the device under test. The reference and modulated signal are mixed with an LO with an offset frequency f_{offset} from the millimeter wave source. The two Pacific Millimeter harmonic mixers extract interference information caused by f_{offset} and sends this to the ROACH-2 field programmable gate array (FPGA) board where the two signals are correlated.

TK tiles are 25 mm $\times$ 25 mm square tiles that can be tessellated to cover a flat surface. The pyramidal structures ($\sim$2.5 mm in pitch and height) on the optical surface are designed to reduce the specular reflection and scattering in the 100 – 1000 GHz region.

Although the TK tiles and the MMA tiles both have pyramidal structures on the optical surface, they function differently. Pyramids in the MMA tiles, with the sub-wavelength scale, act more as a layer of medium with changing index of refraction; while pyramids in the TK tiles works more within the geometric optics regime to increase the number of bounces of the incoming radiation, due to the adopted surface geometry [62]. The TK tiles have long been

Figure 3.6: MMA measurement sample. MMA tiles are individually bolted into a 3D-printed plate such that each absorbing surface sits flat to form a 30.5×30.5 cm testing surface.

the preferred absorbers in millimeter wavelengths due to their optical performance. The measurement of the TK tiles (≥ 200 GHz) are available in the product website and published literature [63]. Because the MMA tiles are optimized to perform well at the operating wavelengths, an improvement in performance is expected. Even though the measurement only verifies the performance within $90-170$ GHz, the MMA tiles are designed to work from $90-270$ GHz following the same physical principles.

3.4 Reflection Measurement

Once the setup is aligned using an aluminum plate in place of the sample, a calibration data set is taken by measuring the specular reflectance of the same aluminum plate as a function of frequency. The sample measurements are then normalized using the aluminum plate data.

Fig. 3.3 shows the reflected power measured for the MMA and TK samples, with the MMA tiles measured from 90 GHz to 170 GHz and the TK tiles measured from 90 GHz to 110 GHz. The measured results demonstrate the relative performance of the two. For the

MMA tiles, specular reflection is at sub-percent levels (<-20 dB) for all angles of incidence except for 65° (∼-15 dB). Note that 65° is higher than the angle of incidence upper limit in the SO optical design (see Section 3.2). To demonstrate the effectiveness of the anti-reflection coating, a flat carbon-loaded polyethylene (PE) sample without an AR-coating was measured. During the test, a proper flat molding material sample was not available. Therefore, I measured the carbon-black loaded PE sample—with a lower dielectric function—as a lower limit of the reflectance from a flat molding material sample. With the coating, the MMA tiles reduce the specular reflection by ~ -20 dB. Meanwhile, the specular reflection from the TK tiles is 5–10 dB higher than that from the MMA tiles at different angles of incidence.

3.5 Scattering Measurement

The scattered power off the surface of the sample is determined by measuring the received power as a function of the receiver's angle, fixing the source feed horn at a set angle (Fig. 3.4). The source (incident) and receiver (scattered) angles are controlled by two rotary stages. The radiative source sends one frequency and is held at a constant position (i.e. angle of incidence), while the receiver sweeps across different angles. Fig. 3.7 shows the scattering measurement with a 110 GHz source at four angles of incidence: 15°, 30°, 45°, and 60°. To account for the uneven surface of the samples, scattered power is measured and averaged over 17 rotations of the sample (Fig. 3.6). Then error bars (in Fig. 3.7) are estimated from the 17 measurements as the standard error of the mean. The measurements show that wide-angle scattering is suppressed to $<$-40 dB (< 0.01 %). All measurements are referenced to the specular reflection data from the aluminum plate.

The integrated scattering power is calculated by integrating the scattering over the corresponding solid angles (Eq. 3.1). The sample's fractional integrated scattering power, denoted as S, is normalized by the total integrated input power where B is the sample measurement,

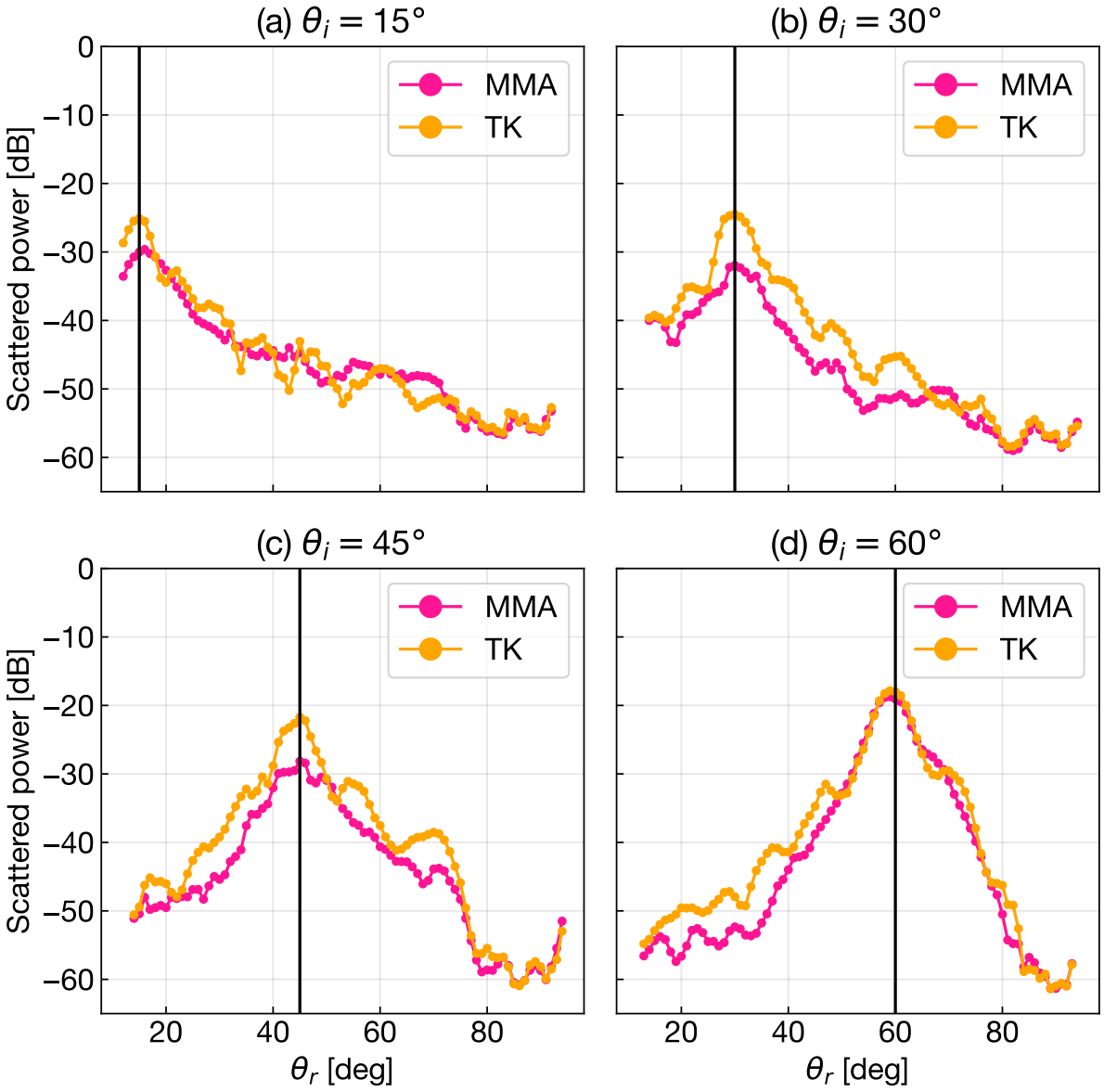

Figure 3.7: Scattering measurement. The four panels show front scattered power off the sample with the source located at four angles of incidence θ_i: (a) 15°, (b) 30°, (c) 45°, and (d) 65°. The source was set at 110 GHz. Each of the measured data points was averaged over 17 different sample rotation angles, from which the associated error bars were also estimated. The error bars are too small to be visible at these y scales. The vertical black lines indicate the position of the specular reflection directions. The blue data points show the results from the MMA tiles, while the red data points show the results from the TK tiles. The TK tiles are measured to have an overall higher scattering than the MMA tiles, which leads to a higher integrated scattering power, as shown in Table 3.1.

θ_{I}	15°	30°
MMA	$0.49 \pm$	$0.12 \pm$
	0.03%	0.002%
TK	$0.67 \pm$	$0.53 \pm$
	0.02%	0.01%
θ_{I}	45°	60°
MMA	$0.27 \pm$	$1.98 \pm$
	0.01%	0.02%
TK	$0.83 \pm$	$2.24 \pm$
	0.01%	0.02%

Table 3.1: Integrated scattering power (in percentage) with different source angle of incidence θ_{I} at 110 GHz for MMA and TK tiles. Integration is from $\theta_{\mathrm{R}} = 0^\circ$ to 45° away from the specular reflection direction. The cited error is calculated from the standard error of the mean over the 17 repeated measurements for each angle of incidence.

A is the normalized aluminum plate reflection and scattering profile, and θ_r is receiver angle.

$$\mathrm{S} = \int_0^{\frac{\pi}{4}} \mathrm{B}\sin(\theta_{\mathrm{r}})d\theta_{\mathrm{r}} \Big/ \int_0^{\frac{\pi}{4}} \mathrm{A}\sin(\theta_{\mathrm{r}})d\theta_{\mathrm{r}}. \tag{3.1}$$

This work does not include the power beyond 45° ($\pi/4$) away from the specular reflection direction, considering its negligible contribution. I calculate the integrated scattering power for our MMA tiles and the TK tiles, listed in Table 3.1. The results demonstrate the MMA tiles have lower integrated scattering power compared to the TK tiles, meeting the 1% requirement for angle of incidence $\leq 45^\circ$.

3.6 Future Applications

Flat and square MMA tiles were manufactured, in quantities of $> 10,000$, for more general use. The square tiles come in the size of 2.5 cm $\times$ 2.5 cm with the same anti-reflection coating (Fig. 3.8). Each of the flat tiles weigh ~ 4 g. Tessellating features cover the sides of the square tiles: two sides of the square overhang as lips, while the other two sides indent. These features enable seamlessly tessellating copious number of tiles together. Given the limited thickness (~ 6 mm), an injected nut cannot be installed; instead a shaft was designed

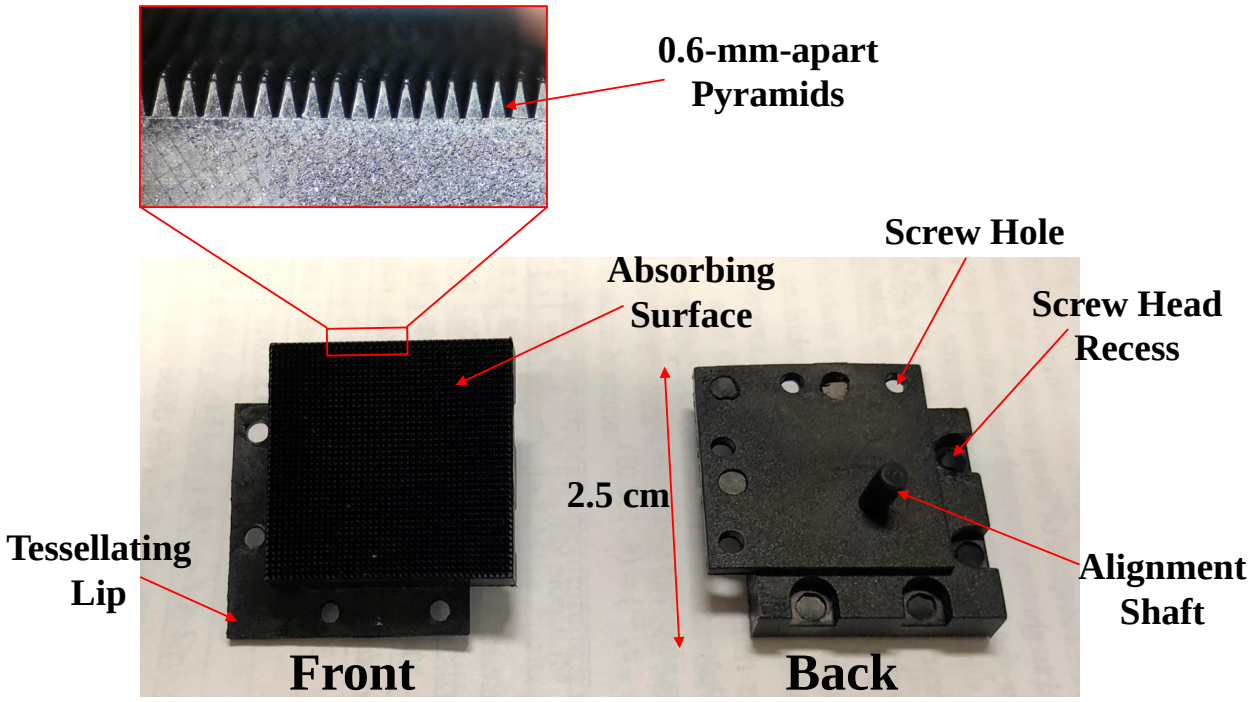

Figure 3.8: Manufactured square tiles. The 2.5 cm × 2.5 cm flat tiles are also manufactured via injection molding with the same pyramidal structure on the absorbing surface. The main photo on the bottom shows two square tiles from the front and the back. Major features on the tiles were denoted as well. A microscope photo of the pyramids is shown on the top left. The photo shows sharp features of the pyramids, which are only 0.6-mm wide and 1.5-mm tall. The pyramids show sharper features compared to the ones in the tilted tiles (Fig. 3.1). That is because the square tiles are smaller with a simpler shape, which facilitates the manufacturing process.

on the back for alignment. For fastening, four over-sized M2 screw holes were designed on the tessellating lip. Correspondingly, four recesses for the screw head (from adjacent tiles) were designed on the tessellating dent (see Fig. 3.8). This version of MMA tile is designed to be applied on any flat surfaces by tessellation. They are already used to cover both sides of the Lyot stop in the SO LATR optics tubes (as shown in Fig. 2.6). The tile-covered Lyot stop assembly has been tested at 4 K for thermal properties.

Given the vast potential in customization, the MMA tiles provides a viable solution to blacken cryogenic surfaces with diverse geometries. Therefore, the technology can be useful for many future cryogenic experiments.

3.7 Discussion

The metamaterial absorber (MMA) provides an effective, novel, and low-cost solution to absorb millimeter-wave radiation at cryogenic temperatures. Once the injection mold is manufactured, the tiles are mass-produced at low cost ($< 1/10$ of conventional methods) with a thousands-per-month production rate. Both the initial mold machining and injection molding were performed completely by an external shop, without any involvement from the research group.

The design philosophy breaks the overall surface into basic tiles, facilitating their application to an extended surface. Unlike painted absorbing surfaces, the modularized design allows for the easy replacement of tiles, should part of the surface be damaged. The wedge-shape tile introduced in this paper is designed to work in a specific cylinder for Simons Observatory and CCAT-Prime. But different geometries, such as flat square tiles, are also available with similar optical performance.

The absorber was successfully cooled down to 1 K with a single thermal contact. The optical properties, including specular reflection and scattering, were measured at different angles of incidence in the frequency band from 90 GHz to 170 GHz. The specular reflection is < -30 dB for angles of incidence $\leq 45°$. Even at $65\,°$, the specular reflection is only ~ -15 dB. The integrated scattering power is less than 1% with the angle of incidence $\leq 45°$. Even though this application was tailored for the frequency band from 90 GHz to 270 GHz, the metamaterial anti-reflection coating parameters can be suitably adjusted for use at longer wavelengths. The carbon grain size of this commercially available material and the injection molding process limit the suitability of direct scaling this design to shorter wavelengths. The use of a similar dielectric mixture with carbon lamp black and a lower volume filing fraction could be employed to address this challenge.

The MMA technology enables a high level of customization in the design. For future cryostat development, customized tiles can be designed and manufactured in this way to achieve the enhanced absorption properties, while fitting the geometry of specific cryostat

designs. As sensitivity of detectors improves in the coming years, this technology to control optical systematics becomes even more critical for achieving the ambitious science goals in cosmology.

Chapter 4

Silicon Properties at Millimeter Wavelengths

4.1 Introduction

Low loss is crucial in the warm optical design. Silicon is a potentially attractive material for such applications. Datta et al. 2013 showed that Silicon can be machined to produce very high quality anti-reflective (AR) meta-surfaces to reduce the reflected power from the natural 30% to levels in the few tenths of a percent range [47]. The key development required is identification of a source of Silicon with low dielectric losses at room temperature. Substitution of a lens with lower dielectric losses could therefore make a substantial impact on the sensitivity of this instrument. To better understand the types of available materials, we have made precision measurements of the dielectric properties of two types of Silicon.

Dielectric loss and its associated thermal emission is a key driver for sensitivity in millimeter wave receivers. A low loss implies low emission from a material, therefore limiting thermal noise propagating through to the detector. The contribution to the thermal noise

due to loss, $T_{\rm sys}$, can be calculated as:

$$T_{\rm sys} = T_{\rm comp}(L-1) \tag{4.1}$$

where $T_{\rm comp}$ is the physical temperature of the component, $L = \exp(2\pi n \tan(\delta)/\lambda_0)$ is the optical loss, n is the index of refraction, $\tan(\delta)$ is the loss tangent, t is the sample thickness, and λ_0 is the free-space wavelength. The noise due to loss can be reduced in two ways: lowering the temperature of the component, and using materials with lower intrinsic loss.

Since it was first reported in Parshin et al. [64] and included in the Lamb 1996 compendium of mm-wave material properties [65], the promise of Silicon as an intrinsically low-loss mm/sub-mm optical material has tantalized the astronomical community. More recently, Krupka et al. 2016 [66] reported on the result of a loss tangent in Ka-band and Q-band ($\approx 27-40\,$GHz) on the order of $\tan(\delta) \lesssim 10^{-5}$ at room temperature ($\approx 300\,K$) for samples of proton-irradiated high purity FZ Silicon, but measurements in W-band ($\approx$90 GHz) and for neutron-irradiated samples are lacking. We address this here using coherent reflectometry measurements.

In Section 4.2 we detail the optical hardware and the receiver electronics used to measure the optical properties. We also describe the two Silicon samples analyzed in this work; intrinsic and neutron-doped Silicon. Section 4.3.1 details the mathematical model and fitting method used to determine the optical properties from reflectivity data. The resulting optical properties are presented in Section 4.4. Lastly, we discuss implications of the results for optical performance of the telescope in Section 4.5[1].

1. The following was published in the proceedings from the 8th ESA Workshop on Millimetre-Wave Technology and Applications in 2018 [19].

4.2 Procedure

Here we describe the hardware used to take the reflectivity measurements of both materials, including optical hardware and receiver electronics.

4.2.1 Optical Hardware

A feedhorn source sends a millimeter wave signal to a parabolic mirror, which sends a plane wave toward the sample, typically at a 10° angle of incidence. For these measurements, the sample is a dielectric slab immersed in air. A portion of the signal is reflected to the first air-dielectric boundary, and the remaining signal propagates through the sample, where it again partially reflects from the second dielectric-air boundary, leading to a Fabry-Perot interference in the dielectric cavity defined by the sample. The reflected signal propagates to a second mirror, followed by the receiver feed horn. The geometry is shown in Figure 3.4.

Eccosorb is placed on surfaces outside the beam in order to reduce and absorb unwanted reflections. The alignment of the receiver is controlled with a three-axis stage. The tilt of the sample is controlled with a three-point micrometer mount. This angle is chosen by placing an aluminum plate in the sample holder and maximizing the received signal at a single frequency. Once the setup is aligned, a calibration data set is taken by measuring the reflectance of the aluminum plate as a function of frequency. This dataset serves to define perfect reflection. The aluminum plate is then replaced with the sample (Silicon here) and the measurement is made. The response of the Silicon sample measurement is divided by the response of the aluminum plate to yield a measurement of the reflectance of the sample as a function of frequency.

4.2.2 Receiver Electronics

A correlation receiver designed for a holography system is used for these measurements. The receiver compares a reference signal to a signal which has passed through the device, creating

an interference pattern between the two. The holographic imaging setup is summarized in Figure 3.5. The Re-configurable Open Architecture Computing Hardware (ROACH2) board correlates the reference and modulated signals [61].

4.2.3 Samples: Neutron-irradiated and Intrinsic Silicon

Two samples were provided by Topsil for testing. The samples as cut exhibited curvature and uneven thickness of approximately 15 mm. A professional third party was contracted to grind and polish the samples flat and parallel. The resulting thicknesses are reported in Table 1, and are accurate to scales $\ll \lambda_0$ measured with a micrometer. The Silicon is made with Float Zone mono growth in an oxygen-free environment, reducing risk of generating thermal donors during high temperature processes [67].

4.3 Reflectometry and Transmissivity

We measured the transmission and reflection of these samples. The data are shown in Figure 4.1. Here we detail the model used to determine the optical properties of the samples, and the MCMC method used to fit the model to our data.

4.3.1 Modeling

We model the dielectric slab with a complex index $n_2 = n_r + in_i$. Air is treated with a purely real index $n_1 =$. The refracted angle in each layer is calculated using Snell's law, where θ_1 is the incident angle and n_1 is the free-space index of the first layer (i.e. n_1 in Eq. 4.2). The setup began at an incidence angle of 10°.

$$\theta_2 = \arcsin\left(\frac{n_1}{n_2}\sin\theta_1\right) \tag{4.2}$$

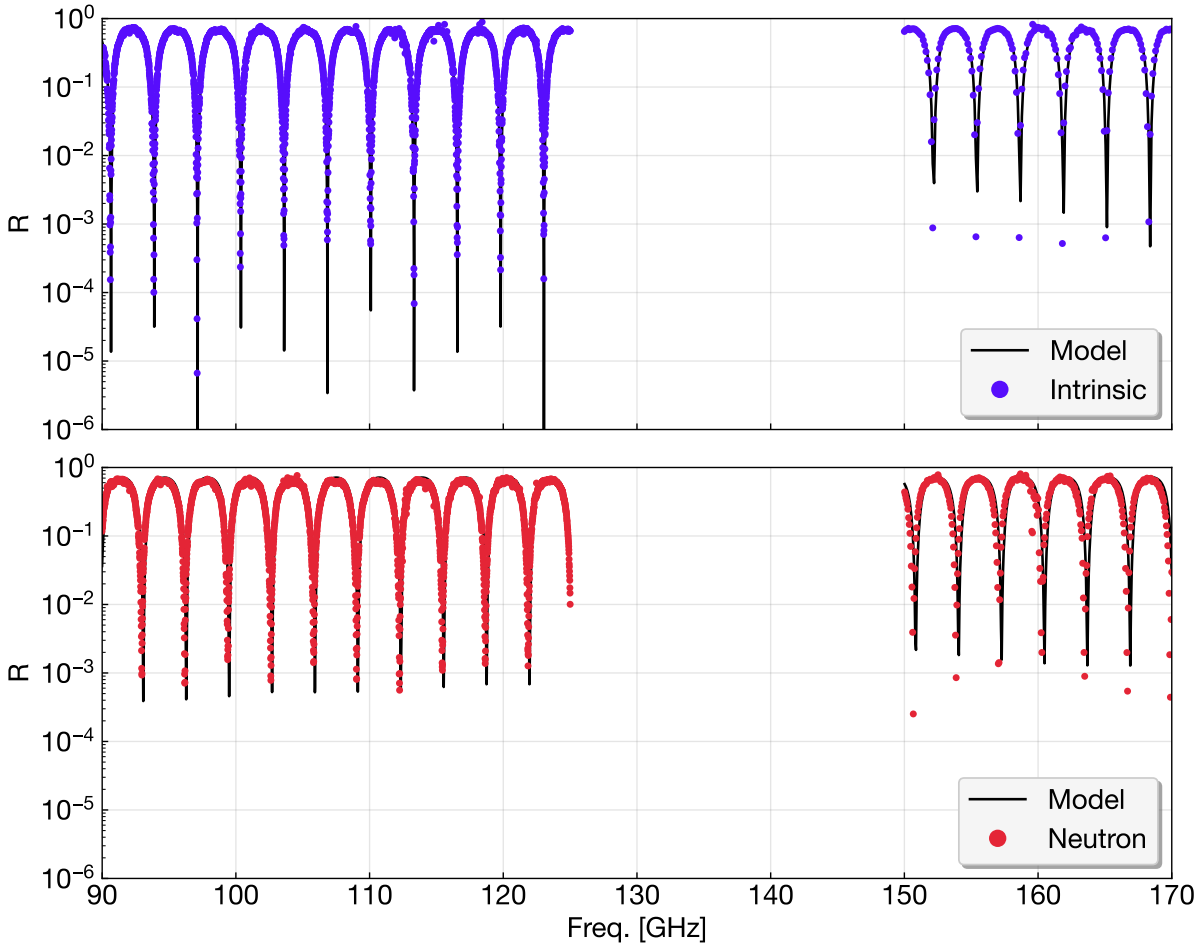

Figure 4.1: Reflectivity of intrinsic (top) and neutron-irradiated (bottom) Silicon against frequency [GHz].

The experiment exclusively uses TM mode signals, where the reflected and transmitted coefficients theoretically predicted by [68]:

$$R = \frac{n_1 \cos\theta_2 - n_2 \cos\theta_1}{n_1 \cos\theta_2 + n_2 \cos\theta_1} \tag{4.3}$$

$$T = \frac{2n_1 \cos\theta_1}{n_2 \cos\theta_1 + n_1 \cos\theta_2} \tag{4.4}$$

$$\tan(\delta) = 2n_i/n_r \tag{4.5}$$

Using Eq. 4.3 and Eq. 4.4, where the parameter n_2 is the fitting parameter, the material index is extracted from measurements.

4.3.2 Fitting

The loss tangent (or equivalently complex part of the index) leads to a reduction in the depth of the reflection nulls for this signal. The cancellation of the incident and reflected waves is more perfect for lower loss tangent. Therefore, the nulls in the reflection are crucial to get a reliable constraint on the loss. We also note that one of the dominant systematic effects is standing waves between the source and receiver horn. This systematic includes a reflection from the sample. Therefore, this noise is minimized near the nulls. For this reason, we fit the data only where the reflectance is below some threshold (typically $R < 0.01$, though, varying this by a factor of a few has no impact on the results). The weighing of each data point scales as the inverse of reflectivity to force the fit to focus on the depth of the nulls. We test that the analysis doesn't depend on this weighting by doing describe. We implemented a Markov Chain Monte Carlo (MCMC) algorithm for fitting the reflectivity model to our measurements using the Python package `pyMC`, with the real and imaginary components of the index of refraction as fitting parameters [69]. The MCMC algorithm samples the probability distribution of each parameter, in this case the probability of two parameters in the reflectivity model matching the measured reflectivity of the sample. This method was used to fit the measurement to the model, yielding, the real and imaginary components of index of refraction of the sample. The loss, $\tan(\delta)$, of the material is then calculated using Eq. 4.5.

The error bars of loss values are calculated with two methods. The first method is the MCMC error computation with the `pyMC` package in Python. To check these values, each null is fit individually using the MCMC algorithm, yielding an array of parameter values. The root-mean-square (RMS) of these values is then calculated, yielding the RMS error. Both methods yielded nearly equivalent loss error results, and we therefore report the MCMC loss

Silicon	Neutron	Intrinsic
n	3.415	3.412
$\tan(\delta) \times 10^{-5}$	28.93 ± 1.21	1.47 ± 0.09
D [mm]	13.68 ± 0.1	13.56 ± 0.1

Table 4.1: Optical properties of Silicon. Properties extracted from the data when fit with the theoretical model. Properties n is the index of refraction, D is the thickness of the sample in millimeters, and $\tan(\delta)$ is the loss tangent.

error in Table 4.1. The error in index of refraction is not reported as it is likely included in the uncertainty of the thickness, while the MCMC reported a negligible error for this parameter.

4.4 Results

The index of refraction of neutron and intrinsic Silicon are nearly identical, with $n = 3.415$ for neutron-irradiated Silicon, and $n = 3.412$ for the intrinsic Silicon samples. The neutron-irradiated sample has $\tan(\delta) = 2.8 \times 10^{-4}$, while the intrinsic Silicon is nearly an order of magnitude better, with $\tan(\delta) = 1.5 \times 10^{-5}$. See Table 4.1 for a summary of the measured and inferred properties.

The reason for the higher loss in the neutron-irradiated sample is unclear, as the loss tangent should improve for materials with higher resistivity if dominated by the conduction loss term. As the resistivities of the neutron-irradiated and unmodified intrinsic Silicon samples were measured by Topsil to be $> 100\,k\Omega - cm$ and $> 50k\,\Omega - cm$, respectively, the expectation is that the neutron-irradiated sample should have less loss. One possible explanation is that the lattice defects introduced by neutron irradiation contribute to the loss.

4.5 Discussion

We have presented the characterization of optical properties for two Silicon samples using a radio holography setup. The resulting values for the loss $\tan(\delta)$ from MCMC fits to our measurements of the unmodified intrinsic Silicon sample are comparable to those reported in Parshin et al. 1995 [64]. Further, our measured low loss in intrinsic Silicon demonstrates it can be a compelling material for use in warm optics. Krupka et al. [66] also report a $\tan(\delta) \approx 1.2 \times 10^{-5}$ for proton-irradiated Silicon, which is lower by more than 3σ than our measurements of intrinsic Silicon, but on the same order of magnitude. Our work shows promise for the use of intrinsic Silicon for room-temperature optical components, such as those required for the lower bands of the Atacama Large Millimeter/Sub-millimeter Array (ALMA) and potential future CMB experiments. While this specific material will not be used on Simons Observatory, the characterization method is broadly applicable to components used in millimeter-wave reflector experiments.

Chapter 5

Characterizing the Large Aperture Telescope Receiver with Radio Holography

5.1 Introduction

Realizing the SO science goals depends on achieving stringent sensitivity requirements and controlling systematic effects to be subdominant to the statistical noise. To achieve this, the optics tubes must have clean beams with well-controlled side-lobe power. Testing these aspects of the optics tube performance in the lab is challenging. Previously, these parameters were verified on ground-based CMB radio telescope systems upon deployment [70, 71]. In this paper, we present a new approach to laboratory testing of these systems using the technique of near-field radio holography. Holography is an instrumentation technique used to measure the complex monochromatic electric field wavefront using the interference between a modulated and non-modulated signal. Radio holography takes advantage of the antenna theory relationship: the far-field radiation pattern of a reflector antenna is the Fourier Transformation of the field distribution in the aperture plane of the antenna [70].

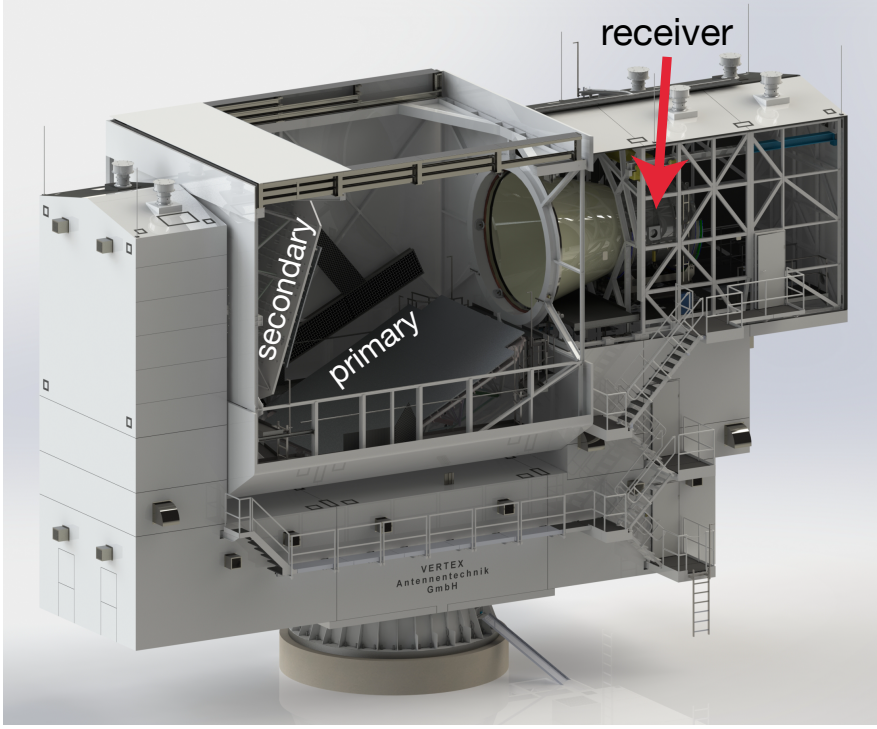

Figure 5.1: The Simons Observatory (SO) Large Aperture Telescope (LAT), featuring a segmented primary and secondary mirror. The mirror's focus is hidden inside the conical baffle near the front of the receiver. The receiver can hold up to thirteen optics tubes. Source: The Simons Observatory Collaboration.

Within radio beam characterization, several techniques exist; 1) scalar beam pattern characterization [72], or measuring only the magnitude of the wavefront, 2) vector beam pattern characterization [73, 74], or measuring the amplitude and phase of the wavefront, and 3) holographic beam pattern measurement [74, 75], which we explore here. While scalar beam pattern characterization requires the beam to be measured at multiple planes along the propagation axis, and vector beam characterization records one complex map, holography records two beam maps (one modulated by the optical element and the other used as a reference) to reconstruct the complex wavefront [70, 76]. Additional use of radio beam characterization is phase retrieval holography, with applications in electron microscopy, optical imaging, and crystallography [77].

Near-field holography allows us to study the wavefront as it emerges from the optics tube, based on the reciprocal theorem, from the cryostat. Using Fresnel diffraction (FD) [78], these

measured fields can be propagated through the optical system to determine the spilled power past the mirrors of the telescope and the far-field beam pattern of the telescope fed by this receiver. Moreover, these beams are useful for the identification and mitigation of optical problems within the receiver (i.e. optical aberrations, focus, scattered power, etc.). These measurements enable a detailed verification of system-level optical performance prior to the deployment of a receiver on a telescope.

In Section 5.2 we describe the optical design and components of the SO optics tube. In Section 5.3 we describe the measurement approach including the cryogenic receiver (5.3.1) and holography hardware (5.3.2) required for measuring beam maps (full details can be found in Appendix A.1). In Section 5.4 we present the measured beam maps. Section 5.4.2 discusses analysis methods to propagate the measured beams into the far-field using FD. We present characterization of the optics tube with and without an infrared-blocking filter in Section 5.5. Section 5.7 details the publicly available code. We conclude with a discussion of future applications of this approach in Section 5.8[1].

5.2 SO Large Aperture Telescope Optics Tubes Design

The LAT is a crossed-Dragone telescope with a 6 m pupil diameter (Fig. 5.1). The LAT Receiver is designed to house thirteen optics tubes, which guide photons onto cryogenic detectors. These optics tubes must maintain excellent beam quality while also limiting the wide-angle scattering. The scattering is critical to the ultimate sensitivity of the SO LAT since every percent that is scattered leads to 3 K of extra noise and a 15(10) % reduction in mapping speed in the 90(150) GHz bands which are critical for the SO science.

Figure 5.2 shows the LATR optics tube [10]. Light enters through a 3 mm thick ultra-high molecular weight polyethylene hexagonal window with an anti-reflection coating [33]. Three anti-reflection coated silicon lenses [47, 48] control the beam size and shape, which re-images

1. The following was published in Applied Optics in 2022 [16], with Section 5.6 added after publication. The paper was selected as Editor's Pick and given a press release here [79].

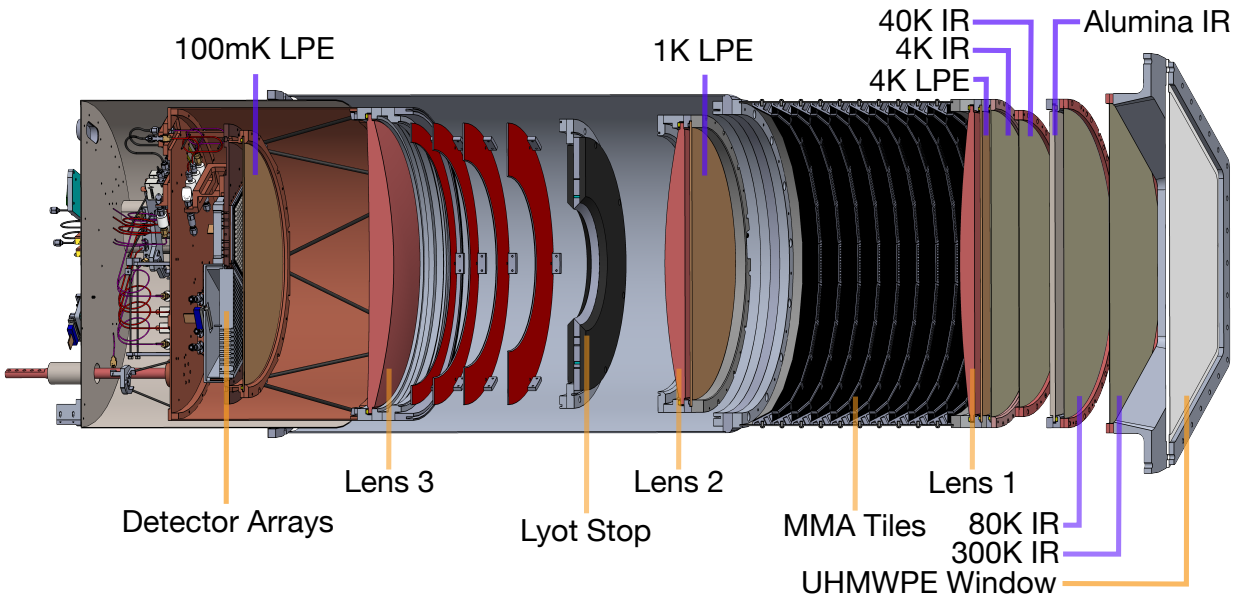

Figure 5.2: The Simons Observatory LATR optics tube. Light enters the optics tube from the right through an ultra-high-molecular-weight polyethylene (UHMWPE) window, and travels through a series of Infrared-Blocking filters (IR), including one alumina IR filter, and passes through the 4 K Low-Pass Edge mesh filter (LPE). The light is focused on the detector arrays on the left by the three lenses, with two additional LPE filters near the 1 K and 100 mK stages. The components within the optics tube are further described in [10].

from the focal plane onto three hexagonal detector wafers. Each lens is accompanied by a low-pass edge filter (LPE) [80]. The light is coupled onto the detector wafers using arrays of drilled spline profile feed horns and the polarization is coupled onto the wafer with an orthomode transducer [81, 82]. Along this path, the light passes through a succession of band-defining and infra-red blocking filters [80]. From the sky side these are a 300 K IR blocking filter, an 80 K IR blocking filter, an 80 K IR rejecting metamaterial anti-reflection coated alumina filter [48, 83], and a 40 K IR blocking filter [84] prior to entering the optics tube. The filter configuration is described in [33]. Between lenses 1 and 2, the walls of the optics tube are coated with baffling metamaterial tiles, described in [85], which control scattering. The full cold-optical design is described in [86]. All optical elements in the optics tube are between 4 K and 100 mK.

5.3 Measurement Approach

Here, we describe the hardware and software used in these holography measurements. Further details can be found in Appendix A.1. For this discussion we divide the system into a cryogenic system mounted in the optics tube and a holography system comprised of a source, correlation receiver, and motion system.

5.3.1 Cryogenic System

The optics tube is housed in a test cryostat called the LATR tester [87]. The cryostat holds and cools a single optics tube and provides support for detector readout. This setup supports up to three detector arrays. In the test configuration, two are bolometric arrays [82] and the third is used for the holography measurements.

The holography array consists of a feedhorn array identical to that used for the bolometric detectors, but with standard wave guide flanges at the outputs. A receiver consisting of a round to rectangular wave guide transition and a harmonic mixer is attached to this feed array. The mixer was designed to operate from 70-110 GHz, but was found to operate satisfactorily up to 170 GHz. For operational simplicity, we used this mixer over our full frequency range from 80-170 GHz. A second identical receiver was also connected for redundancy, but not used in the measurements described here. Two 0-18 GHz coaxial connections were made from the receiver to connectors at the cryostat wall. There are heat sinks spaced along the coaxial cables between the focal plane, which was operated at 4 K while doing holography, and the 300 K cryostat wall. A separate cool down was used to measure the loss along these coaxial feed lines. The loss was found to be 23 dB at the LO frequency (10-13 GHz). Accurate knowledge of the loss along the feed lines is critical for providing the correct amount of power to the mixers in the focal plane. The loss at the intermediate frequencies (IF) (100 MHz) is significantly lower and not critical to the function of this system.

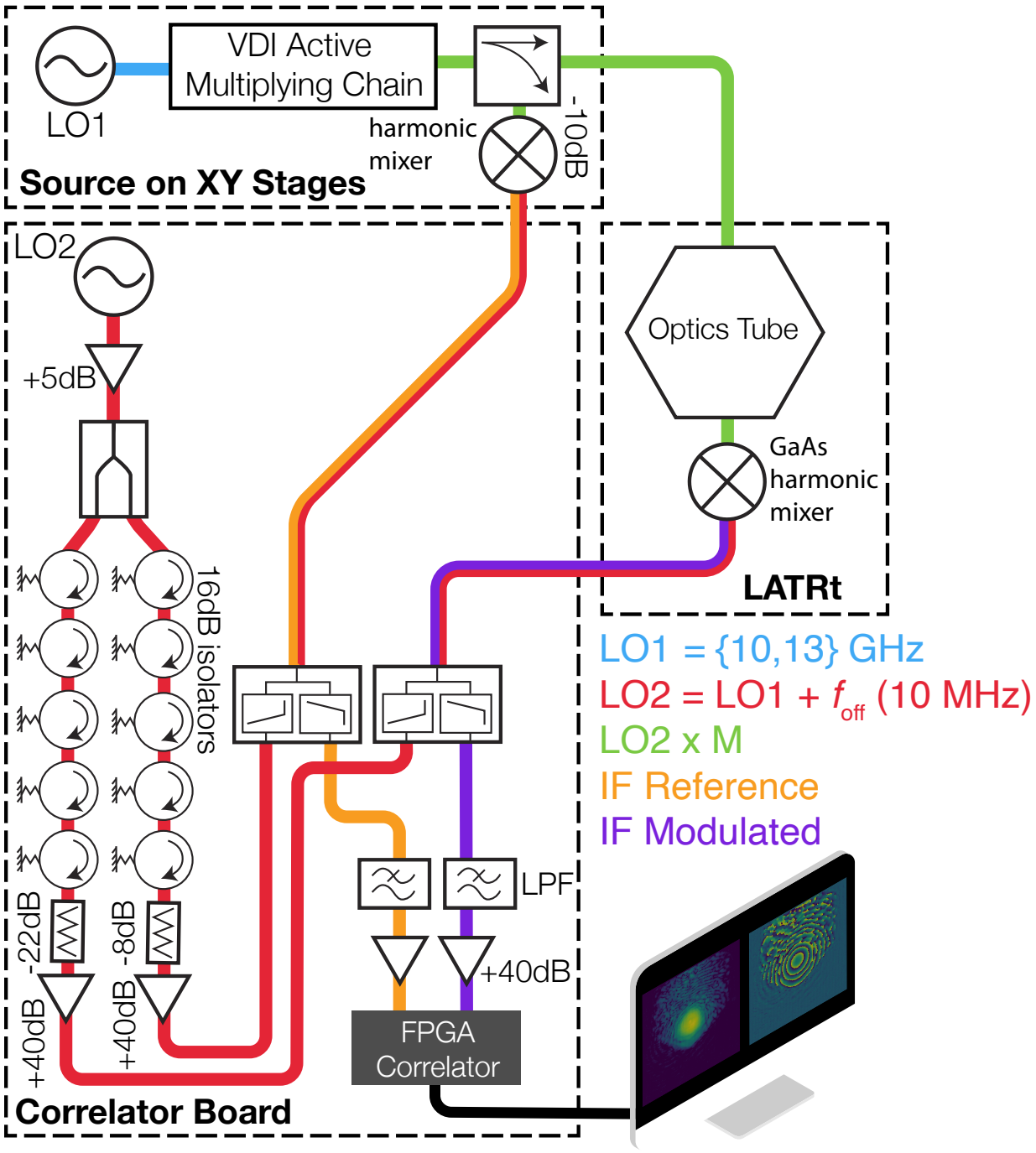

Figure 5.3: Schematic of holography setup. Two local oscillators (LOs) supply frequencies (LO1 and LO2 = LO1 + f_{off}), one of which is multiplied by the active multiplier factor M , while the other serves to down convert the reference and modulated signals into the intermediate frequency.

5.3.2 Holography System

Figure 5.3 shows a schematic overview of the LATR tester (LATRt) holography hardware. Two millimeter-wave sources are used to measure the full SO Mid-Frequency (MF) band: F90 (80-120 GHz) and F150 (130-170 GHz). Only one is mounted at a given time (one of which has a multiplication factor of 8, and the other with 12). These sources are broadcast into the receiver using standard gain feed horns held close to the window (4.5 cm in F90 and 11.5 cm in F150 due to the different attenuator waveguide lengths). We therefore expect different measured beam sizes between the two sets of frequencies, since the beam expands as it leaves the optics tube.

A motorized two-dimensional stage holds the source and is mounted on a support structure above the LATRt. During a measurement, the source (frequency is fixed) is moved over a 50×50 cm range with 0.25 cm steps (black arrows in Figure 5.3). One map takes roughly 12 hours to complete.

A common local oscillator (LO2 in Figure 5.3) is fed to two harmonic mixers: 1) picked off from the source and 2) at the output of the cryogenic receiver. The IF signal from both mixers in the 0-125 MHz band is amplified and passed to a digital correlator (Casper ROACH2 [61]) which computes the complex correlation between the two signals [19]. The FPGA on the ROACH2 board outputs the amplitude and the phase of the correlated output, subdivided into a number of 100 kHz wide bins. Only the bin associated with the IF frequency is used in subsequent analysis. The software to program and analyze output from the FPGA is made public on the *McMahonCosmologyGroup* GitHub page in a package called `holog-exp` [88]. Appendix A.1 provides further details to the hardware of the holography setup.

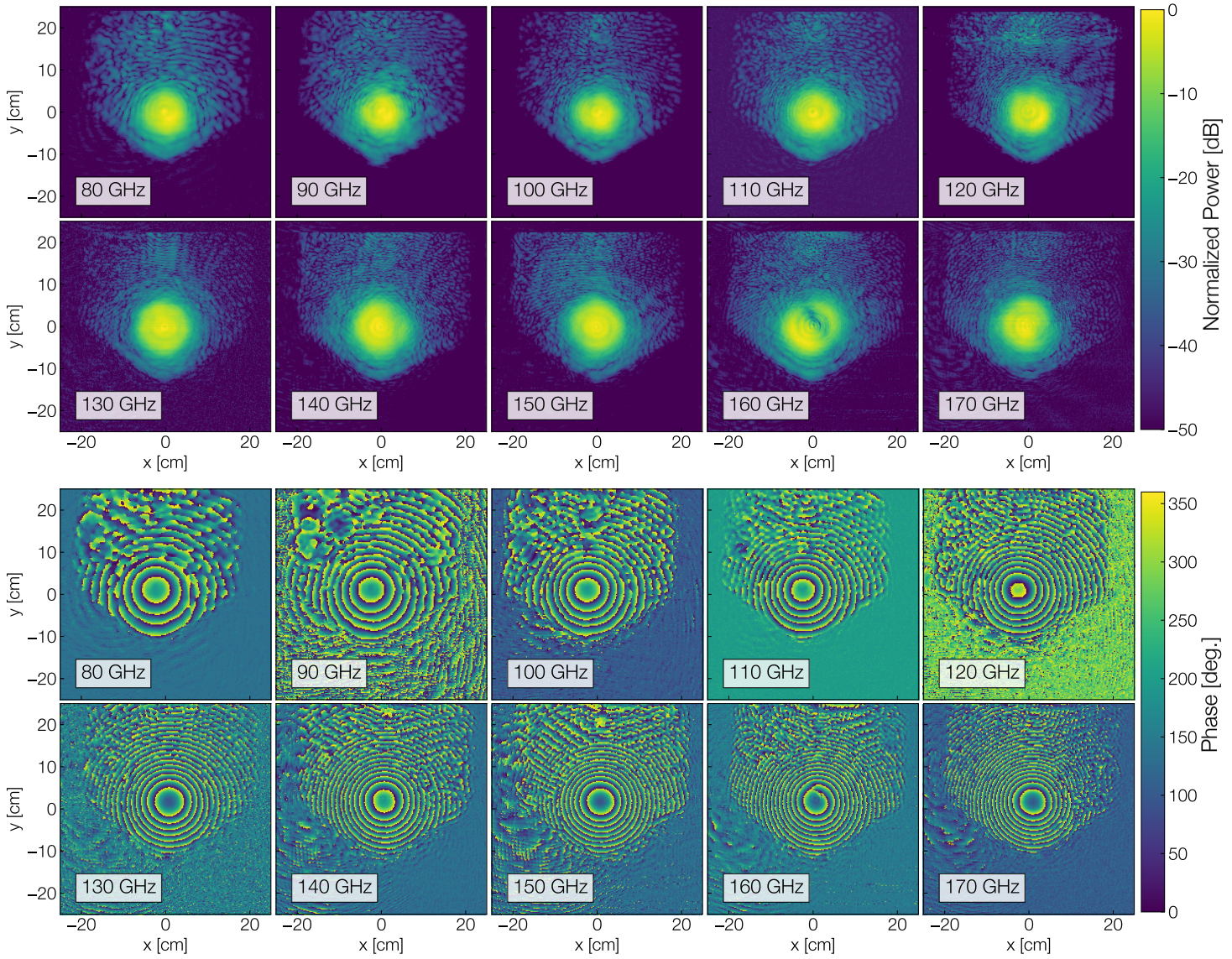

Figure 5.4: Holography beam map measurements in the mid-frequency band. Top: Power at each measured frequency (peak-normalized in each map). The hexagonal side-lobes in the power beam maps are higher in power than the signal-to-noise of the system (45 dB). Bottom: Wrapped phase at each measured frequency.

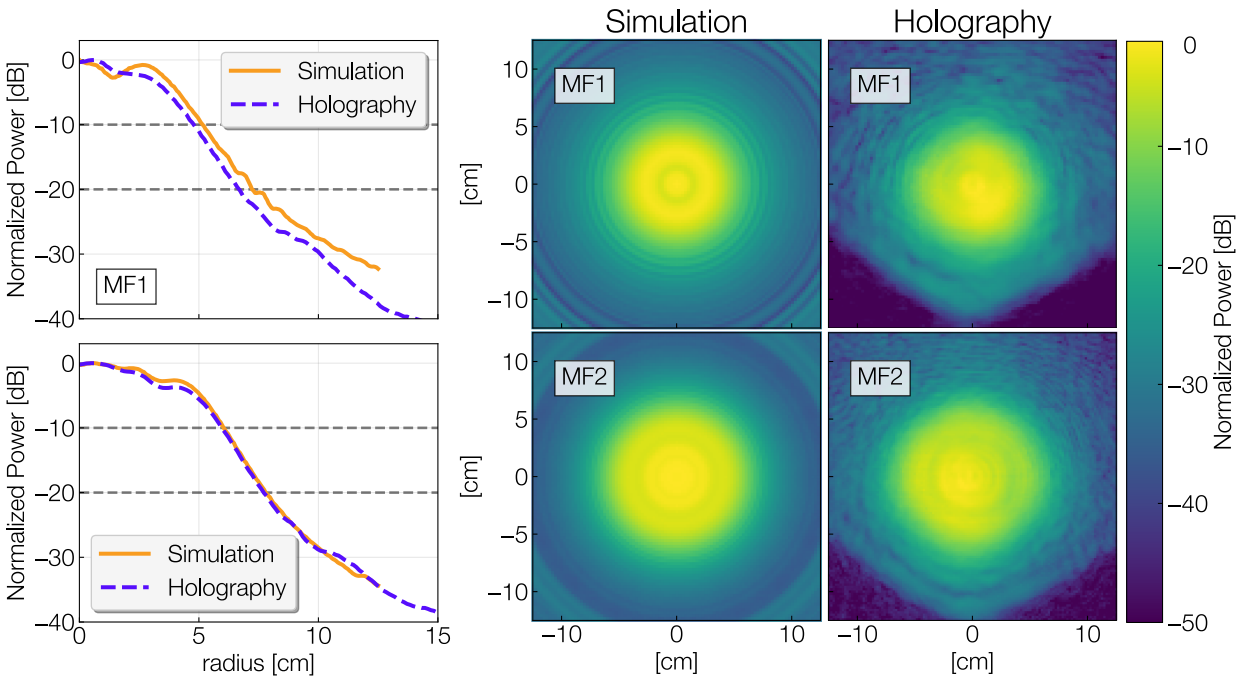

Figure 5.5: Near-field band-averaged MF1 and MF2 beams, simulated and measured with radio holography. Left panel: Radially binned. Right panel: 2D simulated and measured near-field beams.

5.4 Results and Interpretation

5.4.1 Near-Field Beam Maps

Figure 5.4 shows the power and phase of the beam maps at each frequency for which the measurement was carried out. A variable attenuator at the output of the source was used to optimize the amount of signal entering the optics tube, to ensure power was not too high such that the measurement was saturated, but to also ensure the signal was high enough for signal-to-noise greater than 45 dB. As stated in Section 7.5.5.3.2, the F90 source hangs closer to the window than the F150 source (due to different attenuator lengths), and for this reason, we expect the F90 beams to be smaller than the F150 beams.

Figure 5.5 shows the band-averaged near-fields compared to the simulated band-averaged beams. The shape of the main beam was found to be in good agreement with simulations at all frequencies. The asymmetric feature seen in the main beam at 160 GHz is believed to

be associated with an extra mode in the round wave-guide of the receiver. Even with this feature, the radial profile is in very good agreement with the theoretical prediction (within 10% at the -20dB level) (Figure 5.5). The hexagonal side-lobe seen in each beam map are associated with scattering from within the optics tube and out the hexagonal window. The phase indicates the direction of propagation of the beam in space. This suggests that the field of the near-field side-lobes is diverging (or propagating away from the center of the optical path) less quickly than that of the main beam.

5.4.2 Propagation of Fields

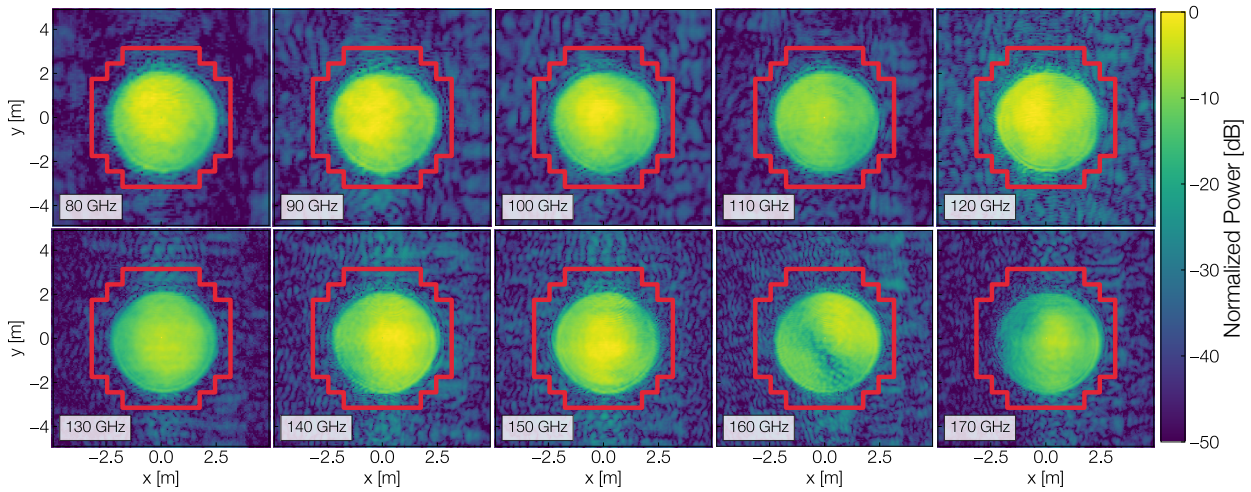

Figure 5.6: All beam maps propagated at the secondary illumination of the Large Aperture Telescope. The spilled power to 300 K is calculated by integrating power outside the boundary of the secondary (red line) with respect to total integrated power of the map.

The performance of the LAT optical system is assessed in detail by using the amplitude and phase of the measured beams to calculate the fields as they propagate through a virtual telescope. This enables calculation of the far-field beam of the telescope, and the amount of signal "spilled", or lost, at the LAT secondary mirror. This represents a unique capability of holography measurements which is critical in assessing the overall performance of this system.

Fields at Secondary Illumination

To determine the amount of power spilled to 300 K, we propagate the measured fields forward and onto the plane of the secondary mirror (approximately 12 m away from the measurement plane. This is carried out by using the Fourier relationship between the near-field $E(x, y)$ and far-field $B(\theta_x, \theta_y)$ beams [70, 89]:

$$B(\theta_x, \theta_y) = \int_{\text{aperture}} E(x, y) e^{i\frac{2\pi}{\lambda}(\theta_x x + \theta_y y)} dx\, dy \tag{5.1}$$

where the complex electric field $E(x, y)$ is integrated over the area of the aperture, and λ is the wavelength.

Figure 5.6 shows beam maps propagated to the secondary mirror of the LAT, with the boundary of the secondary mirror in red. To quantify the spilled power, we integrate the power outside the boundary, and then normalize to the total integrated power of the beam map. We find the average spilled power in the F90(150) detector band is 0.65 (0.68)% with no significant frequency dependence. This is below the design target of 1% and indicates the sensitivity of SO should not be compromised by spilled power to 300 K. This estimate excludes the LATR forecone, a reflective cone of 31.5° in front of the LATR focal plane, which reflects spilled power onto the secondary mirror [42]. Therefor, this method over-estimates the amount of spilled power to 300 K [14].

Far-Fields

To propagate the measured near-fields into the far-field, we use a virtual telescope to produce the fields from a distant (100 km) point source on the measurement plane. We then multiply this field with the measured near-field beam in the corresponding plane. Integrating the resulting field over the area of the focal plane produces the amplitude and phase of the far-field at that point. We then rotate the telescope in azimuth and elevation and repeat this process to produce a full beam map in the sky.

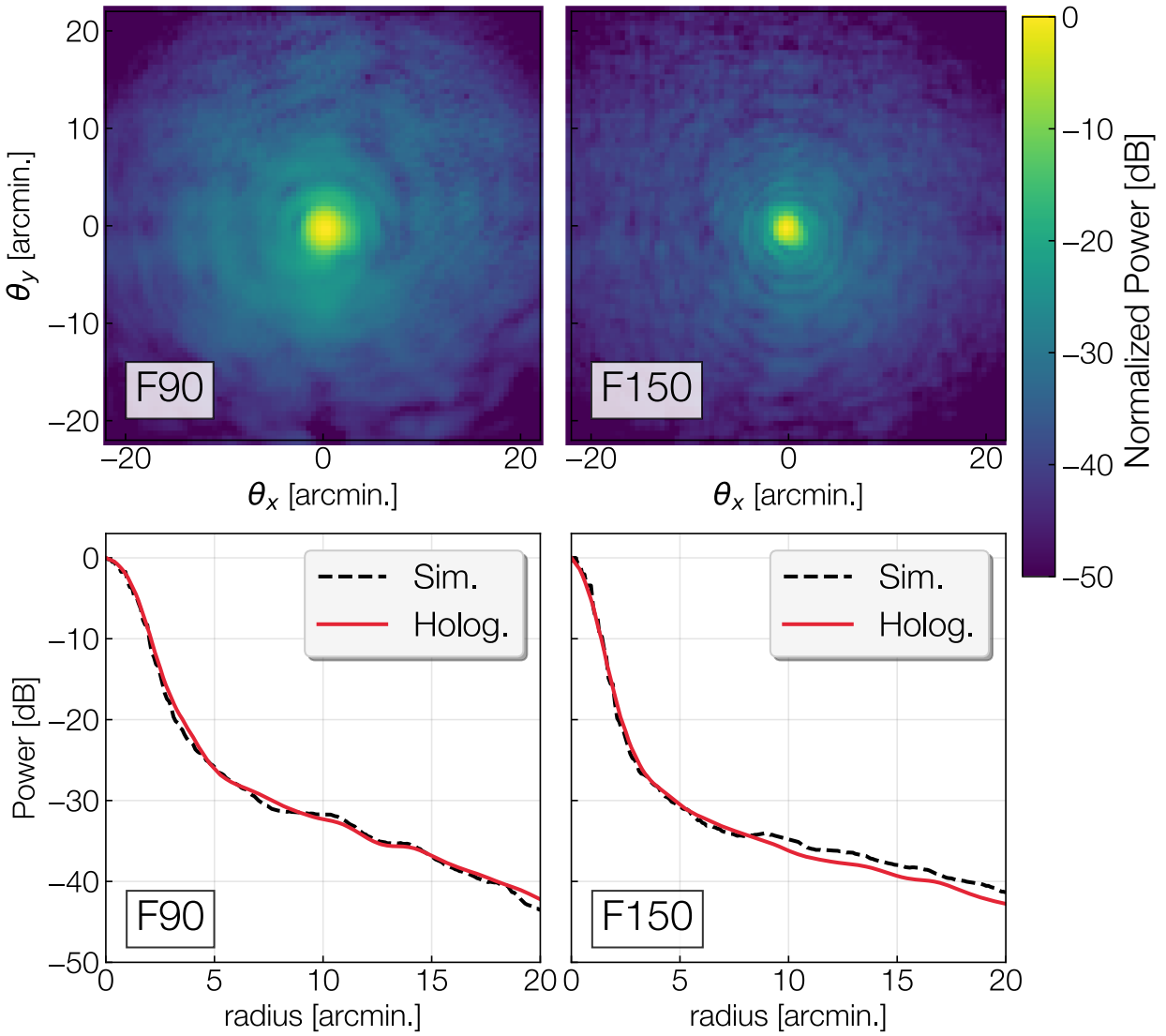

Figure 5.7: Top row: Using FD, the LATRt measurements are propagated through the LAT from the near-focal plane, to the far-field. Bottom row: Radial profile of the measured(simulated) far-field beams in the F90 and F150 bands, plotted in red(black). The lack of diffraction rings in the radial average is explained by the convolution of the measurement(simulation) due to the rectangular source aperture physically in the setup (artificially in the model, see Appendix A.2).

The holography source emits its signal out of a rectangular feedhorn with a finite size. The resulting near-field beam is convolved by this rectangular aperture [78]. This method of convolution is commonly used when analyzing fields measured with rectangular horn faces [90, 91]. Interpreting this measurement requires accounting for this effect, which amounts to a convolution of the electromagnetic field from the optics tube with the field

pattern on the aperture of the feedhorn. The impact of this convolution is to broaden the F90(150) far-field beam by 12.2(4.7)% and to create square diffraction spikes in the raw far-field calculation [78].

We account for this effect with forward modeling, which is described in Appendix A.2. To fully simulate the far-field beam of the LAT including the optics tube, we first simulate the optics tube using `solat-optics` as described in [92]. This produces the near-field beam at the front of the optics tube, which is then propagated into the far-field the same way the measured near-field beams are propagated through the virtual telescope. The resulting far-fields after diffraction spike removal are shown in Figure 5.7. These plots are band averaged, including data from 80-110 GHz in the F90 band and 130-170 GHz in the F150 band. The radial binned far-field holography data are compared to simulations. These comparisons show that the holography data are consistent with the predicted F90(150) FWHM is $2.18(1.38)'$ and with low ellipticity with no unexpected features such as the "little-buddies" seen in the ACTPol experiment [14, 93].

5.5 Filter Removal

We have described the holography results from the final instrument configuration. However, in the initial SO configuration, which contained an additional filter (1K Low-Pass Edge (LPE) filter in Figure 5.2), we found extra signal outside the main beam from the window (hexagon at -20dB) at all frequencies. While these side-lobes did not significantly change the spilled power to 300 K, they would have reduced optical efficiency and led to an enhancement of near side-lobes of the on-sky beam.

To study the frequency dependence of side-lobe power, we computed the integrated fractional power outside the main beam. We define the main beam radius as 13.5 cm, where the beam drops below -20 dB. Figure 5.8B shows the integrated fractional power outside the main beam as a function of frequency, and also the measured reflectivity of the 1 K 6.8 cm^{-1}

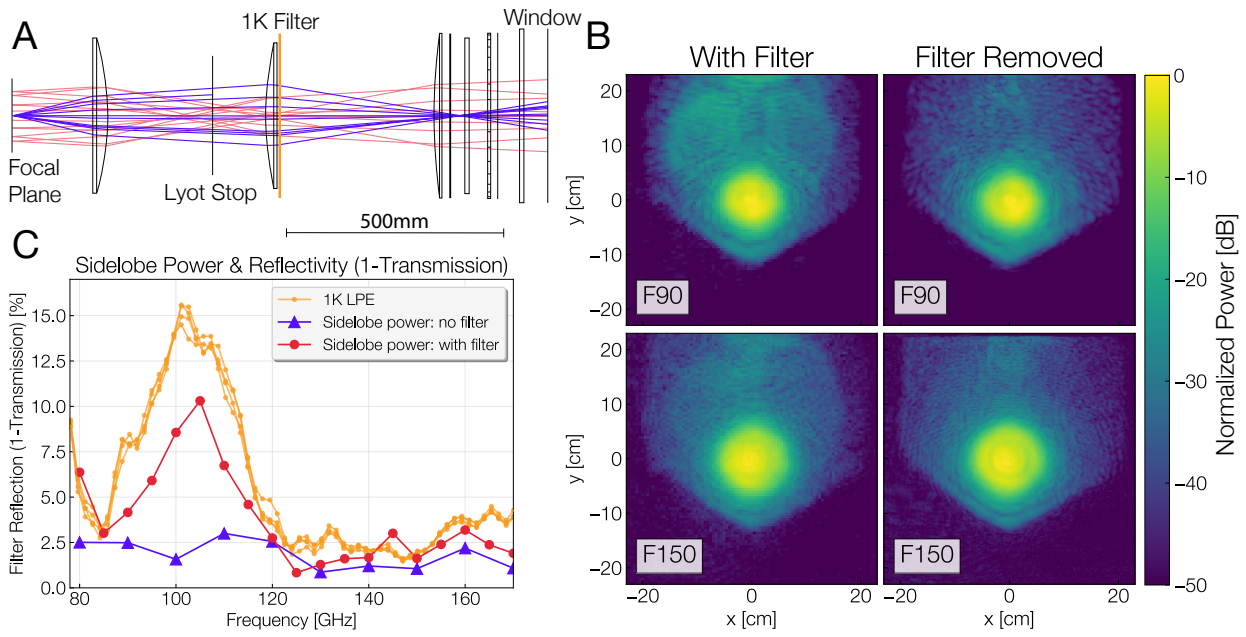

Figure 5.8: A) Time-reversed ray-trace of the SO LAT Optics Tube (OT) with one filter (orange), near the second lens. With 0% on-axis reflectivity of the filter, rays(blue) emerge from the focal plane and exit the OT window. With an on-axis reflectivity of 5.64 % (average LPE filter reflectivity in the full band), rays reflected off of the filter(red) go back to the reflective focal plane (copper and reflective), and then propagate out the front of the window. This is verified in the simulation, as the main beam in front of the OT shows the shape of the focal plane at -25 dB. B) In orange is the measured reflectivity (1-transmission) of the 6.8 cm^{-1} LPE filter, which is placed at the 1-K stage in the optics tube. The red(blue) line shows the measured integrated fractional power outside the main beam at each frequency with(without) the filter in the optics tube. C) Band-averaged near-field beam maps with and without the filter in the optics tube. With the filter, beam maps show extra scattering in the top parts of the map, through the upper portion of the LATRt hexagonal window (hexagonal power around the main beam at roughly -20 dB due to reflection).

LPE filter [80].

Comparing the side-lobe power to the reflectivity measurements of all filters in the optics tube, we noticed the closest resemblance to the 1 K LPE filter. To investigate the effect of a reflective 1 K LPE filter, a simulation in Zemax [94] shows the expected measured signal due to reflectivity of a filter (Fig. 5.8A). The simulation predicts that rays are reflected off the filter and end up outside the main beam as the rays exit the LATRt window.

After removing the LPE filter from the optics tube and repeating the holography measurements, we measured a decrease in side-lobe power. Figure 5.8C shows the reduced near-field

side-lobe power following the removal of the filter, and the comparison of the side-lobe power with the filter in place. With the filter removed, the new side-lobe fractional power across the band is 1.9%, a factor of 3 lower. The tests presented above do not include this filter. This provides a concrete example of how holography measurements can be used to optimize cryogenic optical systems.

5.6 Cross-Polarization

Because the holography source is linearly polarized, we measure the polarization modulation of the optics tube. The source emits the TM-mode out of the rectangular waveguide, which is measured by the coherent receiver at the back of the optics tube. To modulate the polarization of the signal entering the optics tube, we use a polarization grid which separates the two linear polarizations.

We measure the polarized signal for a co- and cross-polarized source. The co-polar source outputs a TM-mode aligned to the harmonic mixer's waveguide in the focal plane. We attach a 90° twist waveguide such that the source's TM output is perpendicular to the harmonic mixer's waveguide.

5.6.1 Modeling

We separate the polarization in the model as three sources of polarization modulation: the polarizing grid, the instrument (optics tube), and the detector (to account for any cross-polarization from the feedhorn). To model the power measured by the detector P_{out} received at the back of the optics tube, we modulate a linearly polarized source with Mueller matrices:

$$\vec{P}_{\text{out}}(\theta) = \vec{S}_d(\phi_d, \epsilon) \cdot \vec{M}_{\text{OT}} \cdot \vec{M}_g(\theta, \eta_g) \cdot \vec{S}_s \tag{5.2}$$

where θ is the rotation of the polarizing grid, ϕ_d is the angle of the detector, ϵ is the cross-polarization of the detector, and η_g is the efficiency of the polarizing grid. The receiver is

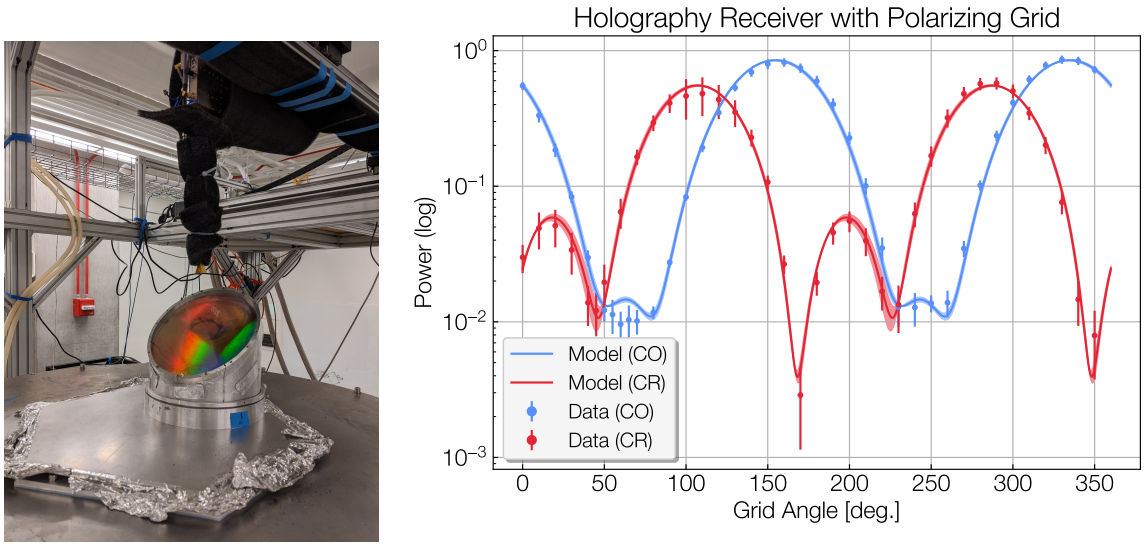

Figure 5.9: Left: Polarization measurement setup on the LATRt. The dielectric polarizing grid sits over the holography receiver's beam path and rotates about the vertical axis, polarizing the source as it enters the cryostat. A hexagonal aluminum plate covers the rest of the window and is secured in place with aluminum tape. Right: Polarized beam power (band-averaged from 85-120 GHz) as a function of grid rotation, measured with the holography setup described in Section 5.3. Co-polarization (blue) holds the source waveguide aligned with the receiver orientation. Cross-polarization (green) uses a 90° waveguide to make the source aligned perpendicular to the receiver orientation. The polarization model (Eq. B.1) is fit using an MCMC and with no instrument polarization.

already slightly rotated from perfect alignment from the source, since the tester-array required slightly tilted holes to mount the receiver. Therefore, we include this in our polarization model as the parameter ϕ_d. We find a degeneracy between the instrument polarization parameters and therefor exclude them in the fit. The source is modelled as its Stokes parameters $\vec{S}_s$, with intensity $I = 1$ and linear polarization $Q = \pm 1$ (switch the sign of Q when waveguide twist is added to the output of the source horn). The model is derived in detail in Appendix B.

5.6.2 Results

Figure 5.10 shows the measured power (co- and cross-polarized) as a function of grid tilt, for both co- and cross-polarized sources. We measure the received power at 85-120 GHz in

5 GHz increments, and at grid tilts from 0-360°, in 10° increments. From the data, we use an MCMC to constrain the detector tilt $\phi_{\rm det}$, grid efficiency $\eta_{\rm grid}$, and cross polarization ϵ. Error is estimated as the standard deviation across the mid-frequency band f:

$$S(\theta) = \sqrt{\frac{\sum_f P(\theta, f)^2}{N}} \tag{5.3}$$

Figure 5.10 shows the constrained parameters obtained by fitting the holography polarization data to the model (Eq. B.1). The detector angle $\phi_{\rm det}$ is constrained to $-30.62^{\circ}{}^{+0.69}_{-0.67}$, the grid efficiency $\eta_{\rm grid}$ is constrained to $97.00\%^{+0.21}_{-0.22}$, and the cross polarization ϵ less than 1%. The source emits a polarized signal, which is then additionally polarized by the grid. For this reason, the holography data cannot constrain the instrument polarization. We omit the instrument polarization from the model when fitting the holography polarization data.

5.7 Public Code

Here, we describe the software used for the holography data acquisition and analysis, all of which are made public. The software is two-fold; 1) the `solat-optics` module for simulating the near- and far-fields of the LAT telescope from the LATRt holography measurements and 2) Open Source Holography: a website detailing software and hardware to replicate the holography measurements [88].

5.7.1 Optics Simulation

The `solat-optics` code includes several modules: beam simulation of the LATR optics tube, propagation of measured fields to the secondary mirror, and to the far-field (dependencies: [95–100]). This beam simulation includes the lens geometry and computes the beam in the near-field. The code can be adapted to produce the beam as a function of angle, as was used in this paper, or as a function of position in the measurement plane.

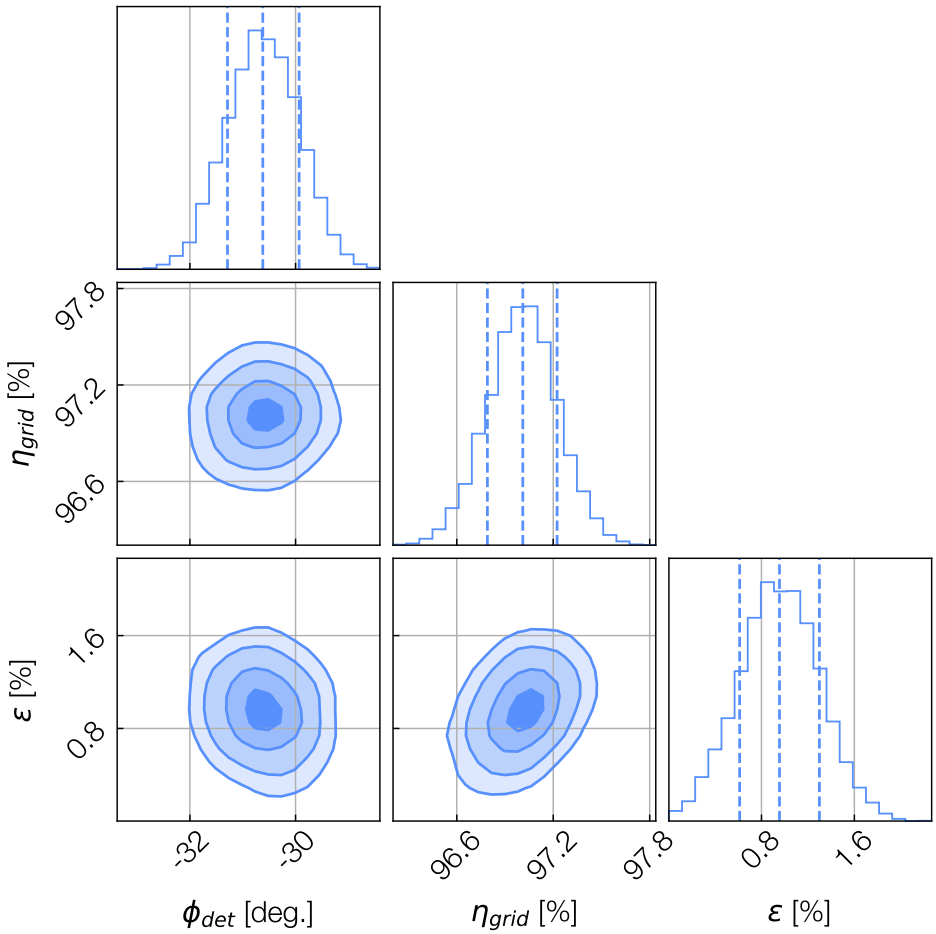

Figure 5.10: Constrained parameters from polarization model (Eq. B.1), detector angle ϕ_{det}, grid efficiency η_{grid}, and cross polarization ϵ. The dashed lines show the 16^{th}, 50^{th}, and 84^{th} quantiles of the fit. We find a cross polarization of less than 1%, a detector tilt of roughly -31 deg, and a grid efficiency of roughly 97%.

The propagation analysis code inverts complex beams either from simulations or holography data, corrects for near-field aberrations using ray tracing and returns the complex fields propagated to a desired plane, either near- or far-field. Notebooks are provided to show how to compute a beam simulation, how to analyze a LATRt holography measurement, and how to propagate a measurement to a desired region. We invite users to adapt this code to any applications they see fit, but ask that publications using this code cite this paper and that code derived from this work remain public.

5.7.2 Open Source Holography

We also provide an open-source holography GitHub website: `holog-exp` [88]. The repository provides both hardware and software details for recreating the holography measurements in this paper, and details on how to adapt the setup for future experiments. The scripts demonstrate how to correlate signals with the FPGA, program the synthesizers, and program the XY stages to produce a holography beam map. Further details can be found in Appendix A.

5.8 Discussion

Refractive holography enables the testing of optical performance prior to deployment, and propagating the measurements into the far-field to predict the beam of the telescope. We have presented holography measurements of the SO LAT optics tube and analysis methods determining its optical performance, including open-source holography for repeating and adapting the experiment. We further provide an open-source package for simulating near-field holography measurements and propagating the measurements into the far-field using FD.

From these data, we characterize the optical performance of the LATR optics tube. We compare near- and far-field measurements to simulations. After propagating the beams to the plane of the LAT secondary mirror, we find sub-percent power spilled to 300 K. We further find the far-field measured beams to be $2.18(1.38)'$ FWHM in the F90(F150) band.

We provide three open-source software packages. The first developed for this work, (`solat-optics` [92]), models the LATRt holography measurements and is customizable to include arbitrary optics and adaptable for other optics experiments. The second, `holog-exp` [88], details the hardware and data acquisition software required in this experiment. And lastly, we publish the data and Python scripts for recreating all figures in this paper [101].

The approach demonstrated here is broadly applicable to the characterization of millimeter-wave optical systems. The ability to characterize the optical performance and systematics

of the optics tube allowed us to determine one source of spurious reflections, and avoid systematics during future observations.

Chapter 6

Preliminary Characterization of the Small Aperture Telescope with Radio Holography

This chapter presents holography measurements of the Simons Observatory Small Aperture Telescope at the University of California, San Diego, and preliminary characterization of its optical performance. This work was made possible by the collaboration of Tommy Alford, Kathleen Harrington and Jeff McMahon from the University of Chicago, Remington Gerras from the University of Southern California, and Joe Seibert, Tran, Tsan, JB LLoyd, Michael Randall, and Kam Arnold from the University of California, San Diego.

6.1 Introduction

We present the laboratory testing of the MF Small Aperture Telescope using the technique of near-field radio holography. "Holography" refers to the measurement of the complex monochromatic electric field wavefront using the interference between a modulated and reference signal. Radio holography takes advantage of the antenna theory relationship: the far-field radiation pattern of a reflector antenna is the Fourier Transformation of the field

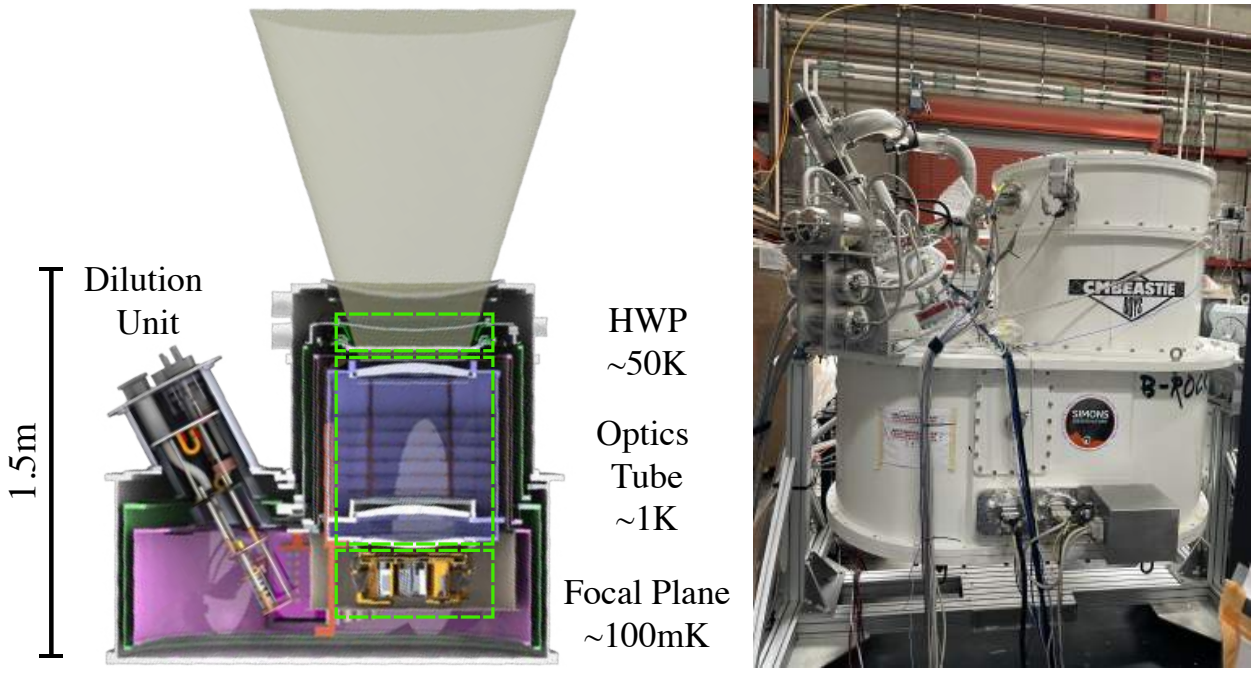

Figure 6.1: Left: Cross-section of the Small Aperture Telescope (SAT) optics tube. Light enters through the high-density polyethylene window (UHMWPE) and through the cryogenic half-wave plate (CHWP). The lenses re-image the beam onto the focal plane, where the holography detector measures power and phase at a given source position. Right: SAT cryostat used in holography testing. Source: The Simons Observatory Collaboration, Remington Gerras.

distribution in the aperture plane of the antenna [70].

Near-field holography of the SAT maps the wavefront emerging from the cryostat. Using Fresnel diffraction (FD) [78], these measured fields can be propagated to determine the far-field beam pattern of the telescope fed by this feedhorn receiver. Moreover, these beams are useful for the identification and mitigation of optical problems within the receiver (i.e. optical aberrations, focus, scattered power, etc.). These measurements enable a detailed verification of system-level optical performance prior to the deployment of a receiver on a telescope.

In Section 6.2 we describe the measurement approach including the cryogenic receiver (6.2.1) and holography hardware (6.2.2) required for measuring beam maps (full details can be found in Appendix A.1). In Section 6.3 we present the measured beam maps. Section 6.3.2 discusses analysis methods to propagate the measured beams into the far-field using FD. We

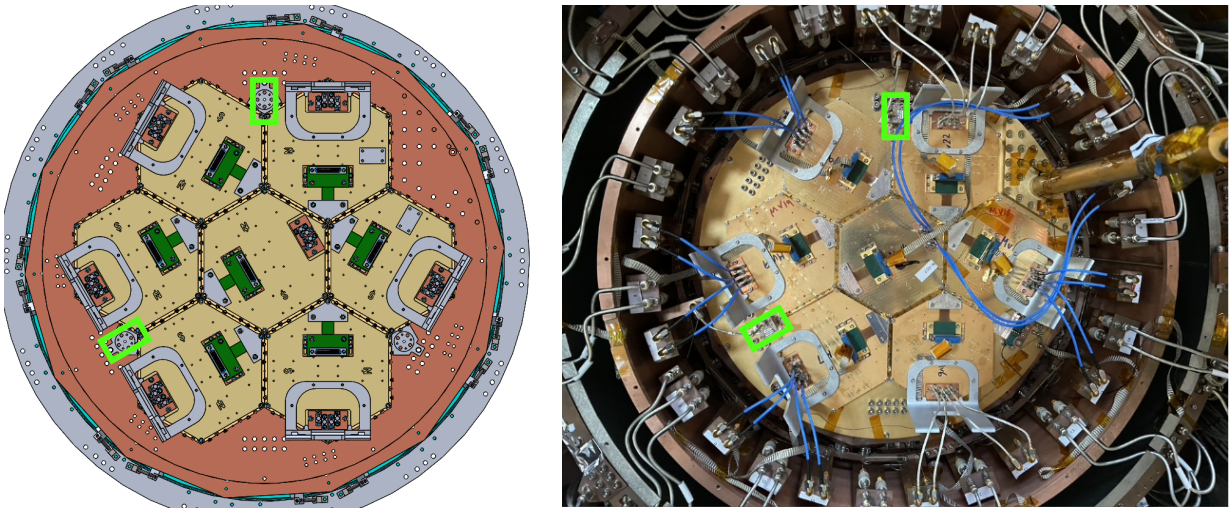

Figure 6.2: SAT Focal Plane. The two holography receivers are outlined in red, separated by 120°. Two receivers are installed for redundancy, but also served as a useful tool when characterizing systematics (such as "ghosting", or spurious signal in the beam maps, and polarization effects).

conclude with a discussion of future applications of this approach in Section 6.4.

6.2 Measurement Approach

Here, we describe the hardware in two sections: 1) a cryogenic optics tube and 2) the holography system comprised of a source, correlation receiver, and motion system. The radio holography setup is modified from the previously described setup in Chapter 5. We detail the key differences here.

6.2.1 Cryogenic System

The optics tube is housed in the SAT cryostat[9]. The cryostat holds and cools the optics tube and provides support for detector readout. This setup supports up to seven detector arrays (Fig. 6.2). In the test configuration, all bolometric arrays [82] are filled in the focal plane, and two holography feedhorns are added to the edges of the focal plane, each separated by 120°.

The holography detectors consist of a feedhorn identical to that used for the bolometric detectors, but with standard wave guide flanges at the outputs. A receiver consisting of a round to rectangular wave guide transition and a harmonic mixer is attached to this feed array. The mixer was designed to operate from 70-110 GHz, but was found to operate satisfactorily up to 170 GHz. For operational simplicity, we used this mixer over our full frequency range from 85-135 GHz.

Two identical receivers are installed in the focal plane for redundancy. Two 0-18 GHz coaxial connections were made from the receiver to connectors at the cryostat wall. These coaxes are heat sunk at various stages between the focal plane, which was operated at 4 K while doing holography, and the 300 K cryostat wall. A separate cool down was used to measure the loss along these coaxial feed lines. The loss was found to be 23 dB at the LO frequency (10-13 GHz). Accurate knowledge of the loss along the feed lines is critical for providing the correct amount of power to the mixers in the focal plane. The loss at the interference frequencies (IF) (100 MHz) is significantly lower and not critical to the function of this system.

6.2.2 Holography System

Figure 5.3 shows the schematic overview of the holography hardware. Two millimeter-wave sources are used to measure the full SO MF band: F90 (80-120 GHz) and F150 (130-170 GHz). Only one source is mounted at a given time. The source is broadcast into the receiver using standard gain feed horns held close to the window ($\approx$ 10 cm) (Figure 6.3). A motorized two-dimensional stage holds the source and is mounted on a support structure above the SAT. During a measurement, the source (frequency is fixed) is moved over a 80×80 cm range with 1 cm steps. One map takes roughly 2 hours to complete.

Due to the presence of the CHWP, the source's polarized signal is modulated upon entering the optics tube. Therefore, to understand the effects of the CHWP, we measure two beam maps at each frequency: with a waveguide twist at the output of the source, and

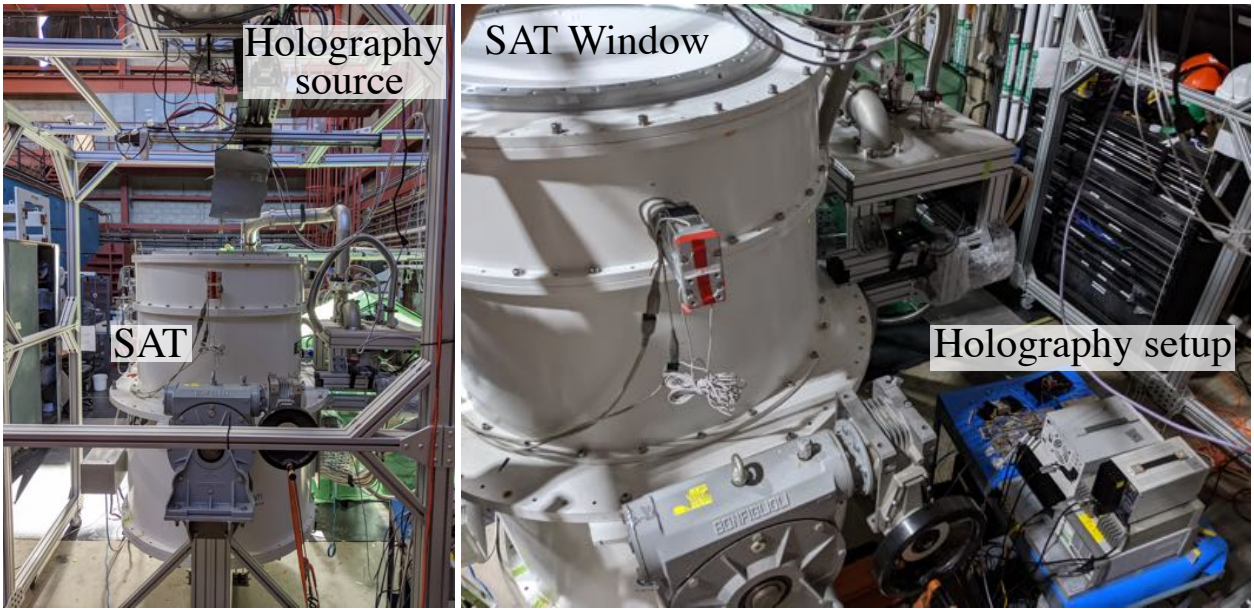

Figure 6.3: Lab photos of the holography setup on the SAT. Left: The holography source, covered in a sheet of eccosorb to control scattering, is centered above the SAT window and points directly into the SAT, sitting below. Right: The holography electronics sit on a cart next to the SAT readout. The SAT window in the top left is made of UHMWPE.

without a waveguide twist. This allows us to measure the response of the optics tube at two source polarizations (the waveguide twist changes the source polarization by 90°).

6.3 Results and Interpretation

6.3.1 Near-Field Beam Maps

Figure 6.6 and Figure 6.8 show the measured power and phase of the beam maps, respectively, at each frequency. A variable attenuator at the output of the source was used to optimize the amount of signal entering the optics tube, to ensure power was not too high such that the measurement was saturated, but to also ensure the signal was high enough for signal-to-noise greater than 35 dB.

Each beam map is labeled either 0° WG, with a straight waveguide at the source output, or 90° WG, with a waveguide twist at the source output. These labels also correspond to the E_x and E_y fields. We assume the source and receiver to be misaligned; to account for

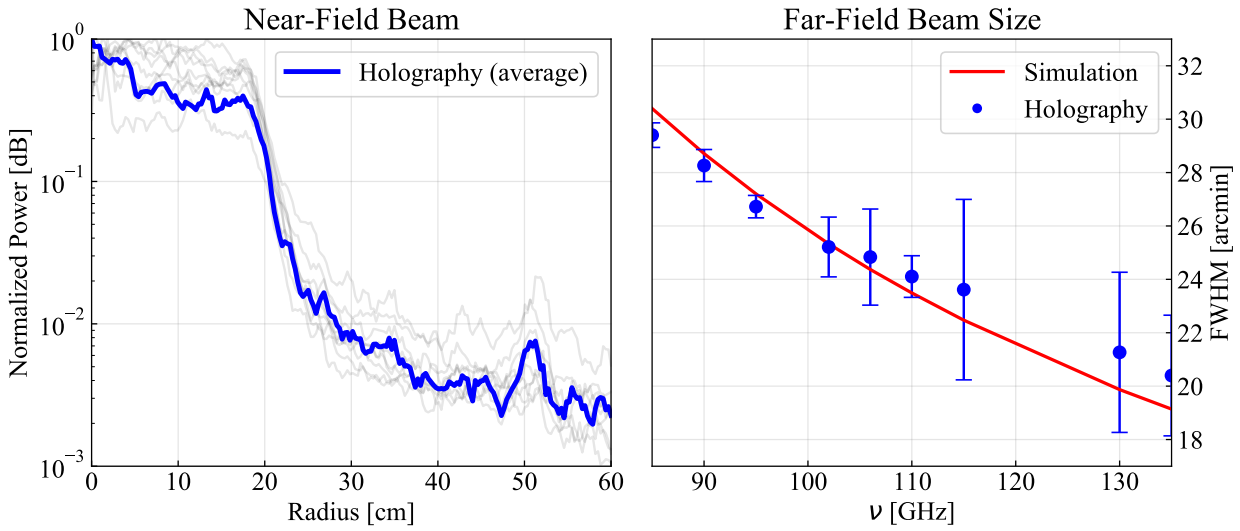

Figure 6.4: Left: Preliminary near-field beam shape of the SAT in MF-1. Beams are averaged over all frequencies measured, and the averaged beam is then radially averaged to get the near-field beam profile. Right: Preliminary beam sizes of the SO SAT in MF-1. Far-field beams measured with holography (blue) are radially binned and the FWHM is obtained from the resulting 1D beam profile. Simulations are obtained using a diffractive optics simulation, and plotted are where the measured beam sizes with 2σ errorbars.

this, we rotate the two beams by θ which is fit to minimize $E_y^{'}$:

$$\begin{bmatrix} E_x^{'} \\ E_y^{'} \end{bmatrix} = \begin{bmatrix} \cos(\theta) & \sin(\theta) \\ -\sin(\theta) & \cos(\theta) \end{bmatrix} \begin{bmatrix} E_x \\ E_y \end{bmatrix} \tag{6.1}$$

The shape of the main beam was found to be in good agreement with simulations at all frequencies (Figure 6.4). The phase measurement indicates the direction of the beam as it exits the window. Figures 6.7 and 6.9 shows the phases across all frequencies; the unwrapped phase is a gradient due to the beam exiting the window at an angle (as the holography detector is far-off from bore sight in the focal plane). However, we further note the change in phase gradient as a function of frequency and have modeled this to be an aliasing effect of the measurement. The aliasing effect creates a directional shift in the on-sky beam, but is negligible for determining the on-sky beam size.

Figure 6.5 shows the average near-field beam(blue), with the individual beams in the background(grey). Because the beam is spread out as it exist the window (in the time-

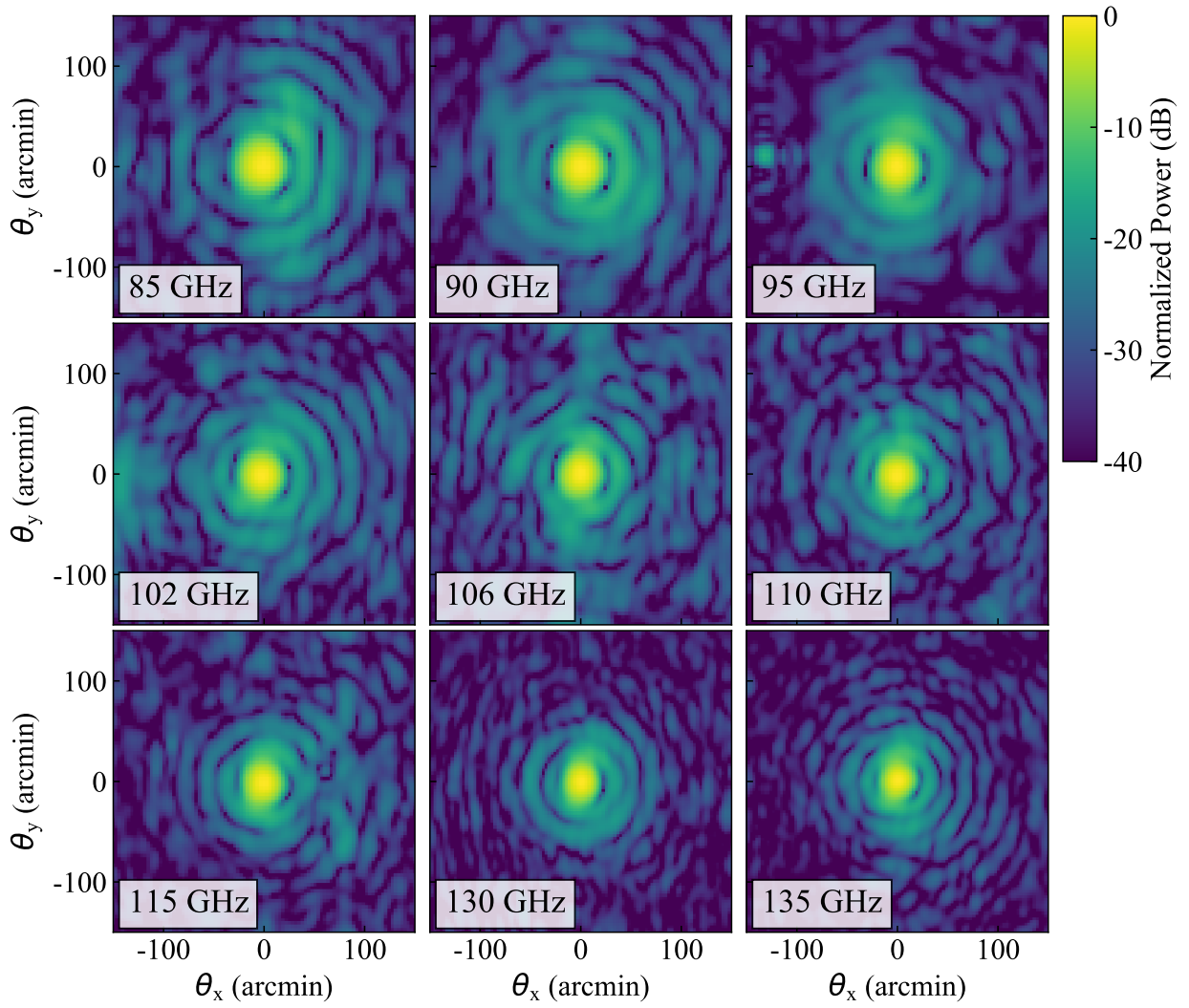

Figure 6.5: Preliminary far-fields of the SAT optics tube in the MF-1. The near-field measured beam is propagated to the far-field for each frequency. The aliasing of the measured phase in the near-field (discussed in Section 6.3) caused an artificial directional shift in the on-sky beam, which we center before plotting.

reverse sense), the signal-to-noise of the holography measurement is significantly lower than that achieved by the LATRt experiment. For this reason, the top and side-lobes of the near-field beam are noisy, but the main shape of the beam indicates the overall beam size is as expected.

6.3.2 Propagation of Fields

The performance of the SAT optical system is assessed in detail by using the amplitude and phase of the measured beams to calculate the far-field. This is carried out by using the Fourier relationship between the near-field $E(x, y)$ and far-field $B(\theta_x, \theta_y)$ beams [70, 89]:

$$B(\theta_x, \theta_y) = \int_{\text{aperture}} E(x, y) e^{i \frac{2\pi}{\lambda} (\theta_x x + \theta_y y)} dx\, dy \tag{6.2}$$

where the complex electric field $E(x, y)$ is integrated over the area of the aperture, θ_x and θ_y are the on-sky angular coordinates, and λ is the wavelength. The resulting (preliminary) far-fields are shown in Figure 6.5. The measured beam size $26.02' \pm 1'$ is consistent with the predicted F90 FWHM of $24.95'$.

6.4 Discussion

We have presented holography measurements of the SO SAT optics tube and analysis methods determining its optical performance. We further provide an open-source package for simulating near-field holography measurements and propagating the measurements into the far-field using Fourier optics. From these data, we characterize the optical performance of the SAT MF optics tube. We compare near- and far-field measurements to simulations. After propagating the beams to the far-field, we find the SAT beam FWHM to be $(26.02' \pm 1')$ in the F90 band, within the expected beam size of $24.95'$, and is sufficient to accomplish SO's science goals at these angular scales.

We also provide `sosat-optics`, an open-source software package, which models the SAT holography measurements and is customizable to include arbitrary optics and adaptable for other optics experiments [102]. The approach demonstrated here follows the successful characterization of the Large Aperture Telescope Receiver tester, and is broadly applicable to other millimeter-wave optical systems [16]. The ability to characterize the optical perfor-

mance and systematics of the optics tube allowed us to determine the SAT optics is in focus and that the beam is within requirement for SO science. Again, this is one of the first uses of this method to measure the far field beam pattern in lab and shows our optics work correctly pre deployment.

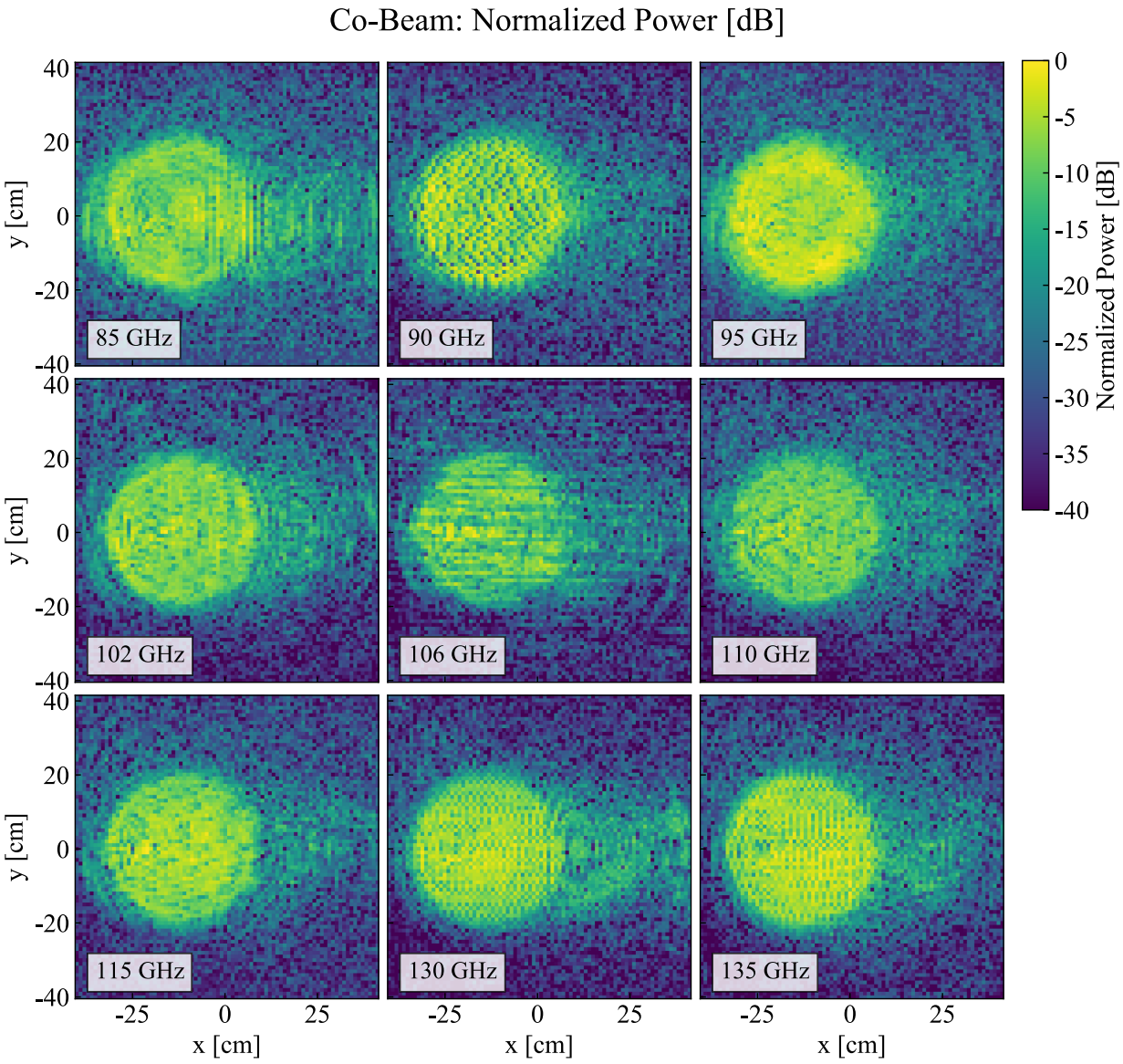

Figure 6.6: Co-polar normalized power of the Simons Observatory Small Aperture Telescope near-field beam.

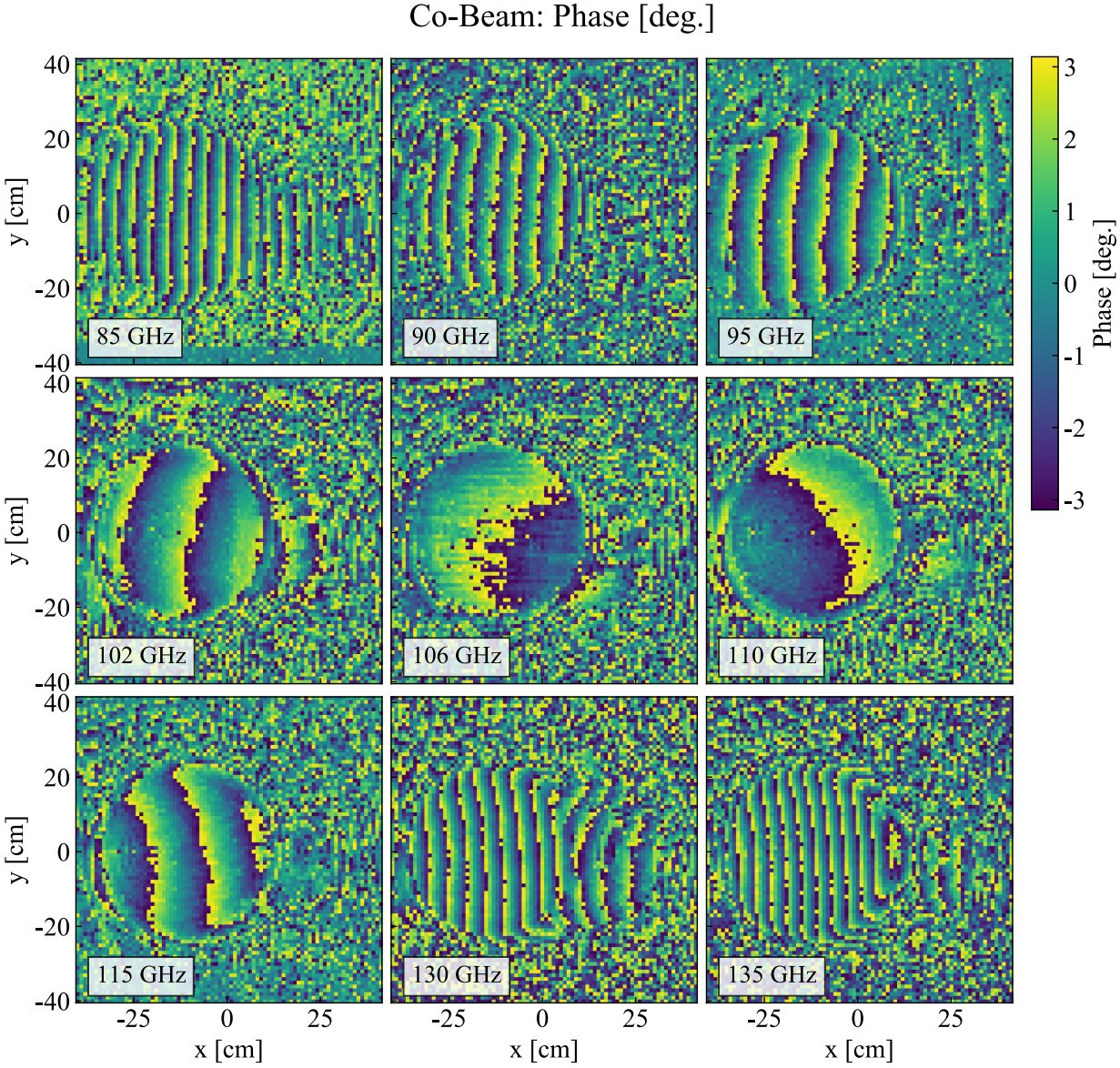

Figure 6.7: Co-polar phase of the Simons Observatory Small Aperture Telescope near-field beam.

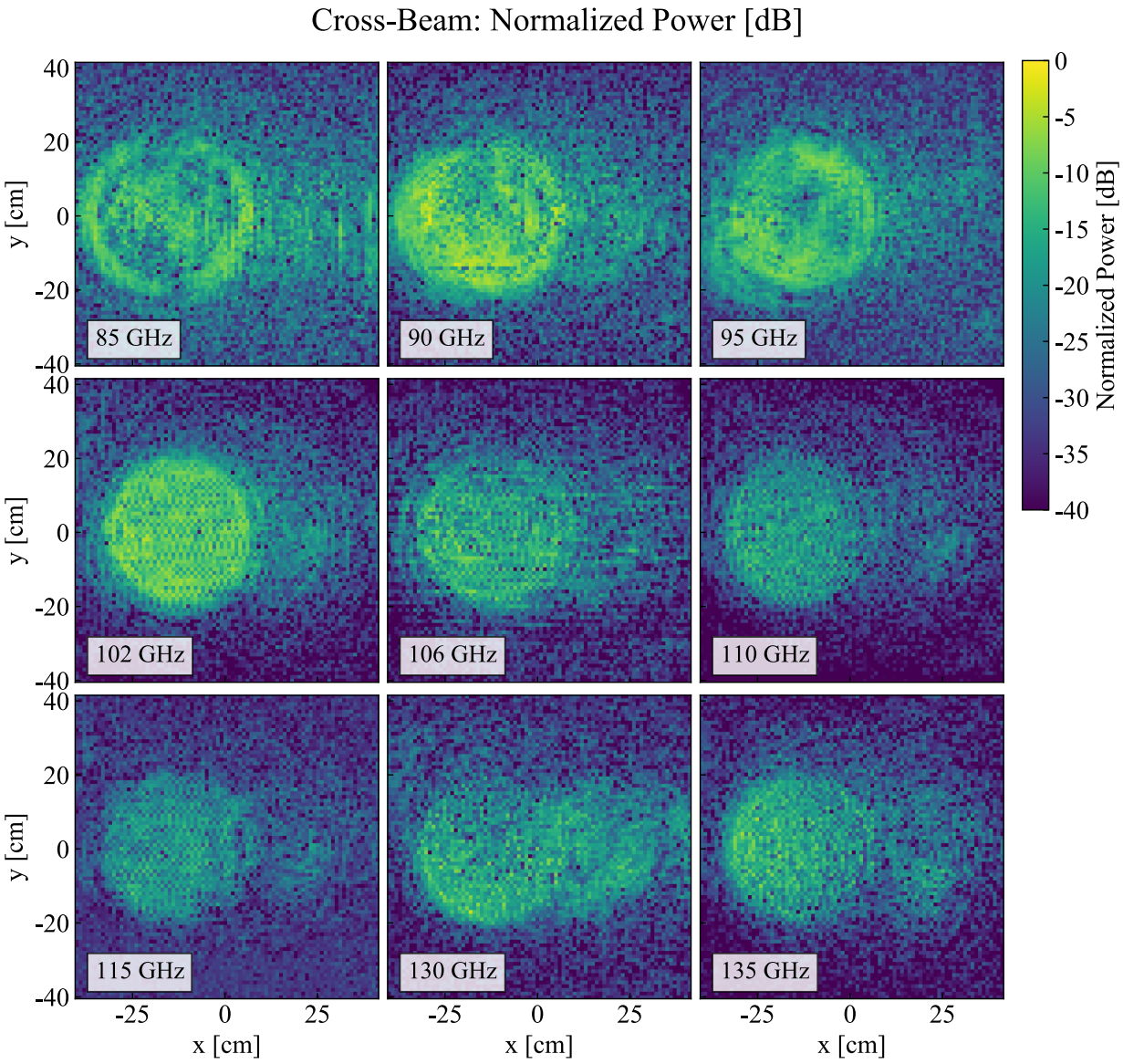

Figure 6.8: Cross-polar normalized power of the Simons Observatory Small Aperture Telescope near-field beam.

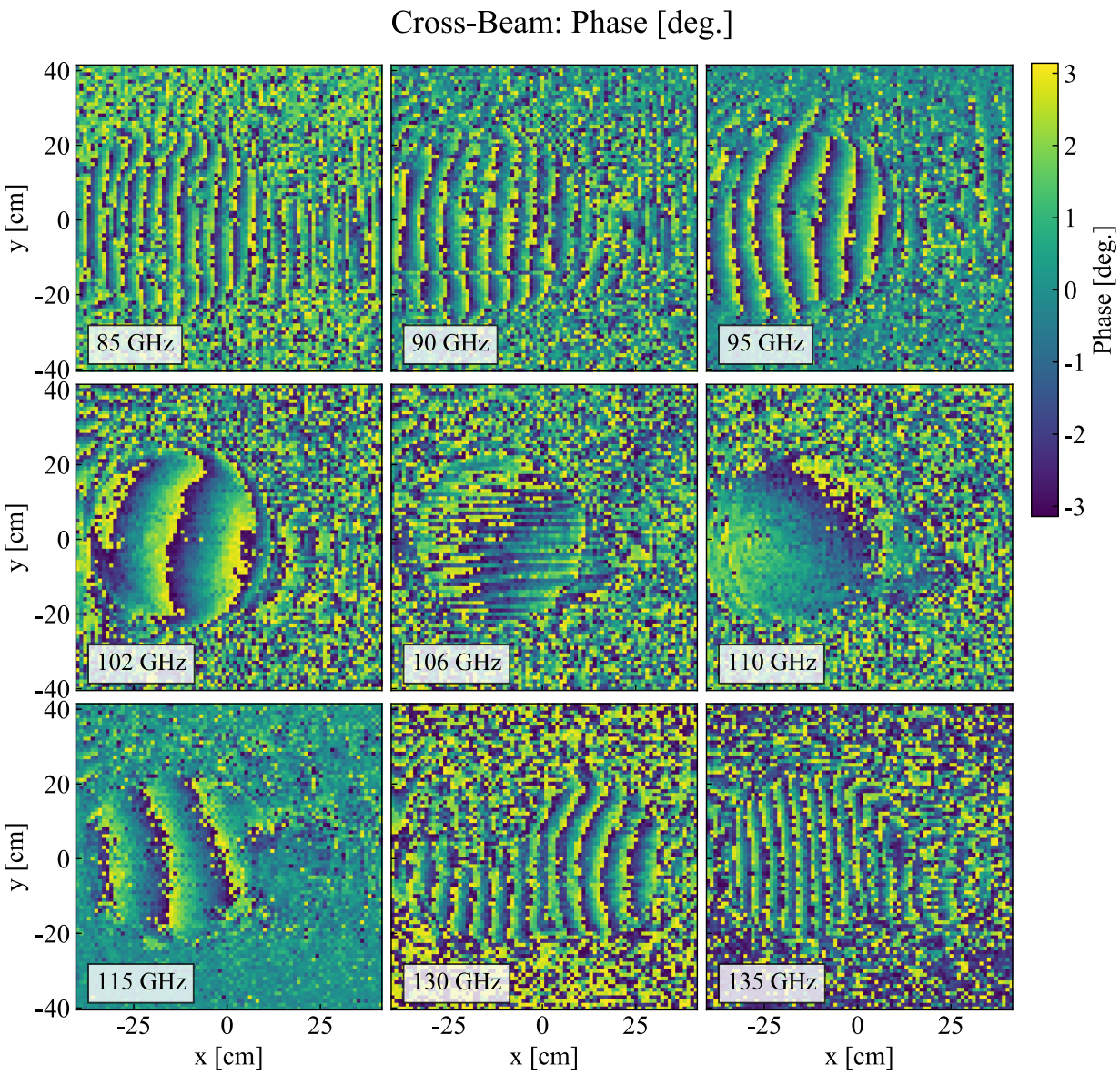

Figure 6.9: Cross-polar phase of the Simons Observatory Small Aperture Telescope near-field beam.

Chapter 7

HoloSim-ML: Machine Learning Applied to the Efficient Analysis of Radio Holography Measurements of Complex Optical Systems

7.1 Introduction

Improvements in sensitivity for a given instrument require careful control over every part of the instrument. Deviations of the mirror surface will redistribute beam power to large angular scales and therefore increase the width of the main beam and reduce the forward gain of the telescope. For this reason, alignment of the reflectors is crucial. In this work we focus on quantifying these effects, and we present the tools needed to mitigate them by aligning the mirror panels of the LAT using holography.

The LAT design is shown in Figure 5.1. The telescope is engineered and built by Vertex Antennentechnik GmbH, the panels forming the primary and secondary mirrors, both 6 m in diameter, were fabricated by Bricon Technology GmbH [103]. A defining feature of this

design is the large focal plane (2 m in diameter). The primary (secondary) mirror is built with 77 (69) panels, and has 385 (345) adjusters in total. The size of each panel is roughly half a square meter and weighs roughly 5 kg [43]. An adjuster is a threaded mechanism allowing for manual adjustment of the position of each panel [104]. Each panel has five adjusters controlling the surface height. We present radio holography tools that allow us to reach a combined reflector surface error of 22 μm RMS or less.

Radio holography has a long history of use in millimeter and sub-millimeter telescopes [70, 105–109]. Typically, these applications require aligning a single mirror, which can be measured in isolation [110, 111]. A particular challenge of this application is that we must measure both mirrors simultaneously and then extract the adjuster errors from each of the two mirrors. This complex optical system requires the development of new fitting tools for efficient analysis. Towards this end, we developed an efficient simulation code and used it to train a machine learning (ML) model to do this extraction.

Practical holography measurements of telescopes of this size must be carried out with a bright monochromatic source in the near-field. The analysis of near-field holography is described in great detail in several references [70, 107, 112]. The CCAT-prime Collaboration carried out a parallel work simultaneously with ours, which details measurement methods [113]. The method described is commonly referred to as "near-field vector beam mapping" and employs a coherent source and phase sensitive receivers. For a given desired accuracy, this requires a lower signal-to-noise than Out-of-Focus Holography (OFH), which reconstructs the telescope aperture phase through comparison of far-field power maps taken in and out of focus with a coherent source and incoherent detectors in the focal plane [114]. In this work, we examine the impact of mirror alignment on measurements of the CMB, explore the sampling of the focal plane required to arrive at a given mirror RMS, and present a new approach to fitting complex optical systems that we expect to be far more general than the present example.

In Section 7.2 we quantify the scientific impact of improving the mirror surface. In Sec-

tion 7.3 we describe the simulations we use to model these holography measurements. In Section 7.3 we describe our analysis of near field holography data using ray-tracing to determine the near field corrections. In Section 7.4 we describe how we use these simulations to train a machine learning code to efficiently and accurately extract the adjuster errors from holography data. We discuss how the number of measurement positions impacts the remaining degeneracies in the panel errors. In Section 7.5 we explain the method for performing this measurement, including hardware tolerances and alignment. Section 7.6 details the publicly available code. We conclude with a discussion of other potential applications in Section 7.7[1].

7.2 Motivation

Measurements of the CMB are typically expressed as power spectra computed from all-sky maps using the spherical harmonic transform. Therefore, the impact of the scattering of power due to mirror surface deviations can be understood by transforming these beams into ℓ-space window functions. These window functions encode how the beam shape rolls off the CMB power spectrum as a function of $\ell \sim 180^\circ/\theta$. This transformation is equivalent, in the flat sky limit, to Fourier transforming the beam and averaging its magnitude squared in bins of constant wave number. For reference, $\ell = 1000$ corresponds to an angular scale of 0.18°.

The upper panels of figure 7.1 show simulations of the LAT beam pattern with varying levels of panel setting errors at 150 GHz, one of our key science bands. These simulations were generated using the method described in Section 7.3 in the far-field. We note that the calculation extends to a larger angle, but we have truncated it in the figure for clarity of presentation. It is apparent that the panel errors lead to significant scattering of light from the main beam into near side-lobes.

The plots of Figure 7.1 display these window functions for the simulated beams (top

1. The following was published in Applied Optics in 2021 [17]. This publication was featured on the cover of the Applied Optics journal.

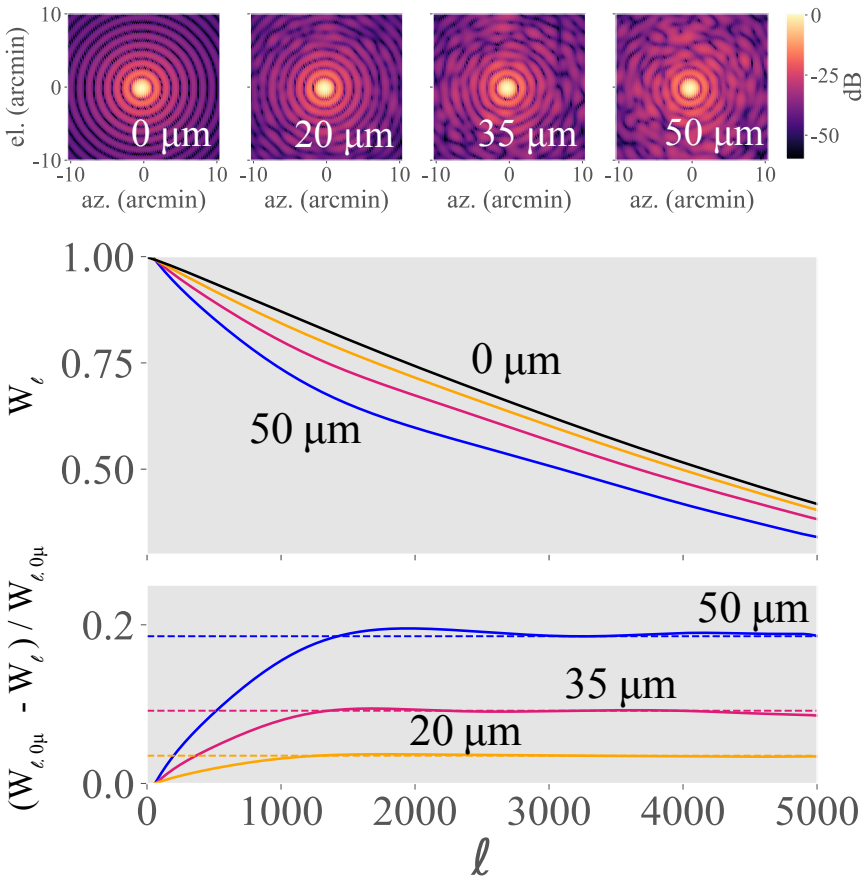

Figure 7.1: Top: Far-field beam simulation of a 150 GHz source, with surface error RMS of 0 μm, 20 μm, 35 μm, and 50 μm. The side-lobes around the central beam increase as RMS of panel errors increases. Center: Window function W_ℓ of far-field beams at 150 GHz with combined surface RMS of 50 μm, 35 μm, 20 μm, and 0 μm. Bottom: Difference of window functions W_ℓ in top plot, w.r.t. window function of far-field beam with surface error RMS of 0 μm, $W_{\ell,0\mu}$.

row) and the difference between the window functions with panel errors and that of a perfect mirror (bottom). For reference, the vendor will deliver the telescope mirrors with a half-wave front error (HWFE) of 50 μm. The current method of panel alignment using a laser tracker achieved a surface error of the panels to $20-25\,\mu m$ for the 6 m primary mirror of the Atacama Cosmology Telescope [7]. The surface error budget for the SO LAT give a 35 μm HWFE if similar panel errors are achieved. This leads to a 10% loss in signal in the $1000 < \ell < 5000$ range that is crucial for much of the SO science [37]. This matches the prediction of the Ruze formula [115] once one accounts for the fact that the power spectrum (and window function)

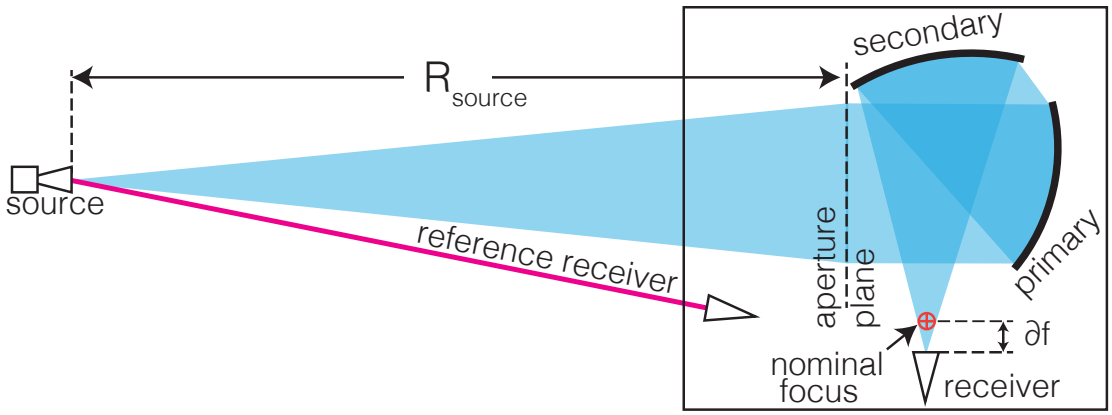

Figure 7.2: Holography geometry. A source on a 5 m tower sits at a distance $R_{\rm source}$ above the aperture plane of the LAT. Two receivers, one "reference" receiver pointed straight at the source, and the receiver in the focal plane, measure the amplitude and phase of the source. The focal plane receiver is offset δf from the nominal focus.

are proportional to the square of the beam. Since the calibration of the power spectrum is based on cross-correlating with data from the Planck Satellite [25] for $\ell \lesssim 1600$, the variation in the window function in this range represents a potential systematic challenge. Reducing the half-wave front error to below 22 μm would simplify calibration and recover most of this lost sensitivity. The error budget for our telescope shows that this requires measuring and setting each of the primary and secondary mirror to an accuracy of better than 5μm RMS, which we take as a goal for this work.

7.3 Beam Simulation

The SO LAT is shown in Figure 5.1 and described in [42]. We compute its beam pattern in the near-field and far-field using physical optics [14, 116] implemented in a code we call `HoloSim-ML`, available at GitHub.com/McMahonCosmologyLab [117].

A two-dimensional representation of the three-dimensional geometry used in these simulations is shown in Figure 7.2. We specify the positions and rotational state of the mirrors, the location of the receiver feed, and the location of the source. For these simulations, we refocus the telescope on the near-field source by displacing the receiver a distance δf from

the nominal telescope focus. We ray-trace from a receiver position through the telescope to an aperture plane chosen at an arbitrary position a few meters in front of the telescope. The results do not depend on this arbitrary choice. Each ray is given an amplitude based on a modeled beam pattern for the receiver feed horn. A reference receiver, placed outside the telescope, points directly at the source and, in combination with the receiver feed, determines the phase of the source. For the results presented here, the beam width of the receiver feed was assumed to be 44° with a Gaussian profile. We typically use a 100 x 100 grid of points on the aperture plane. This telescope model is rotated, and this calculation is repeated for every azimuth and elevation pointing to simulate the two-dimensional diffraction pattern.

To model misalignment of the mirrors, the surface z_{surf} of each mirror panel, is parameterized as a polynomial function of the five parameters a_n:

$$z_{\text{surf}} = a_1 + a_2 r_x + a_3 r_y + a_4(r_x^2 + r_y^2) + a_5 r_x r_y \tag{7.1}$$

where r_x and r_y are coordinates centered in each individual panel. The a_n parameters are determined by fitting this equation to the surface offsets δ_z at the positions of the five mirror adjusters. Thus, there is a one-to-one mapping between adjuster offsets and the parameters in this model. The surface machining errors for each panel will be a few micrometers and the adjuster system is the same as was used for SPT where a similar model was fit successfully [118]. Therefore, this panel model is expected to be adequate for these purposes.

The output of this step in the code is the amplitude and path length to the aperture plane from the receiver feed. Figure 7.3 shows the resulting variation in the path length across the aperture plane for one realization of panel errors from the primary mirror (left) to the secondary mirror (right) and the combination of both (bottom). It is clear that the errors due to the secondary and primary mirror panel misalignments occur at slightly different physical positions and scales in the aperture plane. This means that a single holography measurement may suffice to extract the panel errors.

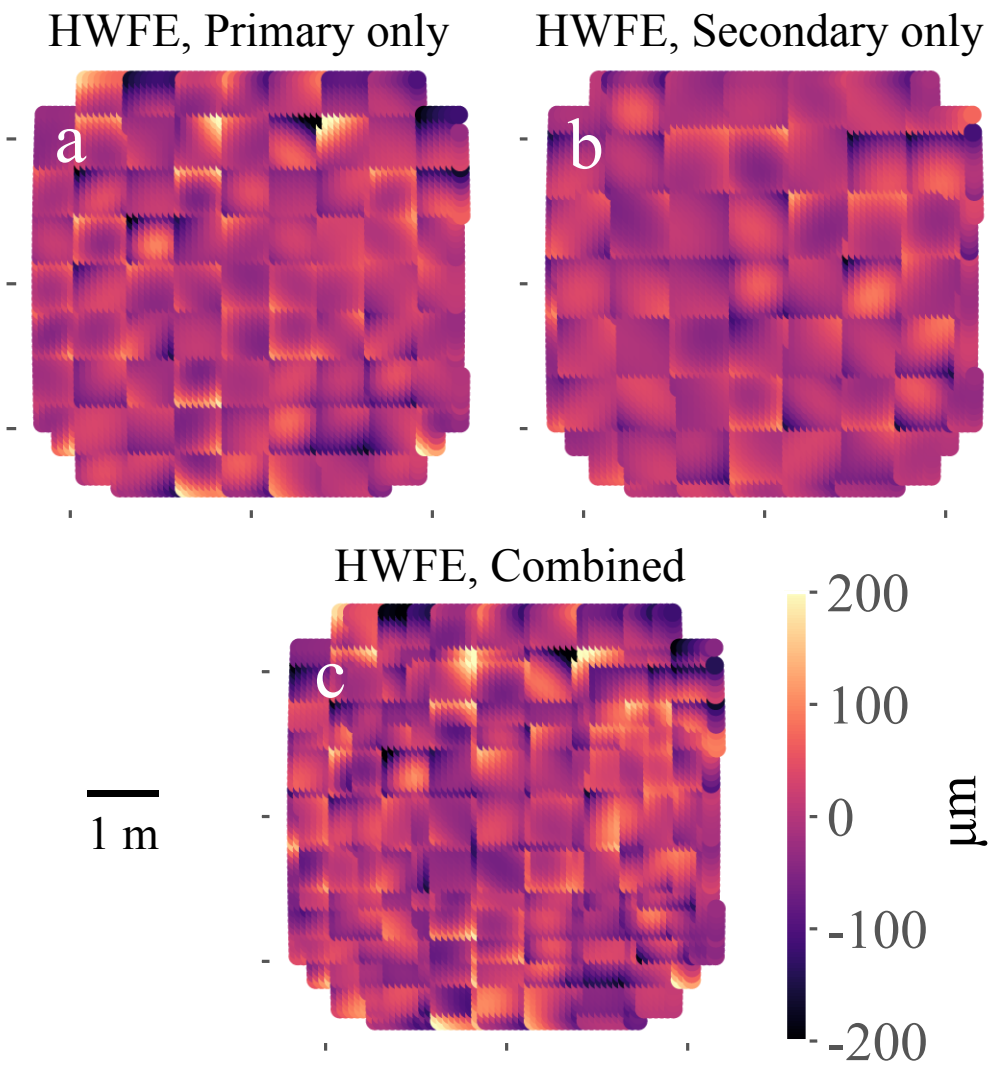

Figure 7.3: Simulated HWFE at the aperture plane with surface errors of 35 μm RMS on a) only M1, b) only M2, and c) both M2 and M1.

The next step in the calculation is to determine the straight line path length from each point in the aperture plane to a source. The source is chosen to be at $R = 1 \times 10^6$ m for the far-field and $R = 1 \times 10^3$ m for near-field holography. The elevation θ and cross-elevation ϕ of this source are varied to map out the beam. This results in a total path length from the source to the receiver. The beam $B(\theta, \phi)$ is then calculated using:

$$B(\theta, \phi) = \sum_j E_j e^{i\rho_j(\theta,\phi)2\pi/\lambda} \tag{7.2}$$

where j is an index for the rays in the simulation, E_j is the electric field amplitude of a ray, and $\rho_j(\theta, \phi)$ is the path-length from receiver through the telescope and to the source tower for a given pointing, and λ is the wavelength. We note that we can also compute the diffraction pattern in the aperture plane by fixing the source's position and varying the receiver position in the focal plane.

Radio holography consists of measuring the electric field amplitude and phase of the beam, and then utilizing the Fourier transform relationship between the aperture fields and beam to extract the fields and phase on the aperture plane. In our case, variations in the phase of the aperture plane are interpreted as two times the errors in the mirror surface.

For practical reasons, and to reduce the impact of atmospheric turbulence, these measurements are usually carried out with a near-field transmitter. This introduces de-focus and other geometrical aberrations that must be removed in order to interpret these data. In previous analyses, these have been corrected by fitting out functional forms that capture these effects [70]. Here we use our ray tracing code to model the aberrations by computing the phase on the aperture plane, including contributions internal to the telescope and between the telescope and the source. This requires that we measure the position of the source and the position of the receiver. After we apply this phase correction, we also remove a constant and gradients from the aperture fields to account for any small pointing errors. This approach has been checked against the standard series expansion and generalizes easily to include additional corrections, including for the phase of the receiver feed horn. The left panel of Figure 7.4 shows the simulated holography measurement of SO that results from this calculation.

7.4 Panel Fitting with Machine Learning

To extract the adjuster offsets from the aperture field, we must simultaneously fit a model of all panels on both mirrors, including the geometric effects of the telescope. While standard fit

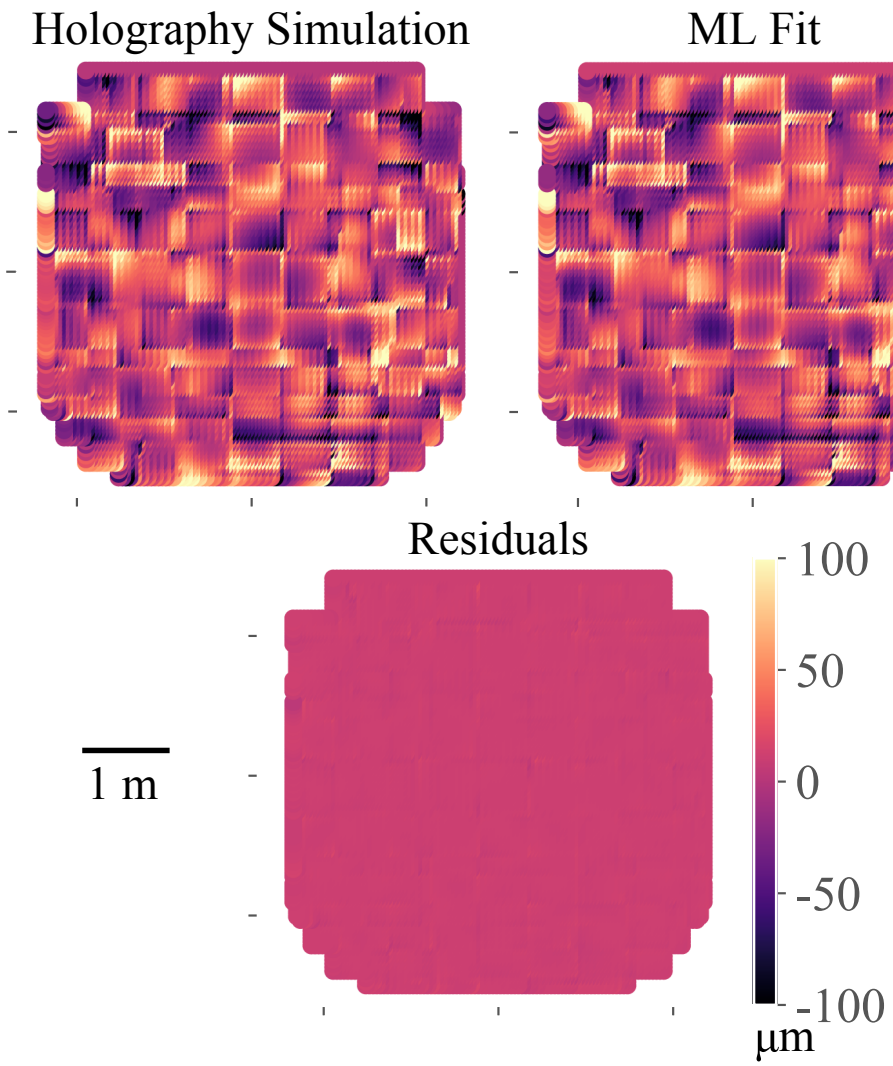

Figure 7.4: Results from simulation. The top left panel shows the input simulation, which had 35 micrometer RMS HWFE. The top right panel shows the predicted aperture phase given the ML determined estimates for the panel errors, and the bottom shows the residuals.

techniques can work, they are slow to converge and often yield solutions that are suboptimal in the sense that they under fit the panel errors. This results in a situation where many cycles of holography measurement and analysis are required to correctly set the mirror surface.

Here, we use a machine learning model built from the `scikit-learn` python package [119]. To train this model, we generate a set of 1000 near-field beam simulations, each with a different realization of mirror setting errors. Each beam simulation assumes an angular width of 200 arcmin., with 1 arcmin. spacing, for a total of 40,000 points in a 2d

grid. We then perform the holography analysis described above to yield a simulated data set comprised of aperture fields and the known input adjuster errors. This suite of simulation is used to train a linear regression model. The training took only minutes on a laptop, making the beam simulations the limiting computational step. Once trained, this model will transform an input holography measurement into a set of estimated panel adjuster offsets.

Figure 7.4 shows the results from a simulation. The top left panel shows the input simulation, which had 35 μm RMS HWFE. The top right panel shows the predicted aperture phase given the ML determined estimates for the panel adjuster positions, and the bottom shows the residuals. An impressive feature of ML is that it achieved residuals below 3 μm for the combined HWFE for each of the 10 randomly chosen input simulations we tested.

One issue is that this fit is degenerate, in the sense that anti-correlated errors on the primary and secondary can cancel when measured from a single feed position. To explore this, we plot the errors on the Primary and Secondary in Figure 7.5. We also compute the half-wave front error on the aperture plane as a function of feed position across the large 2 m focal plane used by SO to explore how the cancellation of this degeneracy varies with position. The top row considers holography taken in the classical way with a single receiver position. The middle row considers binocular holography, where two measurements taken at two positions are analyzed jointly to break degeneracies. The bottom row further considers trinocular holography, where three measurements taken at three positions are analyzed jointly to further break degeneracies.

These results show that standard single receiver holography leads to anti-correlated errors of 10 μm on each mirror, which cancel to less than 6 μm over most of a 2 m focal plane. The binocular results improve the mirror residuals to 6.5 μm RMS, but still suffer from correlated errors that lead to HWFE marginally worse than for the single position holography. These are below 6.5 μm over much of the focal plane.

The trinocular method improves the single mirror precision to 4 μm with suppressed degeneracies which cancel to better than 4 μm HWFE over all but the edges of the focal

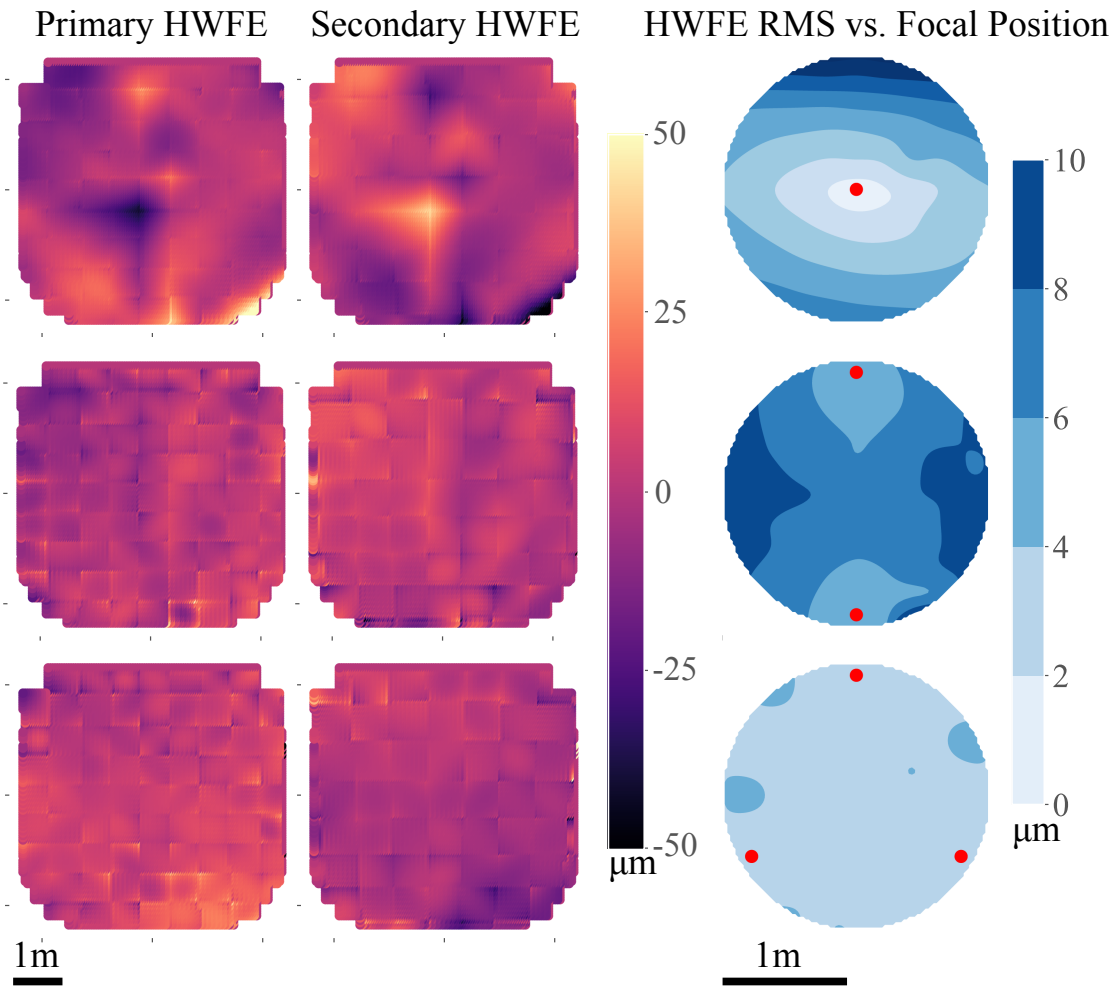

Figure 7.5: The left and middle columns show the surface errors on the Primary and Secondary mirrors after holography has been used to correct the mirror surfaces. The right column shows the HWFE as a function of focal plane position. The top row shows results for holography taken at a single position (see red dot). The middle row shows results for binocular holography (combining measurements from two positions, see red dots). The bottom row shows results for trinocular holography (combining measurements from three positions, see red dots).

plane. We have presented these results for a single realization of mirror errors, but we repeated the calculation 10 times and found the results to be robust. Reducing the HWFE from panel setting to be below 5 μm requires trinocular holography.

7.5 Measurement Practicalities and Robustness of Method

Achieving results at this precision requires measurement hardware and methods with sufficient sensitivity and control of systematic effects, both of which are within reach.

The simulations were informed by the geography of the SO LAT site. A 1 km transmitter distance was chosen since the transmitter can be placed on the slope of Cerro Toco, a nearby mountain peak, at this distance and an elevation of 10°. Given this choice, we can determine requirements on signal-to-noise and the knowledge of the location of the transmitter and receiver with respect to the telescope by varying these in our simulations. Table 7.1 presents the results of this sensitivity analysis.

We also tested the robustness of the ML method to differences between the (simulated) measured mirror surface and the training set. We found that for measurements of mirror surfaces significantly worse than what was in the training set, the method gracefully degrades in a way that it fits out 90 % of the input surface. For example, with a 100 μm HWFE the difference between the input and fit results had an RMS of 10 μm. Repeating the measurement and alignment process a second time would reduce the alignment errors below our 5 μm target.

The signal-to-noise requirement can be met with a source consisting of a Gunn Oscillator phase locked to an Oven Controlled Crystal Oscillator (OCXO). Such a system can output hundreds of mW with a frequency stability of a few parts per billion. This ensures the source remains reliably within a bandwidth of a few hundred Hertz, allowing for aggressive filtering of the received signals. With this filtering, simple receivers based on harmonic mixers (noise temperatures of 100,000 K) can in principle achieve signal-to-noises in excess of 130 dB. This

Minimum signal-to-noise	80 dB
receiver position (arbitrary direction)	2 mm
Tower source (radius)	1.2 m

Table 7.1: Allowed variation in signal-to-noise and positional knowledge needed to keep error contributions from these effects below 2.5 μm HWFE.

enables broad illumination of the telescope to make the measurement immune to the source beam pattern and reduce the received signal power to below 1 mW, a level that comfortably guarantees the detector response is within the linear regime and ensures more than sufficient signal-to-noise.

The position knowledge of the source and receiver can be measured with a combination of metrology and fitting in the analysis code. The distance between the tower source and the telescope can be determined to better than 1 m using a theodolite, which is a standard surveying tool. The angular position of the source will be found with the central peak of the beam map. Any residual errors in this angle are mitigated by the removal of a gradient in the phase on the aperture plane in the holography analysis. The location of the receiver relative to the mirrors can be determined using a laser tracker to better than 1 mm. These positions can be verified by fixing one (e.g., the source distance) and then fitting the other (e.g., the receiver positions) using our simulation code. In this way, we can determine and confirm these distances to ensure the phase corrections are correctly applied.

The x and y positions of the panels are determined by centering the measured aperture fields in the coordinates used in the simulations. We include this centering process in our results. Therefore, this method is robust to alignment errors.

Three remaining issues, which can produce spurious phase variations in the aperture plane, must be considered: atmospheric fluctuations, the phase of the receiver feed, and the phase stability of the reference receiver. The choice of 88 GHz should provide sufficient stability in the Chilean atmosphere at 17,000 feet. This will be verified with repeated measurements. The phase as a function of angle of the receiver feed will be measured in lab using the holography source and receiver. It is straightforward to include this correction in the modeling code to remove its impact on these measurements. Finally, the reference receiver must receive signals from the source without being affected by spurious reflections from the ground, and the cabling from it to the correlation receiver must be phase stable over the duration of the measurement. The first concern can be addressed by feeding the

reference receiver with a relatively high gain antenna, to exclude the ground, and mounting it off of the telescope to ensure its reflections aren't modulated. The stability concern can be addressed with a scan strategy that revisits the beam center often to allow for the removal of drifts. This approach also provides additional suppression of atmospheric phase effects.

This approach and these considerations are similar to what was done for ALMA [70] and SPT [118]. The desired measurement precision is not significantly different from what was achieved in these previous measurements. The SPT alignment residuals (16 μm), were limited by the telescope stability rather than the measurement accuracy. The measurement would take several hours to scan over 2°, with arcminute resolution, once all hardware is fully set up. A measurement at the desired precision is well within reach based on the measurement concept we have presented and these previous examples.

7.6 Public Code

All code used for this paper is available on GitHub under the name `HoloSim-ML`. The code includes two modules: beam simulation and holography analysis with mirror panel error fitting. This beam simulation includes the mirror geometry and panel setting errors and computes the beam in both the near- and far-field regions. The code can be adapted to produce the beam as a function of angle, as was used in this paper, or as a function of position in the focal plane. The later may be more appropriate for a holography measurement using the method described in [113]. The holography analysis code inverts complex beams either from simulations or holography data, corrects for near-field aberrations using ray tracing and returns the mirror surface errors. We also include code that determines the near-field corrections following the analytic expressions presented in [70]. The panel fitting code uses a machine learning algorithm trained with beam simulations. Notebooks are provided to show how to compute a beam simulation, how to analyze holography, and how to set up and run the panel fitting. We invite users to adapt this code to any applications they see fit, but

ask that publications using this code cite this paper and that code derived from this work remain public.

7.7 Discussion

We have presented the simulation and analysis of holography data, including the application of machine learning techniques, to recover panel adjuster errors from a complex optical system comprised of two mirrors that create partially degenerate features seen in the phase on the aperture plane. The power of machine learning is that it enables the efficient analysis of these data to separate the contributions of each mirror with high accuracy on small angular scales. On larger scales, this method creates degenerate solutions which can be addressed with holography from multiple receiver positions. The ML framework makes the analysis of these measurements from many receiver positions straightforward to analyze. We presented an example of the SO dual reflector optical system and demonstrated that this approach can yield $< 5\,\mu$m alignment errors, the requirement for SO science goals.

The approach demonstrated here comprises forward modeling of an optical system, sampling the system from multiple positions in the focal plane, and the application of ML to simultaneously determine many physical parameters which encode errors in the optical system. While a standard fitting method could also work in this application, we found that after one month of fine-tuning, we were only able to fit out half of the RMS of this dual reflector system. The ease of setting up and fitting with these ML tools was striking, while it also improved the quality of the fits for single mirror systems. We anticipate that this approach can be applied to a variety of complex optical systems, including systems with multiple lenses, filters, absorbers, and other optical components. For example, the SO [32] system includes re-imaging optics comprising three lenses, and filters. An immediate future application is to apply these techniques, using holography, forward modeling, and ML to understand the optical properties and interactions within the system. With proper parameterization of the

imperfections and alignment errors, combined with sampling the focal plane at several positions, we anticipate that machine learning will prove to be an increasingly important tool in the characterization and performance optimization of complex optical systems.

This software package developed for this work (`Holosim-ML` [117]) is customizable to include arbitrary optics while remaining simple to script. It is possible to substitute commercial simulation software within this ML framework if necessary. However, we chose to write a self-contained code to create an open access package that is efficient and can be widely shared. This work will enhance the sensitivity of SO to high ℓ (low angular scales), a range where we constrain $N_{\rm eff}$ and n_s, to name a few.

Chapter 8

The Atacama Cosmology Telescope: Beam Estimation for DR6 with point-source Stacking

8.1 Introduction

The Atacama Cosmology Telescope (ACT) is a 6 m off-axis Gregorian telescope located at an altitude of 5190 m in the Atacama Desert of northern Chile. It is designed for millimeter wavelength observations of the cosmic microwave background (CMB) at arcminute resolution. The telescope and receiver are described in [29] and [30] respectively. ACT has produced rich maps covering roughly 45% of the sky. While analysis of the most recent maps is ongoing, the signal-to-noise is so high that beam characterization is critical for cosmology (as detailed in Chapter 2).

This paper describes an alternative method for determining the optical response of the telescope based on stacking point-source observations. This data release includes temperature and polarization data collected by ACT between 2017 and 2021, covering roughly 18,000 square degrees of the sky [30].

Determining the optical response, or "beam", quantifies how the instrumental response is suppressed at small angular scales as a result of the finite resolving power of the optics. For this reason, understanding the telescope beam and its uncertainty is critical for achieving the science goals of ACT. Because the beam has to be de-convolved from the sky maps in order to perform cosmological analysis, incorrectly characterizing the beam directly biases any science by mimicking a spurious scale-dependent signal. Therefore, in order to achieve the science goals set out by ACT, characterization of the instrument beam is crucial. Besides the beam of the instrument, it is also important for a polarimetric instrument like ACT to quantify the amount of temperature-to-polarization leakage. We describe this type of leakage in terms of a so-called "leakage beam", which quantifies the amount of leaked signal from Stokes parameter I to Stokes parameters Q or U at a given angular scale.

Previous work to characterize the ACT instrument beam has done so with planet maps ([120–122]). Planets served as the best candidates for beam characterization of the telescope [123]. Specifically, observations of Uranus achieve adequate signal-to-noise without exceeding the dynamic range of the instrument. Here, we present a novel technique to characterize the instrument beam with map data, which we refer to as "stacking" of the point-sources in a map's catalog. This work provides a detailed recipe for characterizing an instrument's beam using full map data, which we apply to the ACT DR6 maps. While the stacking method is robust, we note that this novel method is applied to preliminary ACT DR6 maps and preliminary planet-derived profiles. This method provides a validation of the planet-derived beam both in temperature T and in the $T \to E$ and $T \to B$ leakage. Such a novel validation is necessary because the Uranus observations are separate observations made with a different strategy than the full maps, have different noise properties and were made using a different map-making technique. The point-source stacking method, presented here, uses the same observations which we use for cosmology, thus providing a check to the beam and leakage inferred from Uranus observations.

The paper is organized as follows. In §8.2 we describe the observations and catalog used to

stack point-sources and characterize the ACT beams. In §8.3 we explain the stacking process, starting from an input map and producing a stacked beam profile. In §8.4 we describe the steps of the map simulation pipeline, then going from simulated point-source maps to a model of the ACT beams and their covariance. In §8.5 we present the preliminary results from the stacking method, including the stacked temperature to polarization leakage, and the temperature beam radial profiles (compared to the preliminary planet-derived profiles, which will be updated in the future). Finally, in §8.6 we discuss assumptions made in the analysis and future directions for ACT beam characterization.

8.2 Observations

The data used in this work are part of the upcoming 6th data release (DR6) of ACT, though the maps are preliminary. DR6 consists of observation taken between 2017 and 2021 using three dichroic detector arrays, PA4, observing using broad frequency passbands roughly centered on 150 and 220 GHz, and PA5 and PA6, both with passbands centered on 98 and 150 GHz. The 3 types of frequency bands are referred to by F090, F150 and F220. On the sky, the observations fall in to the "Advanced Act" region as defined in [5], which includes roughly 45% of the full sky. The observations are taking during both day and night; in this work, we restrict ourselves to the nighttime data, as this subset of the data is the current focus of the cosmological analysis performed by the ACT collaboration. The DR6 data and analyses have not been made public yet at the time of writing.

The DR6 data are divided into 8 non-overlapping subsets and mapped into sky maps. In this work, we only use co-added versions of these 8 maps. We thus consider a single triplet of Stokes I, Q and U maps for each of the 6 combinations of PA4/5/6 and their two frequency bands.

The maps are produced in the Plate-Carrée cylindrical projection (CAR) using a maximum-likelihood (ML) technique that is described in [5]. There is one exception, which is relevant

for this work: the brightest point-sources are mapped with a specialized source mapmaker. This special treatment of bright point-sources is needed because the ML mapmaker produces artifacts when mapping bright localized sources, see [124] for a detailed explanation. In the DR6 maps, the specialized mapmaker is used for a pre-selected set of bright sources. We will refer to the bright sources that underwent this specialized treatment as "Special" sources, while we refer to the fainter sources that were mapped using the regular mapmaker as "ML" sources.

8.3 Methods

Here we walk through the stacking process from input map to beam profile.

8.3.1 Point-source Selection

Prior to stacking, we characterize each point-source to determine whether they are suitable for stacking. The number of point-sources used for the point-source analysis versus the total number of point-sources in the catalog is shown in Figure 8.1.

Select on Catalog

For ease of interpretation, a sky mask is applied that is similar to those used by the various cosmological analyses. This mask removes regions with strong Galactic emission (based on the 353 GHz Planck data) and significantly noisy regions on the sky. The point-source catalog has been estimated from the DR6 maps using a matched filter approach. Through the use of the 3 ACT frequency bands, the catalog also includes an estimate of the type of each source (synchrotron, flat or dusty spectrum, as well as SZ clusters). The catalog will be described in forthcoming publications accompanying the DR6 release.

From the catalog, we obtain a list of RA's and DEC's of point-sources in the map. Additionally, we select only synchrotron point-sources, such that we stack over individual

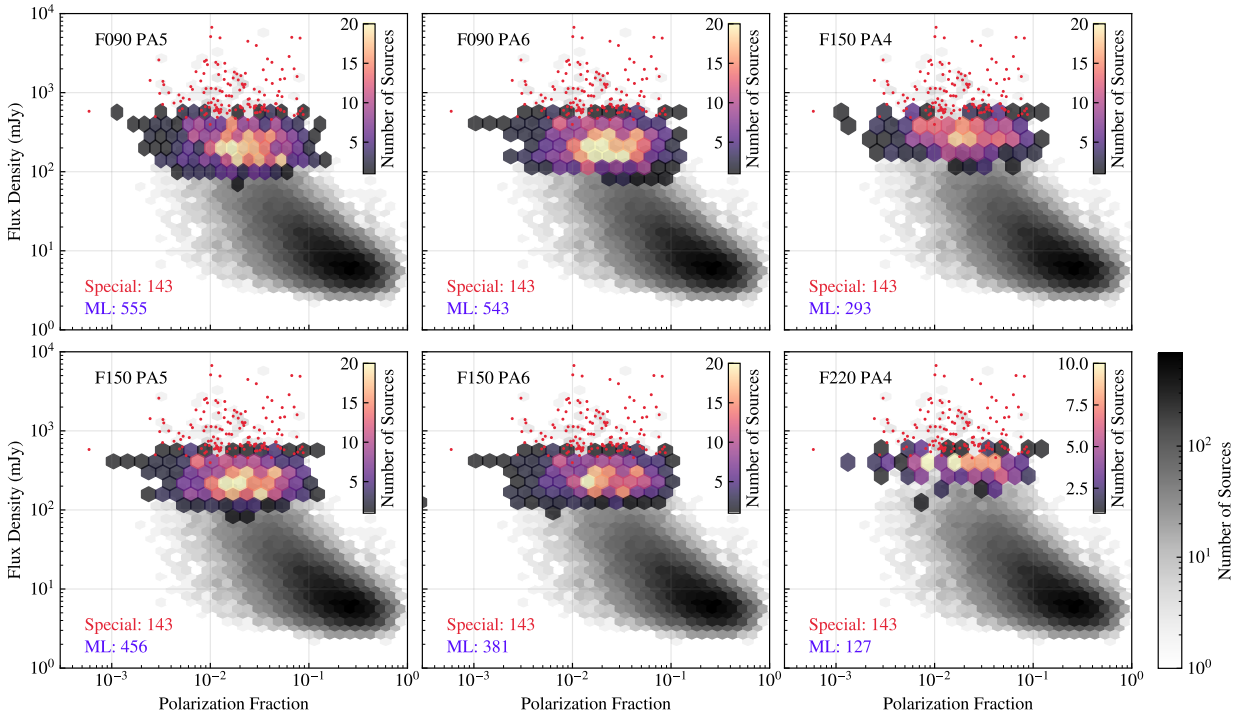

Figure 8.1: Distribution of the total number of point-sources that were in the catalog (greys) and ultimately became part of the final beam analysis (colored) for all arrays combined, shown by observing seasons from 2017–21. point-sources used in the stacking are separated into Special(red dots) and ML(gradient hexagonal bins) sources (the two types of sources are described in §8.3.1).

point-sources, rather than dusty galaxies or galaxy clusters. The brightest sources are synchrotron sources; so these cuts do not significantly reduce signal-to-noise. Rather, this cut simplifies the analysis by removing extended sources while we avoid stacking on sources with different spectral energy densities (and associated differences in optical response).

When stacking point-sources, we restrain the point-sources to a polarization fraction of below 10% such that we are not dominated by highly polarized sources. One would expect the signal to average away due to the sources' random polarization angles. However, this is not the case when a few of the brightest sources are strongly polarized and dominate the stack due to inverse-variance weighting (see Sec 8.3.1), which up-weights sources with the highest signal-to-noise ratios. Once the selection is complete, the geometry of the stamp is

defined to be $40'(30')$ wide at a $0.15'(0.05')$ resolution for the F090 and F150(F220) bands. The region must be large enough such that the stamp will include side-lobe features.

Select on Beam Quality

With the list of point-source locations on our map from the catalog, we further decide which point-sources to use in the stamp based on a stamp's individual features. For example, we don't want to include a stamp with two point-sources, or an off-center point-source, in the stack. To characterize the quality of a point-source, each point-source is re-projected to the same geometry (as specified in the last paragraph). A point-source p_i is first peak-normalized. If the location of its highest peak, $p_{i,1}$, is outside a radius of $0.5'$, p_i is assumed to be off-centered and is discarded.

We next want to determine if the stamp has two point-sources or just one. To do so, we find the second-highest amplitude in the stamp and assume this to be the second peak, $p_{i,2}$. If the amplitude of $p_{i,2}$ is within 10% of the average stamp value (outside the radius $r = \frac{2}{3} r_{\mathrm{FWHM}}$), it is assumed to be dominant, and the point-source p_i is discarded.

Figure 8.1 shows the number of point-sources used in each band and PA from the catalog. We note that the F090 map stacks included the greatest number of point-sources, since the beams are larger and therefore take up a larger area of the stamp's area. Because the F220 beams are much smaller in beam width, we constrain stamps in this band to a radius of $15'$, while the F090 and F150 stamps are at a radius of $20'$.

Special vs. ML Sources

We subdivide the remaining point-sources into two categories: Special and maximum-likelihood (ML) point-sources. When making the maps, as described in §8.2, point-sources are treated with the two differing methods, and thus we want to consider the two groups individually when stacking to note any differences this treatment may have caused. The final distribution of selected point-sources is shown in Figure 8.1.

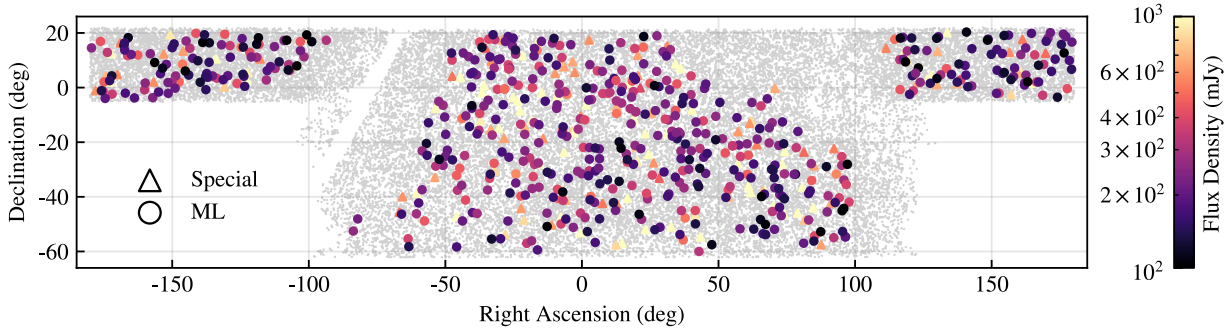

Figure 8.2: Spatial distribution of all point-sources in the catalog(grey) and the selected point-sources used in stacking(colored). The color bar shows the flux of the Special(ML) sources, which are plotted as triangles(circles). The regions of the map with no used point-sources indicate regions which are masked out prior to stacking. The mask ensures that the stacked point-sources are in the same regions of the sky used in cosmology science.

8.3.2 Stacking

This section describes the stacking procedure with the selected sources. Each stamp s_i is re-projected to the same geometry prior to stacking. Each stamp is cut from the map and re-projected to a tangent plane using a bi-cubic interpolation. Re-projecting to a tangent plane ensures stacking multiple sources from different declinations are not stretched by different amounts (as a result of the CAR pixelization of the input map). The bicubic interpolation introduces a small bias, resembling a low-pass filter. Using the simulations presented in §8.4, we find that this bias is small enough to neglect.

Before stacking the reprojected stamps, we subtract an estimate of the large-scale correlated noise component of the stamp. The correlated noise, coming mainly from the CMB and atmosphere, is relatively bright compared to the point-sources (at around the -20 dB level for even the brightest point-sources), making it crucial to remove it prior to stacking. If left in the stamps, the correlated noise is not averaged down enough during stacking as a result of the small number of high signal-to-noise sources in the stack. The resulting stacks show a large amount of noise variance, which prohibits measurements of the non-central parts of the beam. We only perform the subtraction on the Stokes I component of the stamps; the Stokes Q and U components have a relatively small amount of correlated noise, making the

subtraction procedure unnecessary.

We refer to the subtraction method as "inpaint-subtraction". This procedure masks a region centered on the point-source and fills this area with a prediction of large-scale correlated noise using only information from the outer area of the stamp. This inpainted region is then subtracted from the original stamp, resulting in a map of the point-source with substantially reduced large scale correlated noise. The inpainting is done with a simplified version of the method described in [125]. In short: the method uses the conjugate-gradient method [126] to solve for s_l in:

$$\left(S^{-1} + M^{-1}\right) s_l = M^{-1} s \tag{8.1}$$

Here, s denotes the input stamp and S^{-1} denotes the inverse covariance matrix of the correlated noise, modelled as a "$1/f$" spectrum in harmonic space: $1/(1 + \ell/\ell_{\rm knee}^{-3})$ with $\ell_{\rm knee} = 2000$. This is a rough approximation of the actual covariance matrix of the correlated noise, but it works sufficiently well for our purpose. The M^{-1} matrix is modelled in the pixel-domain, where it sets all pixels in the region around the point-source to zero, and all pixels outside the region to a small, but nonzero value. The conjugate gradient method solves Equation 8.1 in roughly 10-20 steps, yielding s_l: a version of the stamp with an inpainted inner region that is smoothly connected to the outer region. The result of the inpainting-subtraction is shown in Figure 8.3.

The above procedure will not bias the point-source signal as long as the signal is zero in the unmasked outer region. In that case the information available for inpainting, i.e. the outer region, is independent of the point-source and thus the inpainting-subtraction is unbiased by construction. However, due to the extended structure of the beam, the point-source signal is not quite zero at the edges of the stamp where we define the outer region. As a result, the inpainting solution will not be perfectly uncorrelated to the point-source signal, which means that once the inpainted stamp is subtracted, a small amount of the

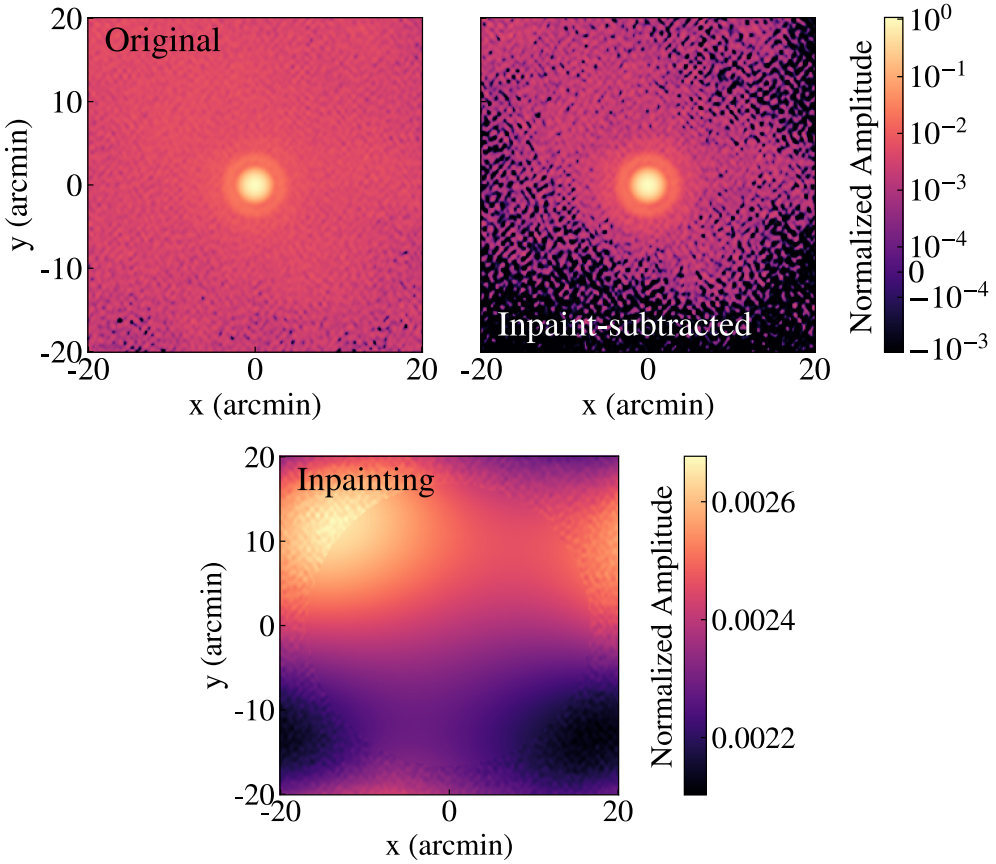

Figure 8.3: Inpainting-subtracted method as described in §8.3.2 for F090 PA5. Top row: Stacked beam without inpainting subtraction (left) and stacked beam including inpainting-subtracted method (right). Bottom: Inpainting signal which is subtracted during the stacking procedure for F090 PA5 (note the linear scale colorbar). This shows the large angular-scale signal which is removed from the stacked beam with the inpainting method.

point-source signal is also subtracted. This type of bias is similar to the one explained in the ACT DR4 beam paper [123]. To minimize the bias, we start the outer region at the radius at which the fiducial planet-derived beam becomes smaller than 10^{-4} compared to its peak value. Using the simulations in §8.4 we validate that the remaining bias is small enough to ignore.

The above inpainting procedure returns our point-source-free stamp, s_l. For each point-source i, we then subtract $s_{i,l}$ from our original stamp, s_i:

$$s_i^{,} = s_i - s_{i,l} \tag{8.2}$$

The final step is weighing each stamp and stacking them together. We employ an inverse-variance weighting, where the weight is always calculated from the intensity I_i stamp, and the same weight is applied the Q_i and U_i stamps. The variance σ^2 is calculated between $r_{\rm in}$ and $r_{\rm out}$ of the stamp, where $r_{\rm in}$ is defined as the radius where the planet-derived beam drops below $-35\,$dB (both $s_i^{\cdot}$ and s_p peak-normalized), and $r_{\rm out} = \frac{4}{3} r_{\rm in}$. The weight of the stamp w_i is then the inverse variance of I within $r_{\rm in}$ and $r_{\rm out}$. Once the above is calculated for all stamps in the set, the final stacked beam is calculated by:

$$\bar{s} = \frac{\sum_i s_i w_i}{\sum_i w_i} \tag{8.3}$$

Figure 8.3 shows an example output of the stacking, for PA5 F090. Without inpaint-subtraction, the stamp appears saturated by large-scale structure (top left of Figure 8.3). The bottom panel shows the signal from inpainting which is subtracted from each point-source stamp prior to stacking, leaving a less saturated stacked beam (top right).

8.3.3 Bias From Stacking

To study this bias, a set of simulated observations are processed through the stacking process. The full simulation pipeline is described in §8.4.

8.3.4 Radial Profiles

Maps are binned into a symmetrized radial profile with bins of varying width, out to a radius of $20'(15')$ for F090 and F150(F220), independently for each detector array, and F-band. The bins are chosen to be logarithmic in radius. We ultimately want to compare the stacked profiles to the planet-derived beams. To do so, we first convert the planet-derived beams to a 2D stamp matching the stamp geometry of the stacked beam. We then radially bin the new planet-derived beam with the same bins used on the stacks.

Error of the radial profiles is obtained by simulating and stacking 100 maps with the

simulation pipeline described in §8.3 and §8.4. The covariance matrix of these 100 simulated radial profiles estimates the error of our "true" stacked profiles at each binned radius.

8.3.5 Beam Window Functions

The window function w_ℓ quantifies the response of an instrument across angular scales, or multipoles ℓ, which is encoded in the instrument's beam. Because the CMB spectra is presented in spherical harmonic ℓ-space, we similarly will compute the instrument's window function in ℓ-space. The window function is defined as

$$w_\ell = B_\ell^2 \ , \tag{8.4}$$

where B_ℓ is a Legendre Polynomial transform of the instrument's beam (the full derivation of the Legendre transform is presented in [123]):

$$B_\ell = \frac{2\pi}{\Omega} \int_{-1}^{1} B(\theta) P_\ell(\cos\theta)\ d(\cos\theta) \ . \tag{8.5}$$

Each B_ℓ is fixed at $\ell = 1050$ for F090 and $\ell = 1525$ for F150 and F220. This ℓ range is the calibration value at which the ACT maps are calibrated to Planck, therefore we set the ratios of stacks to planet-derived beams to unity at this angular scale.

We quantify the leakage beams, or temperature power which has "leaked" into the Q and U polarization maps, by decomposing the Stokes Q and U stamps into E- and B-mode spherical harmonic coefficients [127]:

$$b^E_{\ell m} \pm \mathrm{i} b^B_{\ell m} = -\int \mathrm{d}\Omega(\hat{n})(Q \pm \mathrm{i}U)(\hat{n})\ {}_{\pm2}Y^*_{\ell m}(\hat{n}) \tag{8.6}$$

Here ${}_{\pm2}Y_{\ell m}$ are the spin-±2 spherical harmonic coefficients and the integral is taken over the whole sphere. Q and U represent the Stokes Q and U components of the stack rotated from the equator (where the stacks are centered) to the north pole of the standard spherical

coordinate system. The rotation is done using the `pixell` [1] library and takes into account the mixing of Q and U under rotations. Similar to the reprojection mentioned in §8.3.2 the rotation also makes use of bicubic interpolation. Again, through the simulations, we have validated that the resulting smoothing does not introduce a significant bias.

The $T \to E$ and $T \to B$ leakage beams are obtained from the E- and B-mode spherical harmonic coefficients in Equation 8.6. Here, we only present the symmetric part of the beam, i.e. the $m = 0$ coefficients, though our analysis can also be used to study higher modes ($m = 1, 2$). The symmetric part of the leakage beam is modeled as:

$$B_\ell^{T\to E/B} = b_{\ell 0}^{E/B} \sqrt{\frac{4\pi}{2\ell+1}} \tag{8.7}$$

Where the $\sqrt{4\pi/(2\ell+1)}$ factor converts from spherical harmonic coefficients to Legendre polynomial coefficients, which have the appropriate normalization.

8.4 Simulation Pipeline

We simulate a stacked profile to validate our stacking pipeline and to estimate statistical uncertainty on the radial profiles presented in §8.5. We first simulate a map by combining simulated point-sources (referencing the catalog) along with a simulated CMB and foregrounds, and additionally adding simulated noise. An example of a simulated map (box area of $\pm 2\,\mathrm{deg}$) is shown in Figure 8.4. The four quadrants show the three main components of the simulated maps, followed by the total simulated map, where the prior three components are combined. Here, we detail the construction of the simulations.

1. `https://github.com/simonsobs/pixell`

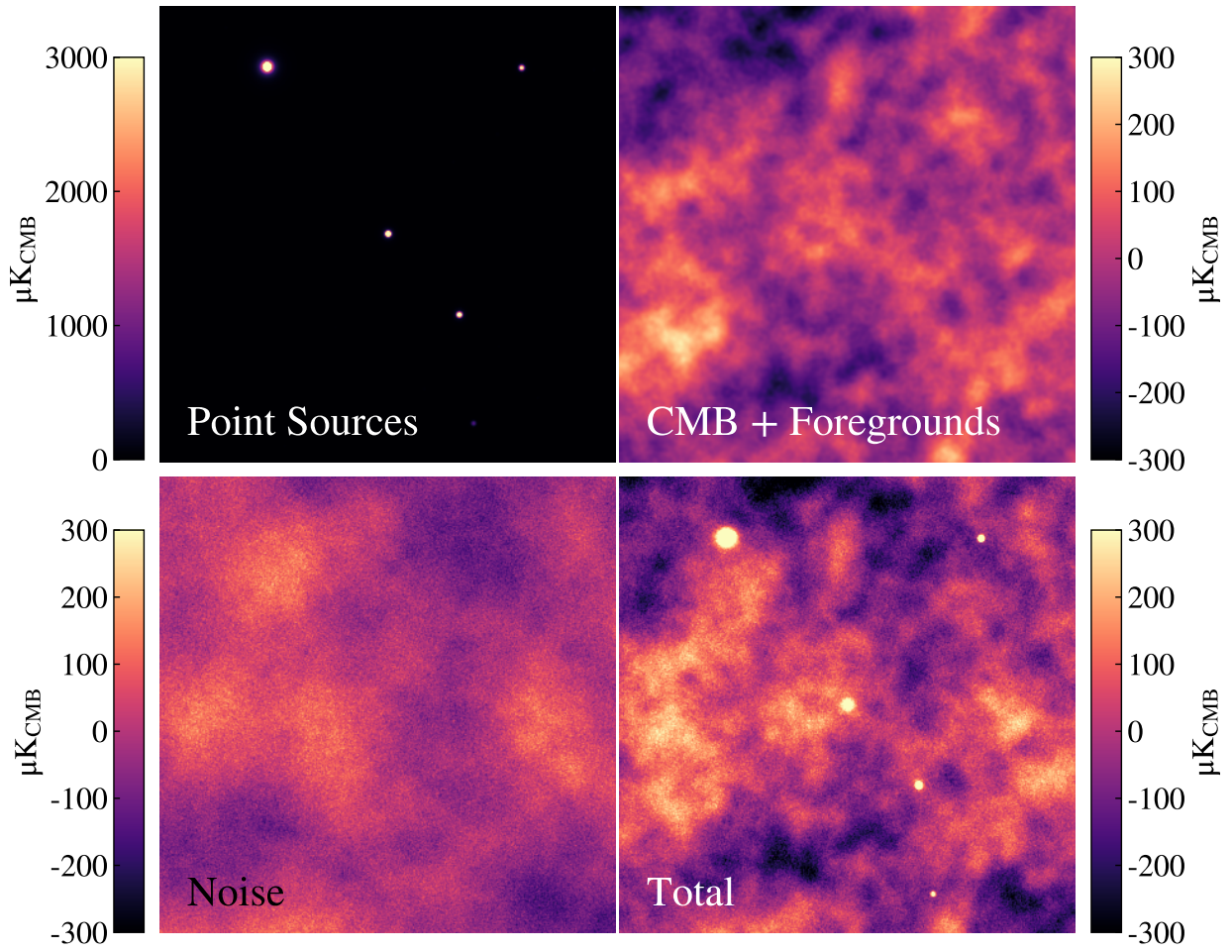

Figure 8.4: Example of a simulated map used to characterize the stacking bias. This example is for PA5 in the F090, zoomed in to an area of 2 deg $\times$ 2 deg. Top left: Point-source map using the input catalog RA and DEC coordinates. Top right: Simulated CMB. Bottom left: Simulated noise [11]. Bottom right: Final simulated map after combining the previous three components. This process is done for each PA and F-band, and repeated 100 times to estimate radial profile errors.

8.4.1 point-source Map Simulation

A point-source map is simulated using the input catalog, and point-source selection described in §8.3.1. The planet-derived beam defines the shape of the point-sources in the simulated map. Fluxes of each point-source are obtained from the catalog and converted to the units of the data maps (μK_{CMB}) using the fiducial beam solid angle and center frequency of the passbands.

The fiducial beam profile, fluxes and coordinates are then given to the `pixell.sim_objects`

function that outputs a simulated point-source map with matching point-sources and map shape as the catalog and DR6 map. We choose to apply to the simulated map a pixel window function that matches that of the data maps for ease of comparison.

8.4.2 CMB Simulation

The second component of the simulation is diffuse sky signal comprised of the CMB and (extra-)Galactic foregrounds. This signal is critical in the simulation because the CMB is a significant source of noise in our stacked profiles at intermediate angular scales. To accurately estimate the uncertainty and bias introduced by the inpaint-subtraction method described in §8.3.2, we must include the CMB in our simulations.

We use the DR4 C_ℓ^{TT} power spectra to draw Gaussian realizations of the diffuse sky signal. An example of this simulated signal is shown in the top right of Figure 8.4. This simulation also contains foregrounds, which are an important contribution at high multipoles.

8.4.3 Noise Simulation

The third component to complete our simulated maps is noise. The estimation of map noise is twofold: 1) a realization of the ACT map-based noise simulations at large angular scales ($\ell < 5000$) and 2) a white-noise realization drawn from the per-pixel variance maps that accompany the DR6 maps.

The ACT map-based noise simulations will be fully described in an upcoming paper accompanying the DR6 release. Noise simulation maps include atmosphere, ACT scan strategy, and a more detailed approach to model correlated instrument noise. An individual noise simulation is used for each individual simulated map.

As the map-based simulations at the time of this analysis only describe the noise on large angular scales ($\ell < 5000$), we manually fill in the noise on small angular scales. We then splice together two noise simulations in ℓ-space, such that the white noise term occupies the lower ℓ-space and map-based noise dominates the high ℓ-space. An example patch of the

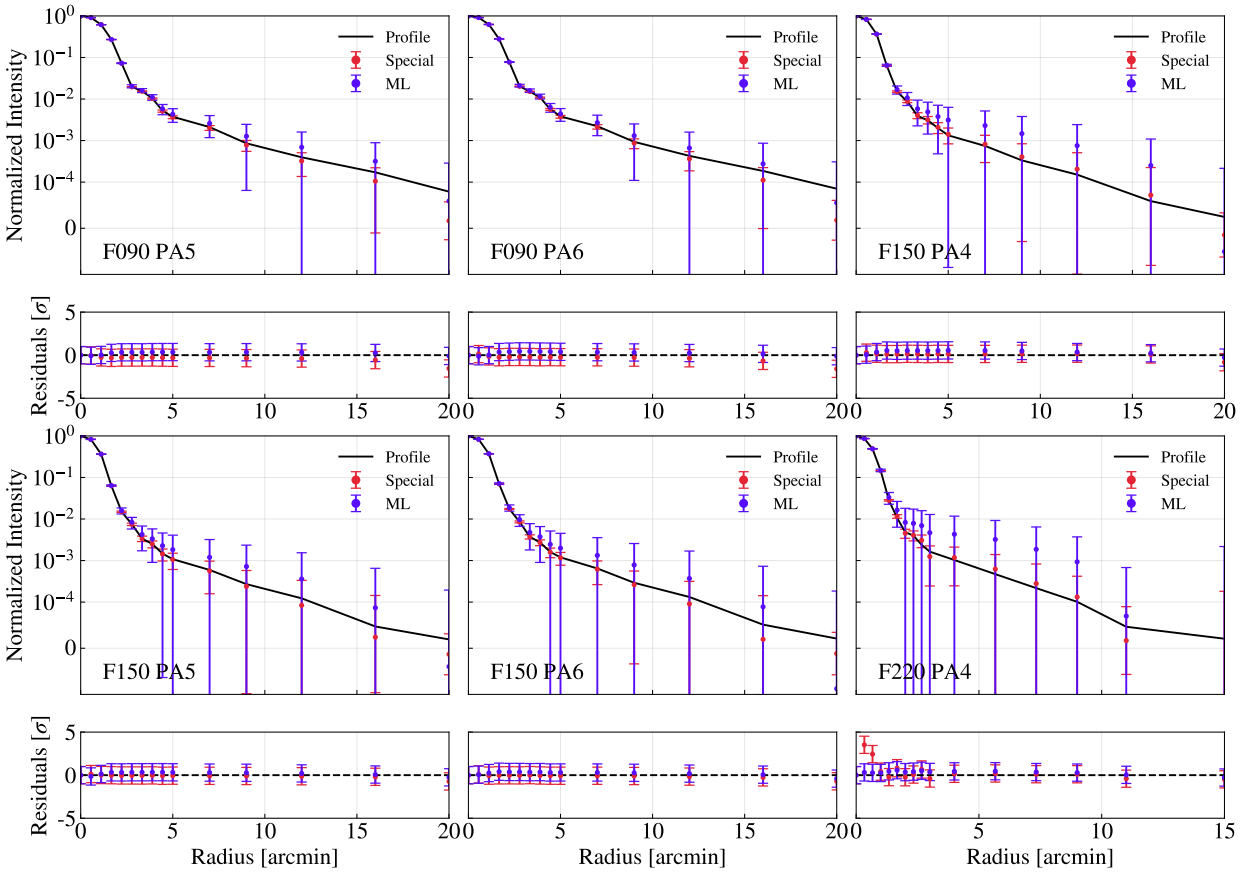

Figure 8.5: Mean simulated radial profile at each F-band and PA, averaged over 100 simulations. Mean simulated profiles are shown for Special(red) and ML(blue) sources, with error bars calculated from the covariance matrix of the 100 profiles. Each profile is then compared to the corresponding planet-derived beam(black) in the bottom panel of each plot. This shows the bias from the stacking procedure is minimal and can be neglected in the subsequent analysis.

noise map is shown in the bottom left of Figure 8.4.

Figure 8.5 shows the mean simulated profile (over 100 simulations) at each PA and F-band compared to the planet-derived beam, plotted in black. From this averaged simulated beam, we determine the stacking procedure to have negligible bias on the resulting beam profile.

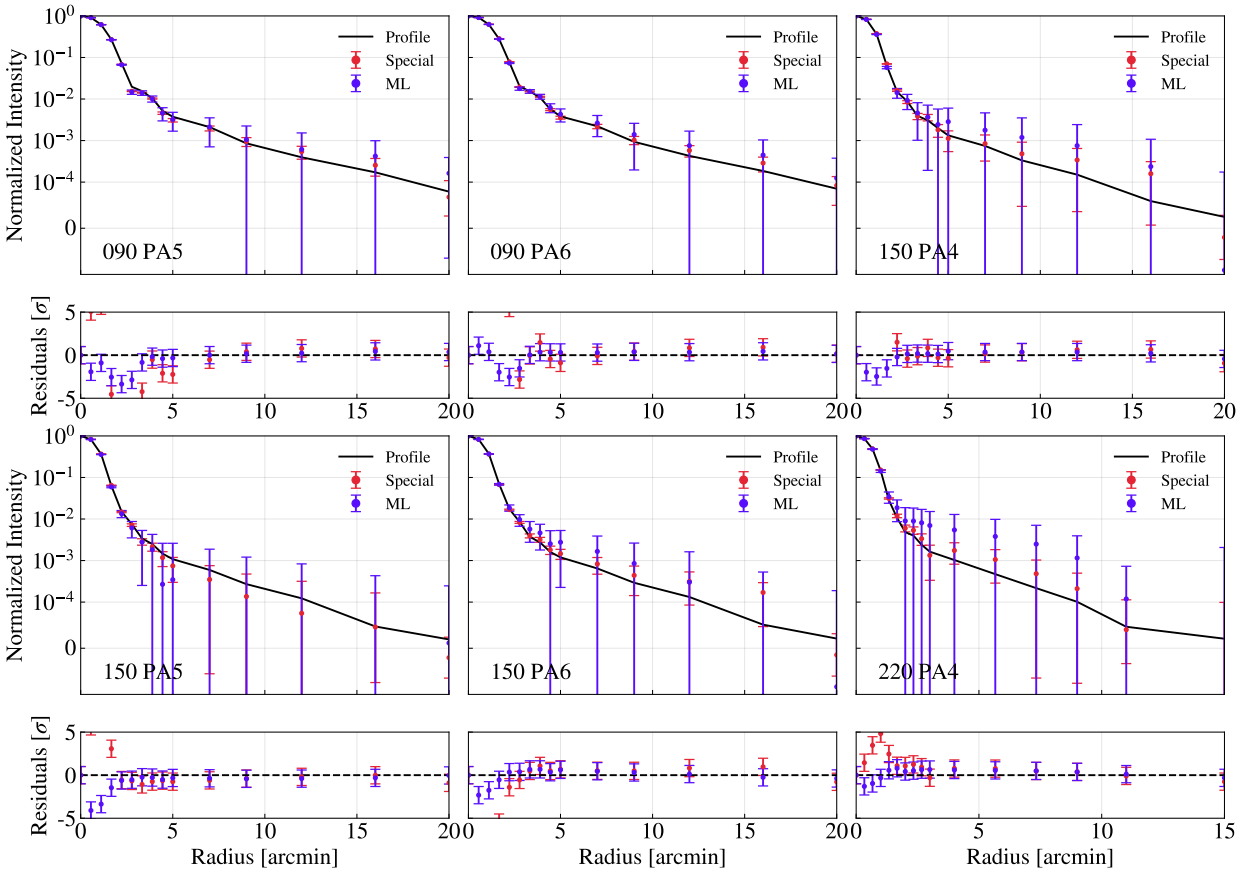

Figure 8.6: Stacked radial profile at each F-band and PA. Profiles are shown for Special(red) and ML(blue) sources, with error bars calculated from the covariance matrix of 100 simulated stacked beams. Each profile is then compared to the corresponding planet-derived beam(black) in the bottom panel of each plot.

8.5 Results

Here, we detail the resulting temperature and temperature-to-polarization leakage beams acquired from the stacking method described above.

8.5.1 Main Beam

This section presents the temperature profiles from stacks and compares them to the existing planet-derived beams from Uranus.

Profiles

The stacked profiles are shown in Figure 8.6. Each profile shows the Uranus planet-derived beam in black, with individual arrays plotted separately. The bottom panel shows the difference between each array's profile to the planet.

Spatial Variation

To study the spatial variation of point-sources, we conducted a "null test" where we stacked four categories of point-sources: high and low, RA and DEC. We separate the catalog in half by considering the median RA and DEC, such that the four categories are $\mathrm{RA}_{\mathrm{low}}$, $\mathrm{RA}_{\mathrm{high}}$, $\mathrm{DEC}_{\mathrm{low}}$ and $\mathrm{DEC}_{\mathrm{high}}$ (separated by their median values). Figure 8.7 shows the resulting window functions B_ℓ for each F-band and PA. The red line in each sub-plot show the full map's B_ℓ for comparison.

From this test, we find the beam derived from the Special sources exhibits a small, but statistically significant, spatial dependence. We find that $\mathrm{DEC}_{\mathrm{low(high)}}$ and $\mathrm{RA}_{\mathrm{high(low)}}$ match in window function, but differ from their opposite. Specifically, the Special sources consistently show larger power at high ℓ's in the $\mathrm{DEC}_{\mathrm{low}}$ and $\mathrm{RA}_{\mathrm{high}}$ than the planet-derived profiles, indicating a tighter beam in these regions of the sky. This effect is most prominent in the F090 PA5/6 and F150 PA4 profiles. The ML sources, however, do not show a statistically significant spatial variation.

8.5.2 Temperature to Polarization Leakage Beam

Here, we present the polarized beams of the stacked point-sources to determine polarization leakage in the instrument. The leakage is relatively small compared to the magnitude of the temperature beam, however the sensitivity of ACT DR6 data is such that this leakage needs to be accounted for in the analysis. Previously, observations of Uranus were used to build an ℓ-space T-to-P leakage function for a given frequency and array in the instrument. Here, we test this method by comparing the leakage to our new method of stacking.

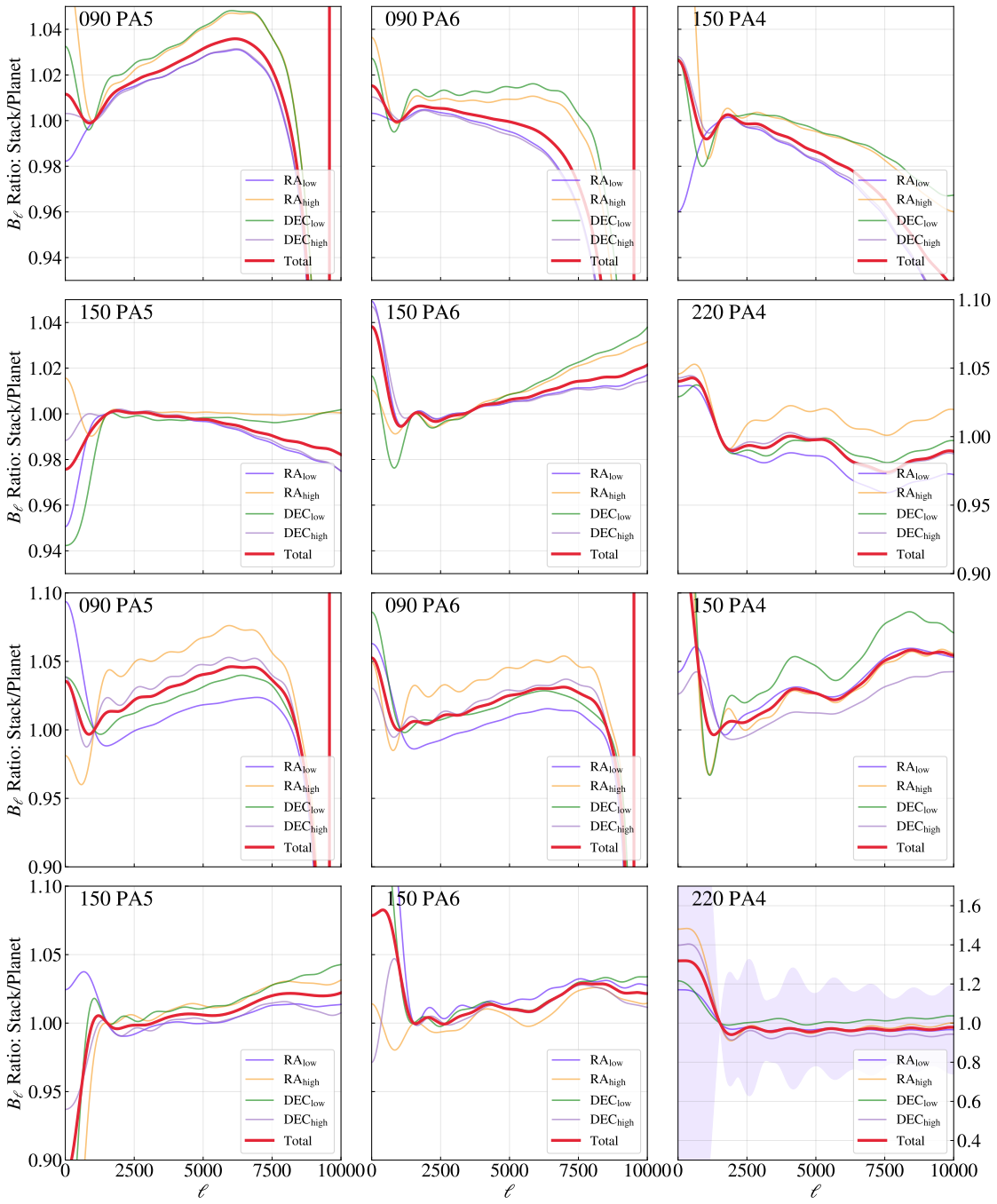

Figure 8.7: The panels show the ratio of the window function derived from the stack to those of the preliminary Uranus-derived window functions, separated by high and low RA and DEC. The top two rows are Special sources, and the bottom two rows are the ML sources. Each ratio is set to 1 at $\ell = 1050$ for F090 and $\ell = 1525$ for F150 and F220. The stack made up of the combined set of point-sources is depicted by the red curve.

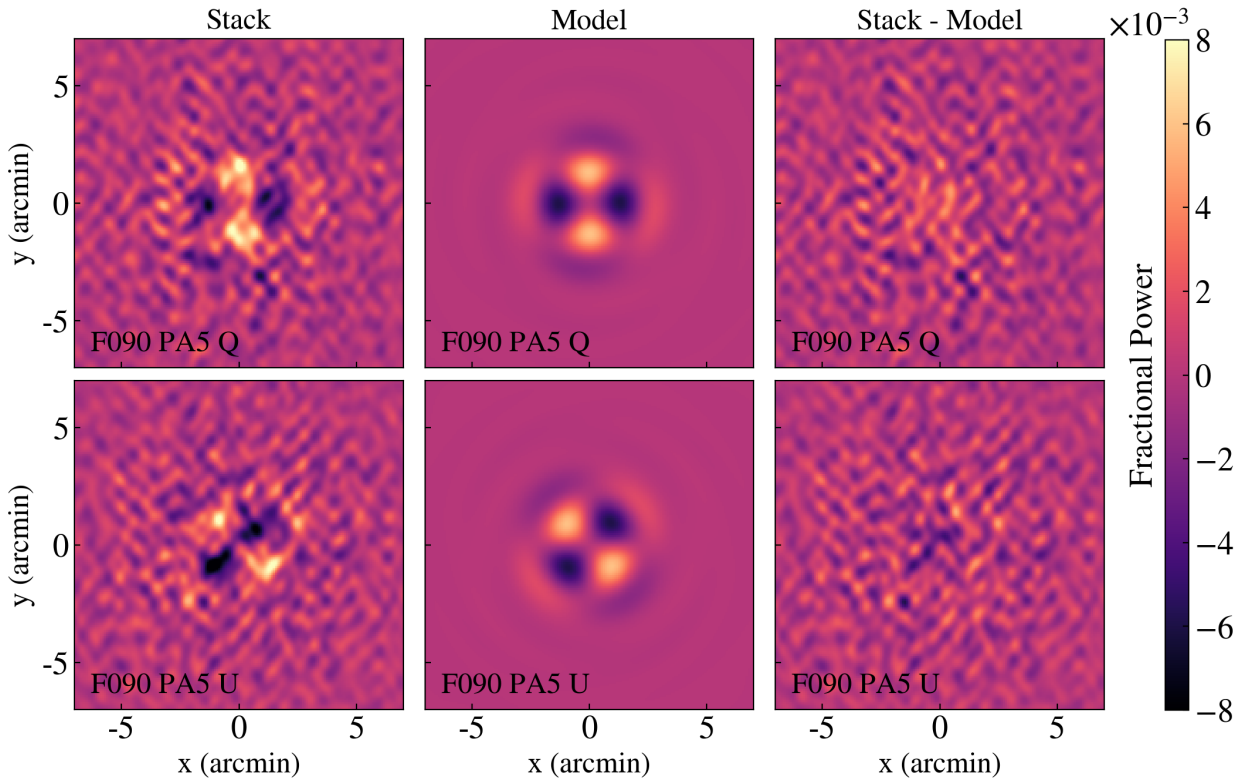

Figure 8.8: Polarization leakage from stacked F090 PA5 beam, for the ML sources. Top row: $T \to Q$ leakage. Bottom row: $T \to U$ leakage. Left column: stacked map, Middle column: modeled polarization leakage, Right column: difference between stacked and modeled beams. The low signal in the right column suggests that the one-dimensional leakage model is able to capture the polarization leakage of the stacked profiles.

Figure 8.8 shows an example of the stacked polarization leakage beam, the modeled beam, and the residual for F150 PA4. Note that the quadrupole shape of the model is due to the reprojection onto the stack geometry: although we model the leakage beam as azimuthally symmetric when located on the pole of the standard spherical coordinate system, the symmetric shape turns into a quadrupole shape when rotated to the stack geometry location, which is centered on the equator. From the window functions, we obtain the window functions of each array's $T \to E$ and $T \to B$ leakage (Figure 8.9). Figure 8.8 further demonstrates that the one-dimensional model of polarization leakage is sufficient to fully characterize the leakage beams for both the stacked and planet-derived profiles.

In Figure 8.9 we compare the ℓ-space $T \to P$ leakage functions derived from the point-

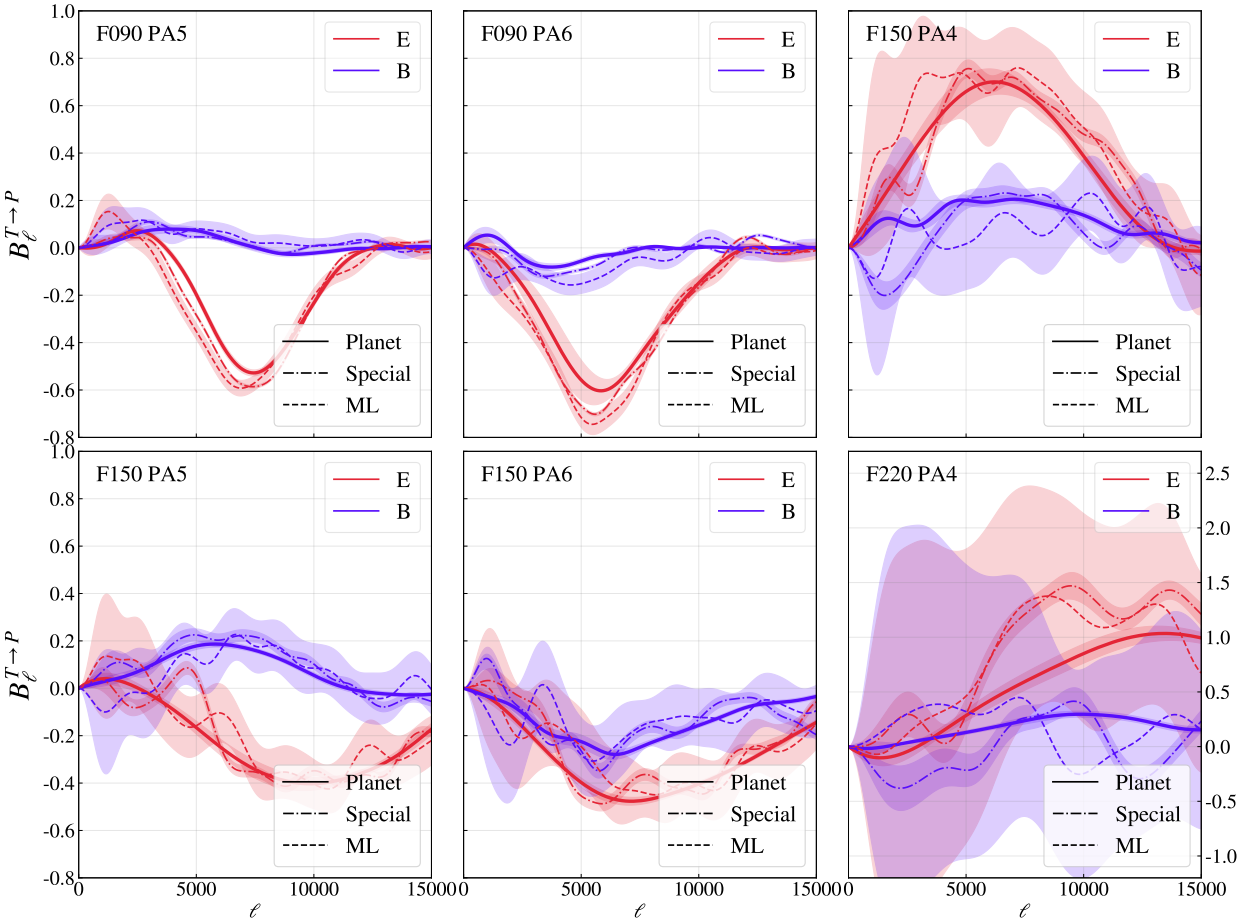

Figure 8.9: Polarization leakage, $B_\ell^{T\to P}$, from stacked and planet-derived profiles. Leakage beams are separated by Special(dashed-dotted) and ML(dashed) sources, with leakage from the planet profile(solid) plotted for comparison.

source stacks to those derived from Uranus. We find that the estimates from the Special and ML stacks are statistically consistent. Furthermore, we see broad agreement between the planet-derived and stacked polarization beams. This provides evidence that the planet-derived leakage estimation is appropriate for use in the actual CMB maps. There remain small, but statistically significant, differences between the planet-derived and point-source-derived leakage beams; the cause of this difference is still being investigated.

8.6 Discussion

We have presented the analysis of the ACT beams for the preliminary maps of DR6 using a novel point-source stacking method, which includes data from 2017–21. We describe the full point-source stacking method, including the use of an inpainting method to remove large-scale structures and improve the signal-to-noise of the resulting stacked profiles. As point-sources are treated with the two differing methods during the map-making, we consider the two groups, ML and Special, separately in the analysis.

The beams derived from the stacking pipeline deviate from the planet-derived beams at the 1-2% level at intermediate angular scales, as well as a spatial variance when the stacks are separated by location on the sky. The spatial variation is especially significant for the Special sources. The cause for this spatial variation is still unknown and requires further investigation. Polarization leakage as determined by the stacks is not significantly different from the predicted leakage by the planet-derived profile. This indicates the planet-derived leakage estimation is sufficient for usage on CMB maps. We find the one-dimensional leakage profile is an adequate method for characterizing the polarized leakage beam, as it models nearly the entire polarized signal from the stack (Figure 8.8).

We believe point-source stacking is a robust method for leakage estimation and instrument profile characterization. This is especially critical to verify the planet-derived profiles commonly used to carry out cosmology science on CMB maps. While this method presents a novel method for characterizing the instrument beam, this method can also be used for constraining cosmological science.

Chapter 9

Conclusion

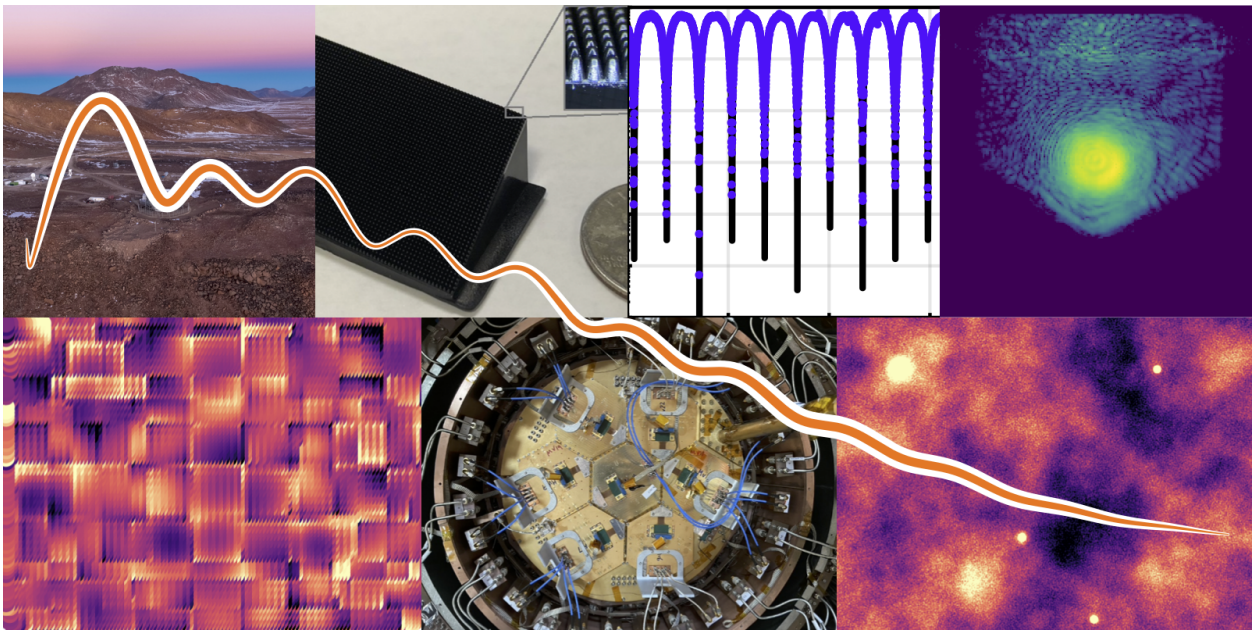

Figure 9.1: A snapshot of every chapter in this thesis, with the temperature power spectrum of the CMB overlaid.

Experimental cosmology is in an era of precision instrumentation. Such precision instrumentation requires understanding optical components in the telescope, careful characterization of its performance, and detailed analysis of its optical performance. In this work, I have presented several advances in instrumentation and optics which will further our understanding

of the universe. I have also presented novel methods for characterizing the instruments to further improve systematics.

9.1 Summary of Research

As detector sensitivity improves, systematics must be mitigated. For example, stray light within an optics tube results in loading onto the detectors, degrading the signal-to-noise of the camera. To control and mitigate unwanted scattering within the optical system, we develop meta-material absorbers which stop the scattering at the front of the telescope prior to entering deeper into the optics tube. As presented in Chapter 3, we use the holography receiver to characterize the meta-material absorbers in the mid-frequency band. We measure the reflectivity and scattering properties of the meta-material absorber, and compare its performance to alternative absorbers used in experimental cosmology. We find the integrated scattering power is less than 1% with the angle of incidence $\leq 45^{\circ}$. Such a reduction of scattered signal has profound impacts on the sensitivity of the telescope and ensures the detectors will not be as loaded with stray light.

Silicon is an optimal material for re-imaging the millimeter-wave photons onto detectors. Its index of refraction provides fast re-imaging of the beam onto the detectors with low loss of signal. The specific index of refraction informs the optical design of the telescope, and thus it is crucial to know the exact loss and optical properties of the lenses during the optical design and characterization of the instrument. The loss tangent is critical to constrain, as it dictates the loss of power as signal propagates through a medium. Chapter 4 reports the measured reflectivity of two silicon samples for potential use in cosmology experiments, where the two samples are studied using a holographic imaging setup. This setup measures the reflectivity over a range of frequencies and is then fit to determine the device's optical properties. From the reflectivity, we determine the loss-tangent of both samples, and find the "intrinsic" silicon has a lower loss-tangent than the neutron-doped silicon across the mid-

frequency band (75-160 GHz), therefore making it a better material for lenses in experimental cosmology.

Integrating and testing the optical performance of a telescope prior to deployment is novel; it is common to characterize the beam of a telescope at the site. However, once at the site, it is nearly impossible to alter the hardware and probe its functionality. In Chapter 5, we present the characterization of the Simons Observatory Large Aperture Telescope Receiver with radio holography. From this optical characterization, we determined a filter to be the source of scattering which, when removed, improved the instrument's efficiency in the mid-frequency band by roughly 5%. Characterizing the fully integrated optical system allowed for multiple tests and the careful discovery of additional sources of scattering prior to deployment. We also determined the on-sky beam prior to deployment by propagating the near-field measured beams through the LAT and into the far-field, verifying the on-sky beam size is within SO's requirement for science.

Following the characterization of the LAT optical system, we presented preliminary results of the SAT optical system measured with the same radio holography receiver (Chapter 6). Though results are preliminary, we determine the on-sky beam to be $(26.02' \pm 1')$ in the F90 band, within the expected beam size of $24.95'$. This further demonstrates the applicability of radio-holography system to other optical systems prior to deployment. The Simons Observatory's ambitious science goals require precise instrumentation across angular resolutions, and the SAT and LAT combined will further our characterization of the CMB and the physics of our universe.

In Chapter 7, we present an application of machine learning to improving instrumentation, namely, the SO's Large Aperture Telescope. To enable large aperture cosmology experiments, it is common to use large reflector mirrors which are made up of many panels. Such reflectors can create wavefront errors due to the Ruze principle. This chapter presented the SO dual reflector optical system (Large Aperture Telescope) and a method of measuring the panel offsets using radio holography paired with machine learning. We found that this

approach can yield $< 5\,\mu$m alignment errors, which is well within the requirement for SO's science goals.

Lastly, Chapter 8 presents a novel method for characterizing the AdvACT instrument's beam using measured point sources. From the maps, point sources are selected based on various criteria and stacked to determine the instrument's temperature and temperature-to-polarization beams. While the current method employs planet-derived radial profiles, this novel method provides a check and validation of the polarization leakage and window function of the instrument. While we find the temperature-to-polarization leakage beams are consistent between the two methods, we obtain inconsistent beams when we divide the point sources into four quadrants based on their sky coordinates and estimate the beam from each subset, suggesting that there is a spatial dependence to the beam shape.

9.2 Forecasting the Future of Cosmology

In this work, I presented the characterization of a variety of optical components for ground-based cosmological experiments. Understanding the optical properties of the materials within the telescope is crucial for predicting its optical performance. This becomes even more critical as detectors will increase in sensitivity; optical systematics need to be tightly constrained.

For example, as telescope reflectors are scaled up (to increase angular resolution), they will require careful calibration to ensure low wavefront errors, as this can drastically lower the telescope's gain. Additionally, the pre-deployment characterization with radio holography will advance the field and ensure optimal optics for the field of precision cosmology. Additional characterization of the instrument's beam, as described in Chapter 8, will become even more critical after measurements begin. This will ensure scan consistency of the instrument and aid the precision of science goals such as gravitational lensing.

The Simons Observatory will see first light within the next year. From the advancements in instrumentation, SO will constrain n_s with an estimated uncertainty of $\sigma(n_s) = 0.002$ [37],

improving the forecasted uncertainty of ACT's DR6 of $\sigma(n_s) = 0.003$. SO will also constrain the Standard Model with its precision measurement of the effective number of neutrinos, N_{eff}. SO will double the precision of ACT DR6, with an uncertainty of $\sigma(N_{\text{eff}}) = 0.05$ [37].

Further down the line, CMB-S4 will further constrain cosmological parameters with advanced instrumentation and analysis techniques, beyond what is currently capable with ACT or even SO. CMB-S4 will extend technologies developed for SO and scale up the large aperture telescope, thus increasing resolution and characterizing small-angular scales, and deploy many Small Aperture Telescopes to characterize the low-ℓ CMB spectra. For example, it will constrain the Hubble Constant to an error of 0.24 km/s/Mpc, beating the precision of SO.

Appendix A

Open Source Holography

A.1 Open-Source Holography

Figure 5.3 shows a schematic of the RF electronics. Two local oscillators (LOs) produce signals between 10 and 13 GHz. The LO1 synthesizer produces a signal between 10 and 13 GHz, while LO2 produces the same frequency with some offset f_{offset} (this offset is chosen to be 10 MHz). The offset frequency is what will eventually produce an intermediate frequency exiting the mixer diplexers. The purpose of the mixer diplexers is to ensure the signal from the first LO travels to the two mixers, and then ensures that the IF output of the mixers travels in the opposing direction down the RF chain to the FPGA.

The LO1 signal goes to the active multiplying chain, where it is multiplied by 8(12), obtaining frequencies in the F90(150)-band. Prior to leaving the source horn, -10dB of the signal splits off, and mixes with LO2 in the harmonic mixer, producing an intermediate frequency IF_1 which then goes through one of the mixer diplexers and to the FPGA. The rest of the signal leaves the source horn, through the components of the LATR optics, and the signal reaching the back of the optics tube mixes with LO2 in a GaAs harmonic mixer, and the subsequent intermediate frequency, IF_2, which also travels to the FPGA. The FPGA used for these measurements is the Re-configurable Open Architecture Computing Hardware

(ROACH-2) board, which correlates the reference and modulated signals [61].

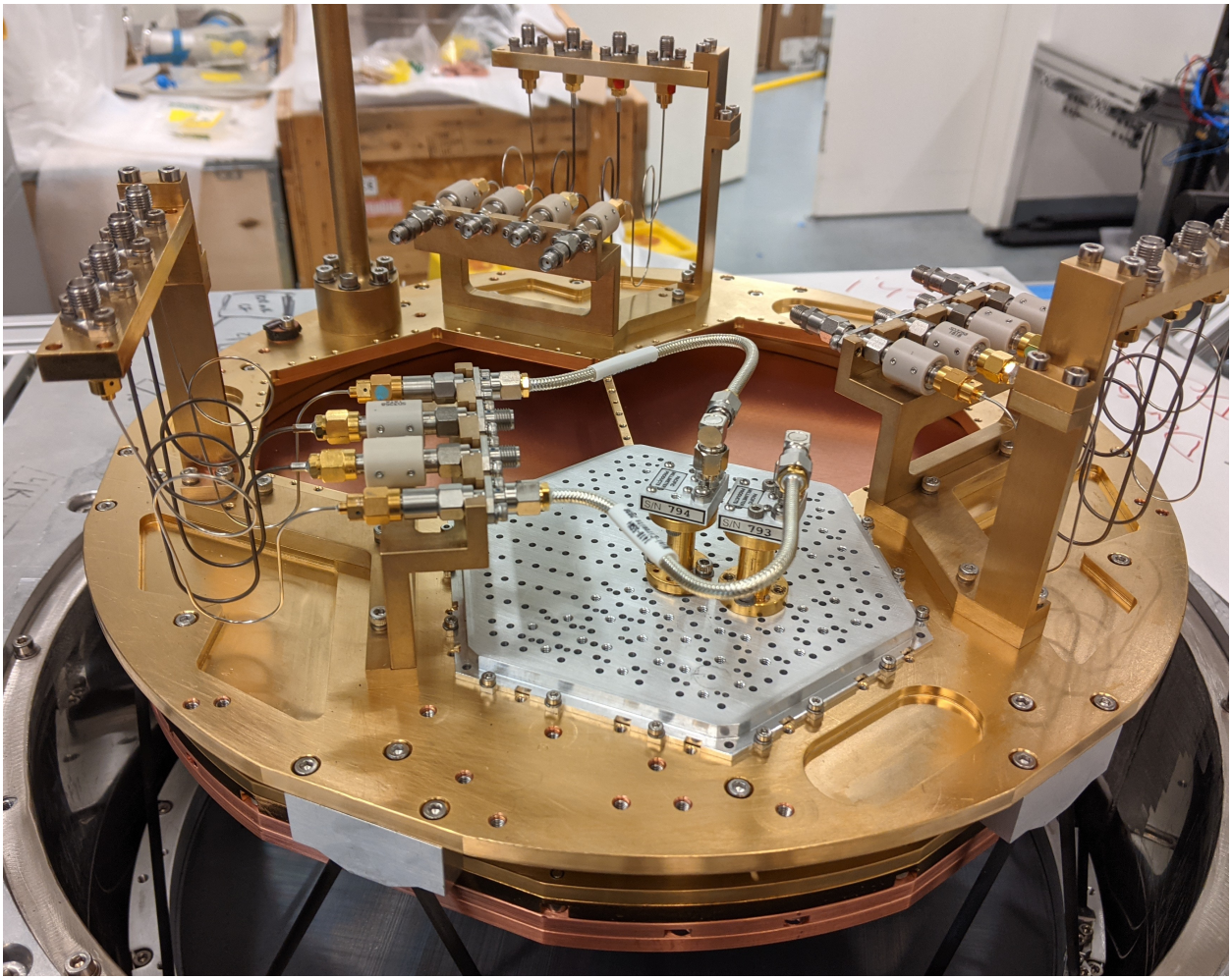

Figure A.1: The Simons Observatory Large Aperture Telescope optics tube focal plane readout, which is cooled to 4 K during measurements. The holography receivers (two receivers for redundancy) are approximately 7.4 cm from the center of the focal plane.

The signal from the source(receiver) needs to be amplified due to high loss levels in the coax path from the harmonic mixer on the source to the reference mixer-diplexer (LATRt readout chain). To overcome this loss, amplifiers with attenuators increase the signal in the RF chain prior to entering the mixer diplexer. The setup uses low phase variation coaxial cables leftover from the DASI experiment [128]. The phase repeatability of the holography setup is within $\approx 3^{\circ}$. We further note that any drift in the map would present itself in the phase map. This phase drift would be removed during the propagation into the far-field when we optimize the position of the beam map in the LAT focal plane.

The source moves in a 2-D grid above the LATRt with motorized XY stages [129]. The source mounts to the stages such that the signal points downwards towards the LATRt window. The laboratory is over 7.5 m tall, and therefore we expect reflection from the walls to be diffuse. Therefore, the reflected signal is diluted before reflecting into the testing system. The dominant reflections are from reflections within the optics tube, as the hexagon side-lobe is the dominant side-lobe feature in the beam maps (Figure 5.4). Figure A.1 shows the holography receiver readout at the back of the optics tube focal plane. An SO MF feedhorn array is adapted for the holography experiment. On the readout side of the array, attachment screws are added for attaching a circular to rectangular transition waveguide. The transition waveguide connects the back of the focal plane (circular) to the GaAs W-band harmonic mixer (rectangular). Though the design of the W-band harmonic mixer is optimized for F90 frequency readout, the W-band harmonic mixer is used for both F90 and F150 measurements (the entire SO MF band), allowing for a wider band of measurements without separate LATRt cool-downs.

A.2 Forward Modelling

As introduced in Section 5.4. 5.4.2, the holography source emits from a rectangular feedhorn, and therefore result in a convolution of the electromagnetic field from the optics tube with the field pattern on the feedhorn aperture. Convolving the simulated fields increases the F90(150) far-field beam by 12.2(4.7)% and results in horizontal and vertical diffraction spikes in the raw far-field calculation [78].

We carry out the forward modelling by building a simulation of the optics tube beam pattern at the measurement plane. This model includes an empirical model of the scattering of the optics tube with the hexagonal outline to model the boundary of the optics tube window, and a similar amplitude and phase to what is measured. The resulting simulated F90(150) beam matched the measured FWHP beam width within in 1.73(0.7)%. The simu-

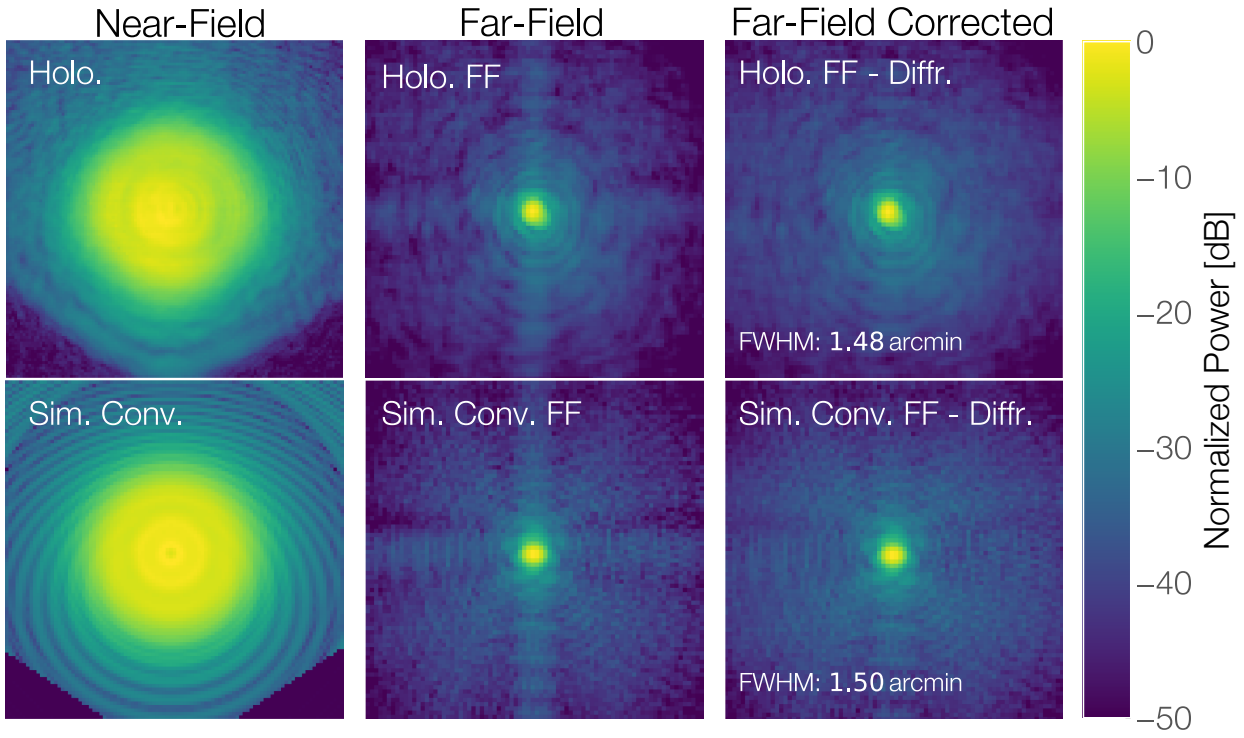

Figure A.2: Forward modelling method with the F150 band-averaged holography data. Column 1: Near-field holography data(top) and convolved simulation with a scattering term(bottom). Square is 12×12 cm. Column 2: Far-field holography data(top) and convolved simulation with a scattering term(bottom). Diffraction spikes consistent with a convolution from a square aperture are present in both the measured far-fields and the simulated far-fields, due to the source horn having a rectangular aperture face. Square is 20×20 arcmin. Column 3: Far-field holography data with diffraction model removal(top) and convolved simulation with a scattering term with diffraction model removal(bottom). Square is 20×20 arcmin.

lation also had the horizontal and vertical diffraction spikes in the far-field due to the impact of the convolution with the holography source feed pattern [78]. The full forward modelling process is shown in Figure A.2.

For visualization purposes, these spikes are removed by subtracting a model $D(\theta_x, \theta_y)$ (amplitude of the electric field) consisting of a sinc function with a Gaussian width along its narrow direction equal to the beam width (Eq. A.1), where θ_x and θ_y are elevation and azimuth, and we fit the 2 parameters σ_{θ_x} and σ_{θ_y}. This model is based on the predicted Fraunhofer diffraction pattern from a rectangular aperture [78] (e.g., the feed) and was shown

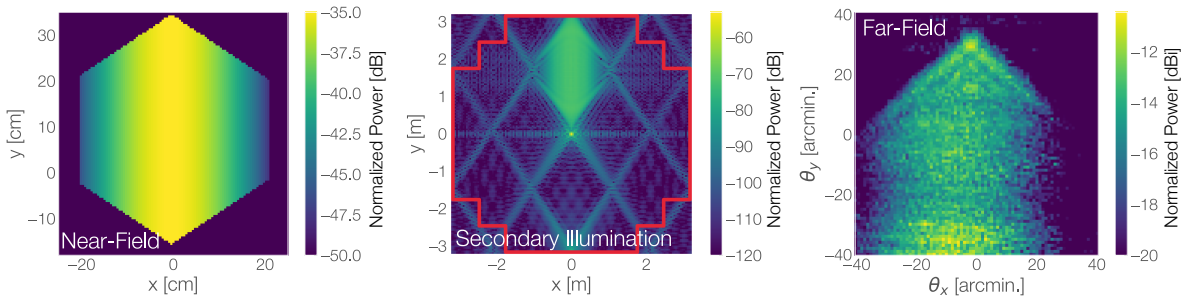

Figure A.3: Simulated scattering term (power) in the near-field(left), at the secondary illumination(middle) and propagated to the far-field(right). Each subplot is the band-averaged simulation over all F150 frequencies.

to match the simulations.

$$D(\theta_x, \theta_y) = \exp^{-(\theta_x^2/4\sigma_{\theta_x}^2 + \theta_y^2/4\sigma_{\theta_y}^2)} \operatorname{sinc}\theta_x \operatorname{sinc}\theta_y \tag{A.1}$$

The holography measurements showed scattering from within the optics tube (hexagonal shape at -20 dB in Figure 5.4). To understand how this scattering propagates through the telescope, we add a scattering term (with both amplitude and phase) to the simulated beam, and then propagate this beam into the far-field. We also investigate how the sidelobes measured outside the main beam (Fig. 5.4) propagate into the far-field (Fig. A.3). Reflections are known to be a problem in near-field beam mapping [73–75]. However, the inferred amplitude of the probe is small, and we do not correct for reflections. The sidelobe spreads out and is localized to 2 meters from the center of the primary and secondary mirrors, and then leads to a 0.85° diffuse structure on the sky that is at the ≈ -15 dBi level.

A.3 Measurement Requirements

Here, we discuss the measurement requirements to meet specific far-field grid resolution and range from near-field data. Near-field beams with three signal-to-noise levels are propagated into the far-field (for 90 and 150 GHz near-field beams); we simulate the near-fields to have 20, 40, and 60 dB signal-to-noise. The signal-to-noise propagated to the secondary

illumination and far-field is listed in Table A.1.

F [GHz]	S/N [dB]		
	NF	Sec.	FF
90	20	21.7	40.0
	40	37.0	43.9
	60	45.4	43.9
150	20	18.0	39.3
	40	35.5	43.8
	60	46.0	43.8

Table A.1: Near-field simulated measurement signal-to-noise and resulting simulated sidelobe power (at the secondary illumination and into the far-field). Signal-to-noise is calculated as the standard deviation of the signal outside an 8.5 cm radius of the peak-normalized beam (same resolution as Table A.2).

When planning the near-field scan, we consider the resolution and how the near-field grid propagates into the plane of the secondary, due to the Fourier relationship between near- and far-fields (Eq. 5.1), and into the telescope's far-field through the modeling described in Section 5.4.2. Table A.2 summarizes the scan size and resolutions and resulting far-field size and resolution grids used in the holography measurements presented here. When planning

F [GHz]	NF [cm]		Sec. [m]		FF [arcmin]	
	Size	Res.	Size	Res.	Size	Res.
90	50	0.25	9.52	0.13	119.72	0.60
150	50	0.20	6.66	0.06	128.40	0.52

Table A.2: Near-field scan size and resolution, and resulting scan size and resolution at the secondary illumination and in the far-field.

the near-field scan, we consider the resolution and how the near-field grid propagates into the far-field, due to the Fourier relationship between near- and far-fields (Eq. 5.1). Table A.2 summarizes the scan size and resolutions and resulting far-field size and resolution grids used in the holography measurements.

Appendix B

Holography Receiver Polarization Through the Large Aperture Telescope Optics Tube

Using the holography experiment, we obtain measurements for the cross-polarization of the LATR tester, including holography linearly polarized source, dielectric polarizing grid, optics tube, and holography receiver. In order to model the polarization response in the setup, we employ Mueller matrix math to modulate the Stokes parameters of the signal throughout the setup.

Here, we derive each component of the polarization modulation using Mueller matrix notation [130]. This model is then fit to the measured response through the polarized grid in the LATR tester optics tube, using the same holography receiver. The power measured by the detector P_d can be modelled as a series of polarization modulations:

$$P_{\mathrm{d}}(\theta) = \vec{S}_d(\phi_d, \epsilon) \cdot \vec{M}_{\mathrm{OT}} \cdot \vec{M}_g(\theta, \eta_g) \cdot \vec{S}_s \tag{B.1}$$

where the source emits the Stokes parameters $\vec{S}_s$, which is then modulated by the grid $\vec{M}_g$. The field then enters the optics tube $\vec{M}_{\mathrm{OT}}$ and is measured by the detector $\vec{M}_d$. These data

were used to quantify the grid efficiency η_g, the cross-polarization of the instrument ϵ (this can be complex), and the tilt-offset of the holography detector ϕ_d. We are fitting our data to this model, where we fit the 3 parameters ϵ, η_g, and ϕ_d.

B.1 General Notation

B.1.1 Stokes Parameters

First, let's define our basis of Stokes parameters and how they physically relate to our setup. The Stokes parameters are:

$$\begin{aligned} I &= |E_x|^2 + |E_y|^2 \\ Q &= |E_x|^2 - |E_y|^2 \\ U &= E_x E_y^* + E_x^* E_y \\ V &= i(E_x E_y^* - E_x^* E_y) \end{aligned} \tag{B.2}$$

B.1.2 Jones into Mueller Matrix

To derive the model, we employ Mueller matrix notation. We often start by modeling a component by its Jones matrix, then converting to its Mueller matrix to interact with the Stokes parameters of the setup. Therefore, here I review this conversion. Converting the Jones matrix J to Mueller matrix M:

$$M = A(J \otimes J^*)A^{-1} \tag{B.3}$$

with the A matrix:

$$A = \begin{bmatrix} 1 & 0 & 0 & 1 \\ 1 & 0 & 0 & -1 \\ 0 & 1 & 1 & 0 \\ 0 & -i & i & 0 \end{bmatrix} \quad \text{and} \quad A^{-1} = \frac{1}{2} \begin{bmatrix} 1 & 1 & 0 & 0 \\ 0 & 0 & 1 & i \\ 0 & 0 & 1 & -i \\ 1 & -1 & 0 & 0 \end{bmatrix} \tag{B.4}$$

B.1.3 Rotation

We often need to convert our Stokes parameter matrix into an instrument's local coordinate system in order to determine how that instrument will modulate our signal. Therefore, we will often use the rotation matrix:

$$M_{\text{rot}} = \begin{bmatrix} 1 & 0 & 0 & 0 \\ 0 & \cos 2\theta & \sin 2\theta & 0 \\ 0 & -\sin 2\theta & \cos 2\theta & 0 \\ 0 & 0 & 0 & 1 \end{bmatrix} \tag{B.5}$$

B.2 Mueller Matrices

Here we list the individual matrices which make up the full model of the measurement. We use Mueller matrices to modulate the polarization of the holography source $\vec{S}_{co,cr}$.

B.2.1 Polarized Source

The Stokes parameters of a general polarized source are expressed by a matrix $\vec{S}$:

$$\vec{S} = \begin{bmatrix} I & Q & U & V \end{bmatrix}^T \tag{B.6}$$

The holography source, specifically, is linearly polarized (TM-mode) (meaning we only include the I and Q Stokes parameters). The Stokes parameters of a linearly polarized source

along the $\theta = 0^\circ$ axis:

$$\vec{S}_{co} = \begin{bmatrix} 1 & 1 & 0 & 0 \end{bmatrix}^T \tag{B.7}$$

The second source polarization was obtained by adding a waveguide twist directly onto the source's output, prior to the rectangular horn. Therefore, the Stokes parameters of the source in the $\theta = 90^\circ$ axis is modeled as:

$$\vec{S}_{cr} = \begin{bmatrix} 1 & -1 & 0 & 0 \end{bmatrix}^T \tag{B.8}$$

B.2.2 Polarizing Grid

The signal is first modulated by the polarized grid prior to entering the optics tube. The purpose of the grid is to transmit one polarization and reflect the other. However, in the case of an imperfect polarizing grid, some of the 2^{nd} polarization may also transmit (a fraction of the 1^{st} polarization). Therefore, we define the Jones matrix as the following, where the majority of the signal along the x-axis is transmitted ($t_x > t_y$):

$$J_g = \begin{bmatrix} t_x & 0 \\ 0 & t_y \end{bmatrix} \tag{B.9}$$

where $t_x \approx 1$ and $t \approx 0$. Now, as before, we convert to the grid's Mueller matrix:

$$M_g = \frac{1}{2} \begin{bmatrix} |t_x|^2 + |t_y|^2 & |t_x|^2 - |t_y|^2 & 0 & 0 \\ |t_x|^2 - |t_y|^2 & |t_x|^2 + |t_y|^2 & 2\,\mathrm{Re}\{(t_x t_y^*)\} & -2\,\mathrm{Im}\{(t_x t_y^*)\} \\ 0 & 0 & 2\,\mathrm{Im}\{(t_x t_y^*)\} & 2\,\mathrm{Re}\{(t_x t_y^*)\} \end{bmatrix} \tag{B.10}$$

The efficiency of our wire grid is defined by the transmission through the x-axis t_x. We want to determine the grid efficiency from our data, so we can re-write our Mueller matrix as:

$$M_g = \frac{1}{2}\begin{bmatrix} 1 & \eta_g & 0 & 0 \\ \eta_g & 1 & 1-\eta_g^2 & -\sqrt{1-\eta_g^2} \\ 0 & 0 & \sqrt{1-\eta_g^2} & \sqrt{1-\eta_g^2} \end{bmatrix} \tag{B.11}$$

Lastly, we rotate the grid via the $M_{\text{rot}}(\theta)$ matrices:

$$M_g(\theta, \eta_g) = M_{\text{rot}}^T(\theta) \cdot M_g(\eta_g) \cdot M_{\text{rot}}(\theta) \tag{B.12}$$

B.2.3 Optics Tube (Generic Instrument)

To model the polarization modulation from the optics tube, we consider a simple Jones matrix:

$$J_{\text{OT}} = \begin{bmatrix} 1 & 0 \\ 0 & Ae^{i\phi} \end{bmatrix} \tag{B.13}$$

Converting this to a Mueller matrix yields:

$$M_{\text{OT}} = \frac{1}{2}\begin{bmatrix} 1+A^2 & 1-A^2 & 0 & 0 \\ 1-A^2 & 1+A^2 & 0 & 0 \\ 0 & 0 & 2A\cos\phi & 2A\sin\phi \\ 0 & 0 & -2A\sin\phi & 2A\cos\phi \end{bmatrix} \tag{B.14}$$

We define the instrument's polarization as $\lambda_P = \frac{1}{2}\sqrt{1-A^2}$. Here's we only consider $\phi = 0$ or else we would find $A < 1$, which isn't physical in our setup. Our Mueller matrix becomes:

$$\vec{M_{\mathrm{OT}}} = \frac{1}{2}\begin{bmatrix} 1-\lambda_P & \lambda_P & 0 & 0 \\ \lambda_P & 1-\lambda_P & 0 & 0 \\ 0 & 0 & \sqrt{1-2\lambda_P} & 0 \\ 0 & 0 & 0 & \sqrt{1-2\lambda_P} \end{bmatrix} \tag{B.15}$$

Our model for instrument polarization is aligned along a specific axis, so we need to rotate this matrix into the appropriate local coordinate system via the rotation matrix M_{rot}.

B.2.4 Detector

We model the detector as an imperfect polarizer, to include any small cross-polarization from the receiver:

$$J_d = \begin{bmatrix} 1 & 0 \\ 0 & \epsilon \end{bmatrix} \tag{B.16}$$

where $\epsilon = \epsilon_0(\cos\delta + i\sin\delta)$. The Mueller matrix then becomes:

$$M_d = \frac{1}{2}\begin{bmatrix} 1+\epsilon_0^2 & 1-\epsilon_0^2 & 0 & 0 \\ 1-\epsilon_0^2 & 1+\epsilon_0^2 & 0 & 0 \\ 1 & 0 & 2\epsilon_0\cos\delta & 2\epsilon_0\sin\delta \\ 1 & 0 & -2\epsilon_0\sin\delta & 2\epsilon_0\cos\delta \end{bmatrix} \tag{B.17}$$

To simplify this down to one parameter, we define $\epsilon_0^2 = \chi$. We rewrite our Mueller matrix then as:

$$M_d = \frac{1}{2}\begin{bmatrix} 1+\chi & 1-\chi & 0 & 0 \\ 1-\chi & 1+\chi & 0 & 0 \\ 1 & 0 & 2\sqrt{\chi} & 0 \\ 1 & 0 & 0 & 2\sqrt{\chi} \end{bmatrix} \tag{B.18}$$

Because the power out from the detector P_{out} is the I component of the Stoke's parameters, we then get the final $\vec{S}_{\text{out}}$ with:

$$\vec{S}_d(\phi_d, \epsilon) = \begin{bmatrix} 1 & 0 & 0 & 0 \end{bmatrix} \cdot M_d \cdot M_{\text{rot}}(\phi_d) \tag{B.19}$$

B.3 Putting It All Together

Combining all components of the model, we fit the following to our polarization holography data:

$$P_{\text{d}}(\theta) = \vec{S}_d(\phi_d, \epsilon) \cdot \vec{M}_{\text{OT}} \cdot \vec{M}_g(\theta, \eta_g) \cdot \vec{S}_s \tag{B.20}$$

where we fit for detector tilt angle ϕ_d, detector cross-polarization ϵ, and grid efficiency η_g.

Appendix C

Harmonic Transform of the On-Sky Beam

Here we show the derivation to convert our beam $B(\theta)$ to its spherical transform b_ℓ. The spherical harmonics are functions defined on the sphere as

$$Y_{\ell m}(\hat{n}) = P_{\ell m}(\cos\theta)\exp\{im\phi\}\ , \tag{C.1}$$

where $P_{\ell m}$ are the associated Legendre polynomials, ℓ and m are multipoles, and θ and ϕ are standard sky coordinates. The associated Legendre polynomials are defined in terms of Legendre polynomials as:

$$P_{\ell m}(x) = (-1)^m\sqrt{\frac{2\ell+1}{4\pi}}\sqrt{\frac{(\ell-|m|)!}{(\ell+|m|)!}}(1-x^2)^{|m|/2}\frac{d^{|m|}}{dx^{|m|}}P_\ell(x)\ , \tag{C.2}$$

The spherical harmonics are orthonormal, and thus obey the relation

$$\int_0^{2\pi}\int_0^{\pi} Y_{\ell m}(\hat{n})Y^*_{\ell' m'}(\hat{n})\sin\theta\ d\theta\ d\phi = \delta_{\ell\ell'}\delta_{mm'}\ , \tag{C.3}$$

where $\overline{z}$ is the complex conjugate of z and δ_{ij} is the Kronecker symbol.

In a spherical harmonic transform, we compute the coefficients $f_{\ell m}$ used to express a function $f(\hat{n})$ as

$$f(\hat{n}) = \sum_{\ell=0}^{\infty} \sum_{m=-\ell}^{\ell} f_{\ell m} Y_{\ell m}(\hat{n}) \ . \tag{C.4}$$

The coefficients can be computed using the equation

$$f_{\ell m} = \int_0^{2\pi} \int_0^{\pi} f(\hat{n}) Y^*_{\ell m}(\hat{n}) \sin\theta \ d\theta \ d\phi \tag{C.5a}$$

$$= \int_0^{2\pi} \int_0^{\pi} f(\hat{n}) P_{\ell m}(\cos\theta) \exp\{-im\phi\} \sin\theta \ d\theta \ d\phi \ . \tag{C.5b}$$

If $f(\hat{n})$ is independent of ϕ (as is approximately true for our beam), then we can write $f(\hat{n})$ $= f(\theta)$ and the equation above becomes

$$f_{\ell m} = \int_0^{2\pi} \exp\{-im\phi\} d\phi \int_0^{\pi} f(\theta) P_{\ell m}(\cos\theta) \sin\theta \ d\theta \ . \tag{C.6}$$

The integral over ϕ then simplifies to

$$\int_0^{2\pi} e^{-im\phi} \ d\phi = 2\pi\delta_{m0} \ . \tag{C.7}$$

So $f_{\ell m}$ is only non-zero for $m = 0$, in which case we have

$$f_{\ell 0} = 2\pi \int_0^{\pi} f(\theta) P_{\ell 0}(\cos\theta) \sin\theta \ d\theta \tag{C.8a}$$

$$= 2\pi \int_{-1}^{1} f(\theta) P_{\ell 0}(\cos\theta) \ d\cos\theta \ . \tag{C.8b}$$

This is the equation for the spherical harmonic coefficients of an axisymmetric function $f(\theta)$. The coefficients F_ℓ of the Legendre polynomial transform of $f(\theta)$ are related to the spherical harmonic coefficients as:

$$F_\ell = f_{\ell m} \sqrt{\frac{4\pi}{2\ell + 1}} \ . \tag{C.9}$$

The beam transform B_ℓ that is used to describe the convolution of the sky with the telescope's beam is defined as the Legendre polynomial transform of the beam function $B(\theta)$ (see e.g. Eq. 48 in [127]).

References

[1] J. C. Mather, E. S. Cheng, D. A. Cottingham, Jr. Eplee, R. E., D. J. Fixsen, T. Hewagama, R. B. Isaacman, K. A. Jensen, S. S. Meyer, P. D. Noerdlinger, S. M. Read, L. P. Rosen, R. A. Shafer, E. L. Wright, C. L. Bennett, N. W. Boggess, M. G. Hauser, T. Kelsall, Jr. Moseley, S. H., R. F. Silverberg, G. F. Smoot, R. Weiss, and D. T. Wilkinson. Measurement of the Cosmic Microwave Background Spectrum by the COBE FIRAS Instrument. *Astrophysical Journal*, 420:439, 1 1994.

[2] G. F. Smoot, C. L. Bennett, A. Kogut, E. L. Wright, J. Aymon, N. W. Boggess, E. S. Cheng, G. de Amici, S. Gulkis, M. G. Hauser, G. Hinshaw, P. D. Jackson, M. Janssen, E. Kaita, T. Kelsall, P. Keegstra, C. Lineweaver, K. Loewenstein, P. Lubin, J. Mather, S. S. Meyer, S. H. Moseley, T. Murdock, L. Rokke, R. F. Silverberg, L. Tenorio, R. Weiss, and D. T. Wilkinson. Structure in the COBE Differential Microwave Radiometer First-Year Maps. *The Astrophysical Journal*, 396:L1, September 1992.

[3] The Story of Our Universe. `https://www.nasa.gov/mission_pages/planck/multimedia/pia16876b.html`, 2014. Online; accessed January 2023.

[4] Sudeep Das, Thibaut Louis, Michael R. Nolta, Graeme E. Addison, Elia S. Battistelli, J Richard Bond, Erminia Calabrese, Devin Crichton, Mark J. Devlin, Simon Dicker, Joanna Dunkley, Rolando Dünner, Joseph W. Fowler, Megan Gralla, Amir Hajian, Mark Halpern, Matthew Hasselfield, Matt Hilton, Adam D. Hincks, René e Hlozek, Kevin M. Huffenberger, John P. Hughes, Kent D. Irwin, Arthur Kosowsky, Robert H.

Lupton, Tobias A. Marriage, Danica Marsden, Felipe Menanteau, Kavilan Moodley, Michael D. Niemack, Lyman A. Page, Bruce Partridge, Erik D. Reese, Benjamin L. Schmitt, Neelima Sehgal, Blake D. Sherwin, Jonathan L. Sievers, David N. Spergel, Suzanne T. Staggs, Daniel S. Swetz, Eric R. Switzer, Robert Thornton, Hy Trac, and Ed Wollack. The atacama cosmology telescope: temperature and gravitational lensing power spectrum measurements from three seasons of data. *Journal of Cosmology and Astroparticle Physics*, 2014(04):014–014, apr 2014.

[5] Simone Aiola, Erminia Calabrese, Loïc Maurin, Sigurd Naess, Benjamin L. Schmitt, Maximilian H. Abitbol, Graeme E. Addison, Peter A. R. Ade, David Alonso, Mandana Amiri, and et al. The atacama cosmology telescope: Dr4 maps and cosmological parameters. *JCAP*, 2020(12):047, Dec 2020.

[6] Antony Lewis and Anthony Challinor. Code for anisotropies in the microwave background [camb].

[7] D. S. Swetz, P. A. R. Ade, M. Amiri, J. W. Appel, E. S. Battistelli, B. Burger, J. Chervenak, M. J. Devlin, S. R. Dicker, W. B. Doriese, R. Dünner, T. Essinger-Hileman, R. P. Fisher, J. W. Fowler, M. Halpern, M. Hasselfield, G. C. Hilton, A. D. Hincks, K. D. Irwin, N. Jarosik, M. Kaul, J. Klein, J. M. Lau, M. Limon, T. A. Marriage, D. Marsden, K. Martocci, P. Mauskopf, H. Moseley, C. B. Netterfield, M. D. Niemack, M. R. Nolta, L. A. Page, L. Parker, S. T. Staggs, O. Stryzak, E. R. Switzer, R. Thornton, C. Tucker, E. Wollack, and Y. Zhao. Overview of the atacama cosmology telescope: Receiver, instrumentation, and telescope systems. *The Astrophysical Journal Supplement Series*, 194(2):41, jun 2011.

[8] Stephen C. Parshley, Michael Niemack, Richard Hills, Simon R. Dicker, Rolando Dünner, Jens Erler, Patricio A. Gallardo, Jon E. Gudmundsson, Terry Herter, Brian J. Koopman, Michele Limon, Frederick T. Matsuda, Philip Mauskopf, Dominik A. Riechers, Gordon J. Stacey, and Eve M. Vavagiakis. The optical design of the six-meter

CCAT-prime and Simons Observatory telescopes. In Heather K. Marshall and Jason Spyromilio, editors, *Ground-based and Airborne Telescopes VII*, volume 10700, page 1070041. International Society for Optics and Photonics, SPIE, 2018.

[9] Kenji Kiuchi, Shunsuke Adachi, Aamir M. Ali, Kam Arnold, Peter Ashton, Jason E. Austermann, Andrew Bazako, James A. Beall, Yuji Chinone, Gabriele Coppi, Kevin D. Crowley, Kevin T. Crowley, Simon Dicker, Bradley Dober, Shannon M. Duff, Giulio Fabbian, Nicholas Galitzki, Joseph E. Golec, Jon E. Gudmundsson, Kathleen Harrington, Masaya Hasegawa, Makoto Hattori, Charles A. Hill, Shuay-Pwu Patty Ho, Johannes Hubmayr, Bradley R. Johnson, Daisuke Kaneko, Nobuhiko Katayama, Brian Keating, Akito Kusaka, Jack Lashner, Adrian T. Lee, Frederick Matsuda, Heather McCarrick, Masaaki Murata, Federico Nati, Yume Nishinomiya, Lyman Page, Mayuri Sathyanarayana Rao, Christian L. Reichardt, Kana Sakaguri, Yuki Sakurai, Joseph Sibert, Jacob Spisak, Osamu Tajima, Grant P. Teply, Tomoki Terasaki, Tran Tsan, Samantha Walker, Edward J. Wollack, Zhilei Xu, Kyohei Yamada, Mario Zannoni, and Ningfeng Zhu. Simons Observatory Small Aperture Telescope overview. In *Society of Photo-Optical Instrumentation Engineers (SPIE) Conference Series*, volume 11445 of *Society of Photo-Optical Instrumentation Engineers (SPIE) Conference Series*, page 114457L, December 2020.

[10] Zhilei Xu, Tanay Bhandarkar, Gabriele Coppi, Anna Kofman, John Orlowski-Scherer, Ningfeng Zhu, et al. The Simons Observatory: the Large Aperture Telescope Receiver (LATR) integration and validation results. In Jonas Zmuidzinas and Jian-Rong Gao, editors, *Millimeter, Submillimeter, and Far-Infrared Detectors and Instrumentation for Astronomy X*, volume 11453. International Society for Optics and Photonics, SPIE, 2020.

[11] Z. Atkins et al. The Atacama Cosmology Telescope: Map-Based Noise Simulations for DR6. *in preparation*, 2023.

[12] N. Aghanim, Y. Akrami, M. Ashdown, J. Aumont, C. Baccigalupi, M. Ballardini, A. J. Banday, R. B. Barreiro, N. Bartolo, S. Basak, R. Battye, K. Benabed, J.-P. Bernard, M. Bersanelli, P. Bielewicz, J. J. Bock, J. R. Bond, J. Borrill, F. R. Bouchet, F. Boulanger, M. Bucher, C. Burigana, R. C. Butler, E. Calabrese, J.-F. Cardoso, J. Carron, A. Challinor, H. C. Chiang, J. Chluba, L. P. L. Colombo, C. Combet, D. Contreras, B. P. Crill, F. Cuttaia, P. de Bernardis, G. de Zotti, J. Delabrouille, J.-M. Delouis, E. Di Valentino, J. M. Diego, O. Doré, M. Douspis, A. Ducout, X. Dupac, S. Dusini, G. Efstathiou, F. Elsner, T. A. Enßlin, H. K. Eriksen, Y. Fantaye, M. Farhang, J. Fergusson, R. Fernandez-Cobos, F. Finelli, F. Forastieri, M. Frailis, A. A. Fraisse, E. Franceschi, A. Frolov, S. Galeotta, S. Galli, K. Ganga, R. T. Génova-Santos, M. Gerbino, T. Ghosh, J. González-Nuevo, K. M. Górski, S. Gratton, A. Gruppuso, J. E. Gudmundsson, J. Hamann, W. Handley, F. K. Hansen, D. Herranz, S. R. Hildebrandt, E. Hivon, Z. Huang, A. H. Jaffe, W. C. Jones, A. Karakci, E. Keihänen, R. Keskitalo, K. Kiiveri, J. Kim, T. S. Kisner, L. Knox, N. Krachmalnicoff, M. Kunz, H. Kurki-Suonio, G. Lagache, J.-M. Lamarre, A. Lasenby, M. Lattanzi, C. R. Lawrence, M. Le Jeune, P. Lemos, J. Lesgourgues, F. Levrier, A. Lewis, M. Liguori, P. B. Lilje, M. Lilley, V. Lindholm, M. López-Caniego, P. M. Lubin, Y.-Z. Ma, J. F. Macías-Pérez, G. Maggio, D. Maino, N. Mandolesi, A. Mangilli, A. Marcos-Caballero, M. Maris, P. G. Martin, M. Martinelli, E. Martínez-González, S. Matarrese, N. Mauri, J. D. McEwen, P. R. Meinhold, A. Melchiorri, A. Mennella, M. Migliaccio, M. Millea, S. Mitra, M.-A. Miville-Deschênes, D. Molinari, L. Montier, G. Morgante, A. Moss, P. Natoli, H. U. Nørgaard-Nielsen, L. Pagano, D. Paoletti, B. Partridge, G. Patanchon, H. V. Peiris, F. Perrotta, V. Pettorino, F. Piacentini, L. Polastri, G. Polenta, J.-L. Puget, J. P. Rachen, M. Reinecke, M. Remazeilles, A. Renzi, G. Rocha, C. Rosset, G. Roudier, J. A. Rubiño-Martín, B. Ruiz-Granados, L. Salvati, M. Sandri, M. Savelainen, D. Scott, E. P. S. Shellard, C. Sirignano, G. Sirri, L. D. Spencer, R. Sunyaev, A.-S. Suur-Uski, J. A. Tauber, D. Tavagnacco, M. Tenti, L. Toffolatti, M. Tomasi,

T. Trombetti, L. Valenziano, J. Valiviita, B. Van Tent, L. Vibert, P. Vielva, F. Villa, N. Vittorio, B. D. Wandelt, I. K. Wehus, M. White, S. D. M. White, A. Zacchei, and A. Zonca. Planck 2018 results. *Astronomy & Astrophysics*, 641:A6, 9 2020.

[13] S. W. Henderson, R. Allison, J. Austermann, T. Baildon, N. Battaglia, J. A. Beall, D. Becker, F. De Bernardis, J. R. Bond, E. Calabrese, S. K. Choi, K. P. Coughlin, K. T. Crowley, R. Datta, M. J. Devlin, S. M. Duff, J. Dunkley, R. Dünner, A. van Engelen, P. A. Gallardo, E. Grace, M. Hasselfield, F. Hills, G. C. Hilton, A. D. Hincks, R. Hlozek, S. P. Ho, J. Hubmayr, K. Huffenberger, J. P. Hughes, K. D. Irwin, B. J. Koopman, A. B. Kosowsky, D. Li, J. McMahon, C. Munson, F. Nati, L. Newburgh, M. D. Niemack, P. Niraula, L. A. Page, C. G. Pappas, M. Salatino, A. Schillaci, B. L. Schmitt, N. Sehgal, B. D. Sherwin, J. L. Sievers, S. M. Simon, D. N. Spergel, S. T. Staggs, J. R. Stevens, R. Thornton, J. Van Lanen, E. M. Vavagiakis, J. T. Ward, and E. J. Wollack. Advanced ACTPol Cryogenic Detector Arrays and Readout. *Journal of Low Temperature Physics*, 184(3-4):772–779, August 2016.

[14] Jon E. Gudmundsson, Patricio A. Gallardo, Roberto Puddu, Simon R. Dicker, Alexandre E. Adler, Aamir M. Ali, Andrew Bazarko, Grace E. Chesmore, Gabriele Coppi, Nicholas F. Cothard, Nadia Dachlythra, Mark Devlin, Rolando Dünner, Giulio Fabbian, Nicholas Galitzki, Joseph E. Golec, Shuay-Pwu Patty Ho, Peter C. Hargrave, Anna M. Kofman, Adrian T. Lee, Michele Limon, Frederick T. Matsuda, Philip D. Mauskopf, Kavilan Moodley, Federico Nati, Michael D. Niemack, John Orlowski-Scherer, Lyman A. Page, Bruce Partridge, Giuseppe Puglisi, Christian L. Reichardt, Carlos E. Sierra, Sara M. Simon, Grant P. Teply, Carole Tucker, Edward J. Wollack, Zhilei Xu, and Ningfeng Zhu. The Simons Observatory: modeling optical systematics in the Large Aperture Telescope. *Applied Optics*, 60(4):823, February 2021.

[15] Grace E. Chesmore, Adriaan J. Duivenvoorden, et al. The Atacama Cosmology Tele-

scope: Beam Estimation for DR6 with Point Source Stacking. *Journal of Cosmology and Astroparticle Physics*, in progress.

[16] Grace E. Chesmore, Kathleen Harrington, Carlos E. Sierra, Patricio A. Gallardo, Shreya Sutariya, Tommy Alford, Alexandre E. Adler, Tanay Bhandarkar, Gabriele Coppi, Nadia Dachlythra, Joseph Golec, Jon Gudmundsson, Saianeesh K. Haridas, Bradley R. Johnson, Anna M. Kofman, Jeffrey Iuliano, Jeff McMahon, Michael D. Niemack, John Orlowski-Scherer, Karen Perez Sarmiento, Roberto Puddu, Max Silva-Feaver, Sara M. Simon, Julia Robe, Edward J. Wollack, and Zhilei Xu. The simons observatory: Characterizing the large aperture telescope receiver with radio holography, 2022.

[17] Grace E. Chesmore, Alexandre E. Adler, Nicholas F. Cothard, Nadia Dachlythra, Patricio A. Gallardo, Jon Gudmundsson, Bradley R. Johnson, Michele Limon, Jeff McMahon, Federico Nati, Michael D. Niemack, Giuseppe Puglisi, Sara M. Simon, Edward J. Wollack, Kevin Wolz, Zhilei Xu, and Ningfeng Zhu. Simons observatory holosim-ml: machine learning applied to theefficient analysis of radio holography measurements of complex opticalsystems. *Appl. Opt.*, 60(29):9029–9035, Oct 2021.

[18] Zhilei Xu, Grace E. Chesmore, Shunsuke Adachi, Aamir M. Ali, Andrew Bazarko, Gabriele Coppi, Mark Devlin, Tom Devlin, Simon R. Dicker, Patricio A. Gallardo, Joseph E. Golec, Jon E. Gudmundsson, Kathleen Harrington, Makoto Hattori, Anna Kofman, Kenji Kiuchi, Akito Kusaka, Michele Limon, Frederick Matsuda, Jeff McMahon, Federico Nati, Michael D. Niemack, Aritoki Suzuki, Grant P. Teply, Robert J. Thornton, Edward J. Wollack, Mario Zannoni, and Ningfeng Zhu. The simons observatory: metamaterial microwave absorber and its cryogenic applications. *Applied Optics*, 60(4):864, 1 2021.

[19] Grace E. Chesmore, Tony Mroczkowski, Jeff McMahon, Shreya Sutariya, Alec Josaitis, and Leif Jensen. Reflectometry Measurements of the Loss Tangent in Silicon at Mil-

limeter Wavelengths. *Proceedings from the 8th ESA Workshop on Millimetre-Wave Technology and Applications,*, page arXiv:1812.03785, December 2018.

[20] Bernard F. Burke, Francis Graham-Smith, and Peter N. Wilkinson. *An Introduction to Radio Astronomy*. Cambridge University Press, 4 edition, 2019.

[21] S. Weinberg. *Cosmology*. Oxford University Press, 2008.

[22] S. Perlmutter, G. Aldering, G. Goldhaber, R. A. Knop, P. Nugent, P. G. Castro, S. Deustua, S. Fabbro, A. Goobar, D. E. Groom, I. M. Hook, A. G. Kim, M. Y. Kim, J. C. Lee, N. J. Nunes, R. Pain, C. R. Pennypacker, R. Quimby, C. Lidman, R. S. Ellis, M. Irwin, R. G. McMahon, P. Ruiz-Lapuente, N. Walton, B. Schaefer, B. J. Boyle, A. V. Filippenko, T. Matheson, A. S. Fruchter, N. Panagia, H. J. M. Newberg, W. J. Couch, and The Supernova Cosmology Project. Measurements of Ω and Λ from 42 High-Redshift Supernovae. *The Astrophysical Journal*, 517(2):565–586, June 1999.

[23] Boryana Hadzhiyska and David Spergel. Measuring the duration of last scattering. *Physical Review D*, 99(4), feb 2019.

[24] L. Page, G. Hinshaw, E. Komatsu, M. R. Nolta, D. N. Spergel, C. L. Bennett, C. Barnes, R. Bean, O. Dore, J. Dunkley, M. Halpern, R. S. Hill, N. Jarosik, A. Kogut, M. Limon, S. S. Meyer, N. Odegard, H. V. Peiris, G. S. Tucker, L. Verde, J. L. Weiland, E. Wollack, and E. L. Wright. Three year wilkinson microwave anisotropy probe (wmap) observations: Polarization analysis. *The Astrophysical Journal Supplement Series*, 170(2):335–376, jun 2007.

[25] Planck Collaboration, Ade, P. A. R., Aghanim, N., Alves, M. I. R., Armitage-Caplan, C., Arnaud, M., Ashdown, M., Atrio-Barandela, F., Aumont, J., Aussel, H., Baccigalupi, C., Banday, A. J., Barreiro, R. B., Barrena, R., Bartelmann, M., Bartlett, J. G., Bartolo, N., Basak, S., Battaner, E., Battye, R., Benabed, K., Benoît, A., Benoit-Lévy, A., Bernard, J.-P., Bersanelli, M., Bertincourt, B., Bethermin, M., Bielewicz,

P., Bikmaev, I., Blanchard, A., Bobin, J., Bock, J. J., Böhringer, H., Bonaldi, A., Bonavera, L., Bond, J. R., Borrill, J., Bouchet, F. R., Boulanger, F., Bourdin, H., Bowyer, J. W., Bridges, M., Brown, M. L., Bucher, M., Burenin, R., Burigana, C., Butler, R. C., Calabrese, E., Cappellini, B., Cardoso, J.-F., Carr, R., Carvalho, P., Casale, M., Castex, G., Catalano, A., Challinor, A., Chamballu, A., Chary, R.-R., Chen, X., Chiang, H. C., Chiang, L.-Y, Chon, G., Christensen, P. R., Churazov, E., Church, S., Clemens, M., Clements, D. L., Colombi, S., Colombo, L. P. L., Combet, C., Comis, B., Couchot, F., Coulais, A., Crill, B. P., Cruz, M., Curto, A., Cuttaia, F., Da Silva, A., Dahle, H., Danese, L., Davies, R. D., Davis, R. J., de Bernardis, P., de Rosa, A., de Zotti, G., Déchelette, T., Delabrouille, J., Delouis, J.-M., Démoclès, J., Désert, F.-X., Dick, J., Dickinson, C., Diego, J. M., Dolag, K., Dole, H., Donzelli, S., Doré, O., Douspis, M., Ducout, A., Dunkley, J., Dupac, X., Efstathiou, G., Elsner, F., Enßlin, T. A., Eriksen, H. K., Fabre, O., Falgarone, E., Falvella, M. C., Fantaye, Y., Fergusson, J., Filliard, C., Finelli, F., Flores-Cacho, I., Foley, S., Forni, O., Fosalba, P., Frailis, M., Fraisse, A. A., Franceschi, E., Freschi, M., Fromenteau, S., Frommert, M., Gaier, T. C., Galeotta, S., Gallegos, J., Galli, S., Gandolfo, B., Ganga, K., Gauthier, C., Génova-Santos, R. T., Ghosh, T., Giard, M., Giardino, G., Gilfanov, M., Girard, D., Giraud-Héraud, Y., Gjerløw, E., González-Nuevo, J., Górski, K. M., Gratton, S., Gregorio, A., Gruppuso, A., Gudmundsson, J. E., Haissinski, J., Hamann, J., Hansen, F. K., Hansen, M., Hanson, D., Harrison, D. L., Heavens, A., Helou, G., Hempel, A., Henrot-Versillé, S., Hernández-Monteagudo, C., Herranz, D., Hildebrandt, S. R., Hivon, E., Ho, S., Hobson, M., Holmes, W. A., Hornstrup, A., Hou, Z., Hovest, W., Huey, G., Huffenberger, K. M., Hurier, G., Ili´c, S., Jaffe, A. H., Jaffe, T. R., Jasche, J., Jewell, J., Jones, W. C., Juvela, M., Kalberla, P., Kangaslahti, P., Keihänen, E., Kerp, J., Keskitalo, R., Khamitov, I., Kiiveri, K., Kim, J., Kisner, T. S., Kneissl, R., Knoche, J., Knox, L., Kunz, M., Kurki-Suonio, H., Lacasa, F., Lagache, G., Lähteenmäki, A., Lamarre, J.-M., Langer, M., Lasenby, A., Lattanzi, M., Laureijs, R. J.,

Lavabre, A., Lawrence, C. R., Le Jeune, M., Leach, S., Leahy, J. P., Leonardi, R., León-Tavares, J., Leroy, C., Lesgourgues, J., Lewis, A., Li, C., Liddle, A., Liguori, M., Lilje, P. B., Linden-Vørnle, M., Lindholm, V., López-Caniego, M., Lowe, S., Lubin, P. M., Macías-Pérez, J. F., MacTavish, C. J., Maffei, B., Maggio, G., Maino, D., Mandolesi, N., Mangilli, A., Marcos-Caballero, A., Marinucci, D., Maris, M., Marleau, F., Marshall, D. J., Martin, P. G., Martínez-González, E., Masi, S., Massardi, M., Matarrese, S., Matsumura, T., Matthai, F., Maurin, L., Mazzotta, P., McDonald, A., McEwen, J. D., McGehee, P., Mei, S., Meinhold, P. R., Melchiorri, A., Melin, J.-B., Mendes, L., Menegoni, E., Mennella, A., Migliaccio, M., Mikkelsen, K., Millea, M., Miniscalco, R., Mitra, S., Miville-Deschênes, M.-A., Molinari, D., Moneti, A., Montier, L., Morgante, G., Morisset, N., Mortlock, D., Moss, A., Munshi, D., Murphy, J. A., Naselsky, P., Nati, F., Natoli, P., Negrello, M., Nesvadba, N. P. H., Netterfield, C. B., Nørgaard-Nielsen, H. U., North, C., Noviello, F., Novikov, D., Novikov, I., O´Dwyer, I. J., Orieux, F., Osborne, S., O´Sullivan, C., Oxborrow, C. A., Paci, F., Pagano, L., Pajot, F., Paladini, R., Pandolfi, S., Paoletti, D., Partridge, B., Pasian, F., Patanchon, G., Paykari, P., Pearson, D., Pearson, T. J., Peel, M., Peiris, H. V., Perdereau, O., Perotto, L., Perrotta, F., Pettorino, V., Piacentini, F., Piat, M., Pierpaoli, E., Pietrobon, D., Plaszczynski, S., Platania, P., Pogosyan, D., Pointecouteau, E., Polenta, G., Ponthieu, N., Popa, L., Poutanen, T., Pratt, G. W., Prézeau, G., Prunet, S., Puget, J.-L., Pullen, A. R., Rachen, J. P., Racine, B., Rahlin, A., Räth, C., Reach, W. T., Rebolo, R., Reinecke, M., Remazeilles, M., Renault, C., Renzi, A., Riazuelo, A., Ricciardi, S., Riller, T., Ringeval, C., Ristorcelli, I., Robbers, G., Rocha, G., Roman, M., Rosset, C., Rossetti, M., Roudier, G., Rowan-Robinson, M., Rubiño-Martín, J. A., Ruiz-Granados, B., Rusholme, B., Salerno, E., Sandri, M., Sanselme, L., Santos, D., Savelainen, M., Savini, G., Schaefer, B. M., Schiavon, F., Scott, D., Seiffert, M. D., Serra, P., Shellard, E. P. S., Smith, K., Smoot, G. F., Souradeep, T., Spencer, L. D., Starck, J.-L., Stolyarov, V., Stompor, R., Sudiwala, R., Sunyaev, R., Sureau, F.,

Sutter, P., Sutton, D., Suur-Uski, A.-S., Sygnet, J.-F., Tauber, J. A., Tavagnacco, D., Taylor, D., Terenzi, L., Texier, D., Toffolatti, L., Tomasi, M., Torre, J.-P., Tristram, M., Tucci, M., Tuovinen, J., Türler, M., Tuttlebee, M., Umana, G., Valenziano, L., Valiviita, J., Van Tent, B., Varis, J., Vibert, L., Viel, M., Vielva, P., Villa, F., Vittorio, N., Wade, L. A., Wandelt, B. D., Watson, C., Watson, R., Wehus, I. K., Welikala, N., Weller, J., White, M., White, S. D. M., Wilkinson, A., Winkel, B., Xia, J.-Q., Yvon, D., Zacchei, A., Zibin, J. P., and Zonca, A. Planck 2013 results. i. overview of products and scientific results. *A&A*, 571:A1, 2014.

[26] Steve K. Choi, Matthew Hasselfield, Shuay-Pwu Patty Ho, Brian Koopman, Marius Lungu, Maximilian H. Abitbol, Graeme E. Addison, Peter A. R. Ade, Simone Aiola, David Alonso, Mandana Amiri, Stefania Amodeo, Elio Angile, Jason E. Austermann, Taylor Baildon, Nick Battaglia, James A. Beall, Rachel Bean, Daniel T. Becker, J. Richard Bond, Sarah Marie Bruno, Erminia Calabrese, Victoria Calafut, Luis E. Campusano, Felipe Carrero, Grace E. Chesmore, Hsiao-mei Cho, Susan E. Clark, Nicholas F. Cothard, Devin Crichton, Kevin T. Crowley, Omar Darwish, Rahul Datta, Edward V. Denison, Mark J. Devlin, Cody J. Duell, Shannon M. Duff, Adriaan J. Duivenvoorden, Jo Dunkley, Rolando Dünner, Thomas Essinger-Hileman, Max Fankhanel, Simone Ferraro, Anna E. Fox, Brittany Fuzia, Patricio A. Gallardo, Vera Gluscevic, Joseph E. Golec, Emily Grace, Megan Gralla, Yilun Guan, Kirsten Hall, Mark Halpern, Dongwon Han, Peter Hargrave, Shawn Henderson, Brandon Hensley, J. Colin Hill, Gene C. Hilton, Matt Hilton, Adam D. Hincks, Renée Hložek, Johannes Hubmayr, Kevin M. Huffenberger, John P. Hughes, Leopoldo Infante, Kent Irwin, Rebecca Jackson, Jeff Klein, Kenda Knowles, Arthur Kosowsky, Vincent Lakey, Dale Li, Yaqiong Li, Zack Li, Martine Lokken, Thibaut Louis, Amanda MacInnis, Mathew Madhavacheril, Felipe Maldonado, Maya Mallaby-Kay, Danica Marsden, Loïc Maurin, Jeff McMahon, Felipe Menanteau, Kavilan Moodley, Tim Morton, Sigurd Naess, Toshiya Namikawa, Federico Nati, Laura Newburgh, John P. Nibarger, Andrina Nicola,

Michael D. Niemack, Michael R. Nolta, John Orlowski-Sherer, Lyman A. Page, Christine G. Pappas, Bruce Partridge, Phumlani Phakathi, Heather Prince, Roberto Puddu, Frank J. Qu, Jesus Rivera, Naomi Robertson, Felipe Rojas, Maria Salatino, Emmanuel Schaan, Alessandro Schillaci, Benjamin L. Schmitt, Neelima Sehgal, Blake D. Sherwin, Carlos Sierra, Jon Sievers, Cristobal Sifon, Precious Sikhosana, Sara Simon, David N. Spergel, Suzanne T. Staggs, Jason Stevens, Emilie Storer, Dhaneshwar D. Sunder, Eric R. Switzer, Ben Thorne, Robert Thornton, Hy Trac, Jesse Treu, Carole Tucker, Leila R. Vale, Alexander Van Engelen, Jeff Van Lanen, Eve M. Vavagiakis, Kasey Wagoner, Yuhan Wang, Jonathan T. Ward, Edward J. Wollack, Zhilei Xu, Fernando Zago, and Ningfeng Zhu. The Atacama Cosmology Telescope: a measurement of the Cosmic Microwave Background power spectra at 98 and 150 GHz. *Journal of Cosmology and Astroparticle Physics*, 2020(12):045, December 2020.

[27] The Polarbear Collaboration: P. A. R. Ade, Y. Akiba, A. E. Anthony, K. Arnold, M. Atlas, D. Barron, D. Boettger, J. Borrill, S. Chapman, Y. Chinone, M. Dobbs, T. Elleflot, J. Errard, G. Fabbian, C. Feng, D. Flanigan, A. Gilbert, W. Grainger, N. W. Halverson, M. Hasegawa, K. Hattori, M. Hazumi, W. L. Holzapfel, Y. Hori, J. Howard, P. Hyland, Y. Inoue, G. C. Jaehnig, A. H. Jaffe, B. Keating, Z. Kermish, R. Keskitalo, T. Kisner, M. Le Jeune, A. T. Lee, E. M. Leitch, E. Linder, M. Lungu, F. Matsuda, T. Matsumura, X. Meng, N. J. Miller, H. Morii, S. Moyerman, M. J. Myers, M. Navaroli, H. Nishino, A. Orlando, H. Paar, J. Peloton, D. Poletti, E. Quealy, G. Rebeiz, C. L. Reichardt, P. L. Richards, C. Ross, I. Schanning, D. E. Schenck, B. D. Sherwin, A. Shimizu, C. Shimmin, M. Shimon, P. Siritanasak, G. Smecher, H. Spieler, N. Stebor, B. Steinbach, R. Stompor, A. Suzuki, S. Takakura, T. Tomaru, B. Wilson, A. Yadav, and O. Zahn. A measurement of the cosmic microwave background b-mode polarization power spectrum at sub-degree scales with polarbear. *The Astrophysical Journal*, 794(2):171, oct 2014.

[28] Simons Observatory Collaboration et al. The simons observatory: science goals and forecasts. *Journal of Cosmology and Astroparticle Physics*, 2019(02):056–056, 2 2019.

[29] J. W. Fowler, M. D. Niemack, S. R. Dicker, A. M. Aboobaker, P. A. R. Ade, E. S. Battistelli, M. J. Devlin, R. P. Fisher, M. Halpern, P. C. Hargrave, A. D. Hincks, M. Kaul, J. Klein, J. M. Lau, M. Limon, T. A. Marriage, P. D. Mauskopf, L. Page, S. T. Staggs, D. S. Swetz, E. R. Switzer, R. J. Thornton, and C. E. Tucker. Optical design of the atacama cosmology telescope and the millimeter bolometric array camera. *Appl. Opt.*, 46(17):3444–3454, Jun 2007.

[30] R. J. Thornton, P. A. R. Ade, S. Aiola, F. E. Angilè, M. Amiri, J. A. Beall, D. T. Becker, H-M. Cho, S. K. Choi, P. Corlies, K. P. Coughlin, R. Datta, M. J. Devlin, S. R. Dicker, R. Dünner, J. W. Fowler, A. E. Fox, P. A. Gallardo, J. Gao, E. Grace, M. Halpern, M. Hasselfield, S. W. Henderson, G. C. Hilton, A. D. Hincks, S. P. Ho, J. Hubmayr, K. D. Irwin, J. Klein, B. Koopman, Dale Li, T. Louis, M. Lungu, L. Maurin, J. McMahon, C. D. Munson, S. Naess, F. Nati, L. Newburgh, J. Nibarger, M. D. Niemack, P. Niraula, M. R. Nolta, L. A. Page, C. G. Pappas, A. Schillaci, B. L. Schmitt, N. Sehgal, J. L. Sievers, S. M. Simon, S. T. Staggs, C. Tucker, M. Uehara, J. van Lanen, J. T. Ward, and E. J. Wollack. The atacama cosmology telescope: The polarization-sensitive actpol instrument. *The Astrophysical Journal Supplement Series*, 227(2):21, dec 2016.

[31] M. D. Niemack, P. A. R. Ade, J. Aguirre, F. Barrientos, J. A. Beall, J. R. Bond, J. Britton, H. M. Cho, S. Das, M. J. Devlin, S. Dicker, J. Dunkley, R. Dünner, J. W. Fowler, A. Hajian, M. Halpern, M. Hasselfield, G. C. Hilton, M. Hilton, J. Hubmayr, J. P. Hughes, L. Infante, K. D. Irwin, N. Jarosik, J. Klein, A. Kosowsky, T. A. Marriage, J. McMahon, F. Menanteau, K. Moodley, J. P. Nibarger, M. R. Nolta, L. A. Page, B. Partridge, E. D. Reese, J. Sievers, D. N. Spergel, S. T. Staggs, R. Thornton, C. Tucker, E. Wollack, and K. W. Yoon. ACTPol: a polarization-sensitive receiver

for the Atacama Cosmology Telescope. In Wayne S. Holland and Jonas Zmuidzinas, editors, *Millimeter, Submillimeter, and Far-Infrared Detectors and Instrumentation for Astronomy V*, volume 7741, page 77411S. International Society for Optics and Photonics, SPIE, 2010.

[32] Nicholas Galitzki et al. The Simons Observatory: instrument overview. In Jonas Zmuidzinas and Jian-Rong Gao, editors, *Millimeter, Submillimeter, and Far-Infrared Detectors and Instrumentation for Astronomy IX*, volume 10708, pages 1 – 13. International Society for Optics and Photonics, SPIE, 2018.

[33] Ningfeng Zhu, John L. Orlowski-Scherer, Zhilei Xu, Aamir Ali, Kam S. Arnold, Peter C. Ashton, Gabriele Coppi, Mark J. Devlin, Simon Dicker, Nicholas Galitzki, Patricio A. Gallardo, Shawn W. Henderson, Shuay-Pwu Patty Ho, Johannes Hubmayr, Brian Keating, Adrian T. Lee, Michele Limon, Marius Lungu, Philip D. Mauskopf, Andrew J. May, Jeff McMahon, Michael D. Niemack, Lucio Piccirillo, Giuseppe Puglisi, Mayuri Sathyanarayana Rao, Maria Salatino, Max Silva-Feaver, Sara M. Simon, Suzanne Staggs, Robert Thornton, Joel N. Ullom, Eve M. Vavagiakis, Benjamin Westbrook, and Edward J. Wollack. Simons Observatory large aperture telescope receiver design overview. In Jonas Zmuidzinas and Jian-Rong Gao, editors, *Millimeter, Submillimeter, and Far-Infrared Detectors and Instrumentation for Astronomy IX*, volume 10708, page 1070829. International Society for Optics and Photonics, SPIE, 2018.

[34] John L. Orlowski-Scherer, Ningfeng Zhu, Zhilei Xu, et al. Simons Observatory large aperture receiver simulation overview. In Jonas Zmuidzinas and Jian-Rong Gao, editors, *Millimeter, Submillimeter, and Far-Infrared Detectors and Instrumentation for Astronomy IX*, volume 10708, pages 644 – 657. International Society for Optics and Photonics, SPIE, 2018.

[35] Gabriele Coppi, Zhilei Xu, et al. Cooldown strategies and transient thermal simulations

for the Simons Observatory. In Jonas Zmuidzinas and Jian-Rong Gao, editors, *Millimeter, Submillimeter, and Far-Infrared Detectors and Instrumentation for Astronomy IX*, volume 10708, pages 246 – 258. International Society for Optics and Photonics, SPIE, 2018.

[36] Aamir M. Ali et al. Small Aperture Telescopes for the Simons Observatory. *Journal of Low Temperature Physics*, 200(5-6):461–471, April 2020.

[37] P. R. Ade et al. The simons observatory: science goals and forecasts. *Journal of Cosmology and Astroparticle Physics*, 2019(02):056–056, 2 2019.

[38] M. Tucci, L. Toffolatti, G. de Zotti, and E. Martínez-González. High-frequency predictions for number counts and spectral properties of extragalactic radio sources. New evidence of a break at mm wavelengths in spectra of bright blazar sources. *Astronomy and Astrophysics*, 533:A57, September 2011.

[39] D. P. Marrone, J. S. Spilker, C. C. Hayward, J. D. Vieira, M. Aravena, M. L. N. Ashby, M. B. Bayliss, M. Béthermin, M. Brodwin, M. S. Bothwell, J. E. Carlstrom, S. C. Chapman, Chian-Chou Chen, T. M. Crawford, D. J. M. Cunningham, C. De Breuck, C. D. Fassnacht, A. H. Gonzalez, T. R. Greve, Y. D. Hezaveh, K. Lacaille, K. C. Litke, S. Lower, J. Ma, M. Malkan, T. B. Miller, W. R. Morningstar, E. J. Murphy, D. Narayanan, K. A. Phadke, K. M. Rotermund, J. Sreevani, B. Stalder, A. A. Stark, M. L. Strandet, M. Tang, and A. Weiß. Galaxy growth in a massive halo in the first billion years of cosmic history. *Nature*, 553(7686):51–54, dec 2017.

[40] C. Dragone. Offset multireflector antennas with perfect pattern symmetry and polarization discrimination. *The Bell System Technical Journal*, 57(7):2663–2684, 1978.

[41] Michael D. Niemack. Designs for a large-aperture telescope to map the cmb 10 times faster. *Appl. Opt.*, 55(7):1688–1696, 3 2016.

[42] Zhilei Xu, Shunsuke Adachi, Peter Ade, J. A. Beall, Tanay Bhandarkar, J. Richard Bond, Grace E. Chesmore, Yuji Chinone, Steve K. Choi, Jake A. Connors, Gabriele Coppi, Nicholas F. Cothard, Kevin D. Crowley, Mark Devlin, Simon Dicker, Bradley Dober, Shannon M. Duff, Nicholas Galitzki, Patricio A. Gallardo, Joseph E. Golec, Jon E. Gudmundsson, Saianeesh K. Haridas, Kathleen Harrington, Carlos Hervias-Caimapo, Shuay-Pwu Patty Ho, Zachary B. Huber, Johannes Hubmayr, Jeffrey Iuliano, Daisuke Kaneko, Anna M. Kofman, Brian J. Koopman, Jack Lashner, Michele Limon, Michael J. Link, Tammy J. Lucas, Frederick Matsuda, Heather McCarrick, Federico Nati, Michael D. Niemack, John Orlowski-Scherer, Lucio Piccirillo, Karen Perez Sarmiento, Emmanuel Schaan, Maximiliano Silva-Feaver, Rita Sonka, Shreya Sutariya, Osamu Tajima, Grant P. Teply, Tomoki Terasaki, Robert Thornton, Carole Tucker, Joel Ullom, Eve M. Vavagiakis, Michael R. Vissers, Samantha Walker, Zachary Whipps, Edward J. Wollack, Mario Zannoni, Ningfeng Zhu, Andrea Zonca, and The Simons Observatory Collaboration. The simons observatory: The large aperture telescope (lat). *Research Notes of the AAS*, 5(4):100, apr 2021.

[43] Stephen C. Parshley, Jörg Kronshage, James Blair, Terry Herter, Mike Nolta, Gordon J. Stacey, Andrew Bazarko, Frank Bertoldi, Ricardo Bustos, Donald B. Campbell, Scott Chapman, Nicolas Cothard, Mark Devlin, Jens Erler, Michel Fich, Patricio A. Gallardo, Riccardo Giovanelli, Urs Graf, Scott Gramke, Martha P. Haynes, Richard Hills, Michele Limon, Jeffrey G. Mangum, Jeff McMahon, Michael D. Niemack, Thomas Nikola, Markus Omlor, Dominik A. Riechers, Karl Steeger, Jürgen Stutzki, and Eve M. Vavagiakis. CCAT-prime: a novel telescope for sub-millimeter astronomy. In Heather K. Marshall and Jason Spyromilio, editors, *Ground-based and Airborne Telescopes VII*, volume 10700, page 107005X. International Society for Optics and Photonics, SPIE, 2018.

[44] Herter Terry, Nicholas Battaglia, Kaustuv Basu, Benjamin Beringue, Frank Bertoldi,

Scott Chapman, Steve Choi, Nicholas Cothard, Dongwoo Chung, Jens Erler, Michel Fich, Simon Foreman, Patricio Gallardo, Jiansong Gao, Urs Graf, Martha Haynes, Terry Herter, Gene Hilton, Johannes Hubmayr, Doug Johnstone, Eiichiro Komatsu, Benjamin Magnelli, Phil Mauskopf, Jeffrey McMahon, Daan Meerburg, Joel Meyers, Avirukt Mittal, Michael Niemack, Thomas Nikola, Stephen Parshley, Dominik Riechers, Gordon Stacey, Juergen Stutzki, Eve Vavagiakis, Marco Viero, and Michael Vissers. The CCAT-Prime Submillimeter Observatory. In *Bulletin of the American Astronomical Society*, volume 51, page 213, September 2019.

[45] Ningfeng Zhu, Tanay Bhandarkar, Gabriele Coppi, Anna M. Kofman, John L. Orlowski-Scherer, Zhilei Xu, Shunsuke Adachi, Peter Ade, Simone Aiola, Jason Austermann, Andrew O. Bazarko, James A. Beall, Sanah Bhimani, J. Richard Bond, Grace E. Chesmore, Steve K. Choi, Jake Connors, Nicholas F. Cothard, Mark Devlin, Simon Dicker, Bradley Dober, Cody J. Duell, Shannon M. Duff, Rolando Dünner, Giulio Fabbian, Nicholas Galitzki, Patricio A. Gallardo, Joseph E. Golec, Saianeesh K. Haridas, Kathleen Harrington, Erin Healy, Shuay-Pwu Patty Ho, Zachary B. Huber, Johannes Hubmayr, Jeffrey Iuliano, Bradley R. Johnson, Brian Keating, Kenji Kiuchi, Brian J. Koopman, Jack Lashner, Adrian T. Lee, Yaqiong Li, Michele Limon, Michael Link, Tammy J. Lucas, Heather McCarrick, Jenna Moore, Federico Nati, Laura B. Newburgh, Michael D. Niemack, Elena Pierpaoli, Michael J. Randall, Karen Perez Sarmiento, Lauren J. Saunders, Joseph Seibert, Carlos Sierra, Rita Sonka, Jacob Spisak, Shreya Sutariya, Osamu Tajima, Grant P. Teply, Robert J. Thornton, Tran Tsan, Carole Tucker, Joel Ullom, Eve M. Vavagiakis, Michael R. Vissers, Samantha Walker, Benjamin Westbrook, Edward J. Wollack, and Mario Zannoni. The Simons Observatory Large Aperture Telescope Receiver. *The Astrophysical Journal Supplement Series*, 256(1):23, September 2021.

[46] Heather McCarrick, Erin Healy, Zeeshan Ahmed, Kam Arnold, Zachary Atkins, Ja-

son E. Austermann, Tanay Bhandarkar, James A. Beall, Sarah Marie Bruno, Steve K. Choi, Jake Connors, Nicholas F. Cothard, Kevin D. Crowley, Simon Dicker, Bradley Dober, Cody J. Duell, Shannon M. Duff, Daniel Dutcher, Josef C. Frisch, Nicholas Galitzki, Megan B. Gralla, Jon E. Gudmundsson, Shawn W. Henderson, Gene C. Hilton, Shuay-Pwu Patty Ho, Zachary B. Huber, Johannes Hubmayr, Jeffrey Iuliano, Bradley R. Johnson, Anna M. Kofman, Akito Kusaka, Jack Lashner, Adrian T. Lee, Yaqiong Li, Michael J. Link, Tammy J. Lucas, Marius Lungu, J. A. B. Mates, Jeffrey J. McMahon, Michael D. Niemack, John Orlowski-Scherer, Joseph Seibert, Maximiliano Silva-Feaver, Sara M. Simon, Suzanne Staggs, Aritoki Suzuki, Tomoki Terasaki, Robert Thornton, Joel N. Ullom, Eve M. Vavagiakis, Leila R. Vale, Jeff Van Lanen, Michael R. Vissers, Yuhan Wang, Edward J. Wollack, Zhilei Xu, Edward Young, Cyndia Yu, Kaiwen Zheng, and Ningfeng Zhu. The simons observatory microwave squid multiplexing detector module design. *The Astrophysical Journal*, 922(1):38, 9 2021.

[47] R. Datta, C. D. Munson, M. D. Niemack, J. J. McMahon, J. Britton, E. J. Wollack, J. Beall, M. J. Devlin, J. Fowler, P. Gallardo, J. Hubmayr, K. Irwin, L. Newburgh, J. P. Nibarger, L. Page, M. A. Quijada, B. L. Schmitt, S. T. Staggs, R. Thornton, and L. Zhang. Large-aperture wide-bandwidth antireflection-coated silicon lenses for millimeter wavelengths. *Appl. Opt.*, 52(36):8747–8758, Dec 2013.

[48] Joseph E. Golec, Jeffrey J. McMahon, Aamir M. Ali, Grace E. Chesmore, Leah Cooperrider, Simon Dicker, Nicholas Galitzki, Kathleen Harrington, Rebecca Jackson, Benjamin Westbrook, Edward J. Wollack, Zhilei Xu, and Ningfeng Zhu. Design and fabrication of metamaterial anti-reflection coatings for the Simons Observatory. In Ramón Navarro and Roland Geyl, editors, *Advances in Optical and Mechanical Technologies for Telescopes and Instrumentation IV*, volume 11451, pages 1115 – 1122. International Society for Optics and Photonics, SPIE, 2020.

[49] Jeffrey Iuliano, Joseph Eimer, Lucas Parker, Gary Rhoades, Aamir Ali, John W. Appel,

Charles Bennett, Michael Brewer, Ricardo Bustos, David Chuss, Joseph Cleary, Julianna Couto, Sumit Dahal, Kevin Denis, Rolando Dünner, Thomas Essinger-Hileman, Pedro Fluxa, Mark Halpern, Kathleen Harrington, Kyle Helson, Gene Hilton, Gary Hinshaw, Johannes Hubmayr, John Karakla, Tobias Marriage, Nathan Miller, Jeffrey John McMahon, Carolina Nuñez, Ivan Padilla, Gonzalo Palma, Matthew Petroff, Bastian Pradenas Márquez, Rodrigo Reeves, Carl Reintsema, Karwan Rostem, Deniz Augusto Nunes Valle, Trevor Van Engelhoven, Bingjie Wang, Qinan Wang, Duncan Watts, Janet Weiland, Edward J. Wollack, Zhilei Xu, Ziang Yan, and Lingzhen Zeng. The Cosmology Large Angular Scale Surveyor receiver design. In Jonas Zmuidzinas and Jian-Rong Gao, editors, *Millimeter, Submillimeter, and Far-Infrared Detectors and Instrumentation for Astronomy IX*, volume 10708, page 1070828. International Society for Optics and Photonics, SPIE, 2018.

[50] Elmer H. Sharp, Dominic J. Benford, Dale J. Fixsen, Stephen F. Maher, Catherine T. Marx, Johannes G. Staguhn, and Edward J. Wollack. Design and performance of a high-throughput cryogenic detector system. In William D. Duncan, Wayne S. Holland, Stafford Withington, and Jonas Zmuidzinas, editors, *Millimeter and Submillimeter Detectors and Instrumentation for Astronomy IV*, volume 7020 of *Society of Photo-Optical Instrumentation Engineers (SPIE) Conference Series*, page 70202L, July 2008.

[51] E. J. Wollack, D. J. Fixsen, R. Henry, A. Kogut, M. Limon, and P. Mirel. Electromagnetic and thermal properties of a conductively loaded epoxy. *International Journal of Infrared and Millimeter Waves*, 29(1):51–61, Jan 2008.

[52] Matthew Petroff, John Appel, Karwan Rostem, Charles L. Bennett, Joseph Eimer, Tobias Marriage, Joshua Ramirez, and Edward J. Wollack. A 3D-printed broadband millimeter wave absorber. *Review of Scientific Instruments*, 90(2):024701, February 2019.

[53] E. J. Wollack, A. M. Datesman, C. A. Jhabvala, K. H. Miller, and M. A. Quijada.

A broadband micro-machined far-infrared absorber. *Review of Scientific Instruments*, 87(5):054701, 2016.

[54] Fei Ding, Yanxia Cui, Xiaochen Ge, Yi Jin, and Sailing He. Ultra-broadband microwave metamaterial absorber. *Applied Physics Letters*, 100(10):103506, 2012.

[55] Claire M. Watts, Xianliang Liu, and Willie J. Padilla. Metamaterial electromagnetic wave absorbers. *Advanced Materials*, 24(23):OP98–OP120, 2012.

[56] E. M. Vavagiakis et al. Prime-Cam: a first-light instrument for the CCAT-prime telescope. In Jonas Zmuidzinas and Jian-Rong Gao, editors, *Millimeter, Submillimeter, and Far-Infrared Detectors and Instrumentation for Astronomy IX*, volume 10708, pages 187 – 202. International Society for Optics and Photonics, SPIE, 2018.

[57] Optica. Metamaterial tiles boost sensitivity of large telescopes. *Applied Optics*, 60, 1 2021.

[58] Charles A. Hill, Sarah Marie M. Bruno, Sara M. Simon, et al. BoloCalc: a sensitivity calculator for the design of Simons Observatory. In Jonas Zmuidzinas and Jian-Rong Gao, editors, *Millimeter, Submillimeter, and Far-Infrared Detectors and Instrumentation for Astronomy IX*, volume 10708, pages 698 – 718. International Society for Optics and Photonics, SPIE, 2018.

[59] Alan W. Smith and Ned S. Rasor. Observed dependence of the low-temperature thermal and electrical conductivity of graphite on temperature, type, neutron irradiation, and bromination. *Phys. Rev.*, 104:885–891, Nov 1956.

[60] A. Sihvola. *Electromagnetic Mixing Formulas and Applications*. Institution of Engineering and Technology, London, United Kingdom, Electromagnetic Wave Series edition, 2008.

[61] Casper ROACH (Reconfigurable Open Architecture Computing Hardware). https://casper.berkeley.edu/wiki/ROACH, 2013.

[62] David T. Chuss, Karwan Rostem, Edward J. Wollack, Leah Berman, Felipe Colazo, Martin DeGeorge, Kyle Helson, and Marco Sagliocca. A cryogenic thermal source for detector array characterization. *Review of Scientific Instruments*, 88(10):104501, 2017.

[63] Jussi Säily and Antti V. Räisänen. Characterization of submillimeter wave absorbers from 200–600 ghz. *International Journal of Infrared and Millimeter Waves*, 25(1):71–88, 1 2004.

[64] V. V. Parshin, R. Heidinger, B. A. Andreev, A. V. Gusev, and V. B. Shmagin. Silicon as an advanced window material for high power gyrotrons. *International Journal of Infrared and Millimeter Waves*, 16(5):863–877, May 1995.

[65] James W. Lamb. Miscellaneous data on materials for millimetre and submillimetre optics. *International Journal of Infrared and Millimeter Waves*, 17(12):1997–2034, December 1996.

[66] Jerzy Krupka, Waldemar Karcz, Paweł Kamiński, and Leif Jensen. Electrical properties of as-grown and proton-irradiated high purity silicon. *Nuclear Instruments and Methods in Physics Research Section B: Beam Interactions with Materials and Atoms*, 380:76–83, 2016.

[67] Topsil Global Wafers. Topsil FZ-HIRES. http://www.topsil.com/en/silicon-products/silicon-wafer-products.aspx. Online; accessed January 2023.

[68] John David Jackson. *Classical Electrodynamics*, chapter 7, pages 302–306. Wiley, New York, NY, 3rd edition, 1999.

[69] Anand Patil, David Huard, and Christopher J Fonnesbeck. Pymc: Bayesian stochastic modeling in python. *Journal of statistical software*, 35 4:1–81, 2010.

[70] J. W. Baars, R. Lucas, Mangum J. G., and Lopez-Perez J. A. Near-field radio holography of large reflector antennas. *IEEE Antennas and Propagation Magazine*, 10 2007.

[71] B. Nikolic, R. E. Hills, and J. S. Richer. Measurement of antenna surfaces from in- and out-of-focus beam maps using astronomical sources. *Astronomy & Astrophysics*, 465(2):679–683, 4 2007.

[72] N. G. Czakon, A. Vayonakis, J. Schlaerth, M. I. Hollister, S. Golwala, P. K. Day, J.-S. Gao, J. Glenn, H. LeDuc, P. R. Maloney, B. Mazin, O. Noroozian, H. T. Nguyen, J. Sayers, J. E. Vaillancourt, and J. Zmuidzinas. Microwave kinetic inductance detector (mkid) camera testing for submillimeter astronomy. *AIP Conference Proceedings*, 1185(1):172–175, 2009.

[73] S. J. C. Yates, K. K. Davis, W. Jellema, J. J. A. Baselmans, and A. M. Baryshev. Complex Beam Mapping and Fourier Optics Analysis of a Wide-Field Microwave Kinetic Inductance Detector Camera. *Journal of Low Temperature Physics*, 199(1-2):156–163, February 2020.

[74] Kristina K. Davis, Willem Jellema, Stephen J. C. Yates, Lorenza Ferrari, Jochem J. A. Baselmans, Kotaro Kohno, David Thoen, Vignesh Murugesan, and Andrey M. Baryshev. Proof-of-concept demonstration of vector beam pattern measurements of kinetic inductance detectors. *IEEE Transactions on Terahertz Science and Technology*, 7(1):98–106, 2017.

[75] R.L. Mitchell. On the reduction of stray signal errors in antenna pattern measurements. *IEEE Transactions on Antennas and Propagation*, 43(6):629–630, 1995.

[76] M. Pantaleev, M. Fredrixon, M. Svensson, C. Risacher, V. Vasilev, and V. Belitsky. Scalar beam pattern measurements for characterization of sub-millimeter receivers. In *2006 First European Conference on Antennas and Propagation*, pages 1–6, 2006.

[77] Yoav Shechtman, Yonina C. Eldar, Oren Cohen, Henry Nicholas Chapman, Jianwei Miao, and Mordechai Segev. Phase retrieval with application to optical imaging: A contemporary overview. *IEEE Signal Processing Magazine*, 32(3):87–109, 2015.

[78] Joseph W Goodman. *Introduction to Fourier Optics*. W.H. Freeman, New York, NY, 3 edition, January 2005.

[79] Optica. New analysis approach could help boost sensitivity of large telescopes. *Applied Optics*, 61, 12 2022.

[80] Peter A. R. Ade, Giampaolo Pisano, Carole Tucker, and Samuel Weaver. A review of metal mesh filters. In Jonas Zmuidzinas, Wayne S. Holland, Stafford Withington, and William D. Duncan, editors, *Millimeter and Submillimeter Detectors and Instrumentation for Astronomy III*, volume 6275, pages 248 – 262. International Society for Optics and Photonics, SPIE, 2006.

[81] Sara M. Simon, Joseph E. Golec, Aamir Ali, Jason Austermann, James A. Beall, Sarah Marie M. Bruno, Steve K. Choi, Kevin T. Crowley, Simon Dicker, Bradley Dober, Shannon M. Duff, Erin Healy, Charles A. Hill, Shuay-Pwu Patty Ho, Johannes Hubmayr, Yaqiong Li, Marius Lungu, Jeff McMahon, John Orlowski-Scherer, Maria Salatino, Suzanne Staggs, Edward J. Wollack, Zhilei Xu, and Ningfeng Zhu. Feedhorn development and scalability for Simons Observatory and beyond. In Jonas Zmuidzinas and Jian-Rong Gao, editors, *Millimeter, Submillimeter, and Far-Infrared Detectors and Instrumentation for Astronomy IX*, volume 10708, pages 787 – 798. International Society for Optics and Photonics, SPIE, 2018.

[82] Erin Healy, Daniel Dutcher, Zachary Atkins, Jason Austermann, Steve K. Choi, Cody J. Duell, Shannon Duff, Nicholas Galitzki, Zachary B. Huber, Johannes Hubmayr, Bradley R. Johnson, Heather McCarrick, Michael D. Niemack, Rita Sonka, Suzanne T. Staggs, Eve Vavagiakis, Yuhan Wang, Zhilei Xu, and Kaiwen Zheng. The

Simons Observatory 220 and 280 GHz Focal-Plane Module: Design and Initial Characterization. *Journal of Low Temperature Physics*, 209(5-6):815–823, December 2022.

[83] Joseph E. Golec, Shreya Sutariya, Rebecca Jackson, Jerry Zimmerman, Simon R. Dicker, Jeffrey Iuliano, Jeff McMahon, Giuseppe Puglisi, Carole Tucker, and Edward J. Wollack. Simons Observatory: broadband metamaterial antireflection cuttings for large-aperture alumina optics. *Applied Optics*, 61(30):8904, 10 2022.

[84] Joseph E. Golec, Jeffrey J. McMahon, Aamir M. Ali, Grace E. Chesmore, Leah Cooperrider, Simon Dicker, Nicholas Galitzki, Kathleen Harrington, Rebecca Jackson, Benjamin Westbrook, Edward J. Wollack, Zhilei Xu, and Ningfeng Zhu. Design and fabrication of metamaterial anti-reflection coatings for the Simons Observatory. In Ramón Navarro and Roland Geyl, editors, *Advances in Optical and Mechanical Technologies for Telescopes and Instrumentation IV*, volume 11451, pages 1115 – 1122. International Society for Optics and Photonics, SPIE, 2020.

[85] Zhilei Xu, Grace E. Chesmore, Shunsuke Adachi, Aamir M. Ali, Andrew Bazarko, Gabriele Coppi, Mark Devlin, Tom Devlin, Simon R. Dicker, Patricio A. Gallardo, Joseph E. Golec, Jon E. Gudmundsson, Kathleen Harrington, Makoto Hattori, Anna Kofman, Kenji Kiuchi, Akito Kusaka, Michele Limon, Frederick Matsuda, Jeff McMahon, Federico Nati, Michael D. Niemack, Aritoki Suzuki, Grant P. Teply, Robert J. Thornton, Edward J. Wollack, Mario Zannoni, and Ningfeng Zhu. The simons observatory: metamaterial microwave absorber and its cryogenic applications. *Appl. Opt.*, 60(4):864–874, 2 2021.

[86] S. R. Dicker, P. A. Gallardo, J. E Gudmundsson, P. D. Mauskopf, A. Ali, P. C. Ashton, G. Coppi, M. J. Devlin, N. Galitzki, S. P. Ho, C. A. Hill, J. Hubmayr, B. Keating, A. T. Lee, M. Limon, F. Matsuda, J. McMahon, M. D. Niemack, J. L. Orlowski-Scherer, L. Piccirillo, M. Salatino, S. M. Simon, S. T. Staggs, R. Thornton, J. N.

Ullom, E. M. Vavagiakis, E. J. Wollack, Z. Xu, and N. Zhu. Cold optical design for the large aperture simons observatory telescope, 2019.

[87] Kathleen Harrington, Carlos Sierra, Grace Edith Chesmore, Shreya Sutariya, et al. The integration and testing program for the simons observatory large aperture telescope optics tubes. *Millimeter, Submillimeter, and Far-Infrared Detectors and Instrumentation for Astronomy X*, Dec 2020.

[88] G. E. Chesmore and McMahonCosmologyGroup. Open source holography. `https://github.com/McMahonCosmologyGroup/holog-exp`, 2022.

[89] Gordon McIntosh. Essential radio astronomy. *American Journal of Physics*, 84(12):975–975, 2016.

[90] E. Joy, W. Leach, and G. Rodrigue. Applications of probe-compensated near-field measurements. *IEEE Transactions on Antennas and Propagation*, 26(3):379–389, 1978.

[91] Majid Karimipour, Nader Komjani, and Iman Aryanian. Shaping electromagnetic waves with flexible and continuous control of the beam directions using holography and convolution theorem. *Scientific Reports*, 9, 2019.

[92] G. E. Chesmore and McMahonCosmologyGroup. The simons observatory: Large aperture telescope receiver tester - holography modeling software. `https://github.com/McMahonCosmologyGroup/solat-optics`, 2022.

[93] Marius Lungu, Emilie R. Storer, Matthew Hasselfield, Adriaan J. Duivenvoorden, Erminia Calabrese, Grace E. Chesmore, Steve K. Choi, Jo Dunkley, Rolando Dünner, Patricio A. Gallardo, Joseph E. Golec, Yilun Guan, J. Colin Hill, Adam D. Hincks, Johannes Hubmayr, Mathew S. Madhavacheril, Maya Mallaby-Kay, Jeff McMahon, Kavilan Moodley, Sigurd Naess, Federico Nati, Michael D. Niemack, Lyman A. Page, Bruce Partridge, Roberto Puddu, Alessandro Schillaci, Cristóbal Sifón, Suzanne Staggs,

Dhaneshwar D. Sunder, Edward J. Wollack, and Zhilei Xu. The Atacama Cosmology Telescope: Measurement and Analysis of 1D Beams for DR4. *arXiv e-prints*, page arXiv:2112.12226, December 2021.

[94] Zeemax. `https://www.zemax.com/`, 2021.

[95] Charles R. Harris, K. Jarrod Millman, Stéfan J van der Walt, Ralf Gommers, Pauli Virtanen, David Cournapeau, Eric Wieser, Julian Taylor, Sebastian Berg, Nathaniel J. Smith, Robert Kern, Matti Picus, Stephan Hoyer, Marten H. van Kerkwijk, Matthew Brett, Allan Haldane, Jaime Fernández del Río, Mark Wiebe, Pearu Peterson, Pierre Gérard-Marchant, Kevin Sheppard, Tyler Reddy, Warren Weckesser, Hameer Abbasi, Christoph Gohlke, and Travis E. Oliphant. Array programming with NumPy. *Nature*, 585:357–362, 2020.

[96] Pauli Virtanen, Ralf Gommers, Travis E. Oliphant, Matt Haberland, Tyler Reddy, David Cournapeau, Evgeni Burovski, Pearu Peterson, Warren Weckesser, Jonathan Bright, Stéfan J. van der Walt, Matthew Brett, Joshua Wilson, K. Jarrod Millman, Nikolay Mayorov, Andrew R. J. Nelson, Eric Jones, Robert Kern, Eric Larson, C J Carey, İlhan Polat, Yu Feng, Eric W. Moore, Jake VanderPlas, Denis Laxalde, Josef Perktold, Robert Cimrman, Ian Henriksen, E. A. Quintero, Charles R. Harris, Anne M. Archibald, Antônio H. Ribeiro, Fabian Pedregosa, Paul van Mulbregt, and SciPy 1.0 Contributors. SciPy 1.0: Fundamental Algorithms for Scientific Computing in Python. *Nature Methods*, 17:261–272, 2020.

[97] John D Hunter. Matplotlib: A 2d graphics environment. *Computing in science & engineering*, 9(3):90–95, 2007.

[98] The pandas development team. pandas-dev/pandas: Pandas, February 2020.

[99] Lisandro Dalcín, Rodrigo Paz, and Mario Storti. Mpi for python. *Journal of Parallel and Distributed Computing*, 65(9):1108–1115, 2005.

[100] Casper da Costa-Luis, Stephen Karl Larroque, Kyle Altendorf, Hadrien Mary, richardsheridan, Mikhail Korobov, Noam Yorav-Raphael, Ivan Ivanov, Marcel Bargull, Nishant Rodrigues, Guangshuo CHEN, Antony Lee, Charles Newey, James, Joshua Coales, Martin Zugnoni, Matthew D. Pagel, mjstevens777, Mikhail Dektyarev, Alex Rothberg, Alexander, Daniel Panteleit, Fabian Dill, FichteFoll, Gregor Sturm, HeoHeo, Hugo van Kemenade, Jack McCracken, MapleCCC, and Max Nordlund. tqdm: A fast, Extensible Progress Bar for Python and CLI, September 2021.

[101] G. E. Chesmore and McMahonCosmologyGroup. Latrt holography data and analysis code. `http://knowledge.uchicago.edu/record/3557?&ln=en`, 2022.

[102] G. E. Chesmore and McMahonCosmologyGroup. The simons observatory: Sarge aperture telescope - holography modeling software. `https://github.com/McMahonCosmologyGroup/sosat-optics`, 2022.

[103] Vertex Antennentechnik GmbH. Duisburg, Germany. `https://www.vertexant.com/`, 2021.

[104] David Woody, Dan MacDonald, Matt Bradford, Richard Chamberlin, Mark Dragovan, Paul Goldsmith, James Lamb, Simon Radford, and Jonas Zmuidzinas. Panel options for large precision radio telescopes. In Eli Atad-Ettedgui and Dietrich Lemke, editors, *Advanced Optical and Mechanical Technologies in Telescopes and Instrumentation*. SPIE, July 2008.

[105] Tirupati K. Sridharan, Masao Saito, Nimesh A. Patel, et al. Holographic surface setting of the Sub-millimeter Array antennas. In Joseph Antebi and Dietrich Lemke, editors, *Astronomical Structures and Mechanisms Technology*, volume 5495, pages 441 – 446. International Society for Optics and Photonics, SPIE, 2004.

[106] A. V. Räisänen and J. Ala-Laurinaho. Holographic principles in antenna metrology

at millimeter and submillimeter wavelengths. In *2015 9th European Conference on Antennas and Propagation (EuCAP)*, pages 1–2, 2015.

[107] G. R. Harp, R. F. Ackermann, Z. J. Nadler, Samantha K. Blair, M. M. Davis, M. C. H. Wright, J. R. Forster, D. R. DeBoer, W. J. Welch, Shannon Atkinson, D. C. Backer, P. R. Backus, William Barott, Amber Bauermeister, Leo Blitz, D. C.-J. Bock, Geoffrey C. Bower, Tucker Bradford, Calvin Cheng, Steve Croft, Matt Dexter, John Dreher, Greg Engargiola, E. D. Fields, Carl Heiles, Tamara Helfer, Jane Jordan, Susan Jorgensen, Tom Kilsdonk, Colby Gutierrez-Kraybill, Garrett Keating, Casey Law, John Lugten, D. H. E. MacMahon, Peter McMahon, Oren Milgrome, Andrew Siemion, Ken Smolek, Douglas Thornton, Tom Pierson, Karen Randall, John Ross, Seth Shostak, J. C. Tarter, Lynn Urry, Dan Werthimer, Peter K. G. Williams, and David Whysong. Primary beam and dish surface characterization at the allen telescope array by radio holography. *IEEE Transactions on Antennas and Propagation*, 59(6):2004–2021, 2011.

[108] D. Morris. Phase retrieval in the radio holography of reflector antennas and radio telescopes. *IEEE Transactions on Antennas and Propagation*, 33(7):749–755, 1985.

[109] J. R. Fienup. Phase-retrieval algorithms for a complicated optical system. *Appl. Opt.*, 32(10):1737–1746, 4 1993.

[110] J. Bennett, A. Anderson, P. McInnes, and A. Whitaker. Microwave holographic metrology of large reflector antennas. *IEEE Transactions on Antennas and Propagation*, 24(3):295–303, 1976.

[111] Todd R. Hunter, Frederic R. Schwab, Steven D. White, John M. Ford, Frank D. Ghigo, Ronald J. Maddalena, Brian S. Mason, Jack D. Nelson, Richard M. Prestage, Jason Ray, Paul Ries, Robert Simon, Sivasankaran Srikanth, and Peter Whiteis. Holographic measurement and improvement of the green bank telescope surface. *Publications of the Astronomical Society of the Pacific*, 123(907):1087–1099, September 2011.

[112] Y. Rahmat-Samii and J. Lemanczyk. Application of spherical near-field measurements to microwave holographic diagnosis of antennas. *IEEE Transactions on Antennas and Propagation*, 36(6):869–878, 1988.

[113] Xiaodong Ren, Pablo Astudillo, Urs U. Graf, et al. Holographic surface measurement system for the Fred Young Submillimeter Telescope. In Heather K. Marshall, Jason Spyromilio, and Tomonori Usuda, editors, *Ground-based and Airborne Telescopes VIII*, volume 11445, pages 1129 – 1147. International Society for Optics and Photonics, SPIE, 2020.

[114] E. Serabyn, T. G. Phillips, and C. R. Masson. Surface figure measurements of radio telescopes with a shearing interferometer. *Appl. Opt.*, 30(10):1227–1241, 4 1991.

[115] J. Ruze. Antenna tolerance theory—a review. *Proceedings of the IEEE*, 54(4):633–640, 1966.

[116] Eugene Hecht. *Optics, 5th Edition*. Pearson Education Limited, 2017.

[117] McMahonCosmologyGroup Github. `https://github.com/McMahonCosmologyGroup/holosim-ml`, 2021.

[118] J. E. Carlstrom, P. A. R. Ade, K. A. Aird, et al. The 10 meter south pole telescope. *Publications of the Astronomical Society of the Pacific*, 123(903):568–581, May 2011.

[119] F. Pedregosa, G. Varoquaux, A. Gramfort, V. Michel, B. Thirion, O. Grisel, M. Blondel, P. Prettenhofer, R. Weiss, V. Dubourg, J. Vanderplas, A. Passos, D. Cournapeau, M. Brucher, M. Perrot, and E. Duchesnay. Scikit-learn: Machine learning in Python. *Journal of Machine Learning Research*, 12:2825–2830, 2011.

[120] Matthew Hasselfield, Kavilan Moodley, J. Richard Bond, Sudeep Das, Mark J. Devlin, Joanna Dunkley, Rolando Dunner, Joseph W. Fowler, Patricio Gallardo, Megan B. Gralla, Amir Hajian, Mark Halpern, Adam D. Hincks, Tobias A. Marriage, Danica

Marsden, Michael D. Niemack, Michael R. Nolta, Lyman A. Page, Bruce Partridge, Benjamin L. Schmitt, Neelima Sehgal, Jon Sievers, Suzanne T. Staggs, Daniel S. Swetz, Eric R. Switzer, and Edward J. Wollack. The atacama cosmology telescope: Beam measurements and the microwave brightness temperatures of uranus and saturn. *ApJS*, 209(1):17, Oct 2013.

[121] Thibaut Louis, Emily Grace, Matthew Hasselfield, Marius Lungu, Loïc Maurin, Graeme E. Addison, Peter A. R. Ade, Simone Aiola, Rupert Allison, Mandana Amiri, and et al. The atacama cosmology telescope: two-season actpol spectra and parameters. *JCAP*, 2017(06):031, Jun 2017.

[122] Sigurd Naess, Matthew Hasselfield, Jeff McMahon, Michael D. Niemack, Graeme E. Addison, Peter A. R. Ade, Rupert Allison, Mandana Amiri, Nick Battaglia, James A. Beall, and et al. The atacama cosmology telescope: Cmb polarization at $200 < \ell < 9000$. *JCAP*, 2014(10):007, Oct 2014.

[123] Marius Lungu, Emilie R. Storer, Matthew Hasselfield, Adriaan J. Duivenvoorden, Erminia Calabrese, Grace E. Chesmore, Steve K. Choi, Jo Dunkley, Rolando Dünner, Patricio A. Gallardo, Joseph E. Golec, Yilun Guan, J. Colin Hill, Adam D. Hincks, Johannes Hubmayr, Mathew S. Madhavacheril, Maya Mallaby-Kay, Jeff McMahon, Kavilan Moodley, Sigurd Naess, Federico Nati, Michael D. Niemack, Lyman A. Page, Bruce Partridge, Roberto Puddu, Alessandro Schillaci, Cristóbal Sifón, Suzanne Staggs, Dhaneshwar D. Sunder, Edward J. Wollack, and Zhilei Xu. The atacama cosmology telescope: measurement and analysis of 1d beams for dr4. *Journal of Cosmology and Astroparticle Physics*, 2022(05):044, may 2022.

[124] Sigurd K. Næss. How to avoid X'es around point sources in maximum likelihood CMB maps. *Journal of Cosmology and Astroparticle Physics*, 2019(12):060, December 2019.

[125] Martin Bucher and Thibaut Louis. Filling in cosmic microwave background map miss-

ing data using constrained Gaussian realizations. *MNRAS*, 424(3):1694–1713, August 2012.

[126] Jonathan R Shewchuk. An introduction to the conjugate gradient method without the agonizing pain. Technical report, Carnegie Mellon University, USA, 1994.

[127] Anthony Challinor, Pablo Fosalba, Daniel Mortlock, Mark Ashdown, Benjamin Wandelt, and Krzysztof Górski. All-sky convolution for polarimetry experiments. *PRD*, 62(12):123002, December 2000.

[128] Sarah Church, Peter Ade, James Bock, Melanie Bowden, John Carlstrom, Ken Ganga, Walter Gear, James Hinderks, Wayne Hu, Brian Keating, John Kovac, Andrew Lange, Eric Leitch, Olivier Mallie, Simon Melhuish, Anthony Murphy, Ben Rusholme, Creidhe O'Sullivan, Lucio Piccirillo, Clem Pryke, Andy Taylor, and Keith Thompson. Quest on dasi: a south pole cmb polarization experiment. *New Astronomy Reviews*, 47(11):1083–1089, 2003. Proceedings of the Workshop on The Cosmic Microwave Background Radiation and its Polarization.

[129] Lintech Manufacturing. Screw driven linear motorized tables. `https://www.lintechmotion.com/products2.cfm?ModelNo=160&t=Group6`, 2022.

[130] B. N. Simon, S. Simon, N. Mukunda, F. Gori, M. Santarsiero, R. Borghi, and R. Simon. A complete characterization of pre-mueller and mueller matrices in polarization optics. *J. Opt. Soc. Am. A*, 27(2):188–199, 2 2010.